

NUREG/CR-3816 (3 of 4)

SAND84-1072 (3 of 4)

R3, R7

Printed May 1985

Reactor Safety Research Quarterly Report Reactor Safety Research Program July - September 1984 Volume 31

Reactor Safety Research Department 6420

Prepared by
Sandia National Laboratories
Albuquerque, New Mexico 87185 and Livermore, California 94550
for the United States Department of Energy
under Contract DE-AC04-76DP00789

8507250114 850731
PDR NUREG
CR-3816 R PDR

Prepared for
U. S. NUCLEAR REGULATORY COMMISSION

NOTICE

This report was prepared as an account of work sponsored by an agency of the United States Government. Neither the United States Government nor any agency thereof, or any of their employees, makes any warranty, expressed or implied, or assumes any legal liability or responsibility for any third party's use, or the results of such use, of any information, apparatus product or process disclosed in this report, or represents that its use by such third party would not infringe privately owned rights.

Available from
Superintendent of Documents
U.S. Government Printing Office
Post Office Box 37082
Washington, D.C. 20013-7982
and
National Technical Information Service
Springfield, VA 22161

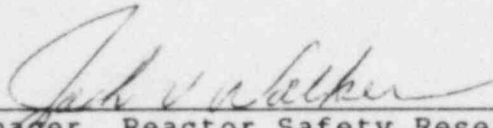
NUREG/CR-3816 (3 of 4)
SAND84-1072 (3 of 4)
Vol. 31
R3 and R7

REACTOR SAFETY RESEARCH
QUARTERLY REPORT
REACTOR SAFETY RESEARCH PROGRAM

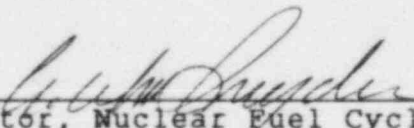
July-September 1984

Printed: May 1985

APPROVED:



Manager, Reactor Safety Research



Director, Nuclear Fuel Cycle Programs

Sandia National Laboratories
Albuquerque, NM 87185
Operated by
Sandia Corporation
for the
U.S. Department of Energy

Prepared for
Division of Accident Evaluation
Office of Nuclear Regulatory Research
U.S. Nuclear Regulatory Commission
Washington, DC 20555
NRC FIN Nos.

(A-1016, A-1019, A-1030, D-1124, A-1181, A-1218,
A-1227, A-1246, A-1263, A-1264, A-1335, A-1390,
A-1342, A-1383, A-1385, A-1389, A-1390, A-1396)

PREVIOUS DOCUMENTS IN SERIES

Reactor Safety Research Quarterly Report January-March 1984,
Vol. 29, NUREG/CR-3816 (1 of 4), SAND84-1072 (1 of 4),
Sandia National Laboratories, Albuquerque, NM, October 1984.

Reactor Safety Research Quarterly Report April-June 1984,
Vol. 30, NUREG/CR-3816 (2 of 4), SAND84-1072 (2 of 4),
Sandia National Laboratories, Albuquerque, NM, December 1984.

FOREWORD

Sandia National Laboratories is conducting, under the USNRC's sponsorship, phenomenological research related to the safety of commercial nuclear power reactors. The research includes experiments to simulate the phenomenology of accident conditions and the development of analytical models, verified by experiment, which can be used to predict reactor and safety systems performance and behavior under abnormal conditions. The objective of this work is to provide NRC requisite data bases and analytical methods to: (1) identify and define safety issues, (2) understand the progression of risk-significant accident sequences, and (3) conduct safety assessments. The collective NRC-sponsored effort at Sandia National Laboratories, is directed at enhancing the technology base supporting licensing decisions.

CONTENTS

	<u>Page</u>
EXECUTIVE SUMMARY.	1
1. CONTAINMENT LOADING AND RESPONSE	23
1.1 Ex-Vessel Core Debris Interactions.	23
1.2 Molten Core-Concrete Interactions	37
1.3 Molten Fuel-Coolant Interactions.	38
1.4 Hydrogen Behavior	52
1.5 Hydrogen Mitigative and Preventive Schemes. .	78
2. FISSION-PRODUCT SOURCE TERM.	105
2.1 High-Temperature Fission-Product Chemistry and Transport	105
2.2 Quantitative Uncertainty Estimation for the Source Term (QUEST)	107
2.3 ACRR Source Term Experiments.	112
3. LWR DAMAGED FUEL PHENOMENOLOGY	122
3.1 ACRR Damaged Fuel Relocation and Quench . . .	122
3.2 ACRR LWR Degraded Core Coolability.	129
4. MELT PROGRESSION CODE DEVELOPMENT (MELPROG). . . .	146
4.1 MELPROG Code Development	148
4.2 Code Testing	149
4.3 Code Applications	150
5. ADVANCED REACTOR ACCIDENT ENERGETICS	152
5.1 Initiation Phase.	152
5.2 Transition Phase.	158
6. POSTACCIDENT HEAT REMOVAL.	164
6.1 Debris Bed Coolability.	164
6.2 Dry Debris Melt Progression	168

LIST OF FIGURES

<u>Figure</u>	<u>Page</u>
1.1 The Large-Scale Melt Facility for Conducting the TURC Tests	25
1.2 Experimental and Predicted Thermocouple Data for the TURC-2 Test.	29
1.3 The Ratio of CO to CO ₂ in the TURC-2 Test as a Function of Time.	31
1.4 The Predicted Dehydration Front Location in the TURC-2 Experiment.	36
1.5 The Predicted Heat Losses for the TURC-2 Experiment	36
1.6 The CORCON Prediction of the Ablation Front in the TURC-2 Experiment.	39
1.7 EXO-FITS II Facility	41
1.8 Experimental Setup	43
1.9 Effect of Baking the Iron Oxide.	49
1.10 Effect of Available Oxygen	50
1.11 Correction on Total Emittance for Band Overlap When Both CO ₂ and Steam Are Present.	55
1.12 Comparative Total Gas Emittance Calculations for Different Pressure and Beam Length Conditions. .	57
1.13 Comparative Pressure Profile for the NTS Pre- mixed Test P21	59
1.14 Comparative Temperature Profile for the NTS Premixed Test P21.	60
1.15 Measured Peak Overpressures in the FLAME Facility	63
1.16 Equivalent Planar Flame Speed for Several Top Venting Areas.	64
1.17 Variation of the Maximum Steady-State Flame Velocity With Mixture Composition in Hydrogen- Air and Hydrocarbon-Air Mixtures	67

LIST OF FIGURES (continued)

<u>Figure</u>		<u>Page</u>
1.18	Variation of the Maximum Steady-State Flame Velocity for Methane-Air Mixtures in Different Diameter Flame Tubes	68
1.19	Variation of the Maximum Steady-State Flame Velocity for Propane-Air Mixtures in Different Diameter Flame Tubes	69
1.20	Maximum Flame Velocities and Transition to Detonation in Hydrogen-Air Mixtures in Different Diameter Flame Tubes	71
1.21	Correlation of Experimental Maximum Flame Velocity and Overpressure With Numerical Simulation for Hydrogen-Air Mixtures in the 5-cm-Diameter Flame Tube	72
1.22	H ₂ -Air-H ₂ O Detonation Cell Size vs. Equivalence Ratio.	76
1.23	Detonation Velocity vs. %H ₂	77
1.24	Finite Difference Grid for an Axisymmetric Simulation of an Empty Sequoya Containment Building	80
1.25	Droplet Diameter Distribution Used in the Baseline Calculation	82
1.26	Position of Spray Droplet Parcels in the Baseline Calculation	84
1.27	Droplet Parcel Velocities in the Baseline Calculation	85
1.28	Air Flow Pattern in the Baseline Calculation	86
1.29	Contour Plot of the Magnitude of Air Velocity in the Baseline Calculation	87
1.30	Radial Velocity vs. Radius in the Baseline Calculation	88
1.31	Axial Velocity vs. Radius in the Baseline Calculation for Three Different Elevations.	89
1.32	Droplet Parcel Velocities for the Calculation With Ice Condensers, Steam Generator Doghouses, and Concentrated Spray Rings	92

LIST OF FIGURES (continued)

<u>Figure</u>	<u>Page</u>
1.33 Air Flow Pattern for the Calculation With Ice Condensers, Steam Generator Doghouses, and Concentrated Spray Rings	93
1.34 Contour Plot of the Magnitude of Air Velocity for the Calculation With Ice Condensers, Steam Generator Doghouses, and Concentrated Spray Rings.	94
1.35 Radial Velocity for the Calculation With Ice Condensers, Steam Generator Doghouses, and Concentrated Spray Rings	95
1.36 View of Spinning Disc Water Drop Generators Installed in Mockup of FITS Combustion Chamber .	97
1.37 Schematic Top View of the Spinning Disc Water Drop Generators Installed in the Plastic Bag Mockup of the FITS Combustion Chamber.	99
1.38 Aerosol Diameter Distribution Obtained With a Cascade Impactor Just Prior to a Hydrogen Burn in the VGES Combustion Chamber	101
2.1 Elemental Distributions of Tellurium and Nickel on the Surface of a 304SS Coupon Exposed in Steam at 700°C	106
2.2 Correlation of Tellurium and Nickel Contents of Local Areas Seen in Figure 2.1	108
2.3 Scatter in Available Data for the Release of Iodine From Fuel	115
3.1 DF-1 Posttest Analysis	124
3.2 View of a Vertical Cut Through Rod 6 Near the 660 mm Cross Section Showing Pellet Bonding. . .	125
3.3 Cross-Section Diagrams of the Experiment, Taken at Six Different Axial Locations	127
3.4 Detail of Cladding to the Right of Rod 9 in the 193 mm Cross Section	129
3.5 Predicted DCC-3 Fluxes (100°C)	133
3.6 Predicted DCC-3 Fluxes (150°C)	133

LIST OF FIGURES (continued)

<u>Figure</u>	<u>Page</u>
3.7 Predicted DCC-3 Fluxes (200°C)	134
3.8 Predicted DCC-3 Fluxes (250°C)	134
3.9 Predicted DCC-3 Fluxes (285°C)	135
3.10 Saturation Profile for a Homogeneous Bed	136
3.11 Saturation Profile for a Stratified Bed.	136
3.12 Dry Zones and Channel Lengths (1.0 DO Flux, 100°C)	139
3.13 Dry Zones and Channel Lengths (1.1 DO Flux, 100°C)	139
3.14 Dry Zones and Channel Lengths (1.0 DO Flux, 285°C)	140
3.15 Dry Zones and Channel Lengths (1.1 DO Flux, 285°C)	140
3.16 Initial Average Fuel Temperature vs. Liquid Inventory.	142
3.17 Vapor Volume After Quench.	142
5.1 Entrainment Forces for a Liquid Cladding Drop on a Flat Surface of UO ₂	154
5.2 Liquid Cladding Entrainment Criterion Used in SANDCMOT Compared to Ishii's Criterion	155
5.3 SAND: IN/CMOT Calculated Clad Motion With Entrainment for STAR-1	157
5.4 Cross Section of the Freezing Channel.	160
6.1 DC-2 Thermocouple Data	170
6.2 DC-2 Ultrasonic Thermometer Data	170

LIST OF TABLES

<u>Table</u>	<u>Page</u>
1.1 The TURC Test Matrix.	24
1.2 Fission-Product Mocks	27
1.3 Gas Analysis Data for TURC-2 Test	30
1.4 Partial Elemental Composition List.	32
1.5 Primary Experimental Values	45
1.6 Secondary Experimental Values	46
1.7 Past Iron Oxide Purchasing Data	46
1.8 Chemical Analysis of the Iron Oxides.	47
1.9 Absorption Band Centers for Radiating Gases . . .	54
2.1 Conditions Expected to Result in High or Low Source Terms for Grand Gulf TC Sequence	109
2.2 Final Distribution of Fission Products In Grand Gulf TC Base Case--(BMI-2104)	111
2.3 Final Distribution of Fission Products in Grand Gulf TC Sequence--"Low" Case.	111
2.4 Final Distribution of Fission Products in Grand Gulf TC Sequence--"High" Case	111
6.1 UO ₂ Particulate for D-13 Bed	167

ACRONYMS

ACRR	- Annular Core Research Reactor
BWR	- Boiling Water Reactor
CEA	- Commissariat a L'Energie Atomique
CDA	- Core Disruptive Accident
CMCI	- Core Melt-Coolant Interaction
CMOT	- Clad Motion Code
CORCON	- Core/Concrete Interaction Code
DCC	- Degraded Core Coolability
DC	- Dry Capsule
DF	- Damaged Fuel
DFR	- Damaged Fuel Relocation
ECCS	- Emergency Core Cooling System
EURATOM	- European Atomic Energy Community
EXO-FITS	- Outside of Fully Instrumented Test Sites
FCI	- Fuel-Coolant Interaction
FITS	- Fully Instrumented Test Site
HECTR	- Hydrogen Event Containment Transient Response
HEDL	- Hanford Engineering Development Laboratory
HIPS	- High Pressure Streaming
INPO	- Institute of Nuclear Power Operation
IRIS	- Inductive Ring Susceptor Technique
KfK	- Kernforschungszentrum Karlsruhe
LCS	- Limestone/Common Sand
LMF	- Large Melt Facility
LMFBR	- Liquid Metal Fast Breeder Reactor
LWR	- Light Water Reactor
MELPROG	- Melt Progression Code
NRC	- Nuclear Regulatory Commission
NTS	- Nevada Test Site
ORNL	- Oak Ridge National Laboratory
PIE	- Postirradiation Examination
PNC	- Power Reactor and Nuclear Fuel Development Corporation
PRA	- Probabilistic Risk Assessment
PWR	- Pressurized Water Reactor
QUEST	- Quantitative Uncertainty Evaluation for the Source Term
RSR	- Reactor Safety Research
RPV	- Reactor Pressure Vessel
S/A	- Subassembly
SPIT	- System Pressure Injection Test
STAR	- Sandia Transient Axial Relocation
SWISS	- Sustained Water Interactions with Stainless Steel
TMBDB	- Thermal Margin Beyond Design Basis
TRAN	- Transition Phase
TURC	- Transient Urania Concrete
TWT	- Transient Water Tests
UT	- Ultrasonic Thermometer
VGES	- Variable Geometry Experimental System

EXECUTIVE SUMMARY

1. CONTAINMENT LOADING AND RESPONSE

1.1 Ex-Vessel Core Debris Interactions

A comprehensive experimental program in which steel melts interact with concrete has provided quantitative observations that are the basis of two important severe accident analysis codes: the CORCON model of core debris-concrete interactions and the VANESA model of radionuclide release and aerosol generation. Since core debris ejected from a reactor vessel would be expected to contain UO_2 , ZrO_2 , and Zr metal (as well as stainless steel), it is desirable to investigate molten oxide and metal core debris-concrete interactions. The establishment of an adequate data base of these interactions is desirable for validation of the models as well as the identification of other important phenomena.

An experiment description, presentation of results, and an analysis of the results using a heat balance approach for the TURC-2 test are presented. TURC-2, a transient UO_2/ZrO_2 concrete interaction test, showed no ablation for the duration of the test. Calculations indicated that stable crusting occurred immediately and prevented any erosion.

The top of the melt pool showed a convoluted surface, as expected from a frozen liquid. Very little UO_2/ZrO_2 material was found on the side walls of the crucible, and no fragmented debris was found on the top surface. These conditions differ significantly from the posttest melt mass observed of the first large melt facility (LMF) test 10, in which molten UO_2/ZrO_2 was slowly teemed from the LMF melt generator. All observations indicated a very rapid teem of the melt into the TURC-2 test crucible. Posttest analysis of the UO_2/ZrO_2 melt charge indicated a bulk density of 6.50 g/cm^3 . The melt pool depth was 17 cm.

An interpretation of these results leads to some rather unusual conclusions regarding the heat transfer mechanism to concrete. The lack of any significant erosion in the TURC-2 test implies that crust behavior is very important in determining the extent of erosion. In the TURC-2 test there was very little superheat in the melt, hence rapid crust growth was expected to occur. Apparently, the crust that grew was of sufficient strength to resist breakup from the gas that was released from the concrete. For the case of UO_2 , the gas release was rapidly suppressed by crust growth because of its low thermal conductivity. If a large amount of superheat had existed, then crust growth would have been inhibited. Superheat in the melt can be generated

EXECUTIVE SUMMARY

by lowering the ratio of heat losses to power generation, and also by lowering the melt point. Both of these phenomena will occur in sustained heating experiments because of heating of the surroundings, which lowers the heat loss, and by dissolution of concrete constituents into the UO_2 , which lowers the melt point.

For the case of stainless steel a different phenomenon is observed. In the earlier TURC-ISS test a heat transfer mechanism that is independent of pool temperature was observed. This was concluded from the observation that the penetration rate was constant and several hundred degrees of superheat were available. A heat balance calculation for the TURC-ISS test indicated that penetration was maintained as long as superheat was present. A mechanism of heat transfer that is independent of the thermal driving force is very unusual. There are several possibilities, and all of them require model development in order to check their validity. Sustained and rapid spallation is one possibility. Another possibility is a heat transfer mechanism driven by phase change. In the steel test, the molten steel could be freezing locally at the interface. The escaping gases would carry the frozen steel back into the bulk of the pool for remelting. Liquid steel would move down from the pool to the surface in order to replace the frozen steel that has been swept away. This mechanism would continue until the steel is either too viscous to support such a mechanism or a solid crust forms that cannot be swept away.

1.2 Core-Concrete (CORCON) Interaction Analysis

The CORCON code, developed by Sandia Laboratories, is intended to provide a detailed, mechanistic model of core-concrete interactions. The code models a two-dimensional axisymmetric ablation process, whereas the experiments are one-dimensional. However, if a very large diameter pool is used, the ablation is essentially one-dimensional. In the experiment there is a significant sidewall heat loss, which cannot be modeled directly by CORCON because there is no provision for a nonablative sidewall. However, if a negative heat source is used in the molten pool, then heat will be extracted and a sidewall heat loss mechanism can be simulated. Thus, in the limits of a large pool diameter with a negative heat source, direct comparisons between CORCON and experiments are possible.

CORCON consists of a number of interacting models that describe the various heat transfer mechanisms. Some of these mechanisms have been assumed to exist with no experimental verification. The experiments reported herein can

EXECUTIVE SUMMARY

be used to determine if the models are adequate to describe the heat transfer. The primary models of concern in these simulations are those that describe the heat transfer from the pool to the melting concrete interface. In CORCON, a film boiling-like mechanism is assumed to exist. This assumption is based upon the large amount of gas that is stored in concrete and rapidly liberated during a high-temperature ablation process. Correlations have been developed by a few investigators based upon simulant fluids.

A comparison was done between the TURC-2 erosion test results and the CORCON prediction. The TURC-2 test, a transient UO_2/ZrO_2 concrete interaction test, showed no ablation for the duration of the experiment. Calculations indicated that stable crusting occurred immediately and prevented any erosion. However, the CORCON comparison showed 4 cm of erosion at 2900 K over the time scale of the calculation. At 2500 K, CORCON showed that the UO_2 eroded the concrete as a solidified block. These results imply that further code development and/or refinement is needed.

1.3 Molten Fuel-Coolant Interactions

The objective of this program is to develop an understanding of the nature of fuel-coolant interactions (FCIs) during hypothetical accidents in light water reactors (LWRs). FCIs can occur in the core region, in the reactor lower plenum, or in the cavity below the vessel. Experiments show that FCIs can occur when melt falls into water or when water falls into melt. The understanding of FCIs achieved in this program should be sufficient to resolve the key reactor safety issues for both terminated and unterminated accidents.

Although there were no FCI experiments conducted at the FITS (fully instrumented test site) facility, construction of a new EXO-FITS facility capable of delivering a 50-kg melt was completed. Also, a detailed review of the instrumentation and experimental practices used during an FCI experiment was initiated.

A study of the iron/alumina thermite used during FCI experiments has been conducted. The study was prompted by two observations: (1) significantly slower reaction rates were recorded during FCI experiments which were conducted in nitrogen compared to those conducted in air, and (2) unusual surface eruptions were observed in the CM series and it was possible that these events could be attributed to the type of thermite used. The objectives of this study were to experimentally determine the reasons for this behavior and to define a technique for achieving a consistent thermite

EXECUTIVE SUMMARY

burn with minimal gas generation that is independent of the ambient conditions.

The data collected from the 55 thermite burns conducted have led us to the conclusion that the quantity of gas generated can be significantly reduced by baking the iron-oxide powder at 800°C for about 6 hours. Baking minimizes the sources of hydrogen and other impurities. The results indicate that the graphite crucible used in an FCI experiment reacts with any available oxygen producing predominantly carbon monoxide with lesser levels of carbon dioxide.

The reaction process and resulting products were also observed, via x-ray, to have settled out into layers of iron and alumina within 2 to 3 seconds after the reaction was complete. This is a very important observation, since past x-ray observations of the thermite products showed a vigorous churning motion for at least 30 seconds after the reaction was complete (i.e., the thermite used in the CM series). Having a semiquiescent melt pool at the time of melt drop during an FCI experiment is very important for experimental consistency and interpretations and code development.

1.4 Hydrogen Behavior

The objectives of this research program are (1) to quantify the threat to nuclear power plants (containment structure, safety equipment, and the primary system) posed by hydrogen combustion; (2) to disseminate information on hydrogen behavior, detection, control, and disposal; and (3) to provide program management and technical assistance to the NRC on hydrogen-related matters.

The HECTR code is a reactor analysis tool used to compute the transport and combustion of hydrogen. Version 1.0 of the code has been frozen in preparation for release. A draft of the user's manual has been completed and is being reviewed. From September 26 to 28, a HECTR workshop was given in Bethesda, MD. Features of the code were described, and sample problems were run with audience participation. Two new models have been added to the current version (2.0) of HECTR. A generalized fan cooler model was developed for use in large, dry PWR calculations. The code was also modified to treat CO and CO₂ from core-concrete interactions. This allows HECTR to be coupled with MARCH and CORCON-2. The equivalent (single) band correlation of Edwards' wide-band model was utilized for radiative heat transfer calculations.

EXECUTIVE SUMMARY

A substantial amount of useful data on premixed and continuous injection hydrogen deflagrations in air and steam has been provided by the large-scale tests performed by EPRI at the Nevada Test Site (NTS). These burns were conducted at sufficient scale to aid in the validation of hydrogen combustion codes. Sandia has completed a detailed evaluation of the quality and self-consistency of some of the data from the premixed tests in conjunction with the HECTR assessment effort. This was done in order to judge the utility of these data in characterizing hydrogen burn environments. It is apparent that the quality of the data from different types of instrumentation varies greatly, and care must be exercised in interpreting the results.

The FLAME facility is a large-scale channel designed to study hydrogen combustion problems relevant to nuclear reactor safety. Initial tests have examined the effects of transverse venting on combustion in an obstacle-free channel. During this period two tests were run, F-15 and F-16, with 13 percent top venting area fraction. The tentative results indicate that the effectiveness of transverse venting in reducing flame acceleration, and presumably transition to detonation, may decrease with increasing scale. The facility had been damaged as a result of a transition to detonation in a previous test and, in view of the overpressures seen in the current tests, we chose not to proceed to higher hydrogen concentrations until permanent repairs were completed. Repairs to the concrete channel were completed and a newly designed sacrificial endplate will be installed next quarter.

The acceleration of a flame in an obstacle field by the positive feedback between the combustion process and the flow field upstream results in either a steady-state turbulent propagation regime compatible with the particular boundary conditions or transition from deflagration to detonation. It is of great practical interest to determine the conditions of turbulent acceleration which trigger the transition to detonation or, if transition does not occur, to determine the magnitude of the final velocity. An experimental program is continuing at McGill University to determine the flame acceleration processes in the common fuel-air mixtures. These experiments have demonstrated the existence of four possible regimes of flame propagation: the quenching regime, the choking regime, the quasi-detonation regime, and the Chapman-Jouguet detonation regime. These regimes are correlated with specific obstacle configurations and degree of confinement.

The relative detonability of H_2 -air-steam mixtures which are predicted to occur following a reactor accident is being

EXECUTIVE SUMMARY

studied in the Heated Detonation Tube (HDT). Prior to the HDT experiments there was wide belief that the effects of initial pressure and temperature would be small for the ranges expected during a reactor accident. We have found, however, that the initial thermodynamic conditions have strong influences on the detonability of a given mixture. During this period the results from the series conducted at 100°C and standard air density in May have been analyzed. The measured detonation cell size, which is inversely proportional to the sensitivity of a mixture, increases with steam dilution of a given mixture as expected. However, the detonation cell size measured in this series for undiluted H₂-air is smaller than for comparable mixtures at 20°C and one atmosphere pressure. This is apparently due to the higher initial density and temperature. Since the presence of steam elevates temperatures, the opposing effects of increased temperature and diluent concentration reduce the effectiveness of steam as a means of preventing hydrogen detonations.

We have initiated several new efforts to improve our understanding and modeling capabilities for diffusion flames in enclosures. On the experimental side there are two bench-scale efforts designed to clarify some aspects of buoyancy-driven mixing. A complementary effort is the development of a two-dimensional simulation for complex flows in enclosures. This is a project that will ultimately produce a computational tool for the prediction of fluid mechanics and heat transfer phenomena produced by diffusion flames in containment-type geometries.

1.5 Hydrogen Mitigative and Preventive Schemes

The objective of the hydrogen mitigative and preventive schemes program is to provide the NRC with information to evaluate proposed equipment concepts and operational schemes to prevent or mitigate the effects of hydrogen combustion during hypothetical LWR accidents. To provide this information, we are investigating the operability and consequences of operation of deliberate ignition systems and their components during hypothetical hydrogen-producing accidents.

We are studying the effects produced by operating the containment water spray system while the deliberate ignition system is activated. We have recently completed an experimental study of the behavior of resistance-heated hydrogen igniters exposed to water sprays and gas flows. To complement this study, the flow of air in nuclear reactor containment buildings due to the introduction of water sprays is being investigated numerically and theoretically. The particular geometry studied is that of Sequoyah, a pressurized

EXECUTIVE SUMMARY

water reactor equipped with an ice condenser. Given the water spray flux specified for Sequoyah, it is found that peak flow velocities of approximately 12-14 m/s are possible in an empty building. This velocity is reduced substantially when account is taken of the presence of ice condensers and steam generators.

We are also studying the effects of liquid water dispersed as drops on the combustion of hydrogen-air mixtures. We are investigating the use of rotating disc generators in the 5.6 m³ FITS combustion chamber to generate monodisperse (single diameter) water drops with suspended water densities in excess of 100 g/m³. Significant advantages over nozzle-generated drops are expected, particularly the avoidance of turbulence in the combustion gases. A pair of these generators has been installed in a transparent mockup of the FITS combustion chamber. Initial tests indicate satisfactory operation up to the maximum rotational velocity.

We are also studying the effects on deliberate ignition of hydrogen-air mixtures that contain aerosols produced in containment by core overheating, breakup of jets of core melt or core-melt/concrete interactions. To measure these effects, we have prepared the 5.1 m³ VGES chamber for the combustion of hydrogen in the presence of aerosols, both simulants of core materials and fission products. This effort has involved installation of extensive aerosol generating and sampling equipment. We have completed one combustion experiment with an inert reactor aerosol simulant, Al₂O₃, and two control experiments without the aerosol; both sets of experiments used quiescent, nominally 6.5 percent hydrogen-air mixtures with spark ignition. Pressure and temperature records are being analyzed.

EXECUTIVE SUMMARY

2. FISSION-PRODUCT SOURCE TERM

2.1 High-Temperature Fission-Product Chemistry and Transport

The purpose of the High-Temperature Fission-Product Chemistry and Transport program is to obtain data on the chemistry and processes that affect the transport of fission products under accident conditions. Baseline thermodynamic and reactivity data are being collected for compounds of fission-product elements of particular interest. An experimental facility has been built to allow the chemistry of fission products in prototypic steam-hydrogen environments to be studied. The interaction of fission products with reactor materials such as stainless steel can be examined in this facility. Results of these experimental studies are compared to predictions of thermochemical models to determine if reaction kinetics play an important role in fission-product transport.

Several tellurium experiments were conducted in steam with Inconel 600 and 304 stainless steel. Te was found by x-ray fluorescence methods on the surface of the Inconel coupons exposed at 800°C. The Te X-ray intensity data correlated with the mass gains observed for the coupons, suggesting that the oxidation of the alloy by steam was minor. There was an enhanced nickel x-ray signal; thus, the formation of one of the nickel telluride compounds was inferred. This is consistent with the thermodynamics that show nickel is not oxidized in steam-hydrogen mixtures, and thus is available to the tellurium. This is also consistent with the previously reported experiments in which lightly preoxidized Inconel coupons were exposed to Te vapor in an argon gas stream and a rapid, complete reaction with Te to form various nickel tellurides was observed.

When stainless steel coupons were exposed to Te vapor at 850°C and above, there was significant oxidation and no measurable Te x-ray fluorescence signal was obtained. However, when stainless steel coupons were exposed at 700°C, there was little oxidation and Te was detected on the surface of the coupon.

Since oxidation is less of a problem with the Inconel alloy, our tentative conclusion is that this alloy will likely take up tellurium vapor from the steam environment of the reactor system. No conclusion can yet be made for the stainless steel alloy when there is concurrent oxidation by steam. Although no surface content of Te was detected when oxidation was prevalent, the possible retention of Te deeper within the oxide has not yet been disproved. Microprobe analyses of the deeper oxide layers is in progress.

EXECUTIVE SUMMARY

2.2 Quantitative Uncertainty Estimation for the Source Term

The Quantitative Uncertainty Estimation for the Source Term (QUEST) program estimates the uncertainty in a few of the calculated radiological source terms reported in the BMI-2401 drafts from Battelle's Columbus Laboratories. In particular, QUEST is considering the TMLB' and S₂D accident sequences in Surry (a PWR with a large, dry containment) and the TC sequence in Grand Gulf (a BWR with a Mark-III containment).

The analysis for the TC sequence at Grand Gulf was completed this quarter. The three dominant uncertainties in the determination of the source term for the Grand Gulf TC sequence are: (1) retention of fission products within the RCS, (2) the effectiveness of the suppression pool in removing fission-product gases and aerosols from the gases passing through it, and (3) the likelihood and potential consequences of a high-pressure melt ejection causing severe disruption of the suppression pool such that most of the fission products released in-vessel and during the high-pressure melt ejection would enter the containment building atmosphere.

The phenomenological uncertainties associated with in-vessel fission-product release and retention within the RCS are essentially the same as for the Surry accident sequences.

The suppression pool in the Grand Gulf BWR design is an extremely important means of reducing radioactivity release to the environment. It is shown that uncertainties associated with the modeling of aerosol removal mechanisms during suppression pool scrubbing lead to a plus or minus factor of 10 uncertainty in the decontamination factor in the modeling. This has a significant impact on the radioactivity release to the containment building since most of the fission products released from the reactor vessel are trapped in the suppression pool. Even for the most pessimistic modeling assumptions on suppression pool effectiveness, however, suppression pool scrubbing is very effective in modeling analysis so that total release fractions are much lower than the "high" estimates for the Surry TMLB' and S₂D sequences.

The largest single uncertainty associated with the Grand Gulf TC sequence concerns suppression pool disruption. It has been predicted that high-pressure melt ejection and the subsequent vessel blowdown could overpressurize the drywell to such an extent that gas flow rates through the suppression pool exceed the fluidization velocity. The suppression

EXECUTIVE SUMMARY

pool would then be dispersed into a droplet flow regime. It is likely that if this were to occur, most of the fission products released in-vessel and during the high-pressure melt ejection would enter the containment, building atmosphere. A much more detailed analysis of this phenomenon than was done for QUEST, including accounting for the tortuous flow path for ejected core melt from vessel to drywell, would be required to eliminate this concern.

2.3 ACRR Source Term Experiment

Release of radionuclides during fuel degradation in a core uncover accident is the first stage in the determination of the amount and nature of the radioactive release from the damaged nuclear plant. Current estimates of the release of the principal fission products over the range of relevant accident conditions are subject to significant uncertainty (e.g., QUEST). A key element in reducing the uncertainty in predicted releases is an improved understanding of fission products from the fuel under severe fuel damage conditions. The ACRR Source Term program is being developed to provide a data base for fission-product release over a range of fuel temperatures, system pressures, and fuel damage states, where little or no data currently exists, to allow the development of improved fission-product release models for use in consequence evaluation. This program is related to out-of-pile programs at ORNL and BCL.

During this quarter, work concentrated on test matrix definition and preliminary test design. The data obtained from the in-pile tests at Sandia and the related experiments at ORNL and BCL will provide an improved data base for the fission-product release models in the mechanistic accident analysis codes being developed by the NRC. Two models currently being developed are the FASTGRASS release model in the SCDAP core degradation model, and the VICTORIA model to be used for both release and transport of radionuclides in the MELPROG meltdown model.

From the modeling standpoint, experimental data needs are found in several areas. The variables important to these areas include temperature, steam and hydrogen pressures, clad state, and damage states. The source term test matrix must cover the relevant ranges of these variables.

Thermophysical data is also needed throughout this variable space, yet must be considered secondary to obtaining key release measurements covering the important ranges of the variables. These variables interact strongly with one

EXECUTIVE SUMMARY

another in the actual course of an accident. Similarly, during integral experiments, it can be difficult to sort out the contributions of various effects to the final release results. For this reason, primary emphasis in the program must be devoted to separate-effects experiments in which we can identify major effects on release.

In addition to separate effects experiments to address release concerns, there is a need for phenomenological accident progression experiments with irradiated fuels. Release data from such experiments may be directly correlated to damage progression during the experiment as a test of the ability of the model to treat combined interactions of the important phenomena. This will also provide a detailed basis for evaluating VICTORIA within the integral context of the MELPROG code, which may be used to model directly such experiments.

EXECUTIVE SUMMARY

3. LWR DAMAGED FUEL PHENOMENOLOGY

Sandia's LWR Damaged Fuel Phenomenology Program includes analyses and experiments that are part of the integrated NRC Severe Fuel Damage (SFD) Research Program. Sandia is investigating, both analytically and in separate-effects experiments, the important "in-vessel" phenomenology associated with severe LWR accidents. This investigative effort provides for two related research programs: the Damaged Fuel Relocation (DFR) program and the Damaged Core Coolability (DCC) program. The focus of these activities is to provide a data base and improved phenomenological models that can be used to predict the progression and consequences of LWR severe core damage accidents. The DFR experiment program provides unique data on in-vessel fuel damage processes that are of central importance in determining the release and transport of fission products in the primary system. The DCC experiment program provides data on the ultimate coolability of damaged fuel configurations.

3.1 ACRR Damaged Fuel Relocation and Quench

The focus of the LWR DFR experiment program is directed toward providing separate-effects phenomenological data on important severe in-vessel fuel-damage processes to aid in the development of second generation severe accident analysis codes. The core-damage configuration, hydrogen generation, and fission-product release are the primary areas of interest. The DF test series uses photography to record the damaged fuel configuration during an in-pile experiment in which accident conditions are simulated in a small LWR rod bundle. The decay heating in these experiments is simulated by fission heating of the fuel in the ACRR. Steam conditions similar to expected accident conditions are provided.

The major effort for this period focused on the assembly of the DF-2 experiment and modifications to the steam skid, optical system, shield plug, and the software for the Data Acquisition and Control System (DACS). The assembly of the DF-2 capsule has been completed and final preparations are being made for the execution of the DF-2 experiment.

The DF-1 experiment package has been disassembled and the test section region, which contains the disrupted fuel bundle, has been potted with resin. A posttest x-radiograph of the DF-1 test section shows substantial bowing of the fuel rod in the upper half of the bundle with evident erosion of some fuel pellets; however, the pellets are generally retained in a rod geometry. Also a 12-cm long by 7-cm diameter globular volume of high density material

EXECUTIVE SUMMARY

enclosing a low-density zone was observed in the lower half of the bundle.

The potted test section was cut to allow metallographic examination of the damaged fuel bundle at several axial locations. These examinations showed that most of the cladding structure was lost in the upper half of the fuel bundle, and the fuel pellets were bonded together by a zirconium-rich oxide that evidently flowed into the pellet-pellet interface in the liquid state. The examination of the upper bundle cross sections also showed thinning and complete oxidation of the cladding shells. The high-density globular formation near the bottom of the fuel bundle contained large quantities of oxidized U and Zr material.

3.2 ACRR LWR Degraded Core Coolability

The LWR Degraded Core Coolability (DCC) program investigated the coolability of damaged core debris in water. The debris is fission heated in the ACRR to simulate the decay heat expected in an LWR severe core-damage accident. The governing phenomenological uncertainties being investigated are pressure effects, deep bed behavior, particle size distributions, stratified beds, bottom coolant feed, and material effects. Each DCC experiment will determine the coolability in three thermal regimes: (1) convection/boiling, (2) dryout, and (3) extended dryout. Experimental results are being used to confirm and/or modify the present analytical models used to predict degraded core coolability.

The DCC-3 experiment is being designed to explore the effects of stratification and bottom injection. The current DCC-3 design calls for a two-layer bed with water injection at the bottom. The lower portion of the bed will be 0.4-m high and consist of 5-mm diameter particles. The upper portion of the bed will be 0.1-m high, and consist of 1.25-mm diameter particles. The noninjected dryout fluxes for this bed are predicted to be between 20 to 26 times lower than those of a homogeneous bed composed of 1.25-mm particles, depending upon the system pressure.

With injection, the dryout fluxes should increase by a factor of about 100. The injection rates proposed for DCC-3 are 0.03, 0.1, and 2.0 kg/m²s. These correspond (at 20°C) to flow rates of 0.00386, 0.0129, and 0.257 gpm and flow velocities of 0.03, 0.1, and 2.0 mm/s, respectively. These injection rates must be delivered precisely and measured accurately if the data is to be of any use. Dryout fluxes for the lower injection rates should be measured first since

EXECUTIVE SUMMARY

the danger of disrupting the layer interface increases with increasing injection rate.

Thermocouple location is very important in detecting dryouts with water injection. The dryouts are predicted to occur within 40 mm of the layer interface. Poor thermocouple placement would result in inaccurate measurements of dryout heat flux.

Pressure constraints require that the maximum allowable fuel temperature during an extended, noninjected dryout be 662°C. This limit can be relaxed for injected dryouts. An extended safety analysis will be conducted at a later date. An order-of-magnitude analysis has indicated that desorption of helium may be responsible for the increase in fill pressure observed in DCC-1 and DCC-2, and measurements are planned to test this hypothesis.

EXECUTIVE SUMMARY

4. MELT PROGRESSION PHENOMENOLOGY

The objective of this program is the development of a mechanistic computer model for the in-vessel phases of severe accidents in LWRs. This model, MELPROG, is implicitly linked with the TRAC-PF1 Reactor Coolant System (RCS) thermal hydraulics models to provide a complete, integrated treatment of the reactor primary system from accident inception up to and through release of core materials and provides materials and thermohydrodynamic input to the CONTAIN reactor containment analysis model.

Integration of the new 2-D FLUIDS module has been initiated. This integration involves modifying the data transfer sections of each module. With these modifications, proper coupling between the FLUIDS module and other modules will be maintained.

Code testing continued by studying the S₁D calculation in more detail to resolve the inconsistencies in the modules and identify areas of improvement. The current testing used all features of the code. This calculation was successfully completed with no major problems detected. The calculation was run from initiation through vessel failure. MELPROG was able to successfully calculate core heatup, cladding oxidation, core slumping, debris formation and meltdown, grid plate heatup and failure, debris-coolant interactions, and vessel heatup and failure. Therefore, the code is now capable of calculating most of the features necessary in a meltdown progression. The major components for a best-estimate calculation currently exist in the code.

Code applications continued by beginning the calculation of a TMLB' in the Surry PWR plant. The calculation was run until fuel rod failure was initiated. At that point, the calculation was stopped to allow the entire code to be reoverlaid in anticipation of the requirements of the 2-D FLUIDS module.

The documentation of the first version of MELPROG (MELPROG-PWR/MODO) has been initiated. This report will provide detailed descriptions of the models in MELPROG.

EXECUTIVE SUMMARY

5. ADVANCED REACTOR ACCIDENT ENERGETICS

The Advanced Reactor Accident Energetics Program addresses the key issues in an LMFBR core-disruptive event that determine the progression and severity of the accident. This program involves a series of in-pile experiments and analyses that focus on key phenomena in two general areas:

- a. Initiation Phase--Fuel/Clad Dispersal Experiments;
- b. Transition Phase--Fuel Freezing and Streaming Experiments.

5.1 Initiation Phase

The Sandia Fuel Dynamics Program provides needed experimental data and analysis for the initiation phase of an LMFBR core-disruptive accident. The motion of clad and fuel in the initiation phase of an LOF accident is an important consideration in the subsequent progression of the accident. Early fuel dispersal can lead to neutronic termination while limited dispersal and blockage formation continues the accident into the transition phase and the possibility of further neutronic activity.

To obtain data on the important phenomena involved in this phase of an LMFBR accident, the USNRC is sponsoring the Sandia Transient Axial Relocation (STAR) experiments in the ACRR test facility. Kernforschungszentrum Karlsruhe (KfK), FRG is cosponsor of this program.

During this report period a dispersed drop flow model for clad motion was installed in the SANDPIN/CMOT code, and used to calculate the clad motion for STAR-1. This model relies on a cladding entrainment criterion that is based on the nonwetting behavior of clad drops moving on a solid substrate. The major result of the entrainment criterion is that entrainment is much easier than in previous models that were based on a film flow such as Ishii's model. The consequence of this easy entrainment is that entrainment should be considered the rule rather than the exception during the LMFBR clad motion phase of initiation phase accidents. Thus, codes that model clad motion should include both a dispersed droplet flow and a film flow regime.

The drop entrainment criteria was used in the SANDPIN/CMOT code to predict clad motion for the STAR-1 experiment. The results of these calculations are presented in this report and a computer-generated movie of clad motion was made. In general, the results of these calculations are strikingly

EXECUTIVE SUMMARY

realistic, and they show very good agreement between the onset of clad motion, the direction and velocity of motion, the fraction of entrainment that occurs, and the extent of clad blockage formation.

5.2 Transition Phase

Many current heterogeneous core designs are characterized by relatively low-sodium void coefficient and incoherent behavior in the initiation phase. These features generally increase the likelihood of a "transition" or "meltout" phase during a core-disruptive accident. The key questions in the transition phase, highlighted in the CRBR safety review, are whether fuel or clad blockages form, leading to a confined or "bottled" core configuration, and whether the behavior and reactivity implication of this pool of fuel-steel in the core region of the fuel blockages do lead to this state.

The TRAN program addresses the question of fuel-inventory reduction by penetration into upper core structure through subassembly gaps to the lower core structure. If deep penetrations occur, nonenergetic shutdown is probable while shallow penetration will lead to a transition phase and the possibility of further energetics. First-of-a-kind in-pile experiments, sponsored jointly by the USNRC and the Japanese Power Reactor and Nuclear Fuel Development Corporation (PNC), are being conducted to provide data to evaluate the various models describing fuel penetration.

Current B-Series activities focused on preparing experiments B-4 and B-5, both of which employ prototypical pin-bundle freezing-channel geometries. The initial bulk melt for experiment B-4 will consist of nearly 300 g of pure UO_2 heated in the double-pulse mode to around 3600 K. The double-pulse heating is necessary in order to generate a sufficiently uniform melt temperature with all fuel above the solidus. Experiment B-4 will investigate the upward injection of this melt into the bare clad five-pin bundle, which has been preheated to 1173 K such that the interface temperature between the steel clad and the molten UO_2 is above the steel melting point. These conditions then are analogous to those employed in the annular experiment, B-3. Experiment B-5 is scheduled to follow B-4 within 4 to 6 weeks with the following difference. The freezing channel in B-5 will consist of five pins with a stainless steel wire wrap. The wire wrap is expected to greatly enhance the potential for steel entrainment through the vigorous convective action of the flowing melt and thereby possibly alter the freezing process.

EXECUTIVE SUMMARY

SIMMER-II has been used to analyze fuel melting in the B-4 geometry with respect to the potential for early fuel movement from pore gas pressurization. A bounding study was performed using the assumptions of either "fully open" or "fully closed" fuel porosity to determine the range of possible effects from the rapid heating of the internal pore gas during the second fuel heating pulse. The results suggest that fuel with tightly trapped porosity gas may experience some early relocation shortly after melting because of a rapid expansion of the gas. A tight gas-liquid momentum coupling aggravates this effect. It was recommended that excessive back pressure in the experiment should be avoided to minimize this effect, because early fuel movement, especially downward movement, is undesirable. The possible use of a melt-away base that might prevent early downward fuel relocation was also examined.

The GAP series of experiments is directed toward providing data on the potential for penetration and freezing of large amounts of molten core material into the subassembly intercanwall gaps. The fuel melting section of the experiment package has been redesigned to give a substantially higher ACRR coupling factor in order to offset the degradation in reactor yield which was observed in the G-1 experiment. This has been accomplished by increasing as much as possible the central cavity neutron thermalization and increasing the fuel enrichment, at the expense of some reduction in the melt volume. The new design will involve about 1.5 kg rather than the original 2-kg mass attempted in G-1. The second GAP experiment, G-2, is planned for the second quarter in 1985.

EXECUTIVE SUMMARY

6. POSTACCIDENT HEAT REMOVAL

6.1 Debris Bed Coolability

The objective of the experimental studies of debris beds is to provide information on the behavior of reactor materials following a core-melt accident. In particular, it is necessary to determine if the heat generated by fuel particles after meltdown (decay heat) is satisfactorily dissipated by the coolant; if not, the dynamics of remelt and containment damage must be ascertained. Sandia's debris bed studies consist of a series of experiments using liquid sodium and urania to serve as a basis for developing phenomenological models. The experiments are fission heated in the ACRR to simulate fission-product heating in a debris bed. Results are sufficiently general to be applicable to all liquid-cooled reactor systems. The program is cosponsored by the USNRC, the PNC (Japan), and EURATOM (JRC, Ispra).

Analysis began on the D-10 experiment. The D-10 experiment has provided a large amount of unique data in the field of debris coolability. The limited evaluations performed to date provide some insight to bed behavior with bottom cooling and at high temperatures; however, a more thorough understanding of heat transfer in the D-10 bed will only be gained by additional, more complete analyses. The specific areas that appear to be most valuable for continued analyses are data interpretation with respect to current models, bed configuration and cohesion, and dry bed thermal conductivity.

The configuration of the bed during the experiment, especially after the disruption event, is critical to more detailed analyses, i.e., to establish the boundary conditions that are the basis for such analyses. The evaluation of the data so far suggest that the disruption event increased the porosity only slightly. The x-ray of the bed taken after the experiment was completed indicates that the bed height varies rather uniformly from 164 to 170 mm, with an average height of 167 mm. This indicates that the average porosity in the bed is about 0.40. A region in the bed extending from 20 to 60 mm, corresponding to the region of maximum temperatures, was evident in the x-ray with density variations that appeared slightly different from the remainder of the bed. Additional data on local porosity will only be gained by disassembly of the experiment, with detailed PIE (postirradiation examination).

Although current models are reasonably consistent with the data from D-10 with the bed in a packed state, the data

EXECUTIVE SUMMARY

after the disruption event are not consistent with that predicted from a channeled model. Whether or not this is due to uncertainty in the bed configuration could be investigated parametrically with the models. However, a fundamental discrepancy appears in the power that is calculated to be removed by channeling prior to dryout. The depth of channel penetration and the size and number of channels that are assumed in the model should be reevaluated in light of the D-10 data.

The "sticking factor," which appeared to suppress channeling until a substantial overpressure was built up in the bed, has a potentially large influence on the coolability of debris in accident scenarios. An increase in coolability by a factor of 2.5 was observed in D-10. The cause of this cohesion should be found in order to determine the relevant mechanisms that influence the phenomenon. These mechanisms may include particle shape, bed porosity, subcooling, bed chemistry, and bed power. Time-dependent aspects of these parameters should also be studied.

The conductivity of UO_2 debris with sodium vapor present is among the most significant data obtained from the D-10 experiment. Two-dimensional analysis conducted to date indicates that the conductivity is significantly higher than models predict. The mechanisms that may be responsible for the increase in conductivity are not clear at this time.

An important step in the continuation of this analysis is the ability to properly interpret the experimental data. This interpretation is dependent on the geometry of the dry zone, which affects heat transfer along the instrumentation. The determination of bed configuration will aid in this area. Furnace testing of instrumentation in environments that simulate the conditions existing during the experiment may be helpful in assessing the data. Additional information may be gained by a study of the processes that account for the observed increase in conductivity. These investigations should concentrate on those effects related to the presence of sodium, as the models are consistent with the data for dry debris in argon, investigated in the SNL DC experiments. Based on a more detailed interpretation of the data, two- and three-dimensional thermal analyses should provide an important evaluation of the data in terms of mechanisms that could be responsible for enhanced conductivity. For example, radiation heat transfer should increase as the fourth power of temperature, conduction should be linear with temperature, and mass transport effects may be discernible.

EXECUTIVE SUMMARY

Also this quarter, preparations continued for the D-13 experiment. Debris Bed Experiment D-13 is the first experiment designed to study the coolability of stratified particle beds that are cooled both by overlying sodium and from below by structures that support the bed. Maximum debris temperatures in excess of 2773 K (2500°C) are planned to be achieved during the experiment in order to investigate phenomena that might occur at high temperature or with relatively large dry zones.

The D-13 experiment is identical in design to the previous D-10 experiment. The only differences are in instrumentation and that the bed will be stratified in D-13. One of the major changes from D-10 is the elimination of the ultrasonic thermometers (UTs) from the experiment. The number of C-type thermocouples in the experiment will be increased from 12 to 16 to make up for elimination of the UTs. Several improvements in the C-type thermocouples are planned including tighter inspection of the rhenium sheaths to avoid flaws, more care in assembly of the transition from the rhenium sheath to the stainless steel cable, better brazing of the sheaths into the containment feedthroughs, and the addition of potting for the lead wires to avoid breaking during assembly. Additionally, HEDL (Hanford Engineering Development Laboratory) will conduct a performance test to characterize the response of the thermocouple to an environment where the maximum temperature is on the sheath above the junction location.

6.2 Dry Debris Melt Progression

In order to establish the release time frame and quantity of radioactive materials following a severe accident, it is necessary to determine the fuel melt dynamics and the characteristics of melting attack by molten fuel on reactor structure and containment barriers should postaccident debris heat removal not be adequate. Simulation of those portions of debris beds undergoing extended dryout and melting is necessary to support modeling activities. This study is aimed at providing such data through in-core experimentation with typical reactor material undergoing sustained, intrinsic heating at temperatures of interest. Models developed are provided to the LWR severe accident code MELPROG as well as to direct analyses of LMFBR debris coolability. This work is cosponsored by the NRC, the Japanese PNC, and EURATOM (JRC, Ispra).

The experiment analysis on DC-1 continued. The DC-1 experiment provided valuable data for model development and validation for use in accident analyses involving debris

EXECUTIVE SUMMARY

coolability, heat transfer, melt progression, and molten pool formation and behavior.

The DC-1 experiment has been x-rayed and indicates that a molten pool containing about 50 percent of the debris (1 kg) was formed in the lower part of the crucible, leaving a sizeable void above the pool and bounded by a fairly uniform dense crust, about 5-mm thick. The overlying crust is intact and may be partially supported by the instrumentation penetrating the experiment.

A two-dimensional meltdown model has been developed at Sandia to calculate such melt phenomena. This model calculates the debris heatup, melting, relocation, crust and void formation, as well as crust remelt, within a debris bed. The model is designed to calculate two stages of postdryout behavior: transient heatup of the dry debris, and debris melting and relocation. The model accurately predicts the final configuration of the DC-1 experiment to include such details as uranium freezing on instrumentation penetrations in the crust area because of increased heat transfer up the instrumentation sheaths. This model has been incorporated into the LWR melt-progression code, MELPROG.

REACTOR SAFETY RESEARCH
QUARTERLY REPORT
JULY-SEPTEMBER 1984

1. CONTAINMENT LOADING AND RESPONSE

In the analysis of severe accidents, several scenarios lead to the release of molten core material and the subsequent interactions involving molten fuel, coolant, structural material, potential in-core retention systems, the reactor vessel, and the reactor cavity boundary. The present program seeks to identify the results of these interactions. The results also will be used to support model development for the containment code (CONTAIN) and to provide data for its verification.

1.1 Ex-Vessel Core Debris Interactions

(D. A. Powers, 6422; J. E. Brockmann, 6422; E. R. Copus, 6422; J. E. Gronager, 6422; W. W. Tarbell, 6422)

A comprehensive experimental program in which steel melts interact with concrete has provided quantitative observations that are the basis of two important severe accident analysis codes: the CORCON model of core debris-concrete interactions and the VANESA model of radionuclide release and aerosol generation.^{1-1.1-2} Since expected core debris composition ejected from the reactor vessel will contain UO_2 , ZrO_2 , and Zr metal (as well as stainless steel), it is desirable to investigate molten oxide and metal core debris-concrete interactions. The establishment of an adequate data base of these interactions is desirable for validation of the models as well as the identification of other important phenomena.

The Transient Urania-Concrete tests (TURC) were initiated to provide a preliminary look at large-scale oxide melt-concrete interactions. The TURC test matrix, shown in Table 1.1, consisted of two metallic melt-concrete tests (TURC-1T, TURC-1SS), a molten UO_2/ZrO_2 concrete test (TURC-2), and a $UO_2/ZrO_2/Zr$ metal-concrete (TURC-3) experiment. Within this report, the TURC-2 test will be discussed in comparison of metallic tests TURC-1T and TURC-1SS.

The following sections describe the experimental facilities, results, and analysis of the TURC-2 experiment.

1.1.1 Experiment Description

The experimental facility for conducting the TURC tests is shown schematically in Figure 1.1. The facility consists of two major components: (1) the melt generator, in which the

Table 1.1

The TURC Test Matrix

- TURC-1T: - 200 kg Thermitic Melt
 - Limestone/Common Sand Concrete
 - Purpose:
 - Comparison Data Base
- TURC-1SS: - 200 kg 304SS
 - Limestone/Common Sand Concrete
 - Melt Temperature: 2350 K
 - Purpose:
 - Comparison Data Base
- TURC-2: - Iris Facility: 200 kg $\text{UO}_2\text{-ZrO}_2$ Melt
 - Limestone/Common Sand Concrete
 - Melt Temperature: 2820 K
 - Purpose:
 - Transient UO_2 -Concrete Interaction
 - Data Comparison
 - Model Validation
- TURC-3: - Iris Facility: 200 kg UO_2 , ZrO_2 , Zr metal
 - Limestone/Common Sand Concrete
 - Melt Temperature: 2100-2820 K
 - Purpose:
 - Oxide-Metal-Concrete Interaction
 - Data Comparison
 - Model Validation

melts are produced; and (2) the interaction chamber, where the concrete interactions take place.

The melt generator, for the TURC-2 test, utilized the Inductive Ring Susceptor (IRIS) technique in Sandia's Large Melt Facility (LMF).

The IRIS technique employs the method developed at Sandia for melting oxide materials.¹⁻³ The technique consists of inductively heating embedded, refractory metal rings within a matrix of UO_2 (70 percent) and ZrO_2 (30 percent). The rings heat the matrix until molten. Once the matrix begins to melt, a pool forms and continues to grow until it reaches the cooler outer boundary, thus freezing and forming a crust. This self-sculing technique provides adequate protection of the outer structural alumina crucible. After approximately 3 hr of heating, melting is complete.

Upon completion of melting, the molten material is teemed down into the 13 m³ interaction chamber, which contains

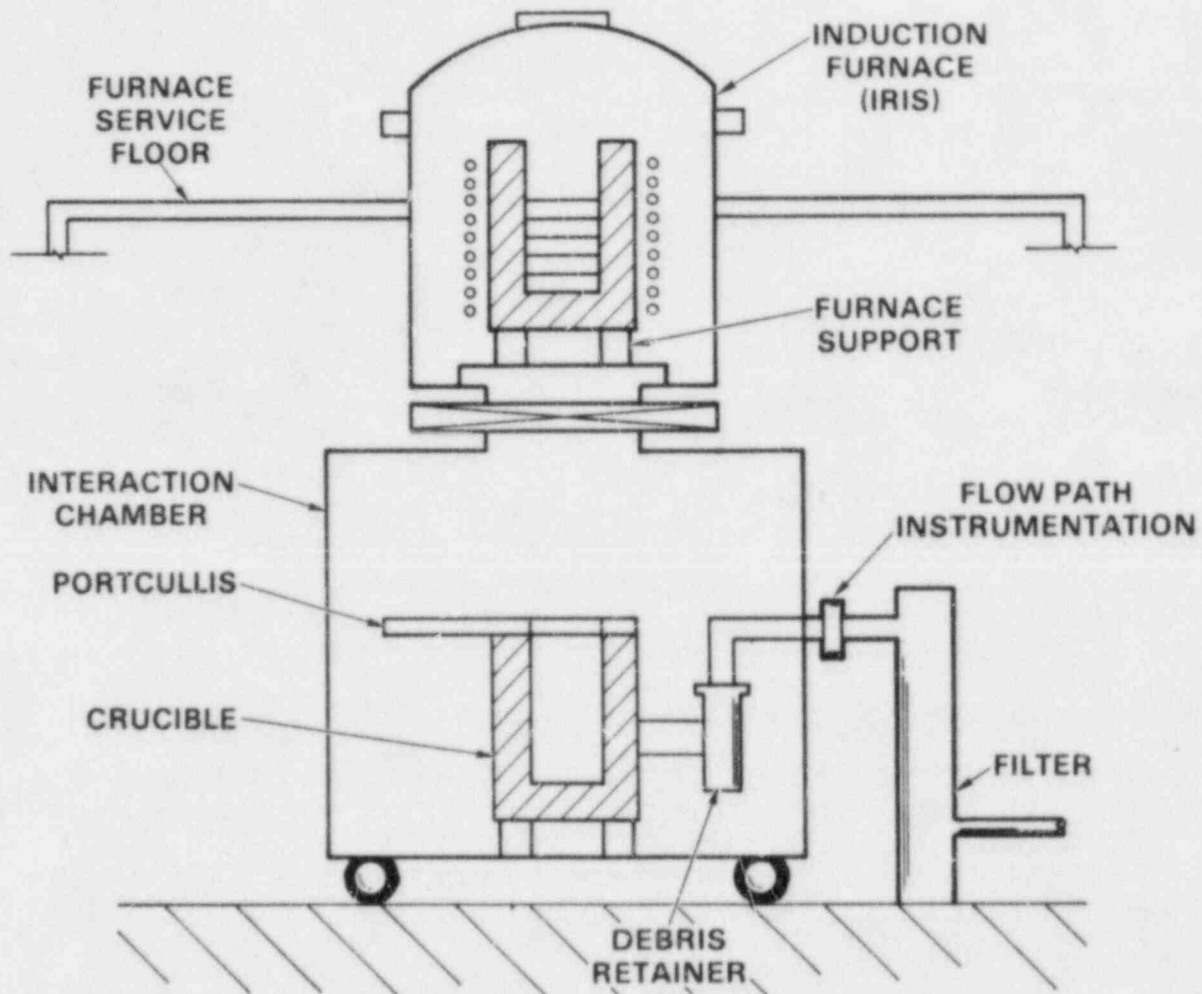


Figure 1.1. The Large Scale Melt Facility for Conducting the TURC Tests

the test crucible and instrumentation. This is accomplished by firing a projectile through the base of the structural alumina crucible, resulting in a 15-cm-diameter hole through which the melt is teemed.

After the teem is complete, the top orifice (or opening) is sealed with a sliding portcullis. Reaction products generated during the interaction are vented through the crucible, and piped out of the interaction chamber and into the gravel filter.

The crucible used for the TURC tests is of a new design and purpose. The crucible consists of an instrumented concrete slug 40 cm in diameter and 30 cm in height, cast at the base of a MgO annulus (40 cm I.D., 70 cm O.D., and 1.2 m in height).

The purpose of this "1-D crucible" is to provide only axial (or one-dimensional) ablation of the concrete slug; thus, all the reaction products of the melt/concrete interactions must pass up through the melt to be released, providing data consistent with conditions found at a horizontal surface in the reactor cavity.

The concrete utilized in the 1-D crucibles is Limestone Common Sand (LCS). The chemical composition of the concrete and its constituents is described in Reference 1-4. LCS concrete was chosen because of its composition medium between limestone and basaltic concrete. The concrete was cured for a minimum of 60 days before the test.

Instrumentation within the crucible consists of K-type thermocouples located within the concrete slug and MgO annulus. Axial temperature profiles were measured at three radial locations within the concrete slug (0, 3.0, and 20 cm from centerline). Overall axial resolution was 0.5 cm. Additional thermocouple arrays located within the MgO annulus measured radial temperature profiles within the crucible at several axial locations.

The thermocouples within the crucible were utilized to determine erosion rates of the concrete and the heat fluxes into the concrete and MgO sidewalls. The data acquisition system was capable of recording the thermocouple data every 10 s. This data rate was acceptable for the erosion rates observed in the TURC experiments.

After teeming and closing the portcullis, an argon purge was initiated in the crucible cavity through the portcullis cover. The purpose of the argon purge was to provide an inert background gas to compare with generation rates of gas species evolved during the tests.

The composition of the gases generated during the test were determined by grab-sample method. During the test, 28 grab samples were taken of the evolved gases at the exit port of the crucible. The gas composition was determined, off-line, by gas chromatography.

In order to quantify fission-product transport, nonradioactive fission-product mocks, listed in Table 1.2, were added to the melt charge (with the exception of Te and CsI placed with the 1-D crucible). Composition of the aerosols would provide an initial look at fission-product transport in oxidic melt-concrete interactions.

Table 1.2

Fission-Product Mocks
Used in the TURC Test Series

<u>Fission Product</u>	<u>Category</u>
Te	Chalcogens
Mn	Early Transition
Mo	Elements
CsI	Halogens
BaO	Alkaline Earths
ZrO ₂	Tetravalents
CeO ₂	
La ₂ O ₃	Trivalentes
Ni	Platinoids

Aerosol samples were taken during the test at the inlet of the gravel filter. The aerosols were collected using Anderson MK III cascade impactors and integral sample filters. Data obtained from the aerosol instrumentation provided the aerosol size distribution, shape, and composition.

1.1.2 TURC Experiment Results

After 150 min of heating in the IRIS melt generator, 142.8 kg of UO₂/ZrO₂ melt was teemed into the experiment 1-D crucible. Ten seconds after the teem was initiated the portcullis was closed, and the airborne reaction products were piped through the gas and aerosol instrumentation.

The top of the melt pool showed a convoluted surface, as one might expect of a frozen liquid. Very little UO₂/ZrO₂ material was found on the sidewalls of the crucible, and no fragmented debris was found on the top surface. These conditions differ significantly from the posttest melt mass

observed of the first LMF test, in which molten UO_2/ZrO_2 was slowly teemed from the LMF melt generator.¹⁻⁵ All observations indicate a very rapid teem of the melt into the TURC-2 test crucible. Posttest analysis of the UO_2/ZrO_2 melt charge indicated a bulk density of 6.50 g/cm^3 . The melt pool depth was 17 cm.

The posttest x-ray of the TURC-2 crucible shows a gap between the melt mass (dark mass) and the crucible. The gap may have been caused by differential thermal expansion of the materials during cooling or may have been an artifact of the interaction.

1.1.2.1 Thermal Response of Concrete

The thermocouple data recorded during the experiment showed that significant concrete erosion did not occur. Figure 1.2 shows the thermocouple traces at various axial depths in the concrete on the radial centerline. (The melting range of limestone common sand concrete is 1420-1675 K.) The thermocouple located 0.44 cm below the melt concrete interface shows that no concrete ablation occurred at this depth. The SLAM calculation which also appears in Figure 1.2 will be discussed later.

Close examination of the thermocouple traces clearly shows a temperature arrest at approximately 3750 K, indicating the release of free water within the concrete. The release of the water is continuous during the interaction, although the rate is obviously decreasing.

1.1.2.2 Gas Composition

The composition of gases drawn during TURC-2 are shown in Table 1.3. The first sample taken 60 s before the teem of the melt shows composition of the interaction atmosphere. As noted earlier, the portcullis was closed 10 s after the initiation of melt teeming. Although erosion of concrete was not observed, conduction of energy into the concrete was driving off H_2O and CO_2 into the crucible. This is apparent from the gas composition after the portcullis was closed.

The H_2 and CO contents of the gases demonstrate that reduction of the gases did occur as they passed through or around the molten pool. As shown in Figure 1.3, considerable amounts of CO_2 were reduced to CO . However, the data does not provide a clear indication of the efficiency of the reduction, due to poor H_2O vapor diagnostics.

An interesting point is the drop in CO_2 reduction shortly after the initiation of the interaction. Since the reduction is sensitive to the debris pool temperature, one would

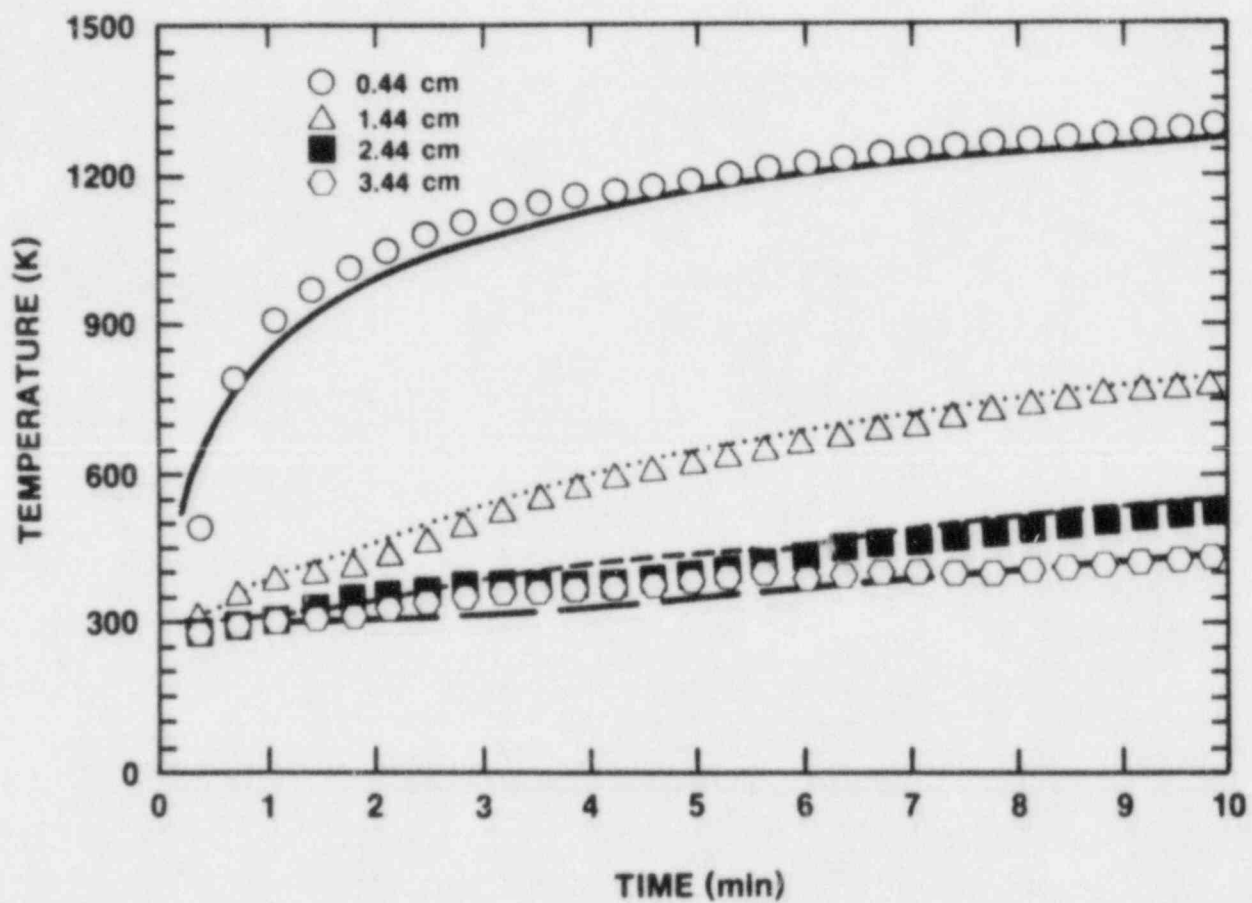


Figure 1.2 Experimental and Predicted Thermocouple Data for the TURC-2 Test

Table 1.3

Gas Analysis Data for TURC-2 Test

Volume Fraction of Gas Species

Time Sec	H ₂	N ₂	O ₂	Ar	Co	CH ₄	CO ₂
-60.0		77.343	20.384	2.273			
6.0		73.836	19.702	6.462			
10.0		73.403	19.632	2.108	2.766		2.902
15.0	23.425	42.863	3.929	9.464	16.668	tr	4.652
20.0	43.151	9.207	0.765	tr	33.766	tr	13.111
25.0	44.975	11.389	0.779	5.083	26.080	tr	11.695
30.0	46.096	10.463	0.833	tr	30.201	tr	12.407
35.0	41.648	11.077	0.849	13.668	22.008		10.751
40.0	39.838	8.887	0.729	20.180	19.744		10.623
45.0	39.837	8.239	0.614	25.896	15.656		9.758
50.0	33.946	6.820	0.536	34.192	14.478		10.028
55.0	30.970	5.853	0.458	39.143	13.845		9.731
58.0	29.180	8.985	0.691	41.358	11.216		8.571
60.0	27.503	9.186	0.733	43.089	10.918		8.171
70.0	26.050	9.763	0.804	45.235	10.089		8.058
90.0	22.256	9.727	0.770	50.717	8.786		7.744
120.0	21.887	6.131	0.563	57.469	6.542		7.408
150.0	18.751	11.342	0.941	54.252	7.195		7.519
180.0	18.791	2.166		69.120	5.532		4.391
210.0	16.976	6.548	1.098	62.028	5.327		8.023
240.0	16.970	5.050	0.792	63.950	4.984		8.255
270.0	16.573	4.457	0.514	64.508	5.574		8.374
300.0	8.633	6.837	0.693	71.686	4.028		8.122
390.0	8.324	36.709	2.304	44.029	3.033		5.601
450.0		87.720	8.278	3.553	tr		0.450
480.0		79.266	20.734				
510.0		79.279	19.875	0.846			
540.0		78.467	20.592	0.941			

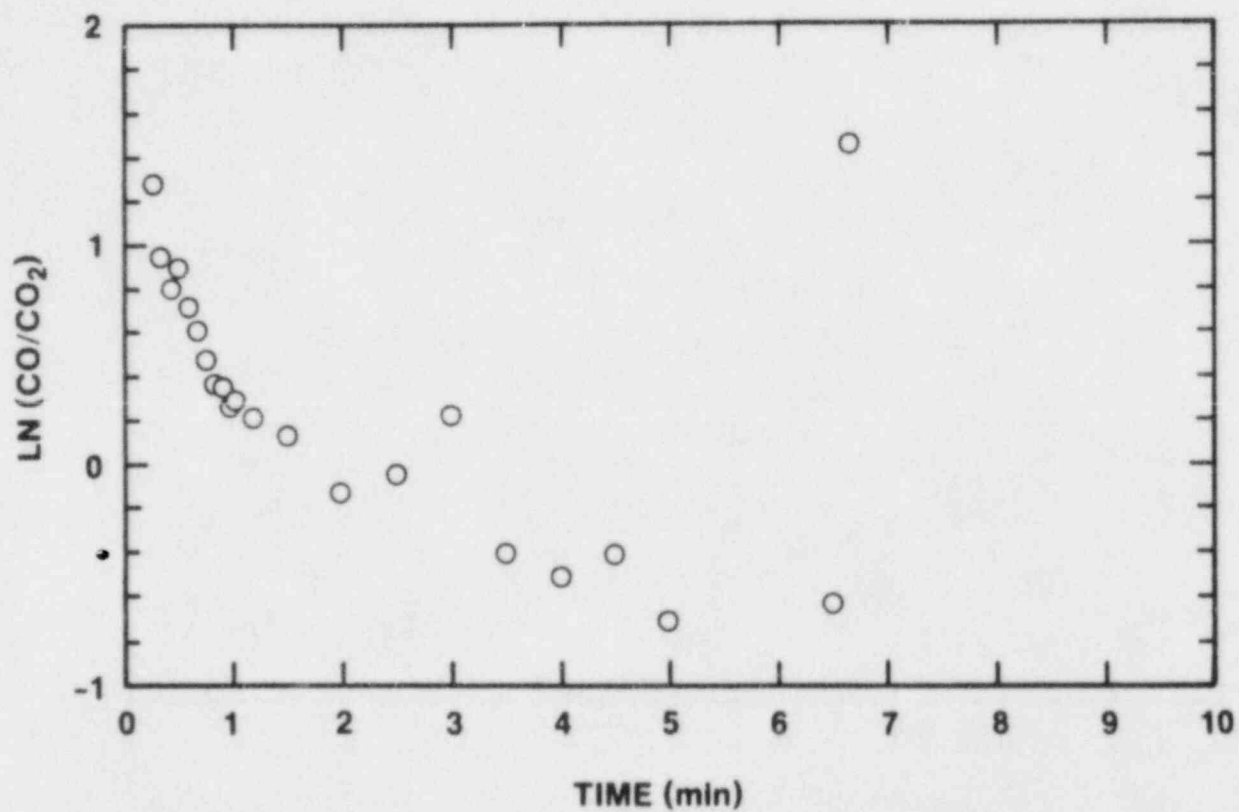


Figure 1.3. The Ratio of CO to CO₂ in the TURC-2 Test as a Function of Time

expect the production of CO to be fairly constant over this time period. Apparently, the gases are not passing up through the melt pool, but bypassing it and flowing around the crust. Since the crust-concrete interface is cooling rapidly, the reduction efficiency would fall also. The posttest x-ray of the TURC-2 test shows a gap in which gases may have flowed around the debris bed.

1.1.2.3 Aerosol Data

The mass mean aerodynamic diameter of aerosols generated during the TURC-2 experiment was found to be 0.1 μm . The distribution appears to be unimodal. Physical examination of the aerosol by SEM shows the formation by condensation of vapors with subsequent agglomeration. The results of a partial elemental analysis, performed by X-Ray Fluorescence (XRF), is shown in Table 1.4. (Note: XRF does not provide the chemical composition of materials.)

Table 1.4

Partial Elemental Composition List

<u>Element</u>	<u>Amount (w/o)</u>	
	<u>0-10 sec</u>	<u>60-120 sec</u>
TE	8.0	7.0
U	2.0	5.0
Mo	1.7	6.5
Ni	2.02	2.0

Trace amounts of: I, Cs, Ce, Si, Fe, Ca, Ba, Mn, Zr

1.1.3 Experiment Analysis for TURC-2

1.1.3.1 Energy Balances

The main purpose in making an energy balance is to help understand what phenomena are occurring in the experiment. In principle, if a large number of different heat flux measurements were made, they could be checked for internal consistency and then conclusions regarding the different phenomena could be drawn. However, only a limited amount of experimental data is available because temperature measurements in the range of interest cannot be made with current technology. Thus, models are substituted for measurements and the only check for internal consistency is the temperature and composition of the pool melt. If the temperature of the pool can be predicted in a consistent fashion from

one experiment to the next, and consistent comparisons with experimental thermocouple data from various points in the system can be made, then one can assume that the energy balance as described by the models is reasonably accurate.

The temperature of the pool is calculated by integrating the various heat losses over time. The differential equation that describes the pool temperature is

$$M_p C_p \frac{dT_p}{dt} = -(q_c A_p + q_R A_p + q_w A_w) \quad (1.1)$$

where

M_p = pool mass--a function of composition

C_p = pool specific heat--a function of composition

A_p = pool surface area πr^2 , r = pool radius

A_w = wall surface area $2\pi r d$, d = pool depth.

The q 's correspond to the three different heat loss mechanisms:

q_c --heat lost into the ablating concrete,

q_R --radiative heat lost from the upper surface, and

q_w --heat lost into the sidewalls of the crucible.

The pool depth is calculated from the materials present, their densities, and the gas volume fraction. The gas volume fraction is a function of the superficial gas velocity and bubble velocity. The bubble velocity in turn depends upon bubble size, properties, and the flow regime, all of which are poorly known during the experiment and undoubtedly change during the course of the experiment. Currently, a crude estimate of 1 m/s is used for the bubble velocity.

From the thermocouple traces shown in the previous section, it is possible to estimate an erosion rate as a function of time. The pool temperature during the erosion process is above the failure temperature of the thermocouples. The time of thermocouple failure is known to within 10 s, since the digital data acquisition system was recording data at that rate for these experiments. Given that the erosion rate is known, it is possible to estimate the heat losses from the melt slug as a function of time by using some simplifying approximations.

The heat loss to the ablating concrete is calculated by the heat transfer formulation described in the Sodium Limestone-concrete Ablation Model (SLAM).¹⁻⁵ The formulation consists of a two-region model--a dry (dehydrated) zone and a wet zone. The boundaries of both regions are allowed to move according to either the ablation rate or the moisture migration rate. Heat transfer and gas release are calculated as a function of time. The input to this model is the ablation rate (obtained experimentally) and the properties of the system.

The heat flux into the sidewalls cannot be calculated exactly from a simple analytic expression because the pool temperature as a function of time is not unique. Rather, the pool temperature depends upon the choice of experimental conditions such as diameter, initial mass, and composition. An approximate expression for the heat flux can be obtained from the analytic expression for the transient heat flux to an infinite medium exposed to a sudden temperature change solved simultaneously with the bulk wall energy equation:

$$q_w = \frac{K(T_p - T_w)}{(\pi \alpha t)^{1/2}} \quad (1.2)$$

$$M_w C_w \frac{dT_w}{dt} = q_w A_w + H_e A_w (T_\infty - T_w) \quad (1.3)$$

where

K = thermal conductivity of the MgO sidewalls

T_p = pool temperature

T_w = bulk wall temperature

α = thermal diffusivity of the sidewall

t = time from initial contact or d/v , whichever is smaller

v = ablation rate

q_w = heat flux into the sidewall

M_w = effective wall thermal mass

C_w = wall specific heat

H_e = outer wall heat transfer coefficient

A_w = wall surface area exposed to the melt

T_∞ = ambient temperature.

These equations are considerably simpler than a fully finite difference formulation of the same phenomenon. It is, however, not as accurate. In spite of its simplicity the predictions compare reasonably well when compared with inverse heat flux calculations derived from experimental data.

Radiative heat loss from the top of the pool is complicated by the effect of splashing and sloshing of the pool that leaves a film of material upon the sidewalls that freezes with time. In addition, during the test a large amount of aerosols are given off that reduce the radiative heat loss. All of these factors make an accurate estimation of the radiative heat loss rather difficult. A simple formula was chosen to estimate the radiative heat loss

$$q_R = \epsilon \sigma T_p^4 - T_w^4 \quad (1.4)$$

where

q_R = the radiative heat flux

ϵ = an emissivity/shape factor

σ = the Stefan-Boltzman constant

T_p = the pool temperature

T_w = the wall temperature.

In spite of all the uncertainties noted in the various heat loss mechanisms, the heat balance and thermal history of the pool turn out to be quite reasonable, because the factors that have the greatest uncertainty turn out to be less important than anticipated when the actual magnitude of the heat losses are calculated.

Figures 1.4 and 1.5 show the results for the TURC-2 test. Figure 1.4 is a plot of the location of the dehydration zone or the wet front. There is no surface ablation in the TURC-2 test. Figure 1.5 is a plot of the heat losses of the various mechanisms. The dominant heat loss in this case is from radiation off the top of the pool. Heat losses into the wall and concrete are less significant because of the rapidly growing crust on these surfaces.

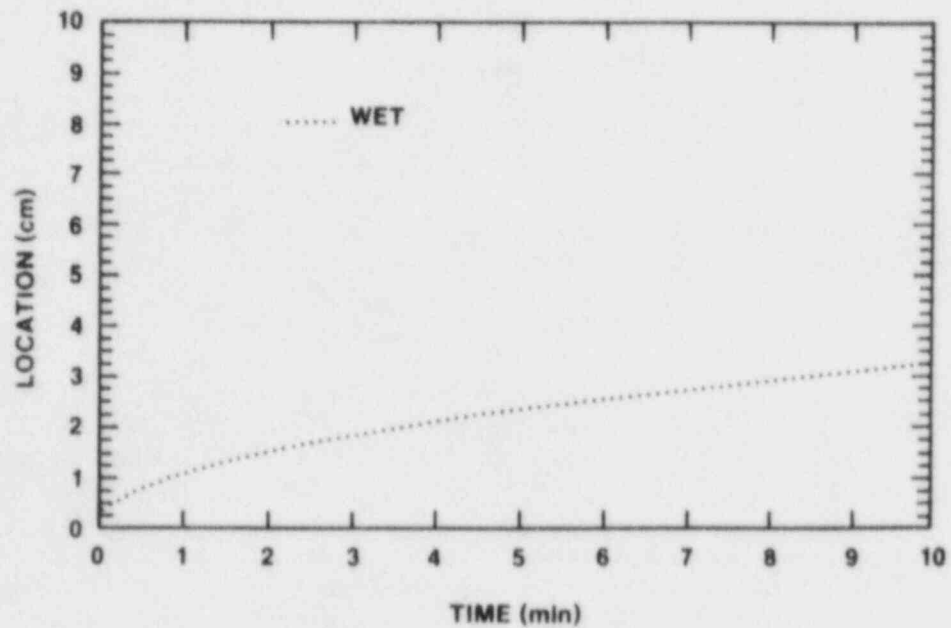


Figure 1.4. The Predicted Dehydration Front Location in the TURC-2 Experiment

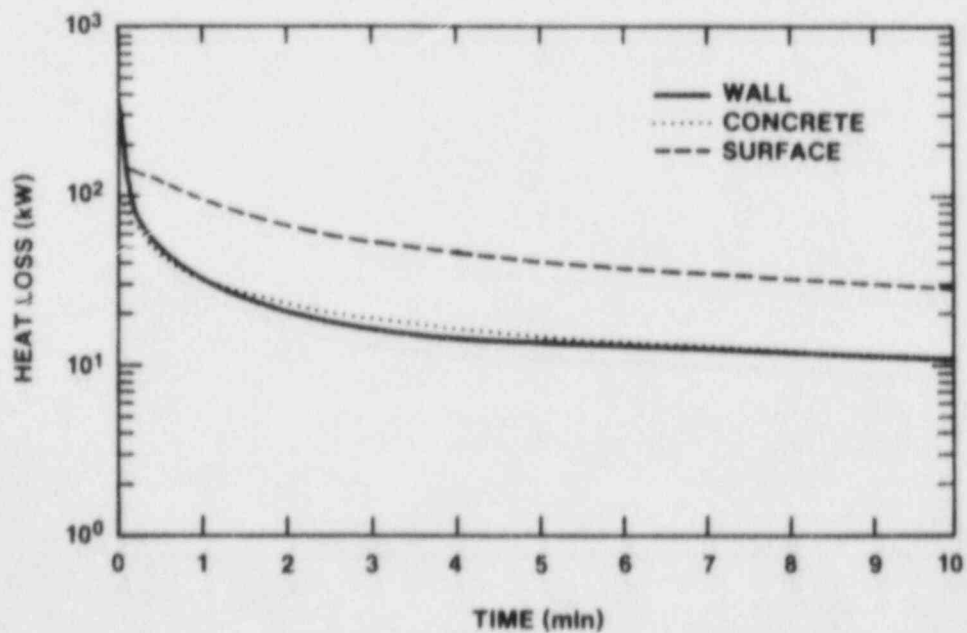


Figure 1.5. The Predicted Heat Losses for the TURC-2 Experiment

1.1.3.2 Implications

An interpretation of these results leads to some rather unusual conclusions regarding the heat transfer mechanism to concrete. The lack of any significant erosion in the TURC-2 test implies that crust behavior is very important in determining the extent of erosion. In the TURC-2 test there was very little superheat in the melt, hence rapid crust growth was expected to occur. Apparently, the crust that does grow is of sufficient strength to resist breakup from the gas that is released from the concrete. For the case of UO_2 , the gas release is rapidly suppressed by crust growth because of its low thermal conductivity. If a large amount of superheat is present, then crust growth is inhibited. Superheat in the melt can be generated by lowering the ratio of heat losses to power generation, and also by lowering the melt point. Both of these phenomena will occur in sustained heating experiments, because of heating of the surroundings (which lowers the heat loss) and by dissolution of concrete constituents into the UO_2 (which lowers the melt point).

For the case of stainless steel, a different phenomena is observed. In the earlier TURC-1SS test a heat transfer mechanism that is independent of pool temperature was observed from the observation that the penetration rate was constant and several hundred degrees of superheat existed. A heat balance calculation for the TURC-1SS test indicated that penetration was maintained as long as superheat was present. A mechanism of heat transfer that is independent of the thermal driving force is very unusual. There are several possible explanations that would require model development in order to check their feasibility. Sustained and rapid spallation is one possibility. Another possibility is a heat transfer mechanism driven by phase change. In the steel test, the molten steel could be freezing locally at the interface. The escaping gases would carry the frozen steel back into the bulk of the pool for remelting. Liquid steel would move down from the pool to the surface in order to replace the frozen steel that has been swept away. This mechanism would continue until the steel is either too viscous to support such a mechanism or a solid crust forms which cannot be swept away.

1.2 Core-Concrete Interaction Analysis (CORCON) (D. R. Bradley, 6425; D. A. Powers, 6422)

The CORCON Code, developed by Sandia Laboratories, is intended to provide a detailed, mechanistic model of core-concrete interactions. The code models a two-dimensional axisymmetric ablation process, whereas the experiments are one-dimensional. However, if a very large diameter pool is used, the ablation is essentially one-dimensional. In the experiment significant sidewall heat loss exists which

cannot be modeled directly by CORCON because there is no provision for a nonablative sidewall. However, if a negative heat source is used in the molten pool, then heat will be extracted and a sidewall heat loss mechanism can be simulated. Thus, in the limits of large pool diameter with a negative heat source, direct comparisons between CORCON and experiments are possible.

CORCON consists of a number of interacting models that describe the various heat transfer mechanisms. Some of these mechanisms have been assumed to exist with no experimental verification. The experiments reported herein can be used to determine if the models are adequate to describe the heat transfer. The primary models of concern in these simulations are those that describe the heat transfer from the pool to the melting concrete interface. In CORCON a film boiling-like mechanism is assumed to exist. This assumption is based upon the large amount of gas that is stored in concrete and which is rapidly liberated during a high temperature ablation process. Correlations have been developed by a few investigators based upon simulant fluids.

Figure 1.6 shows the CORCON prediction for the TURC-2 test erosion. TURC-2 had no measureable penetration. However, the CORCON prediction shows some level of ablation for both of the cases shown in Figure 1.6. The MOD2-2900 K case shows 4 cm of erosion over the time scale of the calculation. In this case the eroded concrete dissolves into the UO_2 and lowers the melt point at a rate that keeps the pool molten long enough for significant erosion to occur. In the MOD2-2500 K calculation the UO_2 eroded the concrete as a solidified block.

1.3 Molten Fuel-Coolant Interactions

(B. W. Marshall, Jr., 6427; M. Berman, 6427)

The objective of this program is to develop an understanding of the nature of fuel-coolant interactions (FCIs) during hypothetical accidents in light water reactors (LWRs). FCIs can occur in the core region, in the reactor lower plenum, or in the cavity below the vessel. They can occur when melt falls into water or when water falls into melt. The understanding of FCIs achieved in this program should be sufficient to resolve the key reactor safety issues for both terminated and unterminated accidents. Models are being developed to determine:

1. The rates and magnitudes of steam and hydrogen generation due to FCIs,
2. The probability and consequences of direct containment failure by steam explosions,

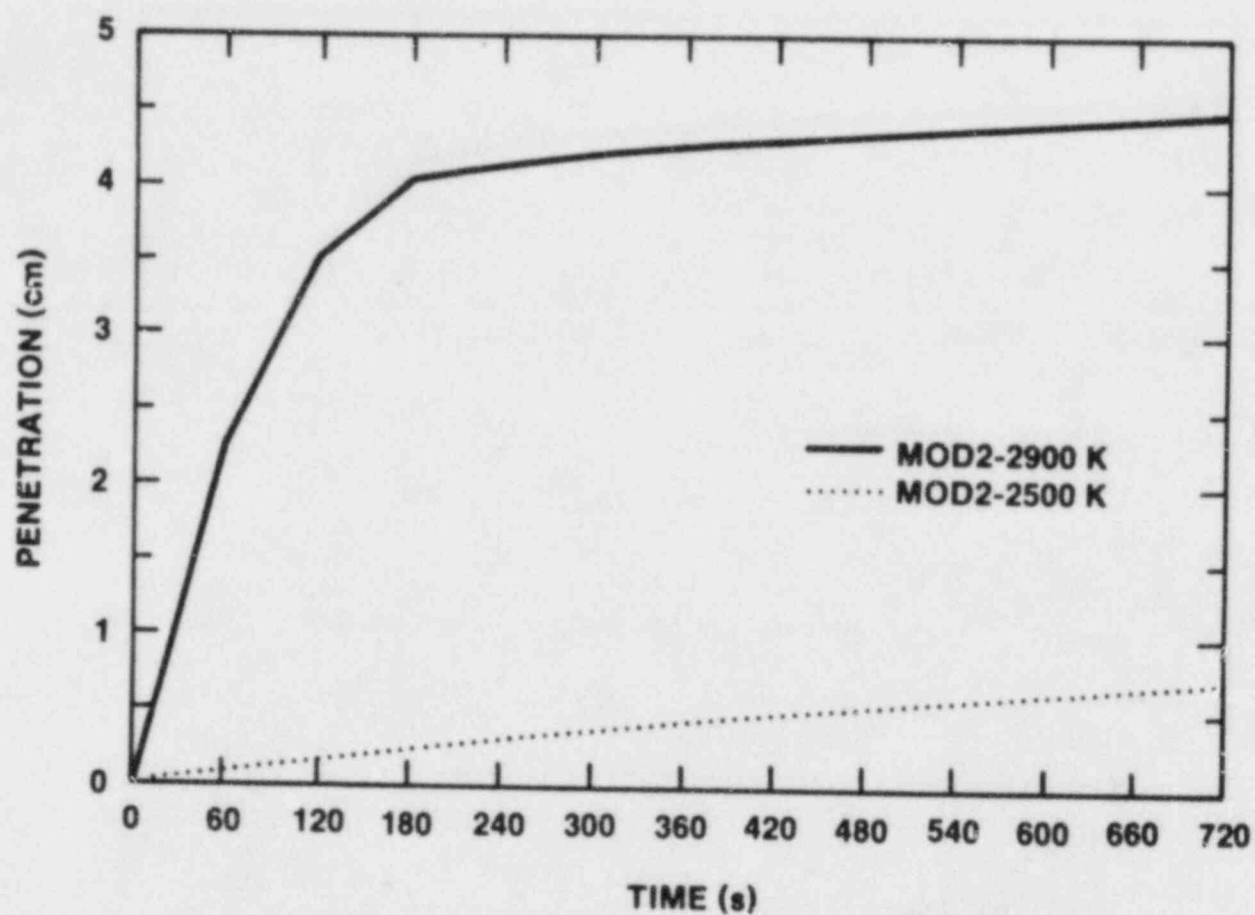


Figure 1.6. The CORCON Prediction of the Ablation Front in the TURC-2 Experiment

3. The influence of FCIs on accident progression and the nature of the source term (including fission-product chemistry, release rate, particle size, and dispersal).
4. The consequences of pouring water on the melt in order to terminate an accident, and
5. The characteristics of the debris produced by FCIs, including particle size distributions, porosity, and coolability.

1.3.1 Experiments, Data Reduction, and Analysis

1.3.1.1 FITSD Experiments

(B. W. Marshall, Jr., 6427; M. S. Krein, 6427)

There were no major experimental efforts for the FCI program at FITS during this reporting period. Preparations continued for the D series. The mass spectrometer systems are on order and should be in-house by the time the D series begins in March or April 1985. Parts were also designed and ordered for the 50-kg crucible and furnace extension to be used on the FITS tank. High-pressure feedthroughs were also investigated.

1.3.1.2 EXO-FITS Experiments

(B. W. Marshall, Jr., 6427; M. S. Krein, 6427)

Final construction and preparations of the new 50-kg EXO-FITS II facility were performed. A schematic of this facility is shown in Figure 1.7. It will be used primarily for developmental and diagnostic purposes. Initially, the ability to deliver 50 kg of molten iron/alumina to water chambers similar to those used in the D series will be pursued. Conscious efforts will be made to duplicate, as close as experimentally possible, the applicable conditions in the FITS tank such as drop height, water chamber cross-section, water depth, etc. Comparisons between the 20-kg and 50-kg melt shapes will be of particular interest in addition to the explosive nature of a 50-kg FCI. These tests will give us an indication of the nature of the FCI that we may expect during completion of the D series.

Questions have been raised by SNL personnel as to the validity of the water phase pressure gage results. In particular, we have been interested in the effect of radiation from the molten fuel and rigidity of the gage mounting support on these measurements. Assessment of the accuracy of the water phase pressure gage measurements will be coupled with the 50-kg developmental experiments.

Recent discussions with NRC and SNL personnel indicated that x-ray measurements of the mixing phenomena and melt entry

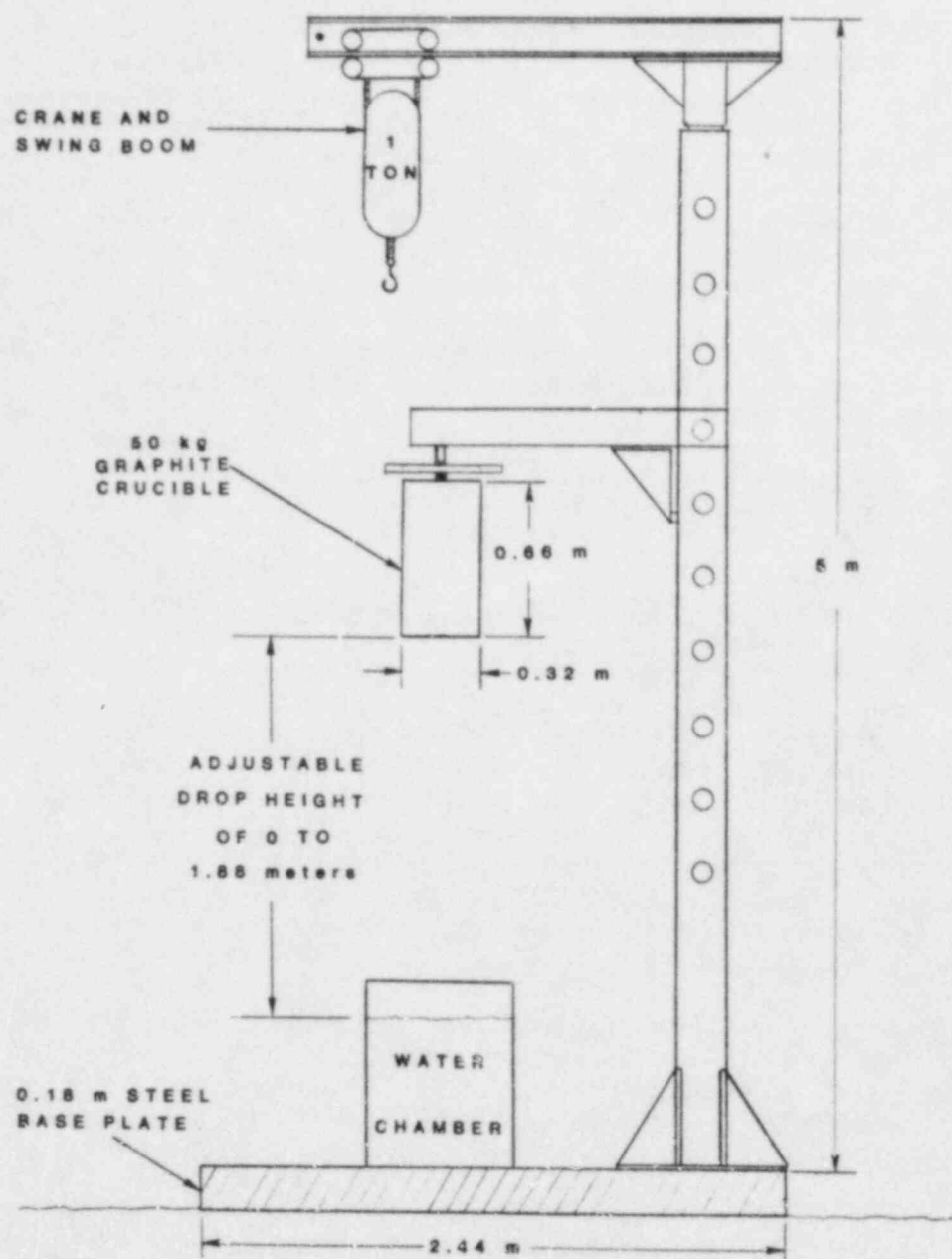


Figure 1.7. EXO-FITS II Facility

conditions should be pursued. We will attempt to make these measurements in the new EXO-FITS II 50-kg experiments. The details of the methods to be used are not currently available, but SNL personnel are working to make such measurements if they are possible.

During the next quarterly period, we expect to complete the construction and implementation of the new EXO-FITS facility. At that point, we will perform approximately five scoping and diagnostic experiments using a 50-kg thermite charge. As mentioned in the above section, we will attempt to solve questions pertaining to the accuracy of the pressure measurements as well as perform x-ray diagnostics on the melt at entry and possibly in the mixture region. We will attempt to duplicate as many of the variables used in the D series as experimentally possible. We currently plan to reproduce the FITS6D experiment. These experiments will be primarily used to diagnose the differences, if any, between a 20-kg melt and a 50-kg melt.

1.3.1.3 The Study of Iron/Alumina Thermite
(B. W. Marshall Jr., 6427; G. B. StClair, 6427;
M. Watkins, 6420)

The study of the iron/alumina thermite used in the SNL fuel-coolant program was prompted by the fact that significantly slower reaction rates were recorded in nitrogen than in air. Additionally, not only did the reaction rate appear to change dramatically, but a visual observation of the melt (from high-speed camera data) led SNL personnel to suspect that the temperature of the molten products was significantly lower than when the reaction took place in air. It therefore became the objective of this study to experimentally define the reason for this behavior and further to define a technique for achieving a consistent thermite burn independent of the surroundings.

The study of the iron/alumina thermite used in the FCI experiments was conducted earlier this fiscal year and is described in Reference 1-6. The experimental set-up and tests performed are described in detail in this reference, but will be quickly reviewed here for convenience.

Fifty-five thermite burns were conducted in the pipe-bomb shown in Figure 1.9. Essentially all of these experiments were comprised of 1.19 kg of aluminum powder and 3.81 kg of Fe_3O_4 iron oxide powder resulting in a 5-kg charge. The thermite was placed in a standard graphite crucible which had an inside diameter of 15.24 cm and an overall length of 17.78 cm. The crucible had removable top and bottom plates which contained the reaction and allowed recovery of the frozen products. During these experiments the pressurization of the chamber, the associated gas temperature, the

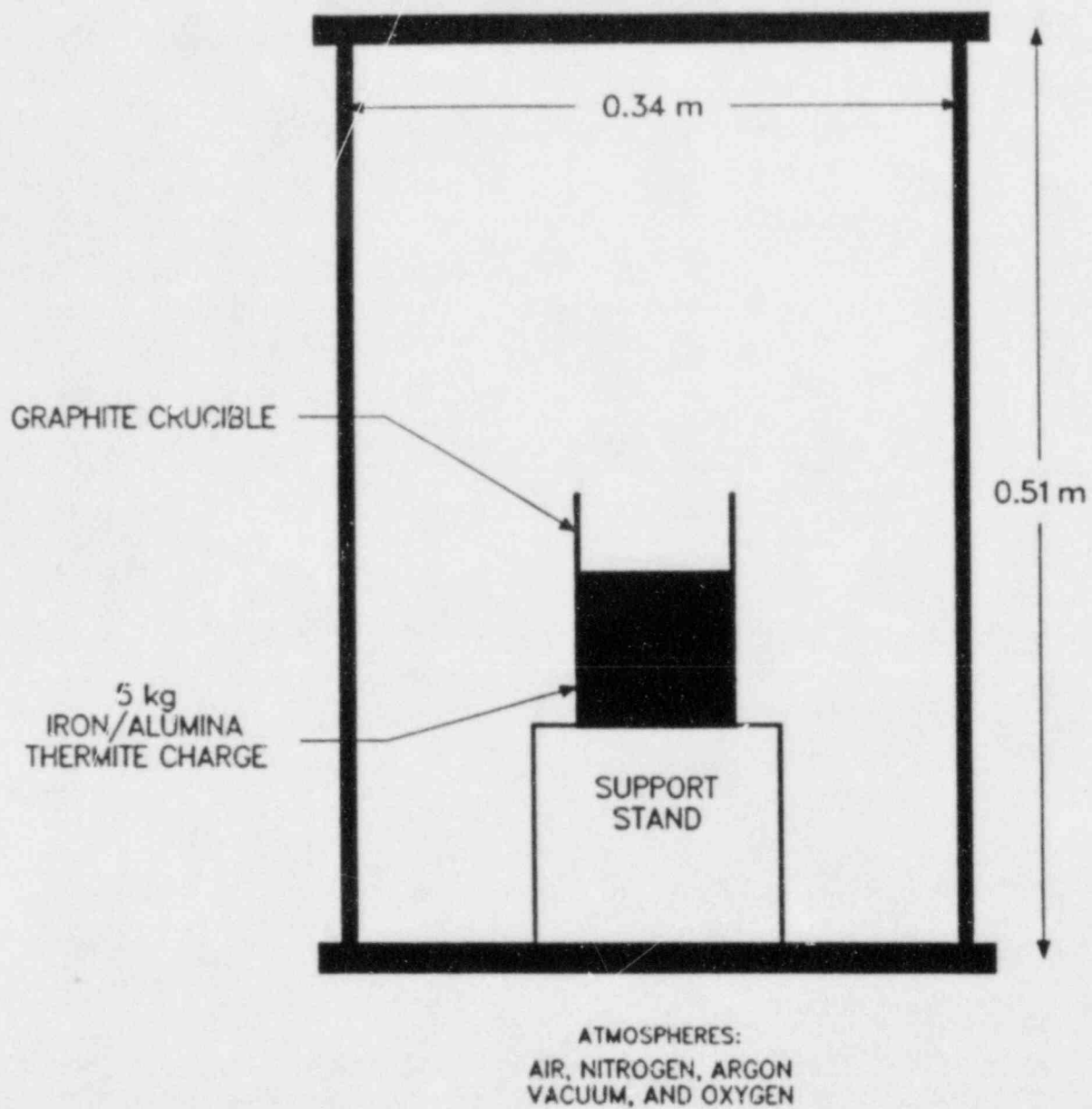
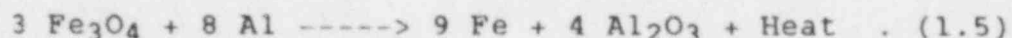


Figure 1.8. Experimental Setup

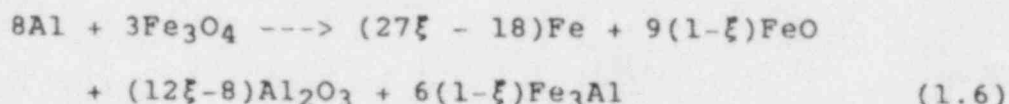
thermite reaction rate, three gas samples (one before and the remaining two after the reaction was complete) of the atmospheric gases, and the product billet weights were recorded. The experiments conducted were purely for diagnostic purposes and not intended to be a complete matrix which would evaluate the sensitivity of the reaction to different parameters. Instead, it was intended to define the parameters that are important to the reaction and further to define experimental methods which would yield a consistent reaction.

1.3.1.3.2 Iron/Alumina Reaction Theory

In theory, the reaction of magnetite powder (Fe_3O_4) with pure aluminum powder should proceed independently of the surrounding conditions. Theoretically, the exothermic reaction will proceed as follows:



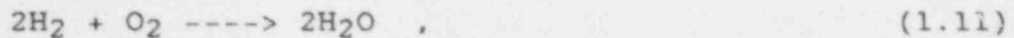
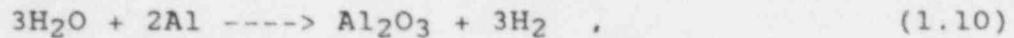
The reaction is self-consistent and no interaction with the surroundings is necessary or should occur. In practice, however, we find this not to be the case. It has been suggested in Reference 1-7 that a more realistic description of the thermite reaction is:



where ξ is the extent of the reaction ($0 < \xi < 1$). The above chemical equation does not, however, provide for reactions with the containment material or the atmosphere surrounding the reaction process if such reactions were to occur.

If the boundary and atmospheric conditions are considered, we should include the reaction of carbon with oxygen, the reaction of available water with aluminum to release hydrogen, and the combustion reactions with the atmospheric gases. To summarize, some possible reactions include:





in addition to the reaction of any impurities that may be in the constituents.

Carbon, supplied from the graphite crucible, reacts easily with oxygen in the containment atmosphere. CO and CO₂ are both thermodynamically favored at melt temperature (around 2500 K), with CO being the dominant product.

The source of hydrogen is moisture absorbed on the surface of the thermite constituents. The water reacts with aluminum at the melt temperature to release H₂. Stoichiometrically, about 0.1 g of hydrogen is produced for every 1 g of water.

1.3.1.3.3 Experimental Results

The primary and secondary variables that were considered during this study are shown in Table 1.5. The two primary variables (iron-oxide baking temperature and atmosphere) are shown with the corresponding levels of interest. In Table 1.6 the secondary variables are shown. Although we have listed three items of interest with each secondary variable, the crucible type and iron-oxide batch is a relatively fixed quantity since graphite crucibles and the iron oxide cannot be changed without major program delays. Therefore, the importance of the primary variables, atmosphere and baking temperature, will be discussed in much more detail than the secondary variables.

Table 1.5

Primary Experimental Variables

Atmospheres:

Air
Nitrogen
Oxygen
Argon
Vacuum (~1 psia)

Crucible Type:

Graphite
Alumina
Magnesium Oxide

Table 1.6

Secondary Experimental Values

Iron Oxide Baking Temperature:

No Baking
 473 K
 873 K
 1073 K
 1273 K

Iron Oxide Batches:

SN 47 7379, used in FITSD series
 SN 31 6942, used in CM, ACM, and RC series
 SN 50 1457, used in FITSC series and CM 1

1.3.1.3.3.1 Iron-Oxide Data

Four different orders for the magnetite powder have been placed by SNL personnel since the early stages of the FCI program. These old purchase requisitions have been gathered and the important results are shown in Table 1.7. Order number 50-1457 and 31-7379 were received marked MS 60, which is a factor designation indicating the particle sizes, while order number 74-7197 and 47-7379 have MS 30 designations. The only difference between the two MS distinctions is the fact that the MS 60 has a somewhat finer particle distribution than does the MS 30 powder. It should be noted that MS 30 batches were specified by SNL personnel.

Table 1.7

Past Iron Oxide Purchasing Data

<u>Batch</u>	<u>PR #</u>	<u>MS #</u>	<u>FITS Tests</u>	<u>% Below 44 μm</u>
1	74-7197	MS-30	MDC, FITS-B, FITS1C	1%
2	50-1457	MS-60	FITS4C, 5C, CM-1	33%
3	31-6942	MS-60	CM2-12, RC, ACM, FITSOD	33%
4	47-7379	MS-30	FITS ₂ D, 5D, 8D, ETE	10%

The differences between the two powders is evident when comparing the weight percentages below a 44- μ m sieve cut.

The two batches having MS 60 designations have approximately 33 percent of their total weight below 44 μm , while the MS 30 have 10 percent or less below 44 μm . SNL personnel responsible for conducting the experiments for the FCI program have noted more vigorous thermite reactions when the two MS 60 batches were used, while relatively mild consistent reactions were observed when the MS 30 batches were used.

In Table 1.8, the results of a chemical analysis of the four different magnetite powders is shown. In these analyses, there was no distinction between the different oxidation levels of iron. These different oxidation states are particularly important to the final products and especially the resulting temperature of the molten pool. Therefore, the batch of iron-oxide (47-7379) presently used in the D series will be analyzed for these different oxidation states. This work is ongoing and will be reported as the results warrant.

Table 1.8

Chemical Analysis of the Iron Oxides

<u>Order Number</u>	<u>Manu. Number</u>	<u>%Fe</u>	<u>0.1 TO 5%</u>	<u>Trace Levels</u>
50-1457	MS-60	95%	Ca,Ti,Mn	Al,Si,S,K,Cr Ni,Co,Cu,Mo
31-6942	MS-60	95%	Ca,Ti,Mn	Al,P,S,K,Cr Mn,Co,Cu,Mo
47-4379	MS-30	Currently being analyzed by Sandia		

1.3.1.3.3.2 Experimental Data and Results

The most useful and important data collected during this series of experiments were the atmospheric pressurization and the atmospheric gas samples. The important result noted from the gas sampling is the fact that both carbon monoxide and carbon dioxide gases are produced independently of the initial atmosphere constituents. That is, in each thermite burn there were noticeable (approximately 1 percent or above) levels of both carbon products. However, the carbon gases are generated as long as there is available oxygen in the atmosphere, as would be expected. The interesting case is when the reaction takes place in an inert atmosphere such as nitrogen and argon; carbon gases are still generated during the reaction process. Further, as previously mentioned, the carbon monoxide appeared as the dominant carbon product.

In Figure 1.9, pressure plots from two different thermite burns in a nitrogen atmosphere are shown. This figure clearly demonstrates the effect of baking the iron oxide powder at 800°C for 6 hr. The significant reduction in gas generation from the thermite reaction is apparent when comparing the late-time pressure differences (approximately 75 kPa) in addition to the initial pressure rises during the reaction (approximately 100 kPa).

The dependence upon the available oxygen in the atmosphere is demonstrated in Figure 1.10, where thermite burns were performed in a graphite crucible. The iron-oxide powder was also unbaked. The important point here is that significant quantities of carbon monoxide and carbon dioxide were generated, generally using all of the available oxygen in the atmosphere. All of the results shown in Figures 1.9 and 1.10 were for the iron oxide that has been used in the D series (batch 47-7379).

The most important point is that any available oxygen, whether from the atmosphere or the thermite reaction process, will be used to form predominantly carbon monoxide with lesser levels of carbon dioxide. This work has also pointed out the importance of baking the iron-oxide powder to minimize the generation of gases. We have come to the conclusion that baking the iron-oxide powder at 800°C for 6 hr minimizes the gas production during the reaction.

1.3.1.3.4 X-ray Observations of the Iron-Alumina Thermite Reaction

The purpose of these experiments was to directly observe the thermite reaction. Of particular importance is the nature (gas generation, settle time, etc.) of the molten products after the reaction process is complete. All of these experiments, with the exception of the final one, were performed inside the steel chamber shown in Figure 1.8. The thermite was placed in the same graphite crucibles described for the above experiments. In all, 11 x-ray observations of the thermite reactions in a nitrogen and vacuum (1 psia) atmosphere were performed. In every case, contrary to past results, the reaction products settled into two layers within 2 s from the time the reaction front contacted the bottom of the crucible. As in the past x-ray observations, the reaction front appeared to burn in a planar fashion.

Two 20-kg thermite burns were also performed to check any scaling effects. The results of these tests were consistent with the 5-kg burns. The reaction settled into two quiescent layers within 2 seconds after the reactions front contacted the bottom.

These results lead us to believe that we can now produce a consistent burn which is independent of the atmospheric

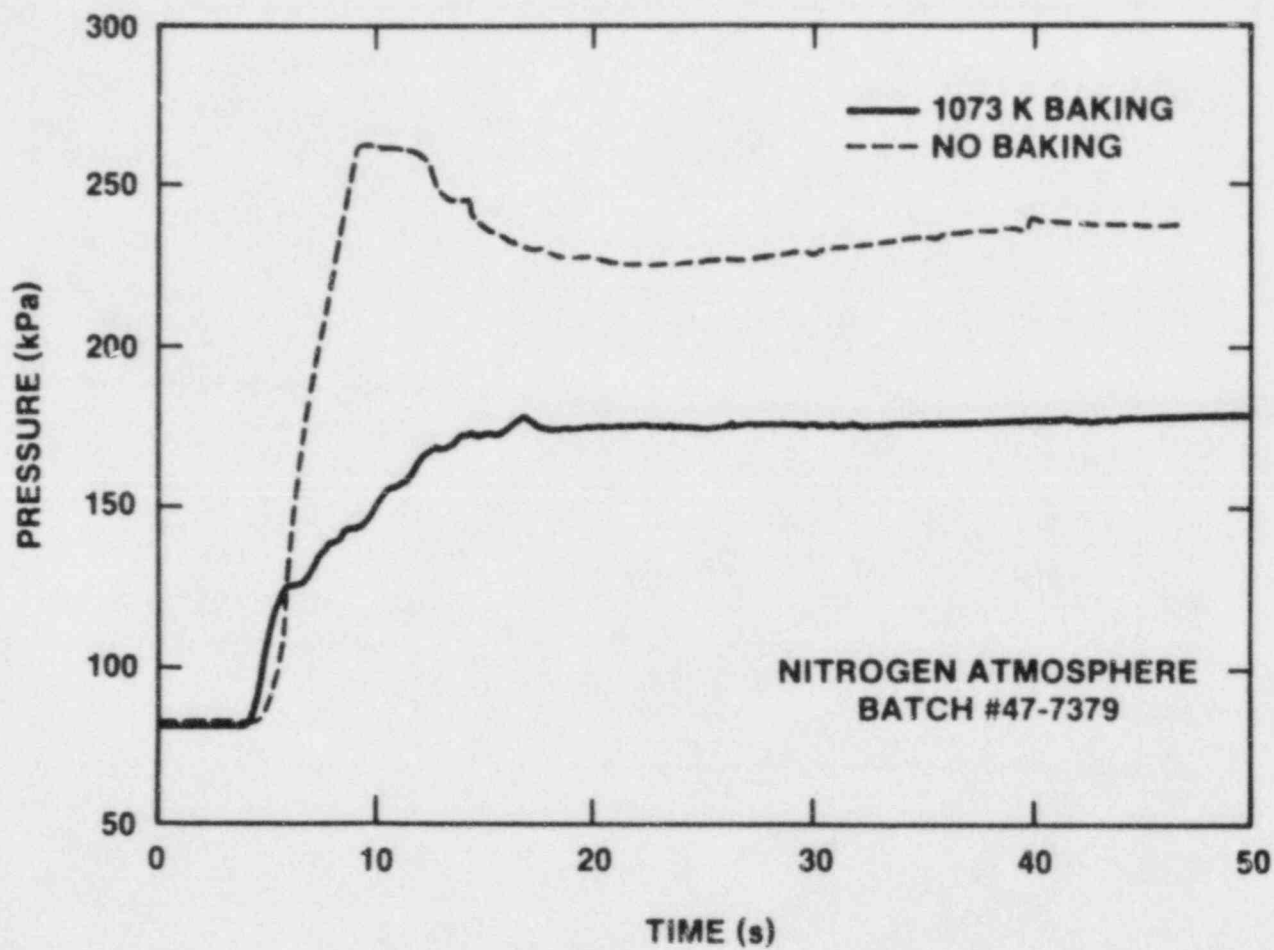


Figure 1.9. Effect of Baking the Iron Oxide

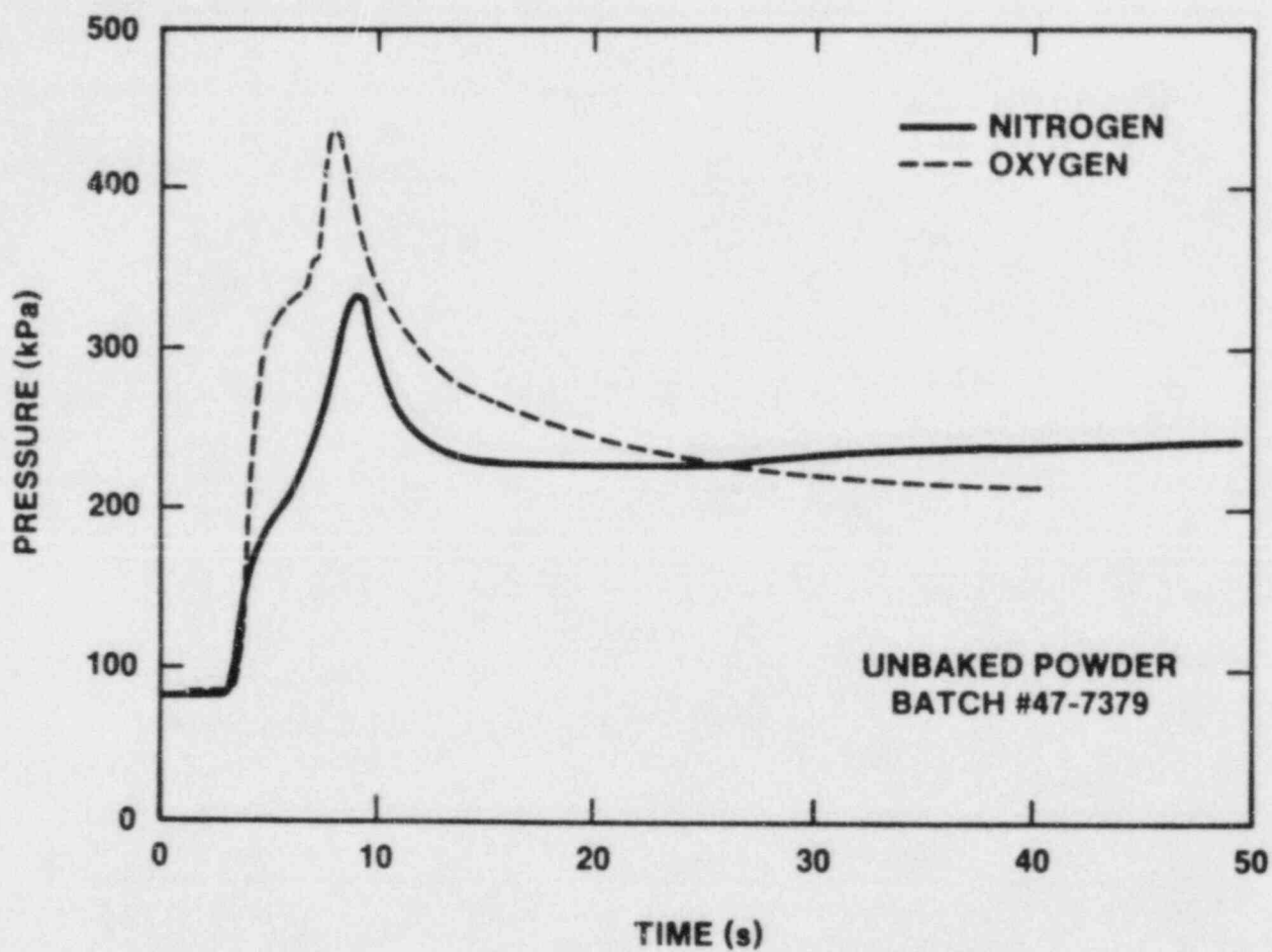


Figure 1.10. Effect of Available Oxygen

conditions. The preparation techniques defined by this series of experiments will be used in the D series of FCI experiments which are performed in a nitrogen cover gas.

1.3.1.3.5 Summary of Results and Conclusions

Some gas generation during a thermite burn will occur no matter what type of crucible and atmosphere in which the reaction is housed. The quantity of gas generation can, however, be significantly reduced by baking the iron-oxide powder at 800°C for approximately 6 hr. Baking minimizes the sources of hydrogen. The aluminum powder was not baked during this process because of potential hazards (e.g., the aluminum powder could ignite and burn as a dust, especially if it were completely free of moisture). We also have experimental data to reinforce the observation that carbon reacts easily with available oxygen in the containment atmosphere. Additionally, as expected, carbon monoxide is the dominant product at the melt temperature. The reaction rate (or burn rate) is consistent at approximately 2.5 cm/s independent of the atmosphere.

The products of the reaction were also observed via x-ray, to have settled out into layers of iron and alumina within 2 s after the reaction was complete. This is probably the most important observation, since past x-ray observations of the thermite produced showed a vigorous churning motion for at least 30 s after the reaction was complete. This type of reaction could possibly lead to a predispersion of the melt, enhancing the fuel-coolant mixing processes during an FCI experiment. Experimentally, this was not a favorable condition to have since we could not quantify the melt condition at coolant entry for each experiment. Having a quiescent melt pool at the time of melt drop during an FCI experiment is most important to both the experimental results and interpretations and to the code development. Thus for the batch of iron-oxide (47-7379) used in the D series, we have concluded that we can produce a consistent melt, which is independent of the atmospheric conditions, and further that the melt is in a quiescent pool at the time of drop.

Currently, we are in the midst of three activities. The first is to have the reactants and products analyzed by SNL personnel. We expect that the results of this work will lead to conclusions about the reaction completeness and about the oxidation state of the iron oxide. Single and 2-color pyrometer measurements of the melt temperature using both direct measurements of the melt surface and thermal wells are being pursued. Although problems have been encountered in the past by SNL personnel, we are hopeful that the preparation techniques defined by this work will work to our advantage. Calorimetry measurements of the actual heat content of the melt have been pursued. The

Thermophysical Properties Division at Sandia has an apparatus that was designed to make these measurements of various thermites.

1.3.2 Model Development and Applications

1.3.2.1 CSQ Calculations (K. Schoenefeld, 6425)

Preparatory scoping calculations were performed with the CSQII hydrodynamic code as a part of the process of developing a model of the SEALS experimental facility. Much of the time was spent in designing the geometric model used in CSQ, studying the impact of various input parameters, and removing bugs in the model. The FITS3B experiment is currently being used to define and model some of the important parameters, such as density in the mixture region and specific energy of the fuel, which will be used as input to model the SEALS experiments. Currently, this work is ongoing and there are no major results or interpretations to report.

1.4 Hydrogen Behavior (J. T. Hitchcock, 6427; M. Berman, 6427)

The objectives of this research program are (1) to quantify the threat to nuclear power plants (containment structure, safety equipment, and the primary system) posed by hydrogen combustion; (2) to disseminate information on hydrogen behavior, detection, control, and disposal; and (3) to provide program management and technical assistance to the NRC on hydrogen-related matters.

1.4.1 Deflagrations

1.4.1.1 HECTR Analysis and Development (C. C. Wong, 6427)

From September 26 to 28, a HECTR workshop was given in Bethesda, MD. The participants were mainly Nuclear Regulatory Commission personnel. In the workshop, features of the code were described, and sample problems were run with audience participation. Overall, the workshop was successful and the participants were pleased with the performance of the code.

During this quarter, besides working on finishing up the HECTR User's Manual and preparing for the HECTR release, we continued to develop new models and incorporate them into the postrelease version (Version 2.0) of HECTR. The latest model that has been developed is a radiative heat transfer model which accounts for the gas emittance from steam, carbon monoxide, and carbon dioxide. In addition, we

continued to assess HECTR against the NTS experiments and also perform sensitivity studies for the purpose of quality assurance.

1.4.1.2 Carbon Monoxide and Carbon Dioxide Emittance Model (C. C. Wong, 6427; A.C. Ratzel, 1513)

In accident scenarios in which core debris penetrates the reactor pressure vessel and cannot be cooled by water in containment, decay heating can maintain the debris at temperatures which can result in thermal decomposition of adjacent concrete. Such decomposition of concrete produces large volumes of water vapor and carbon dioxide which, if it comes into contact with molten metals, can be reduced to hydrogen and carbon monoxide. Combustion of a mixture of these two gases can be a potential threat to safety-related equipment or the integrity of containment.

For the purpose of analyzing any core meltdown accident involving combustion of both hydrogen and carbon monoxide, we have incorporated two additional gas species (carbon monoxide and carbon dioxide) into the HECTR code. In order to accommodate these two new gases (CO and CO_2), major changes were required in the combustion model and in the radiative heat transfer model. The changes in the combustion model have been mentioned and discussed in References 1-8. The detailed changes in the radiative heat transfer model will be presented in this section.

Since both additional gas species (CO and CO_2) are heteropolar molecules, they play an important role in thermal radiative heat transfer. Including these gas species in an environment which contains steam complicates the radiative heat interchange problem because the different radiating bands of each gas may overlap. With the increased number of radiating bands, performing multiple band radiative computations becomes more time consuming. In the preliminary unreleased version (Version 0.3) of HECTR¹⁻⁹ we evaluated a seven-band model for steam emittance, in which two bands were transparent in the initial wide-band formulation. The computational time for the radiative heat exchange calculation was substantial. We improved the computational time significantly by adopting a simple emittance model suggested by Cess and Lian.¹⁻¹⁰ However, a similar emittance model for carbon monoxide or carbon dioxide or a mixture of these gases is not currently available. Hence, another approach is to reconsider the wide-band gas emittance model and perform a band-by-band radiative heat exchange calculation.

As in the HECTR Version 0.3 gas emittance model for steam, the emittance data for carbon monoxide and carbon dioxide can be obtained either from Hottel emittance charts or from the Edwards exponential wide-band formulation. Because the

three gaseous radiators may have overlapping absorbing bands (Table 1.9), additional Hottel charts or other correction techniques are required to account for band overlap ($\Delta\epsilon$), according to a relation similar to that given by the equation,

$$\epsilon_g = \epsilon_{H_2O} + \epsilon_{CO_2} + \epsilon_{CO} - \Delta\epsilon$$

where ϵ_x is the emissivity of the component x . Such corrections are functions not only of the gas composition, but will also depend on the gas temperature and pressure as is shown, for example, in Figure 1.11 for combinations of steam and carbon dioxide. The difficulty in programming such effects favors the approach utilizing the exponential wide-band model.

Table 1.9
Absorption Band Centers for Radiating Gases

<u>Gas</u>	<u>No. of Radiating Bands</u>	<u>Band Centers</u>
Steam	5	1.38, 1.87, 2.7, 6.3 μ m and rotational band
Carbon Monoxide	2	2.35 and 4.7 μ m
Carbon Dioxide	6	2.0, 2.7, 4.3, 9.4, 10.4, and 15.0 μ m

A multiple band-by-band radiative heat transfer model with both carbon monoxide and carbon dioxide present in the steam environment, could have from 15 to 25 bands (many transparent) which would each be a function of gas, temperature, and pressure. The cost of such band-by-band computations would be prohibitive, and unjustified, considering the substantial uncertainty in applying the emittance value in nuclear reactor configurations. (Most of the data base is derived from the laboratory-scale experiments and under atmospheric pressure conditions.)

For the sake of simplicity and efficiency, we selected the equivalent (single) band correlation of Edwards wide-band model, thus avoiding any band-by-band radiative heat transfer calculations. This model utilizes the individual band data weighted by a wavelength-dependent black-body function

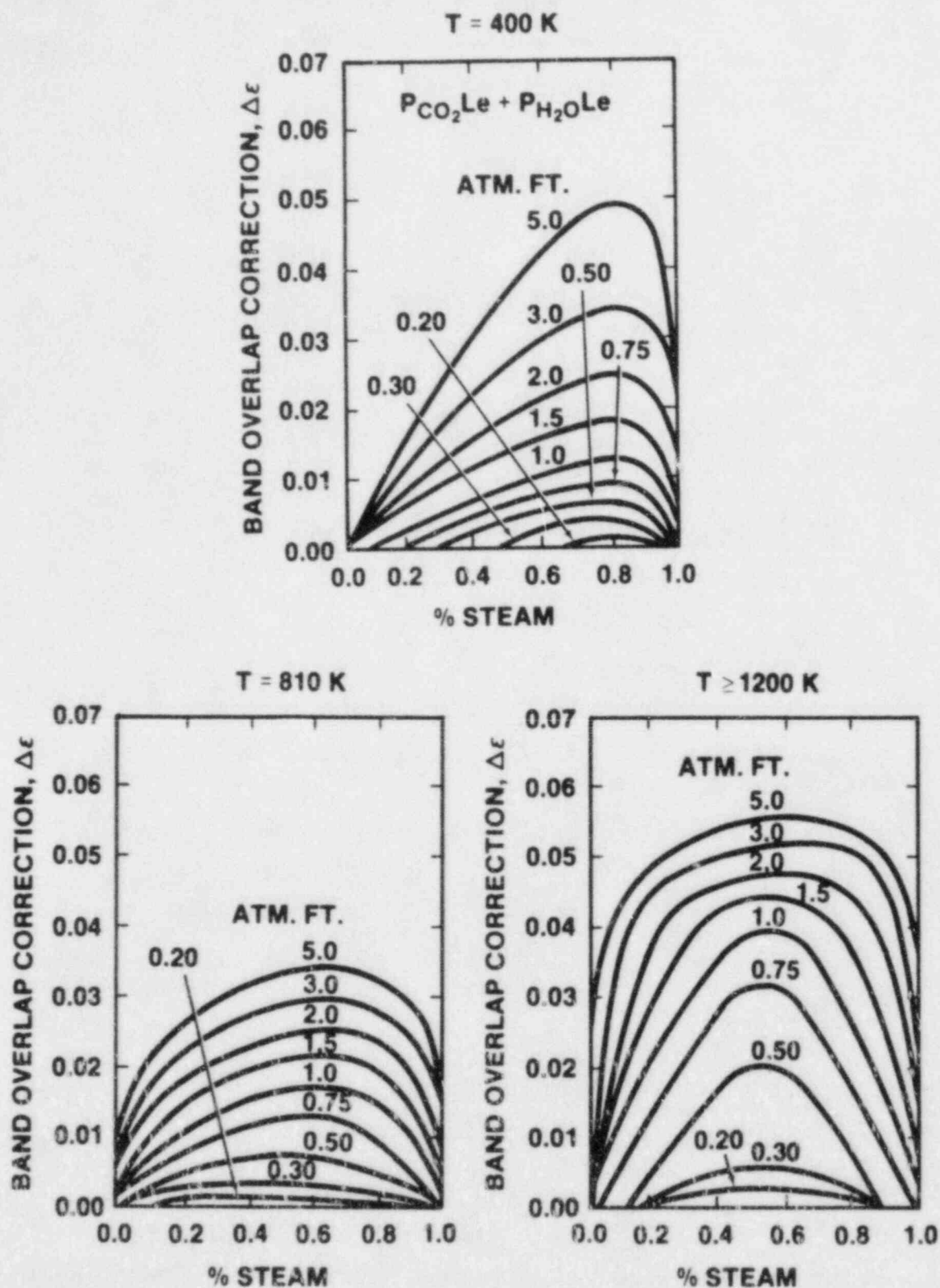


Figure 1.11. Correction on Total Emittance for Band Overlap When Both CO_2 and Steam Are Present (P_x = pressure, L_e = beam width)

to compute the total emittance as given in the following equation,

$$\epsilon_g = \sum_{j=1}^{J \text{ bands}} \bar{\alpha}_j F_{\Delta\lambda_j T} ,$$

where α_j is the band absorptance and $F_{\Delta\lambda_j T}$ is a wavelength and temperature-dependent black-body function.

For the overlapping regions, Edwards¹⁻¹² recommends that each radiating species be treated as an independent gas in an otherwise inert medium. Once the different gas band characteristics (i.e., band minima, maxima, and absorptance) are obtained for each gas, they are ordered in terms of increasing wavelength, and the bands which overlap are broken into different absorbing parts such that the absorptance for each region is obtained from the following equation,

$$\bar{\alpha}_{\text{BAND}} = 1 - \prod_{i=1}^{M \text{ gases}} (1 - \bar{\alpha}_i)$$

where $\bar{\alpha}_i$ is the absorptance of gas species i over the overlapped region.

A Fortran program to calculate the emittance from carbon monoxide and carbon dioxide gas species using Edwards' exponential wide-band model has been coded, debugged, tested, and incorporated into HECTR. This model has been compared with Hottel emittance data for steam-carbon dioxide mixtures. Figure 1.12 summarizes some representative calculations for the total emittance for two conditions. As shown in the figure, the agreement between the Edwards and Hottel emittance predictions is acceptable. Overall, the computation times will increase when carbon monoxide and carbon dioxide are included, but these increase are reasonable when the single equivalent band model is used for radiative heat exchange calculations.

1.4.1.3 NTS Test Data Reduction Analysis

(A. C. Ratzel, 1513; J. E. Shepherd, 1512)

A substantial amount of useful data on premixed and continuous injection hydrogen deflagrations in air and steam has been provided by the large-scale tests performed by EPRI at the Nevada Test Site (NTS). These burns were conducted at sufficient scale to aid in the validation of hydrogen combustion codes. Sandia has completed a detailed evaluation of the quality and self-consistency of some of the data from

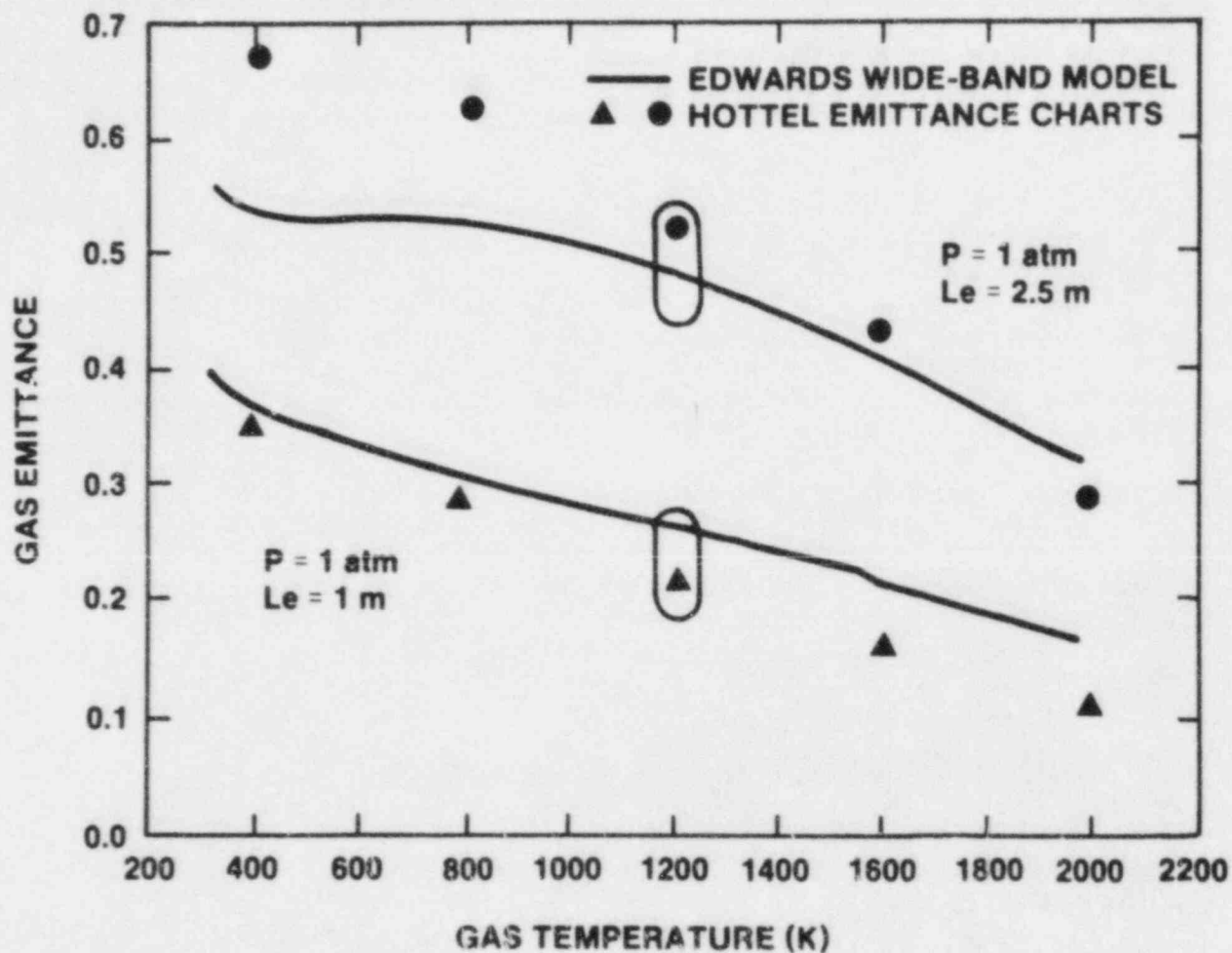


Figure 1.12. Comparative Total Gas Emittance Calculations for Different Pressure and Beam Length Conditions When $X_{\text{H}_2\text{O}} = 15\%$ and $X_{\text{CO}_2} = 12\%$

the premixed tests in conjunction with the HECTR assessment effort. This was done in order to judge the utility of these data in characterizing hydrogen burn environments. It is apparent that the quality of the data from different types of instrumentation varies greatly, and care must be exercised in interpreting the results.

The premixed combustion data reduction and analysis package SMOKE was extended to handle condensation, vessel wall heatup, and the NTS instrumentation data. A significant result is the existence of a transient, forced convection period immediately after a burn. Heat transfer during this period is not adequately modeled by conventional correlations.

All of the available premixed data (21 tests) have been analyzed and the validity of the signals from the instrumentation channels of interest to us assessed. Simulations of selected tests with HYBER and HECTR suggest that the average gas state can be adequately modeled following the initial transient convection period. Measured local heat fluxes can be up to a factor of two higher than the computed average values during the transient convection period.

The data reduction techniques have been extended to handle continuous injection and selected experiments have been analyzed. Our preliminary results indicate that the convective heat transfer coefficient can be taken as constant for the entire duration of most tests.

1.4.1.4 NTS Calculations

(C. C. Wong, 6427; J. F. Kotas, 6427)

A HECTR calculation of NTS test NTSP21 was performed. This analysis differs significantly from the five previous HECTR NTS calculations as the sprays were on for the duration of the transient. All five prior HECTR calculations were performed for NTS tests with sprays off. Thus, not only does this calculation provide an assessment of the HECTR combustion and heat transfer models, but of the HECTR spray model as well. Figures 1.13 and 1.14 compare the HECTR calculated gas pressure and temperature to the experimental results, respectively. For this particular calculation, a combustion completeness of 85 percent was required to match the NTS measured overpressure of 396.7 kPa. HECTR overpredicted both the gas pressure and temperature peaks using the EPRI combustion completeness value of 100 percent. This corroborates the results of the five previous HECTR NTS calculations, and indicates that either the combustion completeness measurements or the heat transfer models, or both are in error. More analysis will be performed to discern the exact reason for this overprediction. In the postcombustion phase of the transient, the HECTR pressure

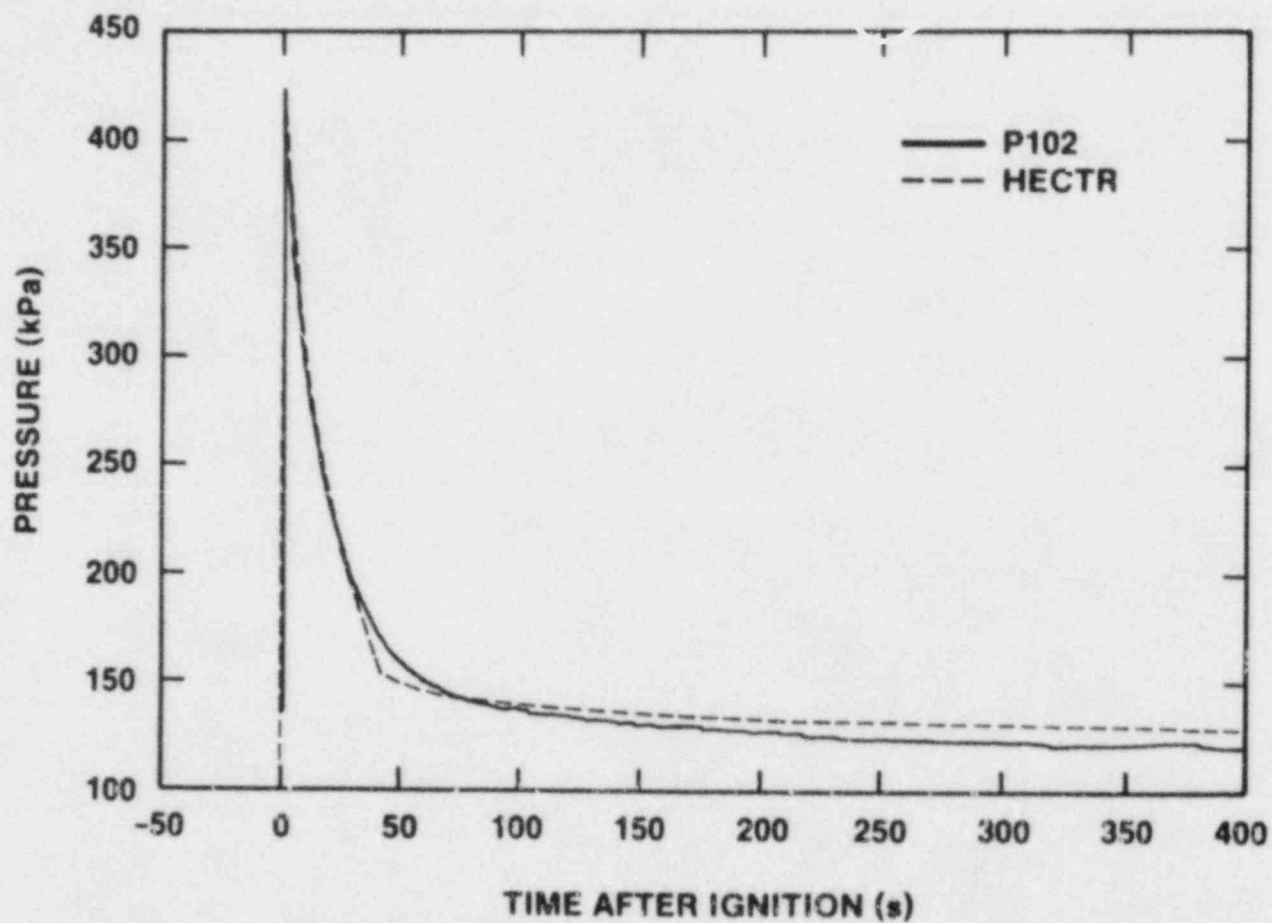


Figure 1.13. Comparative Pressure Profile for the NTS Premixed Test P21 (13% Hydrogen, with Spray and Fan)

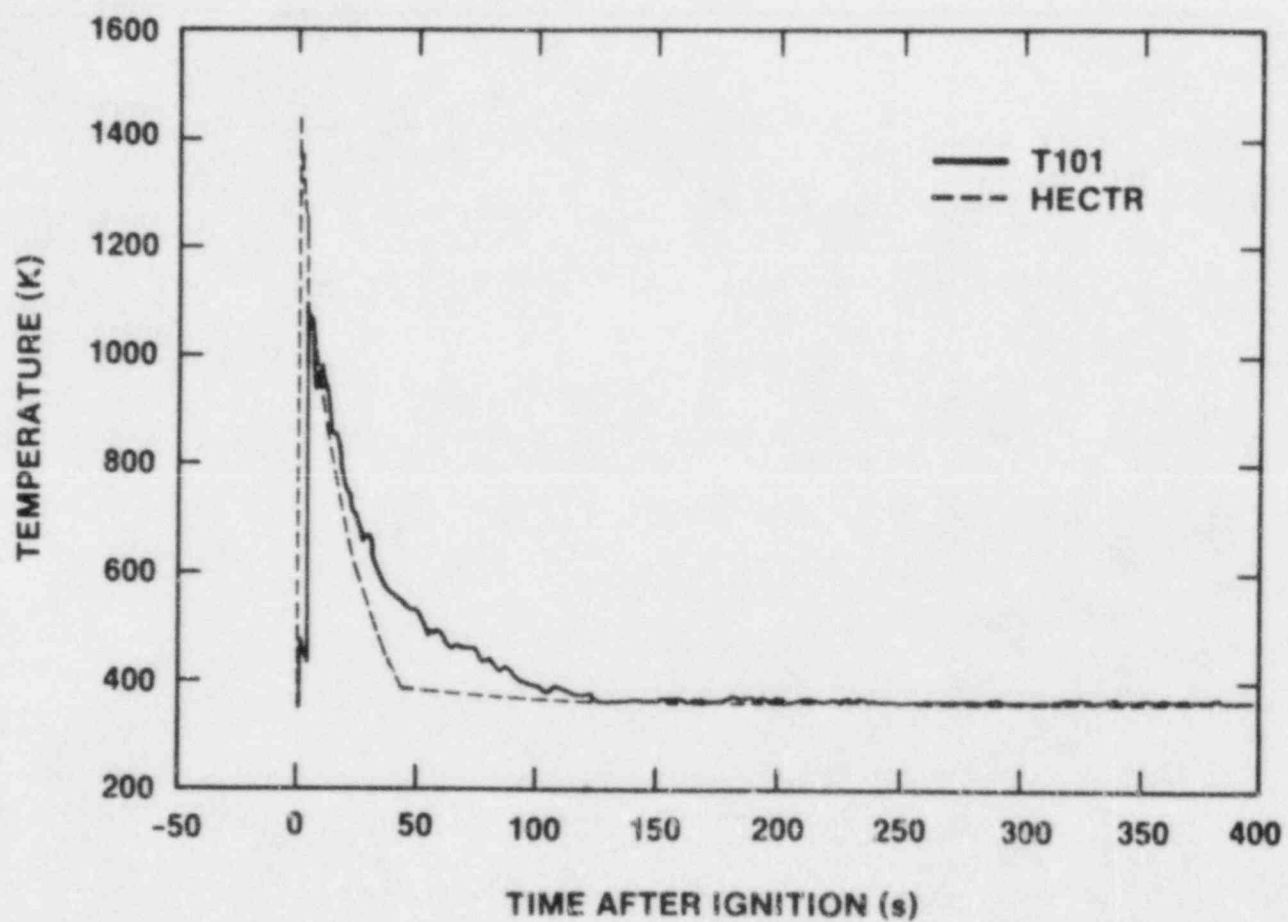


Figure 1.14. Comparative Temperature Profile for the NTS Premixed Test P21 (13% Hydrogen, with Spray and Fan)

and temperature results are in close agreement with the NTS data.

1.4.2 Flame Acceleration and Transition to Detonation

1.4.2.1 The FLAME Facility

(M. P. Sherman, 6427; S. R. Tieszen, 6427; W. B. Benedick, 1131)

FLAME is a heavily reinforced "U"-shaped channel designed to study hydrogen combustion problems relevant to nuclear reactor safety. The internal dimensions are 30.5-m-long by 2.44-m-high by 1.83-m-wide (100 x 8 x 6 ft). Movable steel plates on top the channel provide various degrees of transverse venting. Low energy ignition occurs at the closed end, and the flame propagates toward the open end of the channel. The floor and sidewalls of FLAME are covered with hundreds of high-strength embeds to which obstacles can be attached. Planned experiments include the investigation of flame acceleration mechanisms and the transition to detonation in simulated reactor containment geometries.

The initial tests in FLAME have examined the effects of transverse venting on combustion in an obstacle-free channel. In small-scale tests at McGill University, limited to 12.7 percent hydrogen, it had been found that even small degrees of top venting, ~8 percent, led to a great reduction in flame acceleration. The purpose of our tests is to quantify the effective flame speeds, overpressures, and danger of transition to detonation at large scale.

Prior to this quarterly period two series of tests had been completed. The first series used 50 percent top venting area with no obstacles placed in the channel (other than instrumentation and two small mixing fans); the second series used a closed top and no obstacles. The tests with 50 percent top venting were relatively benign. There was no transition to detonation, even for 28.0 percent hydrogen. (All concentration values quoted are volume fraction or mole fraction of hydrogen.) The overpressures were low. With no top venting the flame speeds, and overpressures were much higher. In two tests, at 24.7 percent and 30.0 percent hydrogen, transitions to detonation occurred. The last test at 30.0 percent hydrogen, F-14, resulted in damage to the FLAME structure.

In this quarter we began testing with 13 percent top venting area fraction. This value of transverse venting was selected because it is close to the value where venting began to have a substantial mitigating effect in the small-scale experiments and it can be obtained with our configuration of steel top plates. Two tests were carried out with 13 percent top venting area, F-15 with 15.4 percent hydrogen and F-16 with 17.6 percent. The speed of propagation of the

flames and the overpressures observed were higher than in the tests with 50 percent top venting area, but below those with 0 percent top venting. Results are shown in Figures 1.15 and 1.16. The two tests conducted were done with temporary repairs to the FLAME facility. In view of the overpressures seen in the 13 percent top venting area tests, it was decided not to continue with testing at higher hydrogen concentrations until permanent repairs were completed.

As described earlier, the FLAME channel was damaged by detonation induced loads during the F-14 test. Although FLAME was designed to withstand detonation loads, the pressures experienced were above the design values. The 5.1-cm-thick steel door and its reinforcing channels at the closed end of the channel were permanently bent by pressure loads due to a shock wave traveling back up the channel from the exit end. The door was bolted to the concrete on the bottom and the two sides using high-strength embeds in the concrete. The concrete near the top three embeds was badly cracked. We made temporary repairs which made test F-15 and F-16 reported above possible. After the tests, the cracked concrete was jack-hammered out. The loose embeds were placed in a form, and new concrete was poured. The repairs to the concrete appear to be excellent.

In place of a steel door, we have designed a sacrificial plywood door, backed up by a strong steel frame. The plywood panel is designed to fail at about 50 psi (340 kPa) overpressure. This should permit tests with deflagrations to be carried out as before, with a rigid end wall, but detonation loads should blow out the plywood. The plywood panels will be easily replaceable. The design of the steel frame was sent out for fabrication and will be installed during the next quarter.

We have the assistance of a visiting scientist from the University of Pisa, M. Carcassi, until the end of January. He is helping us in the analysis of the FLAME data. In particular, he is developing computer programs to compute experimental flame shapes and flame speeds from our flame time of arrival data, and comparing our flame speeds with turbulent flame theory predictions.

1.4.2.2 Terminal Velocity of Turbulent Flames

(J. H. Lee; R. Knystautas; C. K. Chan; C. Guirao, McGill University)

The continuous acceleration of a flame in an obstacle field by the positive feedback between the combustion process and the flow field upstream of the flame results in either a steady-state turbulent propagation regime compatible with the particular boundary conditions (i.e., obstacle configuration and degree of confinement) or transition from

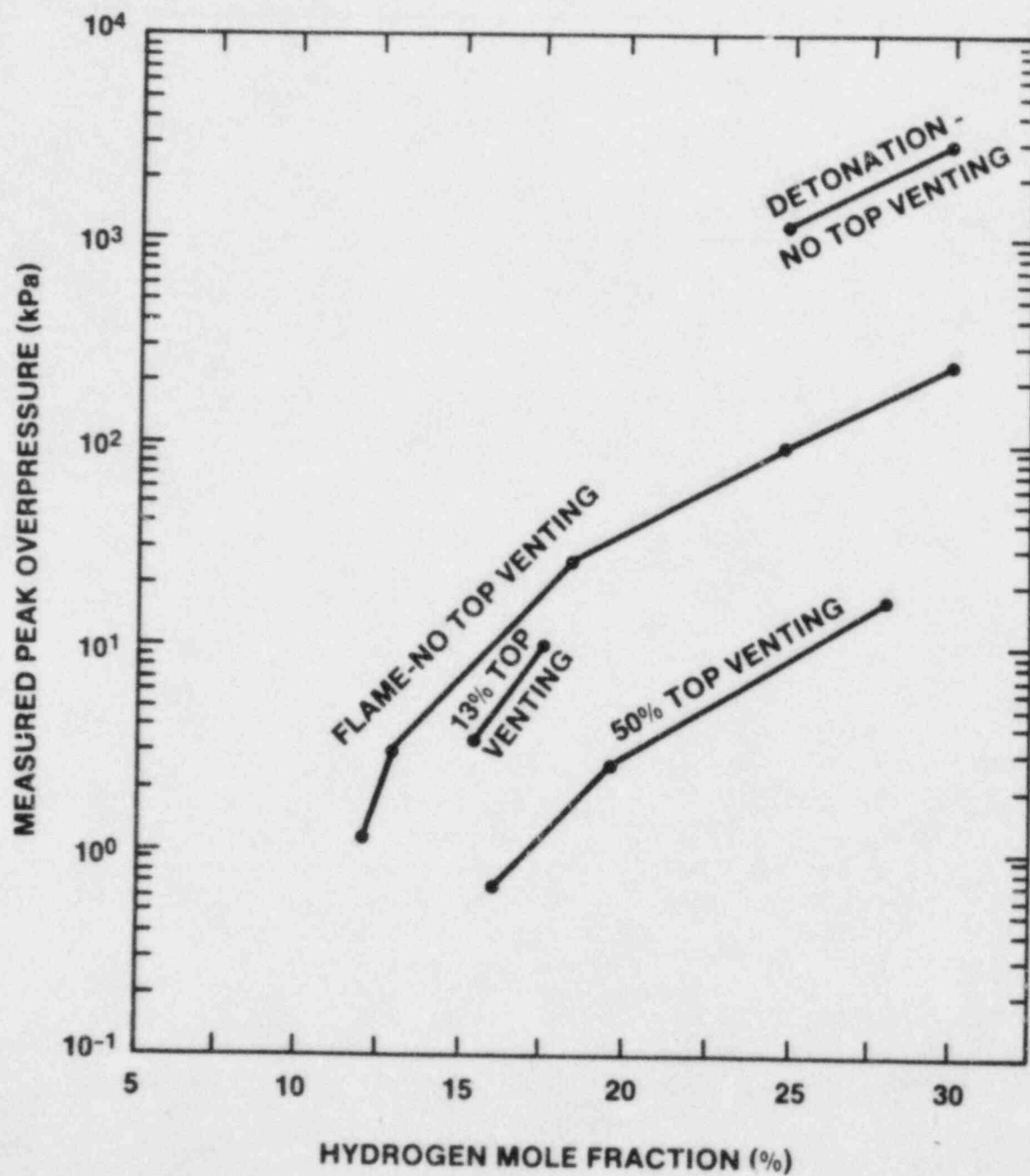


Figure 1.15. Measured Peak Overpressures in "FLAME" Facility

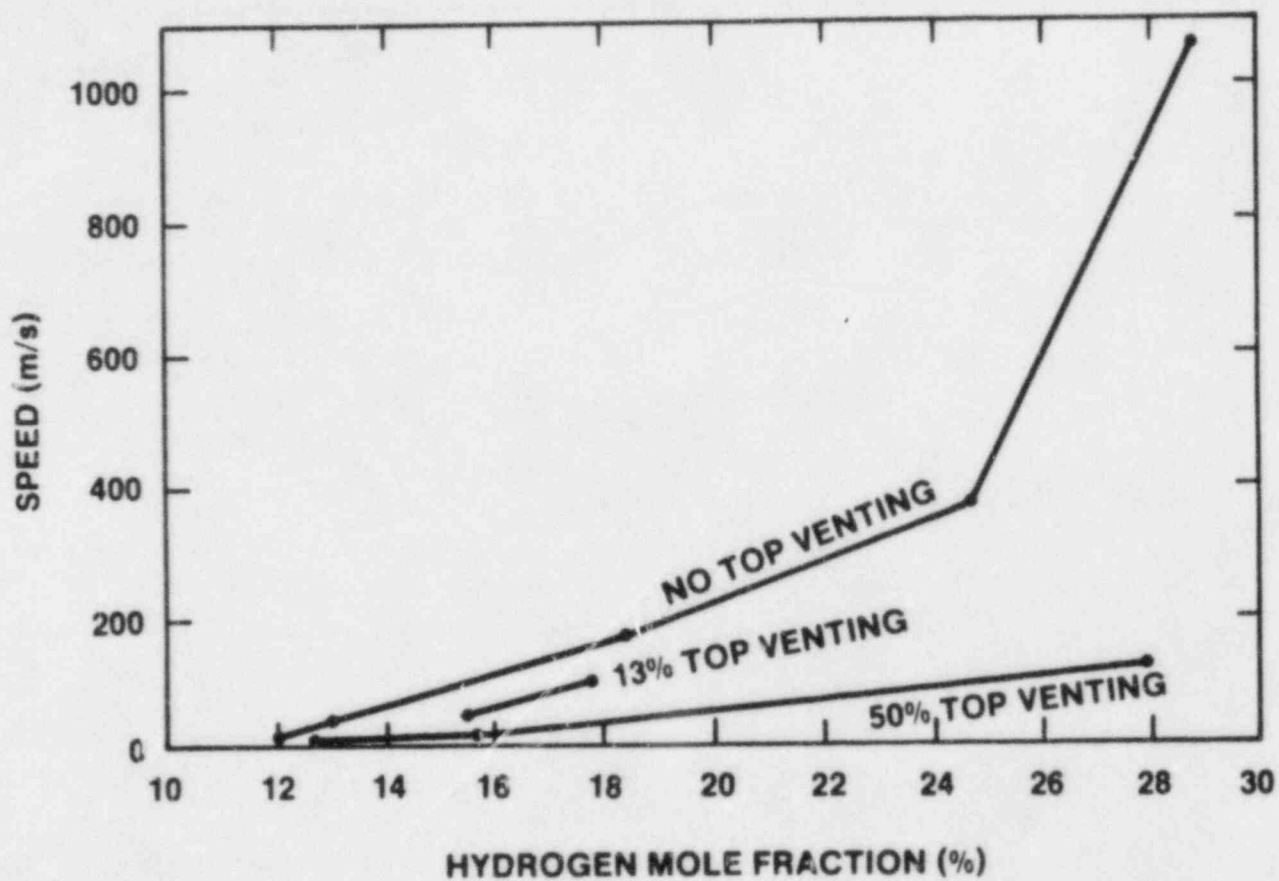


Figure 1.16. Equivalent Planar Flame Speed, m/s for Several Top Venting Areas

deflagration to detonation. It is of great practical interest to determine the conditions of turbulent acceleration which trigger the transition to detonation or, if transition does not occur, to determine the magnitude of the final flame velocity. An extensive experimental program is continuing at McGill University to determine the flame acceleration processes in the common fuel-air mixtures over a wide range of mixture compositions in tubes of different diameters and with obstacles of various configurations (blockage ratios and spacings). This report presents some of the results obtained in an attempt to elucidate the possible different propagation regimes and their dependence on the fuel type, mixture composition, tube diameter, and obstacle configuration.

Three circular tubes of 5 cm, 15 cm, and 30 cm in diameter and 11 m, 15 m, and 17 m long, respectively, were used in the present study. The tubes were closed at both ends. End ignition was achieved by an electrical spark. Circular orifice plates, one tube diameter apart, were used as obstacles. The blockage ratios (defined as $BR = 1 - (d/D)^2$ where d and D denote the orifice and tube diameters) were $BR = 0.44$, 0.39 , and 0.28 for the 5-cm, 15-cm, and 30-cm diameter tubes, respectively. The corresponding orifice diameters are 3.74 cm, 11.72 cm, and 25.46 cm. The obstacle field was long enough to ensure that steady-state terminal velocities were achieved within the obstacle field. Fuel-air mixtures at ambient conditions were prepared in a continuous flow system. The fuels studied are H_2 , C_2H_2 , C_2H_4 , and C_3H_8 . Ionization gages and pressure transducers were mounted along the tube to monitor the time of arrival of the reaction front and the pressure history at various locations.

The experiments have demonstrated the existence of four distinct regimes of flame propagation: the quenching regime, the choking regime, the quasi-detonation regime, and the Chapman-Jouquet (C-J) detonation regime.

In the quenching regime the flame is observed first to accelerate, then to quench itself after propagating through a certain number of obstacles. The propagation mechanism is the successive explosion of the mixture in the combustion chambers interconnected by the orifice plates. Ignition of the mixture in each chamber is achieved by the venting of the hot combustion products from the upstream chamber through the orifice. Quenching occurs when the hot turbulent jet of products fails to cause ignition due to the too rapid entrainment and turbulent mixing of the cold unburned mixture with the hot products of the jet. A quenching criterion has been formulated; quenching occurs when the characteristic chemical reaction time is larger than the turbulent mixing time.

Flame quenching has been observed in the 5-cm diameter tube in near-stoichiometric CH_4 -air mixtures, fuel-lean C_2H_4 -air mixtures (equivalence ratios $\phi = 0.6$ to 0.65) and fuel-lean and fuel-rich C_3H_8 -air mixtures ($0.65 < \phi < 0.8$ and $1.15 < \phi < 1.25$) as well as in fuel-lean C_3H_8 -air mixtures ($\phi < 0.6$) in the 15-cm diameter tube. For purposes of graphical display, a flame propagating in the quenching regime has been assigned zero terminal velocity in Figures 1.17 through 1.19 where the variations of maximum flame velocity with respect to equivalence ratio have been plotted. For near-stoichiometric CH_4 -air mixtures in the 5 cm diameter tube, the experimental results indicate that the conditions are marginal because either flame quenching or steady flame propagation at a velocity close to 800 m/s was observed from shot to shot.

The quenching diameters D^* (i.e., the orifice diameter) of the order of 3.7 cm for CH_4 -air and C_2H_4 -air mixtures are slightly smaller than Thibault's estimates¹⁻¹³ ($D^* \approx 5$ cm) derived from large-scale experiments where the overpressures achieved ($\Delta p \approx 6$ bar close to the constant volume overpressure $\Delta p \approx 8$ bar) are much larger than those expected in the present small-scale experiments. The smaller quenching diameters in the present experiments seem appropriate in view of the strong dependence of the quenching diameter on the overpressure across the orifice plate.

In the present experiments, conditions were such that the quenching regime was not observed for the very sensitive fuels (C_2H_2 and H_2). For the present orifice diameters, the critical compositions for quenching these high burning velocity fuels are near the flammability limits. For example, for H_2 -air mixtures, Thibault reported a critical composition of about 10 percent H_2 -air corresponding to an orifice of diameter $d = 3.74$ cm. For this composition, the mixture is too close to the lean limit for significant flame acceleration and pressure build-up to occur with a blockage ratio of 0.44. A larger blockage ratio with the associated higher overpressure would be required to quench H_2 -air and C_2H_2 -air mixtures in the present tube.

It may be concluded that flame quenching does not occur if the orifice diameter exceeds the critical value reported by Thibault for the transmission of explosions from vented chambers. Thus, the maximum critical orifice diameter can be used as a criterion to delineate the boundary between the quenching and flame propagation regimes.

When quenching does not occur, the flame continuously accelerates to a final, steady-state velocity. The flame propagation can be considered as a one-dimensional, compressible, quasi-steady flow in a pipe with friction and heat addition.

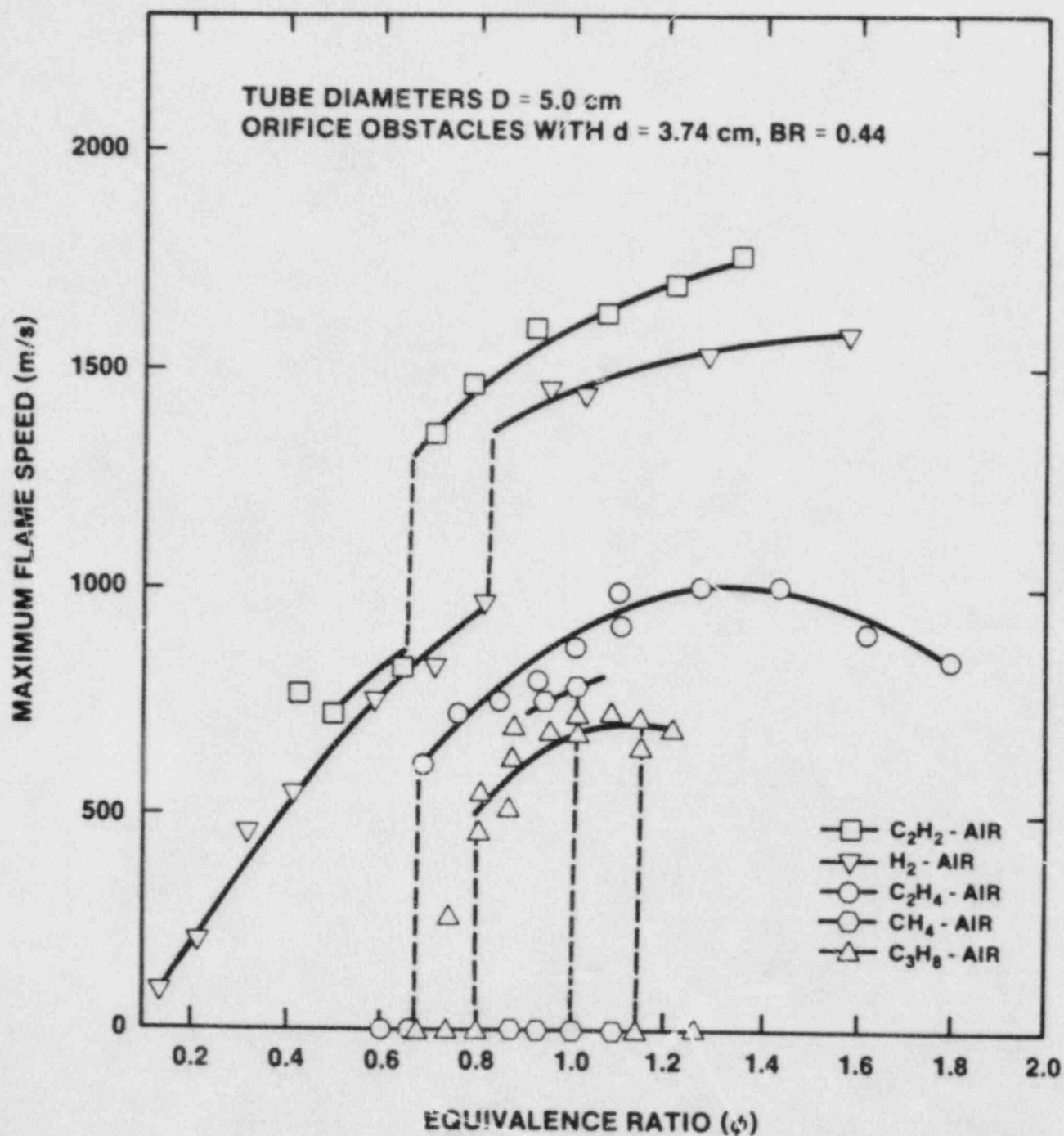
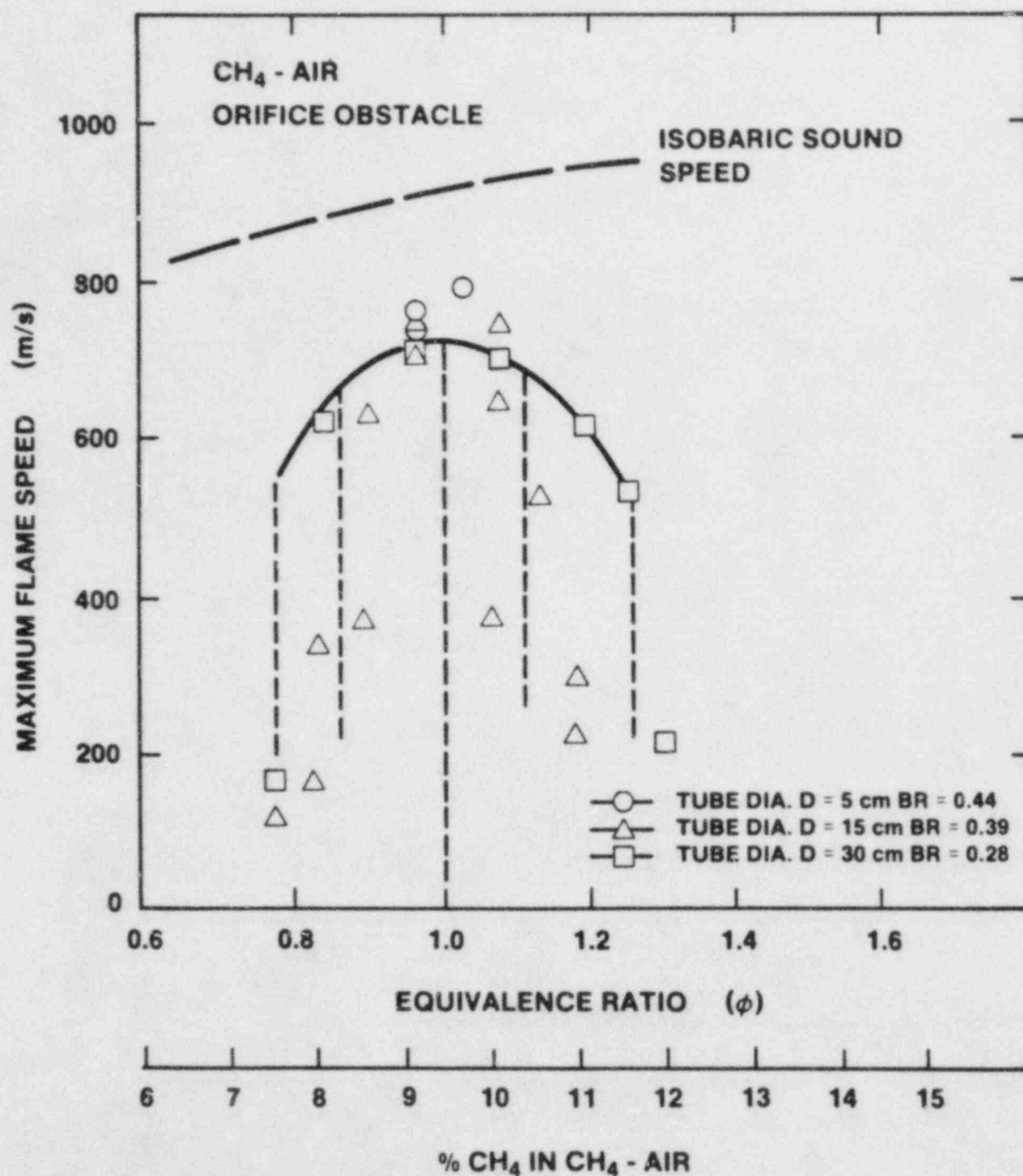


Figure 1.17. Variation of the Maximum Steady-State Flame Velocity With Mixture Composition in Hydrogen-Air and Hydrocarbon-Air Mixtures



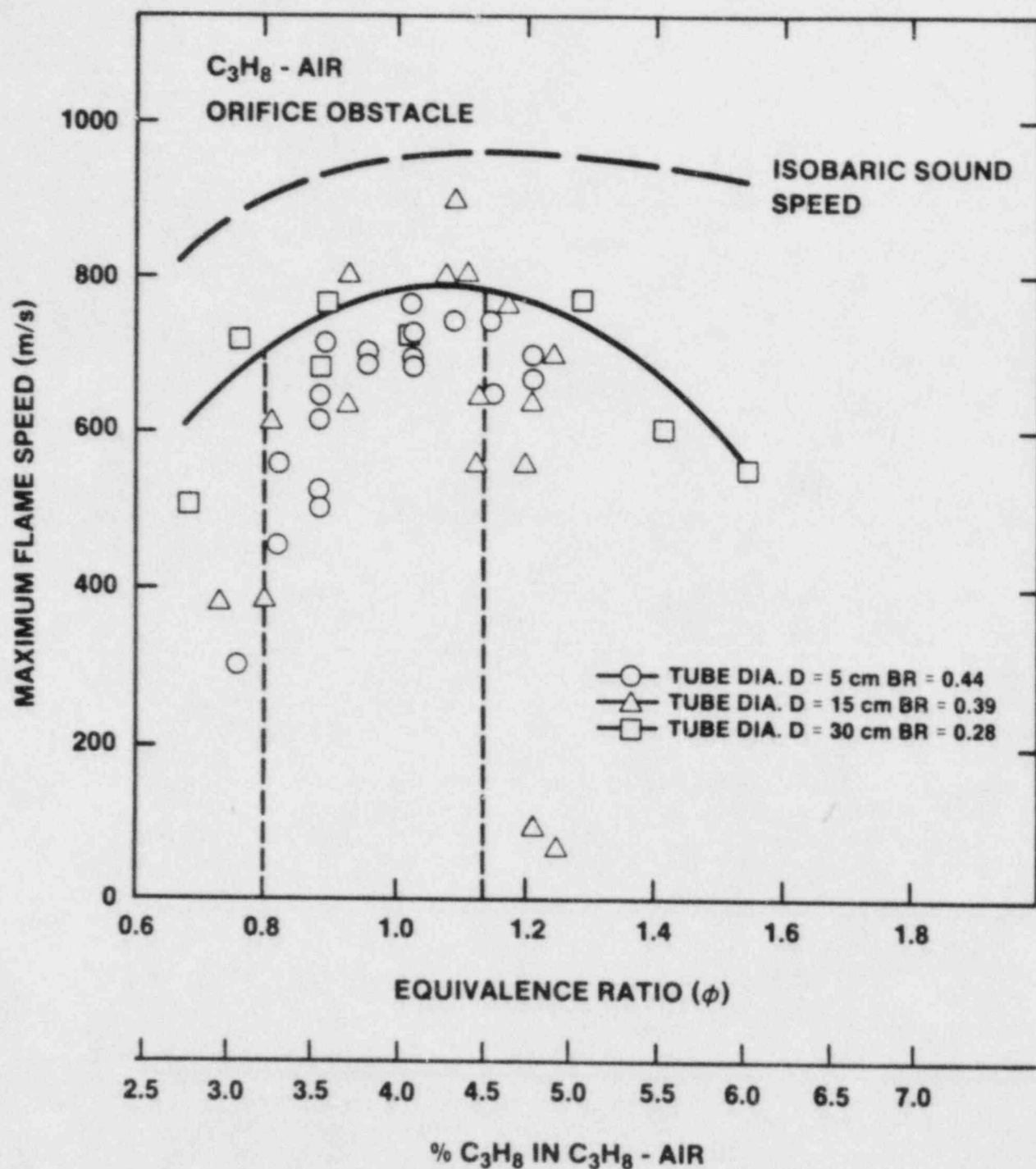


Figure 1.19. Variation of the Maximum Steady-State Flame Velocity for Propane-Air Mixtures in Different Diameter Flame Tubes

The turbulent flame velocity is slightly lower than the sound speed of the burned products due to choking because of mixing of unburned and burned gases in the extended reaction zone of the turbulent flame "brush." This is quite evident in Figures 1.18 through 1.20 for CH_4 -air, C_3H_8 -air, and H_2 -air mixtures where in all cases the isobaric sound speed has been plotted for comparison. For these mixtures, flame velocities in the choking regime are of the order of 800 m/s and lie typically about 100 to 150 m/s below the isobaric sound speeds. It is also observed that the magnitude of the velocity for a particular mixture is insensitive either to the tube diameter or the blockage ratio. This is consistent with choked conditions for compressible flow where the flow behavior is determined entirely by the thermodynamic properties of the mixture.

The present results can be predicted quite adequately by Hjertager's model.¹⁻¹⁴ Figure 1.21 illustrates the very good agreement between his simulation and the measured flame speeds and overpressures over a broad range of H_2 -air mixtures. It should be noted that for mixtures close to the flammability limits, the final steady-state flame speed may be controlled by other mechanisms than the choking mechanism (flame stretching).

Since flame speeds typically attained in the choking regime are of the order of 1000 m/s, transition to detonation may occur if the orifice diameter is sufficiently large. The third regime of propagation observed in the present study is the quasi-detonation regime which corresponds to the propagation of a detonation wave within the obstacle field at a velocity about 20 percent smaller than the C-J detonation velocity. This reduction in velocity results from the severe momentum losses in the obstacle-filled tube. The necessary condition for detonation propagation in such an environment is that the orifice size be sufficiently large to accommodate an adequate number of detonation cells. For a smooth-walled tube, Lee et al.¹⁻¹⁵ have found that transition to detonation occurs for $D/\lambda \approx 1$ (where D and λ are the tube diameter and detonation cell width, respectively). Thus, if transition to detonation is to occur in the obstacle-filled tube, the orifice diameter must be at least of the order of or greater than the corresponding cell size (i.e., $d/\lambda \geq 1$). However, since the detonation is subjected to a sudden expansion as it emerges from the orifice one would expect d/λ to be greater than unity, which is the value for a smooth-walled tube. In the limit of large blockage ratios when the tube diameter is much larger than the orifice diameter, the detonation transmits from the orifice essentially to an unconfined volume. In this limit, it has been well established¹⁻¹⁶ that $d/\lambda \geq 13$. Thus one would expect transition from deflagration to detonation to occur in the range $1 \leq d/\lambda \leq 13$.

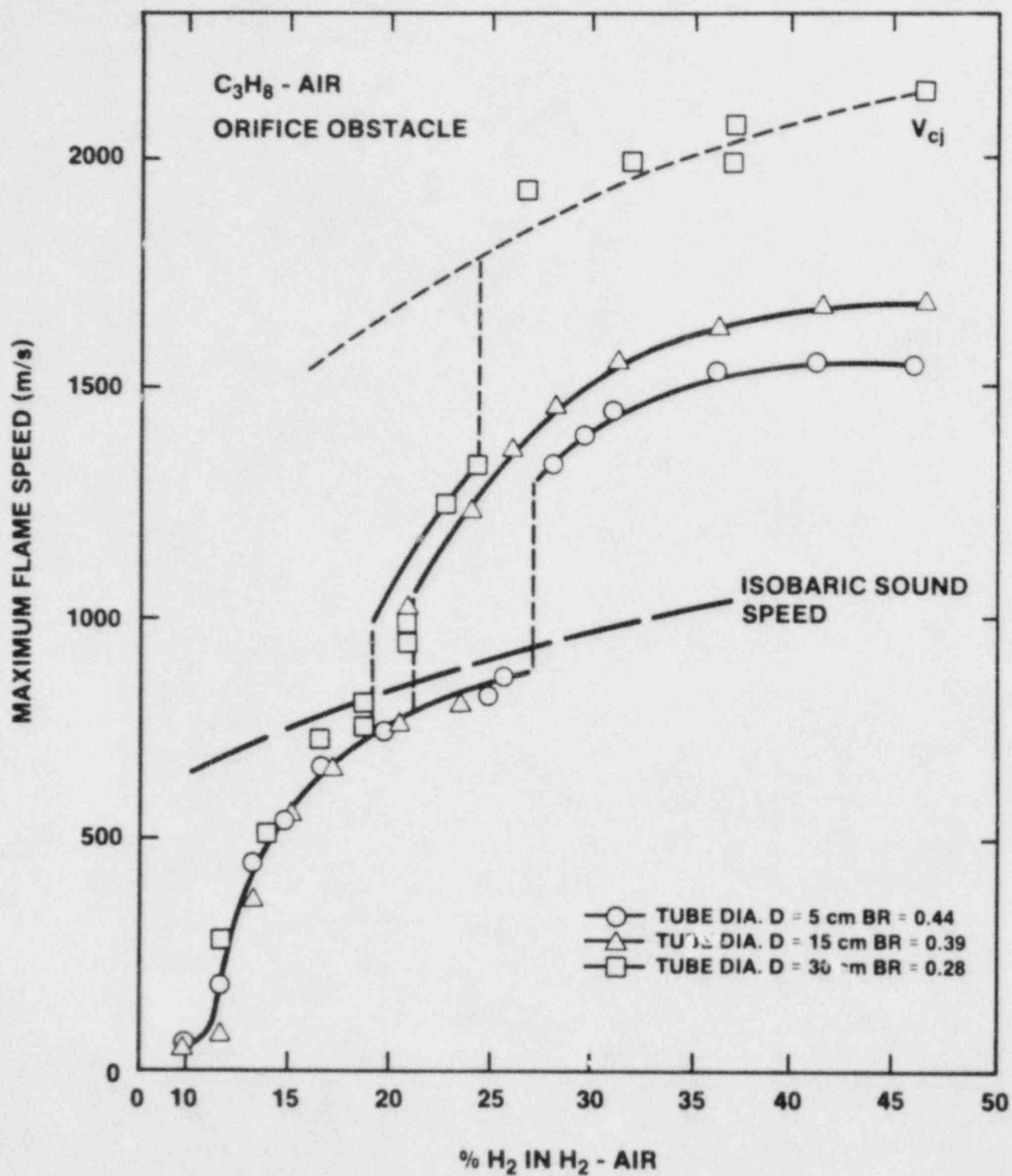


Figure 1.20. Maximum Flame Velocities and Transition to Detonation in Hydrogen-Air Mixtures in Different Diameter Flame Tubes

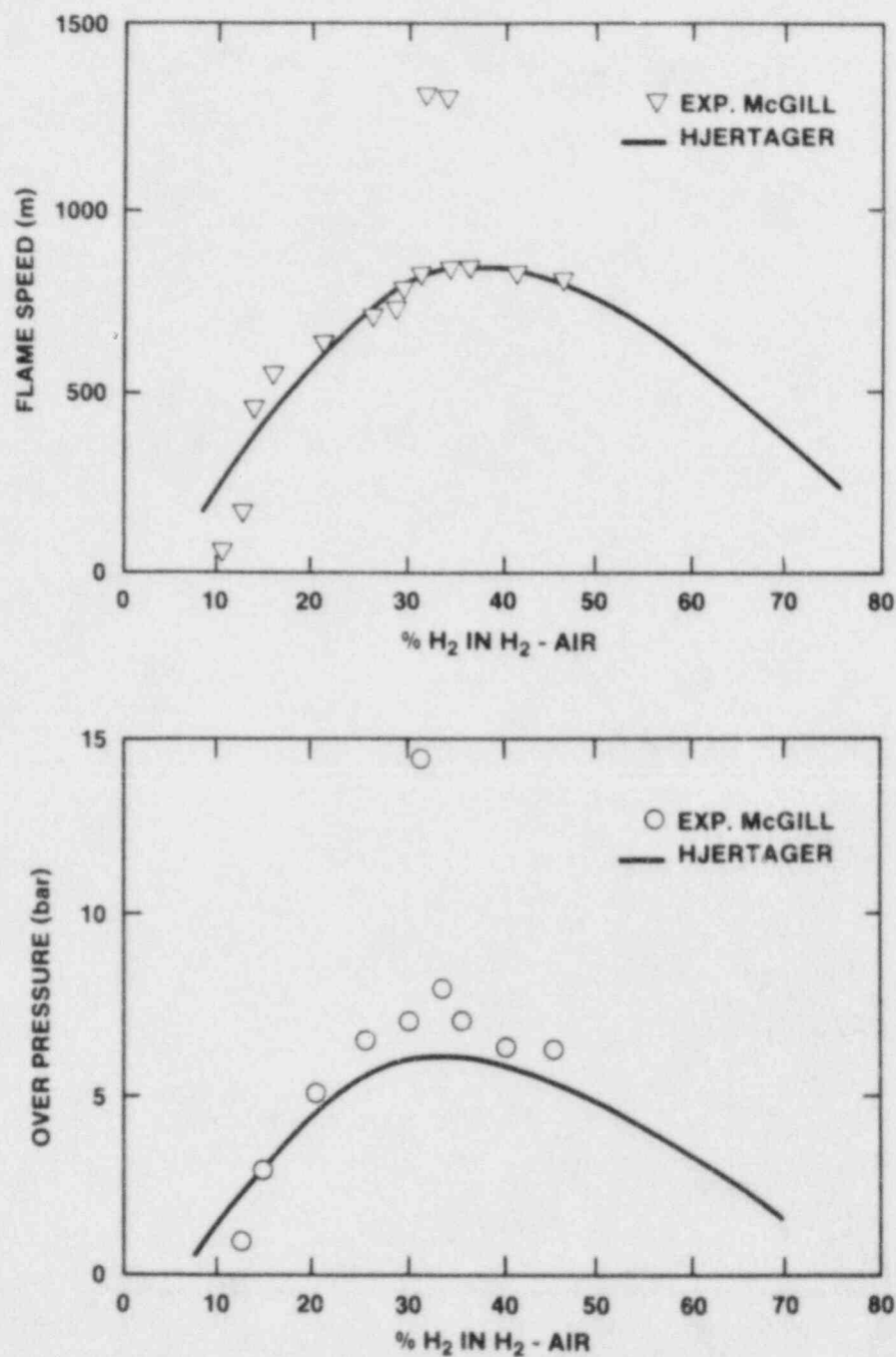


Figure 1.21. Correlation of Experimental Maximum Flame Velocity and Overpressure With Numerical Simulation by Hjertager for Hydrogen-Air Mixtures in the 5-cm-diameter Flame Tube

For H_2 -air mixtures, transition from the choking regime to the quasi-detonation regime occurs at leaner concentrations as the orifice diameter is increased. In the 5-cm, 15-cm and 30-cm diameter tubes, transition occurs around 27 percent H_2 , 21 percent H_2 , and 19 percent H_2 , respectively and corresponds to the critical values $d/\lambda \approx 2.4$, 3.3, and 3.4, respectively. The quasi-detonation regime was not observed in the less sensitive fuels, CH_4 and C_3H_8 . With a value $d/\lambda \approx 0.86$, a self-sustained detonation in stoichiometric CH_4 -air mixtures cannot propagate in the 30-cm diameter tube. However, one would have expected the propagation of a quasi-detonation in stoichiometric C_3H_8 -air since $d/\lambda \approx 4.6$ in the 30-cm diameter tube. The fact that transition to detonation was not observed in C_3H_8 -air mixtures seems to indicate that the ratio of d/λ does not by itself characterize the transition point in a particular tube. There are strong indications that suggest that transition to detonation requires some minimum value of the flame speed in addition to a minimum tube diameter.

It is of interest to note that at around the 24 percent H_2 -air composition there occurs another transition within the detonation regime itself. In this case it is from the sub-C-J quasi-detonation regime discussed above to the C-J detonation regime. As shown in Figure 1.19, the detonation wave propagates at the normal C-J velocity, the propagation being totally insensitive to the blockage effect of the obstacles. If one examines the conditions for this transition one notes that the cell size at the 24 percent H_2 -air composition level is $\lambda \approx 2$ cm. This gives a value of $d/\lambda \approx 13$ which, as mentioned earlier, is the condition at which the detonation propagation would be completely insensitive to wall effects. The significance of the $d/\lambda \geq 13$ criterion is that it derives from the critical tube diameter situation. One may recall that the critical tube diameter is the minimum tube diameter for which a fully confined originally planar one-dimensional detonation wave will continue propagating without attenuation when the confinement is suddenly removed. This represents the most severe form of lateral perturbation to the forward motion of a detonation wave. It seems reasonable to expect that a detonation wave would not be more vulnerable to a weaker perturbation such as that inherent in the obstacle obstructions in the present study. Hence, in this context, the $d/\lambda \geq 13$ criterion is quite plausible for C-J detonation propagation through the obstacle field.

1.4.3 Detonation Studies

1.4.3.1 Heated Detonation Tube

(S. R. Tieszen, 6427; M. P. Sherman, 6427; W. B. Benedick, 1131)

A detonation wave consists of a complex, three-dimensional, cellular structure formed by the multiple interactions of the shockwaves. The characteristic cell width, λ , is a key to determining the important detonation parameters such as critical initiation energy and propagation limits. Small values of λ correspond to highly detonable gas mixtures. the larger the value of λ , the more difficult it is to establish and maintain a detonation wave. Large smoked foils are employed for directly recording the detonation cell structure.

Until recently most experiments on detonations were conducted in small tubes at ambient temperature and pressure. The Heated Detonation Tube (HDT), with its 43-cm ID and capability of operating at temperatures above 100°C, is a unique facility. Prior to the HDT experiments, there was wide belief that the effects of initial pressure and temperature would be small for the ranges expected during a reactor accident. We have found, however, that the initial thermodynamic conditions have strong influences on the detonability of a given mixture.

The primary objective of the current test series is to measure cell sizes for H₂-air-steam mixtures which are predicted to occur following a reactor accident. A second objective is to provide data to assess and calibrate predictive and parametric codes. This is accomplished by investigating the separate effects of temperature, pressure, and diluent concentration.

Initial experiments are investigating mixtures expected to be topical of well-mixed reactor atmospheres. Each mixture is prepared starting with one standard atmosphere of air, to which hydrogen and steam are added. Steam mole fractions of 0, 10, 20, and 30 percent have been examined. Hydrogen concentrations have been varied up to 46 percent. Subsequent tests will investigate mixtures with reduced air density which can occur during transient situations near a break. In these tests the steam concentrations will be set at saturation. To separate the effect of temperature, H₂-air mixtures have been run at both 20 and 100°C. H₂ concentrations varied from 13.5 to 70 percent. The effect of pressure can be established by comparing standard air density tests with tests at one atmosphere total pressure.

During this reporting period previous results from the H₂-Air-H₂O series conducted at 100°C and standard air density ($\rho_a=41.6$ moles/meter³) have been analyzed. Figure 1.22 shows the detonation cell size data versus the equivalence ratio, ϕ . As expected, the detonation cell size increases (relative sensitivity decreases) with increased steam dilution. However, the detonation cell size measured in this series for undiluted H₂-air is smaller than for comparable mixtures at 20°C and one atmosphere pressure. This is apparently due to the higher initial density and temperature for mixtures in the current test series. The current data compare reasonably well with the induction length model developed by Joe Shepherd at Sandia. The model is calibrated using the 20°C and one atmosphere pressure data.

Obtaining detonation cell size data requires interpreting the complex cellular patterns on the smoked foil used to record the data. Two independent teams reviewed the foils. In Figure 1.22 the open symbols represent the readings of Tieszen and Benedick (Sandia), and the closed symbols represent readings of Knystautas and Lee (McGill). The lines connecting the open and closed symbols for each test can be considered as the current uncertainty ranges.

In addition to detonation cell size data, detonation velocity data were also obtained. The results are shown in Figure 1.23. The measured velocities compare very well with the Chapman-Jouguet values. H₂-air detonation experiments conducted at McGill University and Sandia in various tube sizes with comparable mixtures have shown that detonation velocity in marginally detonable mixtures can be considerably less (10 percent) than the Chapman-Jouguet velocity as the tube size decreases. This decrease in velocity is attributed to the effect of boundary layers.¹⁻¹⁷ Tarver¹⁻¹⁸ reviews detonation velocity model development which relates the velocity decrease to energy loss in the boundary layer. The heated detonation tube is large enough to be nearly free of these effects.

To reduce the uncertainty in the detonation cell size measurements, more tests are planned in the H₂-air-H₂O series. Additional testing will be done to quantify the effect of initial temperature and density on detonation cell size.

1.4.4 Diffusion Flames

1.4.2.1 Diffusion Flame Modeling

(M. P. Baer, 1513; J. C. Cummings, 1512; J. E. Shepherd, 1512)

We have initiated several new efforts to improve our understanding and modeling capabilities for diffusion flames

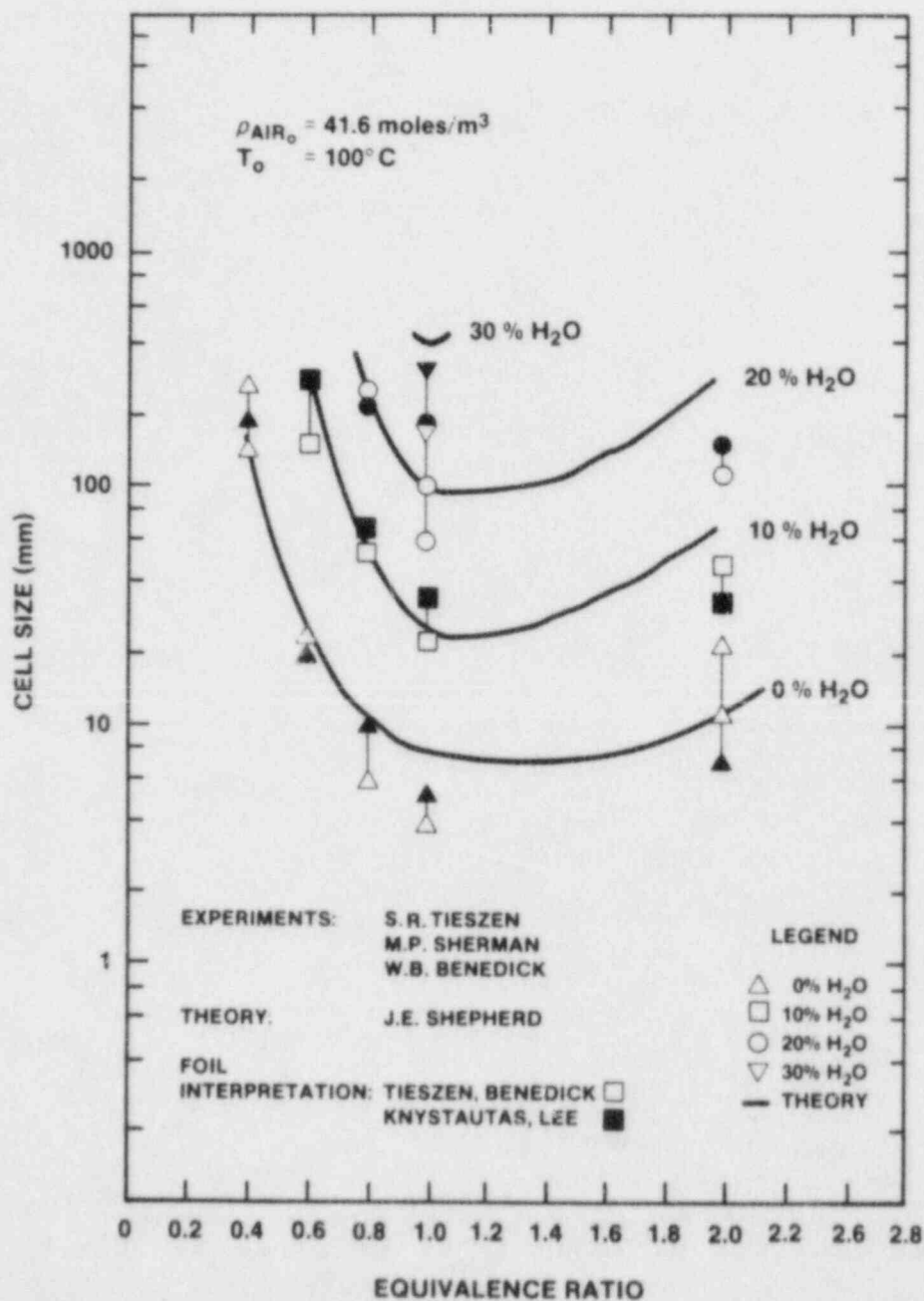


Figure 1.22. H₂-Air-H₂O Detonation Cell Size vs. Equivalence Ratio

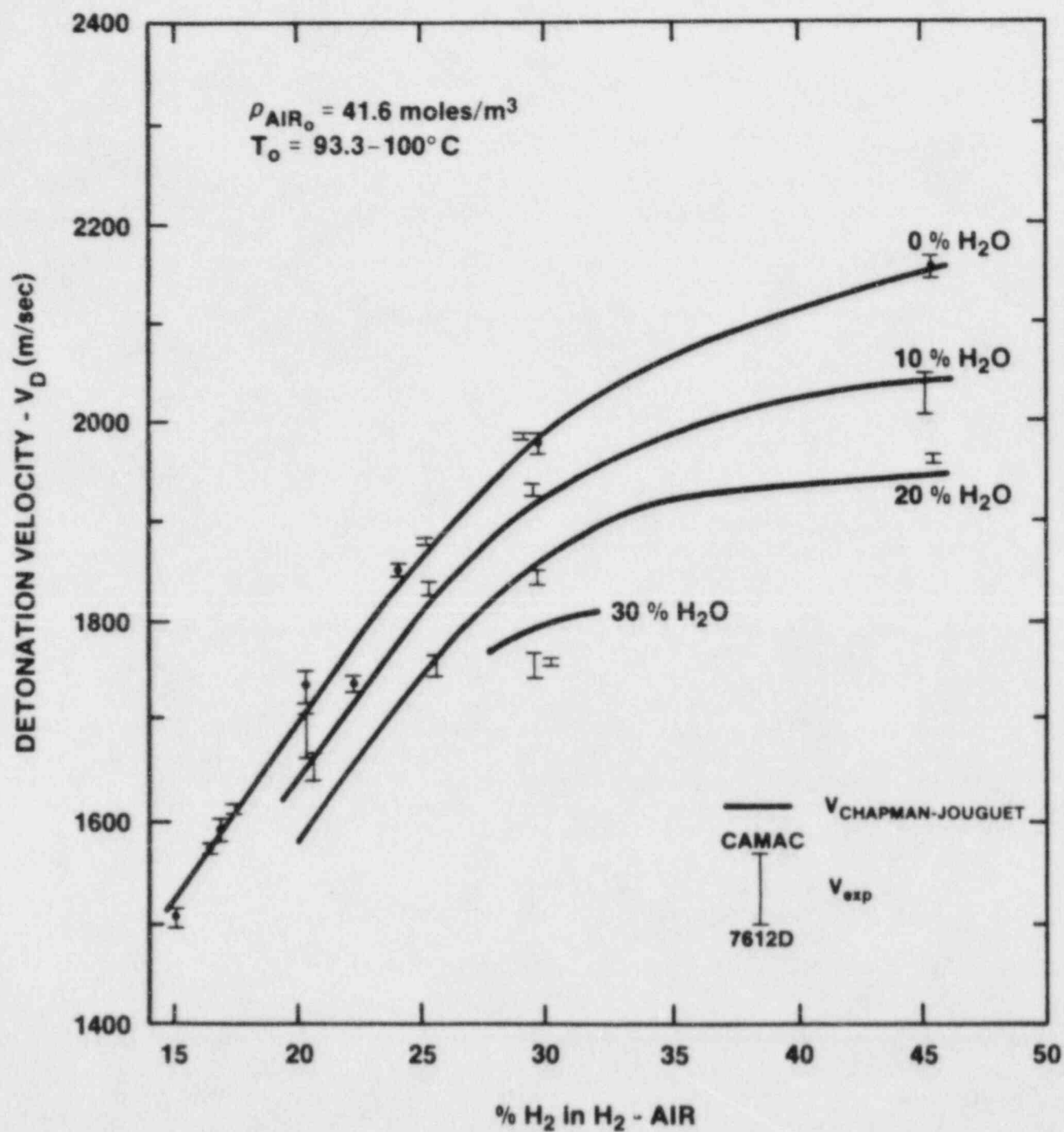


Figure 1.23. Detonation Velocity vs. % H_2

in enclosures. On the experimental side, there are two bench-scale efforts designed to clarify some aspects of buoyancy-driven mixing in compartmentalized enclosures. The experiments involved are buoyant plumes of air generated by an electrical heater and injection of saline solutions into fresh water. The primary instrumentation is flow visualization by smoke or dye injection and videotaping. (Temperatures are also measured as a function of spatial location and time in the hot-air plume experiments.)

A complementary effort is the development of a two-dimensional simulation for complex flows in enclosures. This is a long range project that will ultimately produce a computational tool for the prediction of fluid mechanics and heat transfer phenomena produced by diffusion flames in containment-type geometries. The method originally proposed at NBS, is based on the application of inviscid equations (called "filtered" Navier-Stokes), which eliminate the need for the description of acoustic and dissipative effects. Without the need for the resolution of acoustic phenomena, the characteristic speed in the calculations becomes the local flow velocity and computations can be conducted efficiently using explicit techniques. Flame characteristics are determined by empirical correlations, and the fire is modeled as a distributed heat source.

The first version of an algorithm to treat the fluid mechanics of adiabatic two-dimensional flows is operational. Movies of the experiments described above will be compared to computer-generated movies of the simulations. Ultimately, this model will be used to compute the detailed local conditions and heat loads from standing flames. It is intended to complement HECTR-type analyses which model global processes but cannot provide sufficient spatial resolution near the flame. It will also be used for evaluating the direct scaling of measured material response data.

1.5 Hydrogen Mitigative and Preventive Schemes (L. S. Nelson, 6427; M. Berman, 6427)

1.5.1 Effects of Operating the Water Spray System on Hydrogen Igniters

The deliberate ignition system installed in a nuclear reactor containment is used to prevent excessive accumulation of hydrogen produced during a core uncover accident. However, a second safety-related system, water sprays intended to reduce steam overpressure in similar accidents, may interfere with the proper operation of the numerous hot surface igniters arranged throughout containment as part of the deliberate ignition system.

The effects of the spray operation are thought to be two-fold, via direct impingement of spray drops on the igniters,

and by driving air currents in the containment by entrainment. We have recently completed an experimental study of the behavior of igniters exposed to water sprays and gas flows. To complement these studies we are using computer modeling to estimate the gas flows that would be induced by the water sprays in typical containments.

1.5.1.1 Air Currents Driven by Sprays in Reactor Containment Buildings (K. D. Marx, 8363)

The flow of air in nuclear reactor containment buildings due to the introduction of water sprays is being investigated numerically and theoretically. The particular geometry being studied is that of Sequoyah, a pressurized water reactor equipped with an ice condenser. The numerical approach utilizes a computer code which couples the Navier-Stokes equations for fluid flow with the equations of motion of water droplets in two dimensions. An approximate theoretical description of some aspects of the flow field is derived. Given the water spray flux specified for Sequoyah, peak flow velocities of approximately 12 to 14 m/s are possible in an empty building. This velocity is reduced when account is taken of the presence of ice condensers and steam generators. The dependence of the flow velocities on such parameters as spray flux, spray ring location, droplet size, spray injection characteristics, and the turbulence model is described. Implications for igniter survivability are briefly discussed.

In this report, we discuss: (1) a baseline calculation, and (2) the most realistic reactor simulation that we have carried out so far. The term "baseline" refers to a configuration with a particular set of spray parameters (spray flux, droplet distribution, etc.) in an empty containment building. A large number of additional calculations are presented in Reference 1-19. These primarily involve variations of the spray parameters away from baseline and geometrical configurations intermediate to the two described here. (Note: The summary at the beginning of this report is based on results from several calculations in References 1-19, not just these two.)

The finite-difference grid used for our baseline simulation of an empty containment building is shown in Figure 1.24. An Eulerian calculation is used throughout. The computations are performed in axisymmetric cylindrical geometry, so that all variables are functions of the radial coordinate r and the axial coordinate z .

Conchas-Spray provides for the introduction of a spray of liquid droplets into the gaseous flow field. 1-20, 1-21 This is done by considering a number of droplet "parcels."

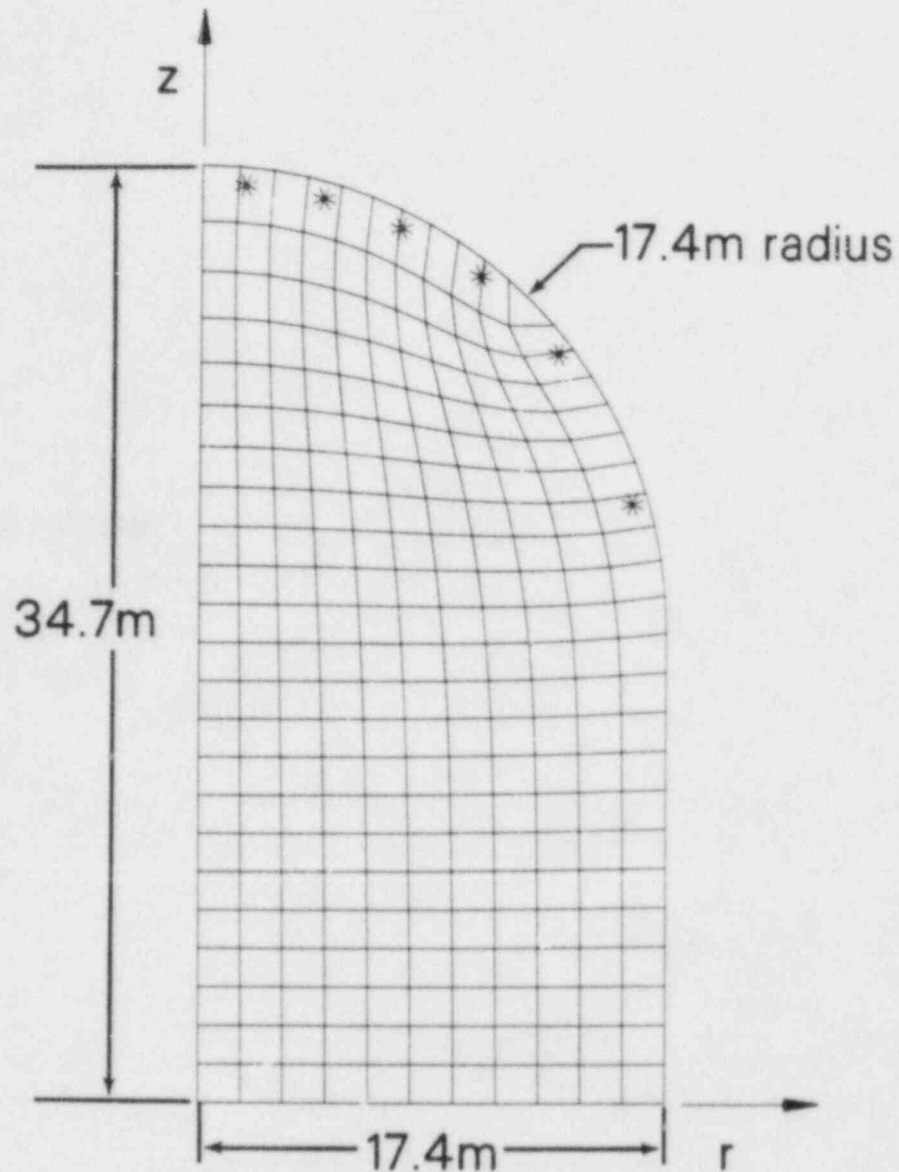


Figure 1.24. Finite-Difference Grid for an Axisymmetric Simulation of an Empty Sequoyah Containment Building. The building consists of the volume obtained by rotating the outer boundary of the grid about the z axis. The positions of the spray rings used in the baseline calculation are indicated by asterisks (*). This grid was used for the baseline calculation. The mesh spacing was reduced by a factor of two in the grid used in the calculation involving ice condensers and steam generator doghouses, and the spray rings were concentrated between radii of 5.8 m and 9.9 m.

The containment building is assumed to be filled with air saturated with water vapor at 300 K and a pressure of 1 atm. The species densities of the unperturbed gas mixture are as follows: $\rho_{N_2} = 0.866 \text{ kg/m}^3$, $\rho_{O_2} = 0.265 \text{ kg/m}^3$, $\rho_{H_2O} = 0.026 \text{ kg/m}^3$, for a total density of $\rho = 1.157 \text{ kg/m}^3$. Argon, carbon dioxide, and other trace elements are ignored. Evaporation or condensation is not considered, and the Mach numbers are small. Hence, the above densities remain approximately constant throughout the flow, except for slight deviations due to gravity and Bernoulli's law.

The spray consists of water drops at 300 K. The distribution of droplet diameters is shown in Figure 1.25. It is a distribution provided for a Spraco Model 1713A hollow cone nozzle,¹⁻²² except that it has been smoothed above 1300 μm . The Conchas-Spray code simulates spray behavior by following the motion of many (several hundred to a few thousand at any one time) droplet parcels. Each parcel behaves as an individual droplet, but represents many droplets of the same size and velocity. To this end, the equations of motion for single droplets are solved, taking into account gravity and the coupling to the gas flow via the drag force. The effect of the droplets on the gas flow is accounted for by computing the volumetric drag force on the gas within each computational zone which results from all droplets in all parcels within the zone. The number of droplets per parcel depends on the total mass flow rate of spray, the distribution of spray rings, and the frequency with which parcels are injected. (The latter is a computational parameter; it is not practical to inject continuously, because of computer memory limitations.) The initial number of droplets per parcel is of the order of 10^6 to 10^7 in these calculations.

Six spray rings are uniformly spaced in the radial direction for the baseline calculation, as shown in Figure 1.24. The rate at which droplets are emitted from each ring is proportional to radius so that the flux is essentially uniform in the radial direction. (The uniformity is limited by the discreteness of the rings.) The total flow rate is such that there is an average spray flux Φ equal to $0.622 \text{ kg/(m}^2\text{-s)}$ ($0.915 \text{ gal/(ft}^2\text{-min)}$). The injection angles are distributed uniformly over $\pm 90^\circ$ from the normal to the containment dome. The injection velocities of the drops are uniformly distributed over the range 1.25 m/s to 3.5 m/s. This very crudely corresponds to the velocity distribution for the Spraco Model 1108-1214 solid cone nozzle.¹⁻²³ The droplet diameter, injection angle, and injection velocity for each droplet parcel is obtained by random sampling from the appropriate distribution.

One of the major achievements in this work is the recognition of the importance of droplet coalescence due to collisions, and the implementation of a model which accounts for

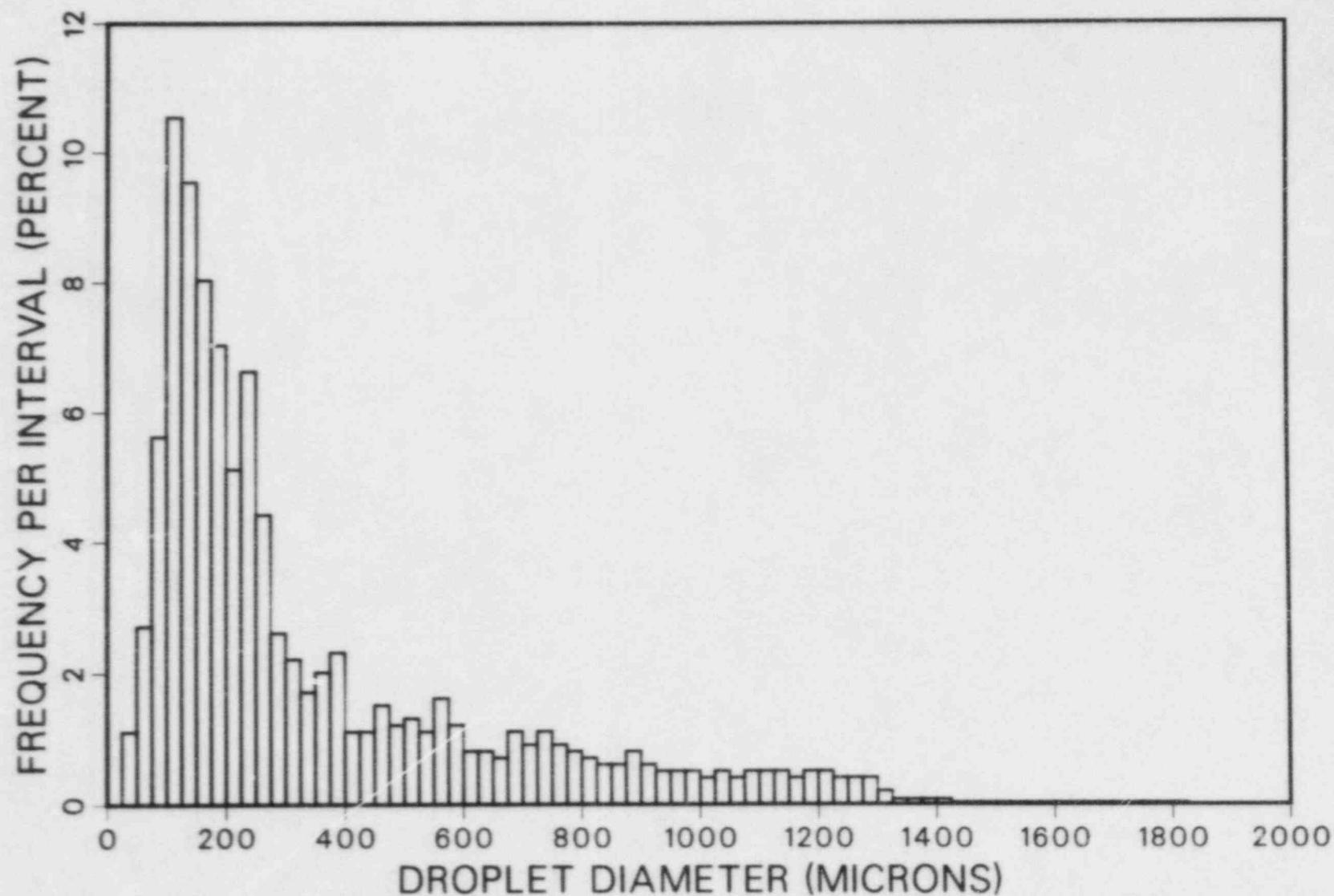


Figure 1.25. Droplet Diameter Distribution Used in the Baseline Calculation. Note that the distribution, although small between 1425 μm and 1825 μm , is non-zero there. The frequency in that range is 0.025%.

it. Coalescence reduces the population of small droplets and increases the size of the large ones. Among other things, this has the effect of reducing the amount of water that can circulate upwards, because only the lighter droplets avoid falling out at the floor of the building. Such droplets would increase the drag which retards the air flow. Hence, it is necessary to eliminate them through coalescence in order that this retardation is not overestimated.

The Conchas-Spray code employs the Subgrid Scale turbulence model as given by Deardorff.¹⁻²⁴ Accordingly, the kinematic viscosity at any point is increased over the laminar value by an eddy viscosity

$$v_T = \sqrt{2} k_D^2 (\Delta x)^2 S \quad (1.5)$$

where Δx is the maximum distance across a cell, S is the square root of the contraction of the strain rate tensor (roughly the gradient of velocity), and k_D is a coefficient which was set equal to 0.176 for the class of problems considered by Deardorff, but can be adjusted for consistency with any known experimental data. In the absence of any experimental data, our baseline value of k_D has been set equal to

$$k_D^{\text{baseline}} = \frac{0.176}{2} = 0.088 \quad (1.6)$$

This choice results in conservatively high estimates of the magnitudes of the air flow velocities. Laminar viscosity is of little consequence because the eddy viscosity dominates it in this application.

The boundary condition on the tangential air velocity at the walls of the building are set by fitting the law-of-the-wall velocity profile in the zones next to the wall.¹⁻²⁰

Results of the numerical simulation of the configuration described above are given in Figures 1.26 through 1.31. This calculation was started by suddenly introducing droplet injection into initially quiescent air. The situation shown here is that which is reached when the computation has progressed to essentially a steady state; it is slowly approached through an irregular process in which eddies are generated in the air. There is no convergence to a true steady state because there always remain some fluctuations



Figure 1.26. Positions of Spray Droplet Parcels in the Baseline Calculation. This is a "snapshot" taken at a time after the computation has reached steady state.



Figure 1.27. Droplet Parcel Velocities in the Baseline Calculation. The lengths of the vectors are proportional to the velocities. The maximum velocity is 18.0 m/s.

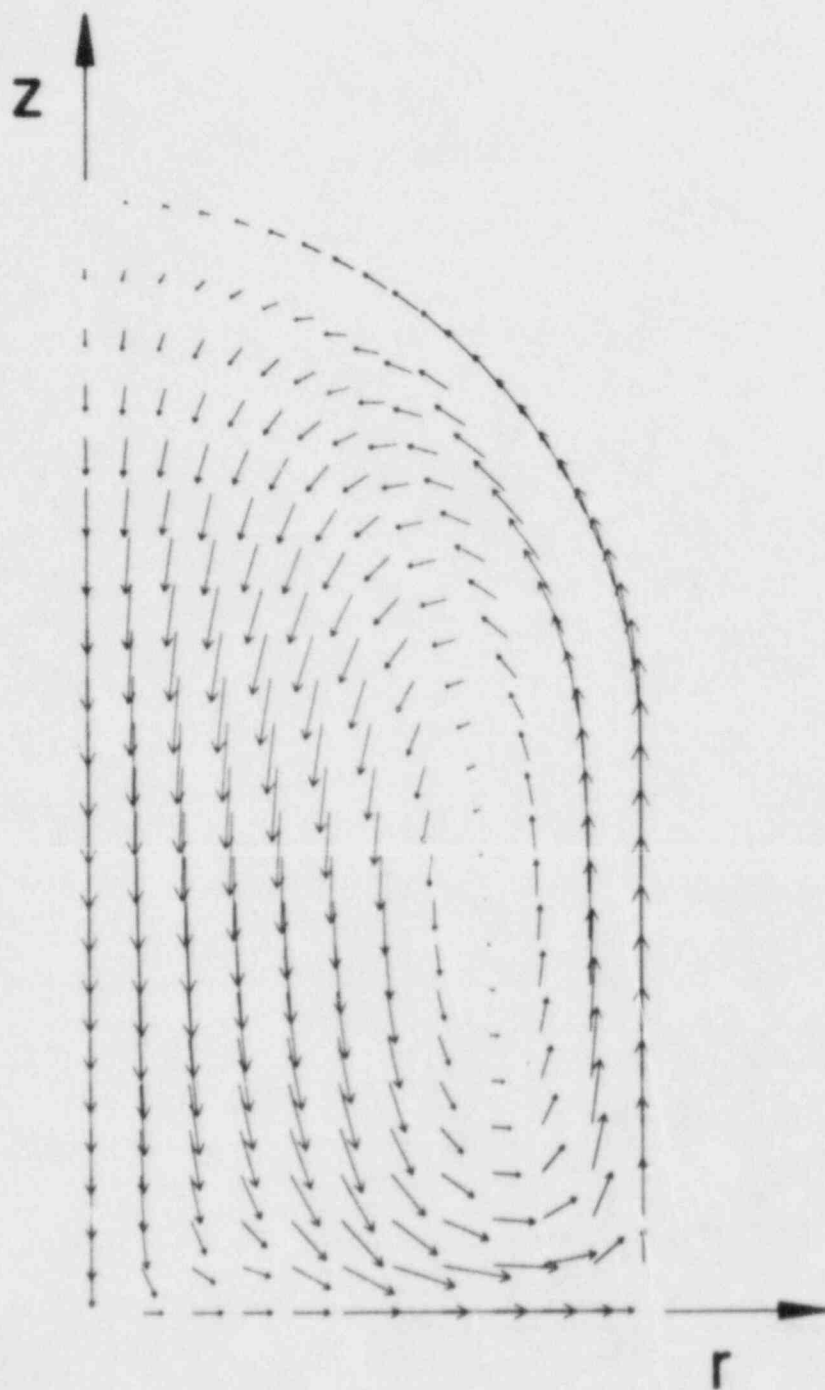


Figure 1.28. Air Flow Pattern in the Baseline Calculation. The lengths of the vectors are proportional to the velocity at each point on the finite-difference grid. The maximum velocity is 14.3 m/s.

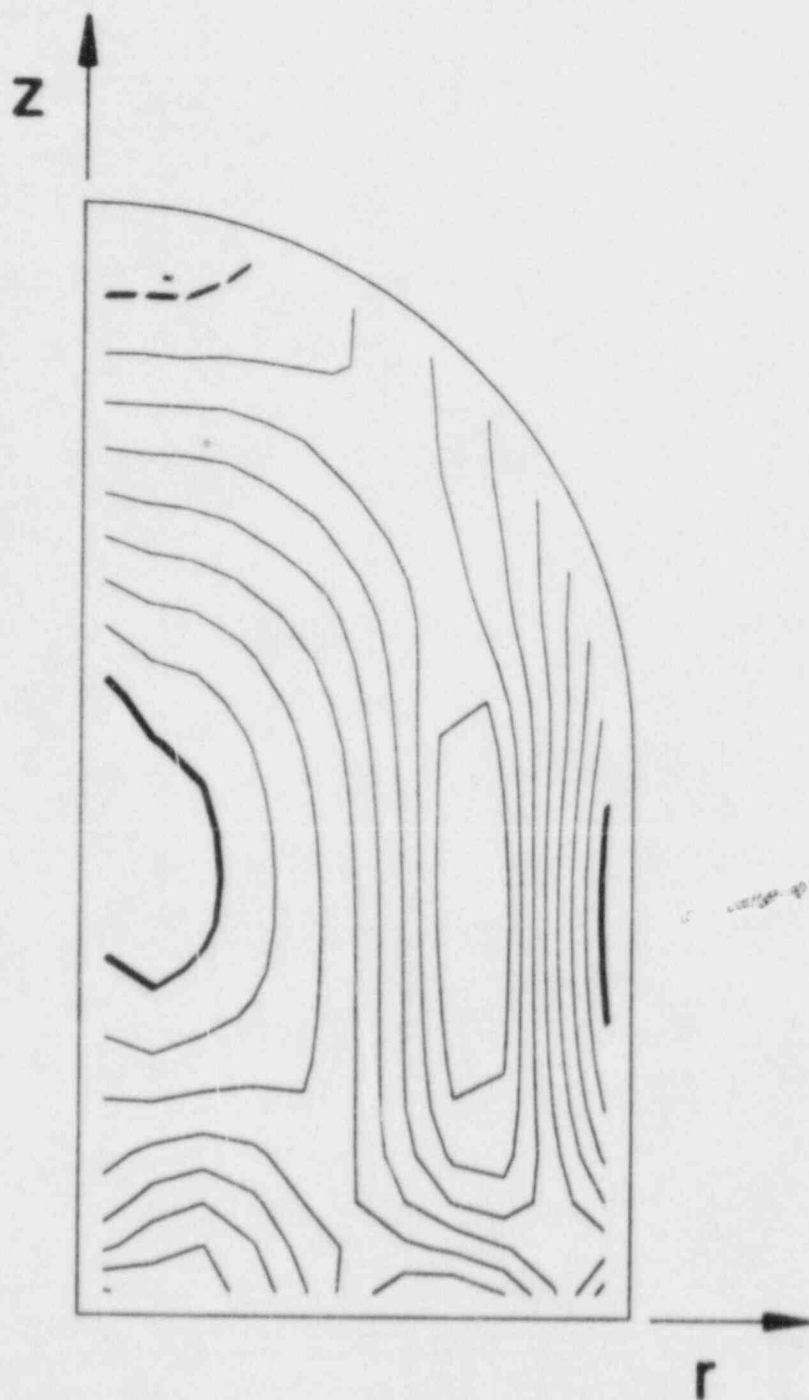


Figure 1.29. Contour Plot of the Magnitude of Air Velocity $|u|$ in the Baseline Calculation. The velocity on the heavy dashed contour is 2.2 m/s, and that on the heavy solid contour is 12.0 m/s. The eight velocity increments for contour lines between these are uniform, and are equal to approximately 1.2 m/s.

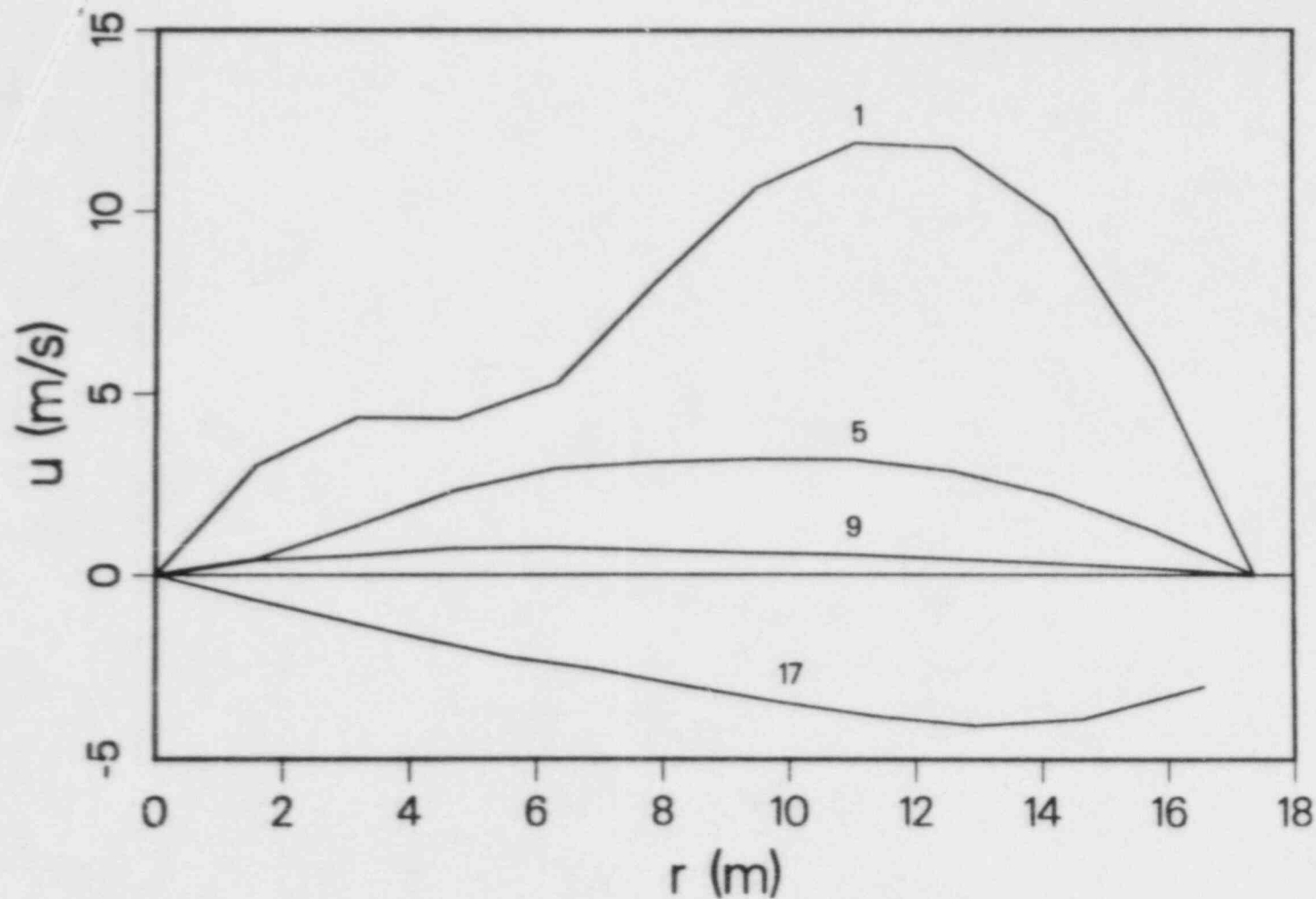


Figure 1.30. Radial Velocity Versus Radius in the Baseline Calculation. The curves correspond to four different elevations which are identified by their grid indices, as follows: 1 ($z = 0$ m), 5 (5.8 m), 9 (11.6 m), and 17 (22.6 m).

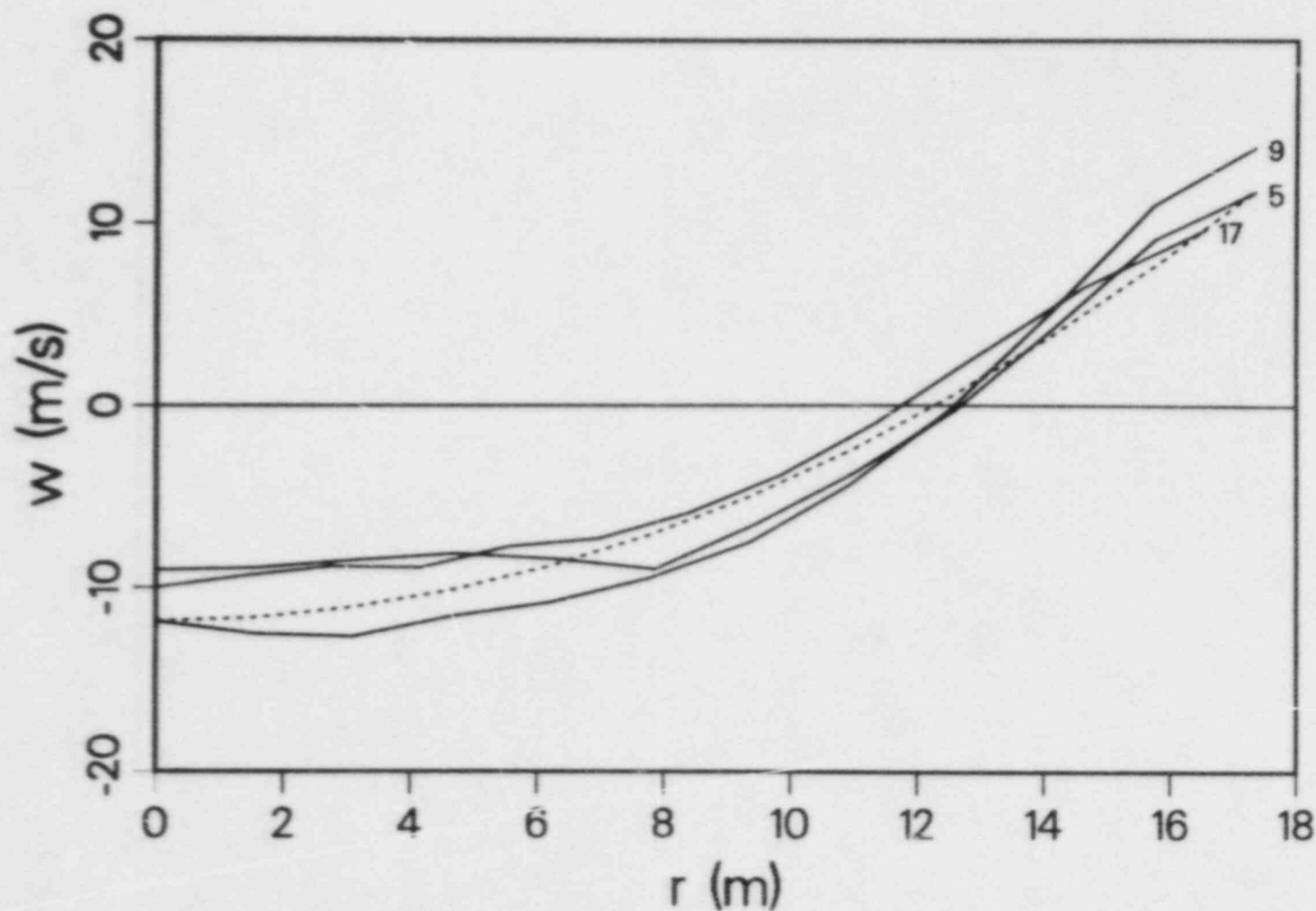


Figure 1.31. Axial Velocity Versus Radius in the Baseline Calculation for Three Different Elevations as Follows: 5 ($z = 5.8$ m), 9 ($z = 11.6$ m), and 17 ($z = 22.6$ m). The dashed line shows an approximate theoretical formula derived in Reference 1, which has been normalized by forcing agreement with the velocity on the axis at $z = 11.6$ m.

due to the random sampling of the parameters describing droplet injection. Furthermore, it is possible that some internal waves still exist that are being damped only very slowly, or that are perhaps even metastable. At any rate, the fluctuations in peak velocity have settled down to less than 10 percent when this computational steady state is reached. The calculation required about one-half hour of cpu time on a Cray 1-S computer.

Note that the peak radial velocity u_{\max} is about 12 m/s, and the peak axial velocity w_{\max} is about 14 m/s. (See Figures 1.29 and 1.30). This shows that the inference of velocities on the order of 10 m/s in the spray test in the empty Zion containment building¹⁻²⁵ is reasonable.

Some theoretical arguments are given in Reference 1-19 which explain why the system evolves to the state shown here. An approximate formula is derived there which permits estimation of the magnitude of typical air flow velocities \bar{u} . It is

$$\bar{u} = \sqrt{2g\bar{H}_s} \quad (1.7)$$

where $g = 9.8 \text{ m/s}^2$ is the acceleration of gravity and \bar{H}_s is the average height of the spray rings. The average height \bar{H}_s is about $3H/4$. For $H = 34.7 \text{ m}$, one obtains $\bar{u} = 23 \text{ m/s}$, which is slightly higher than the velocities which occur in the computational results of Figures 1.26 through 1.31, but is of the same order of magnitude. It is not surprising that the velocity is overestimated, since we have ignored some losses.

Equation (1.7) has the remarkable property that the velocity is independent of spray flux Φ . This is contrary to intuition and is not really true. It happens to give about the right result for the particular spray flux specified for the Sequoyah reactor, as explained in Reference 1-19.

We now describe the calculation in which the boundaries of the configuration are modified to account for the presence of the ice condensers and the steam generators within the containment building. In this case, the locations of the spray rings are concentrated between radii of 5.8 m and 9.9 m to correspond to those in some nuclear reactors such as Sequoyah and Catawba.¹⁻²⁶

This calculation represents a very crude approximation to the perturbation of the flow in a real containment building, because there the structures are not axisymmetrical. By

assuming such symmetry, we are imposing two-dimensionality on a configuration which is very three-dimensional.

The results are shown in Figures 1.32 through 1.35. The flow pattern is fairly complex, as seen in Figures 1.32 and 1.33. Because of the strong vortex formed above the steam generators, there is a large region over the steam generators and ice condensers in which very few droplets appear.

The most crucial information for igniter survivability is contained in Figure 1.34, the contour plot of $|u|$. It is seen that the air flow velocities are reduced substantially from those occurring in the baseline case. The peak value of $|u|$ is now 7.6 m/s, compared to 14.3 m/s.

Except for some reservations regarding three-dimensional effects, these estimates of air flow velocities should be conservatively high. The primary reason for this is that the calculations have utilized very regular geometries. This ~~prevents~~ prevents the formation of large, strong, well-ordered vortices, which lead to greater flow velocities. From this standpoint, the two-dimensionality is a conservative assumption. The inclusion of more structures in the building, such as the overhead crane, etc., would impede the air flow. Another less significant conservative factor is that the eddy viscosity has been purposely reduced.

The following can be stated regarding numerical accuracy: In the interest of keeping computing costs down, the finite-difference grid has been somewhat coarse at times, and the number of droplet parcels has been too low in some regions to provide really good statistics. However, we have experimented with variations in these parameters and have not observed significant changes in the results.

For these reasons, it is felt that one can use the contour plots of $|u|$ to obtain reasonable estimates of the flow velocity in regions where igniters are placed. Experimental data indicates that the igniters will fail due to convective cooling if they are exposed to air flows in excess of 10 m/s. Our results indicate that there are regions of significant extent where the flow velocities are less than this. This appears to be an optimistic indication for igniter survival.

We are not prepared to offer quantitative answers to the question of igniter failure due to sprays blowing up under the igniter shields and onto the igniters. The spray droplet statistics in these calculations are not good enough to provide reliable estimates of upward spray fluxes, as these fluxes are crucially dependent on the population of small droplets. Before an accurate calculation of spray

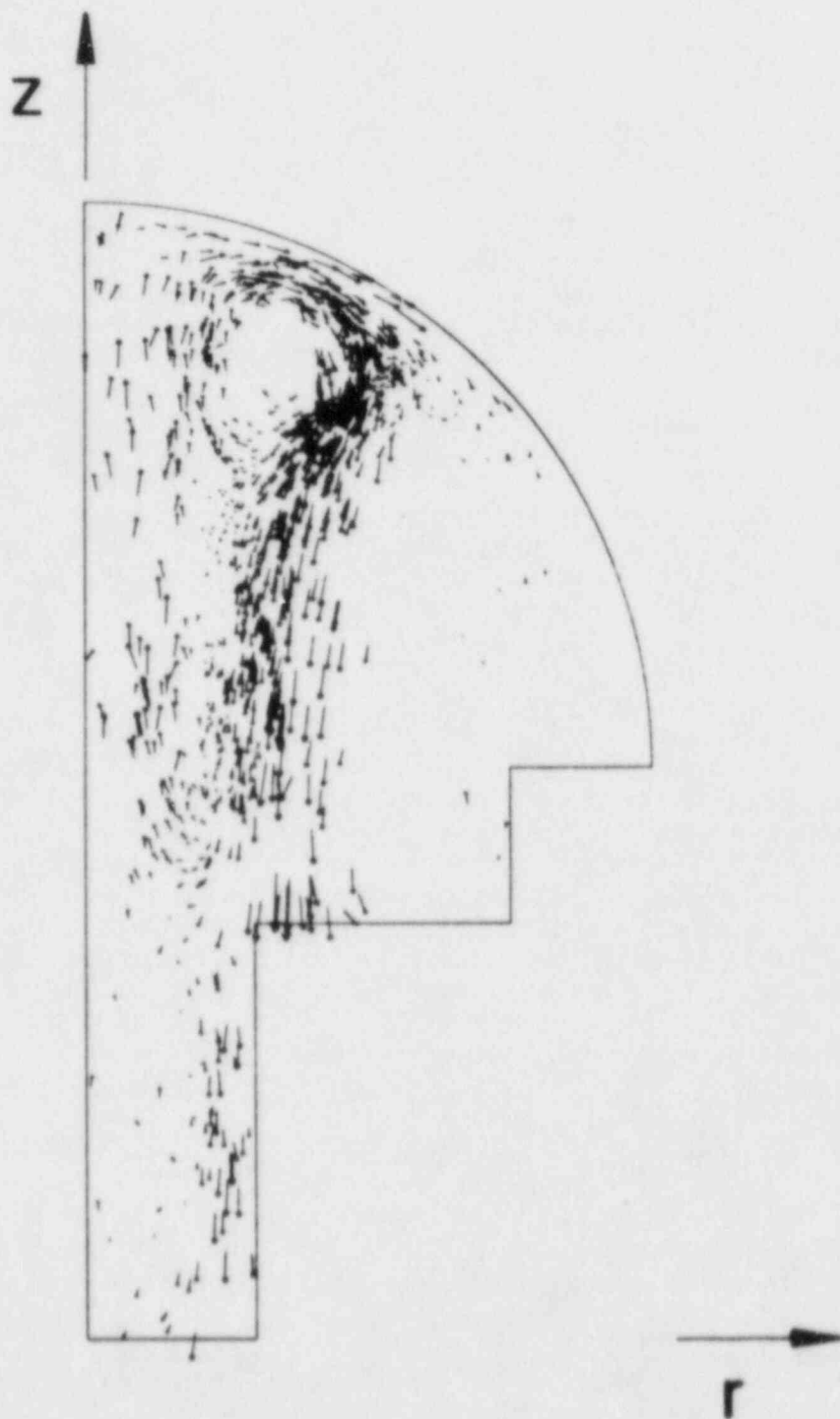


Figure 1.32. Droplet Parcel Velocities for the Calculation With Ice Condensers, Steam Generator Dog-houses, and Concentrated Spray Rings. The maximum velocity is 13.7 m/s.

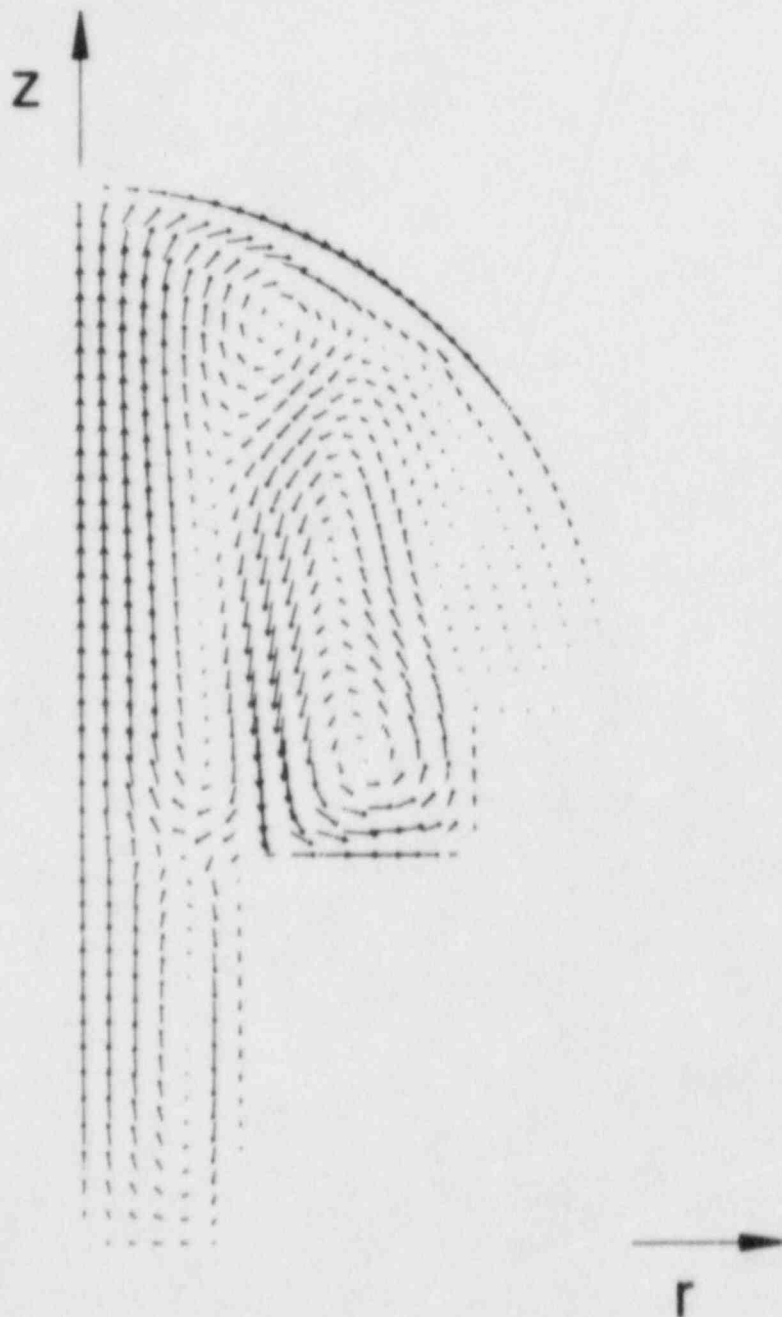


Figure 1.33. Air Flow Pattern for the Calculation With Ice Condensers, Steam Generator Doghouses, and Concentrated Spray Rings. The maximum velocity is 7.6 m/s.

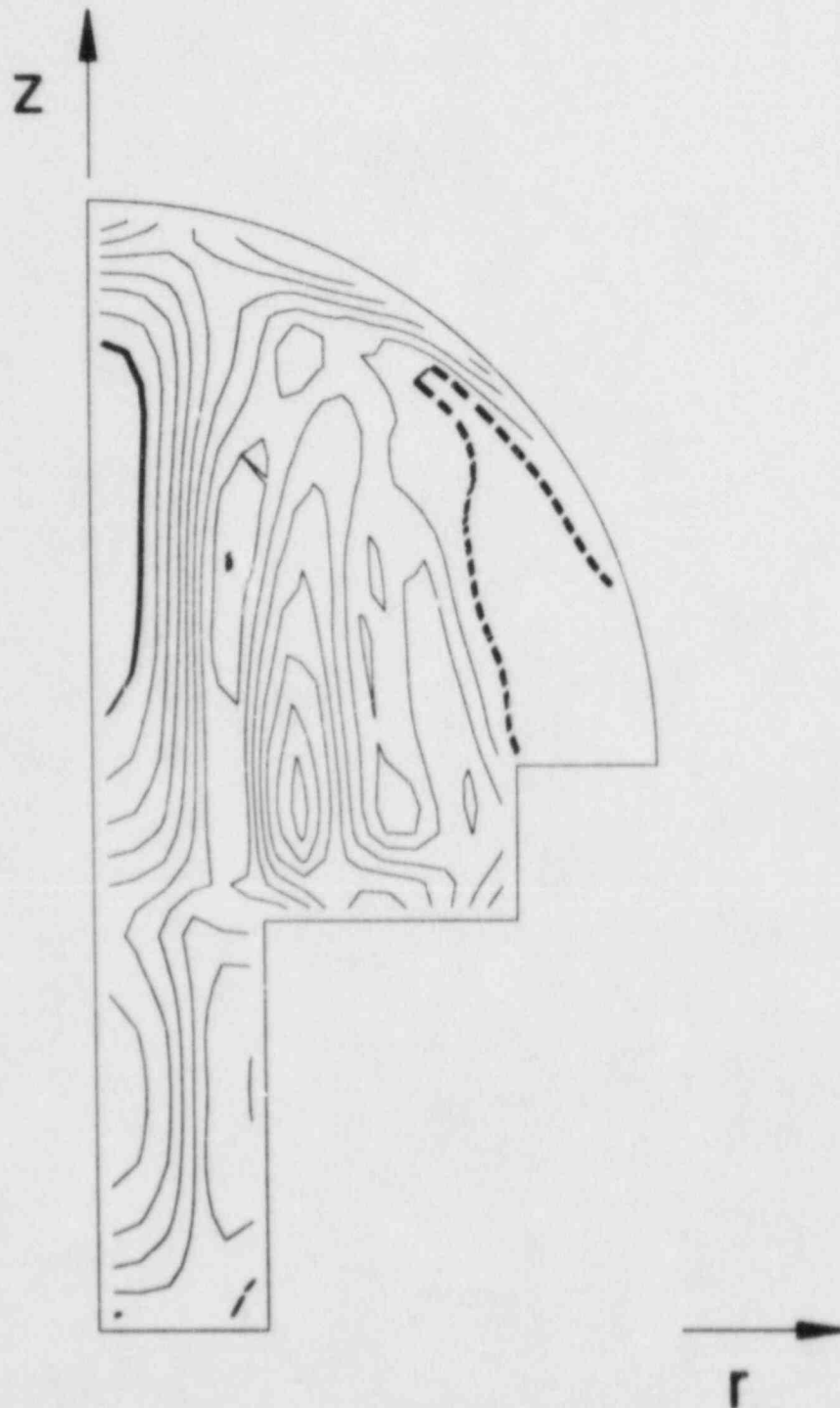


Figure 1.34. Contour Plot of the Magnitude of Air Velocity $|u|$ for the Calculation With Ice Condensers, Steam Generator Doghouses, and Concentrated Spray Rings. The velocity on the heavy dashed contour is 0.8 m/s, and that on the heavy solid contour is 6.8 m/s. The eight velocity increments for contour lines between these are equal to approximately 0.8 m/s.

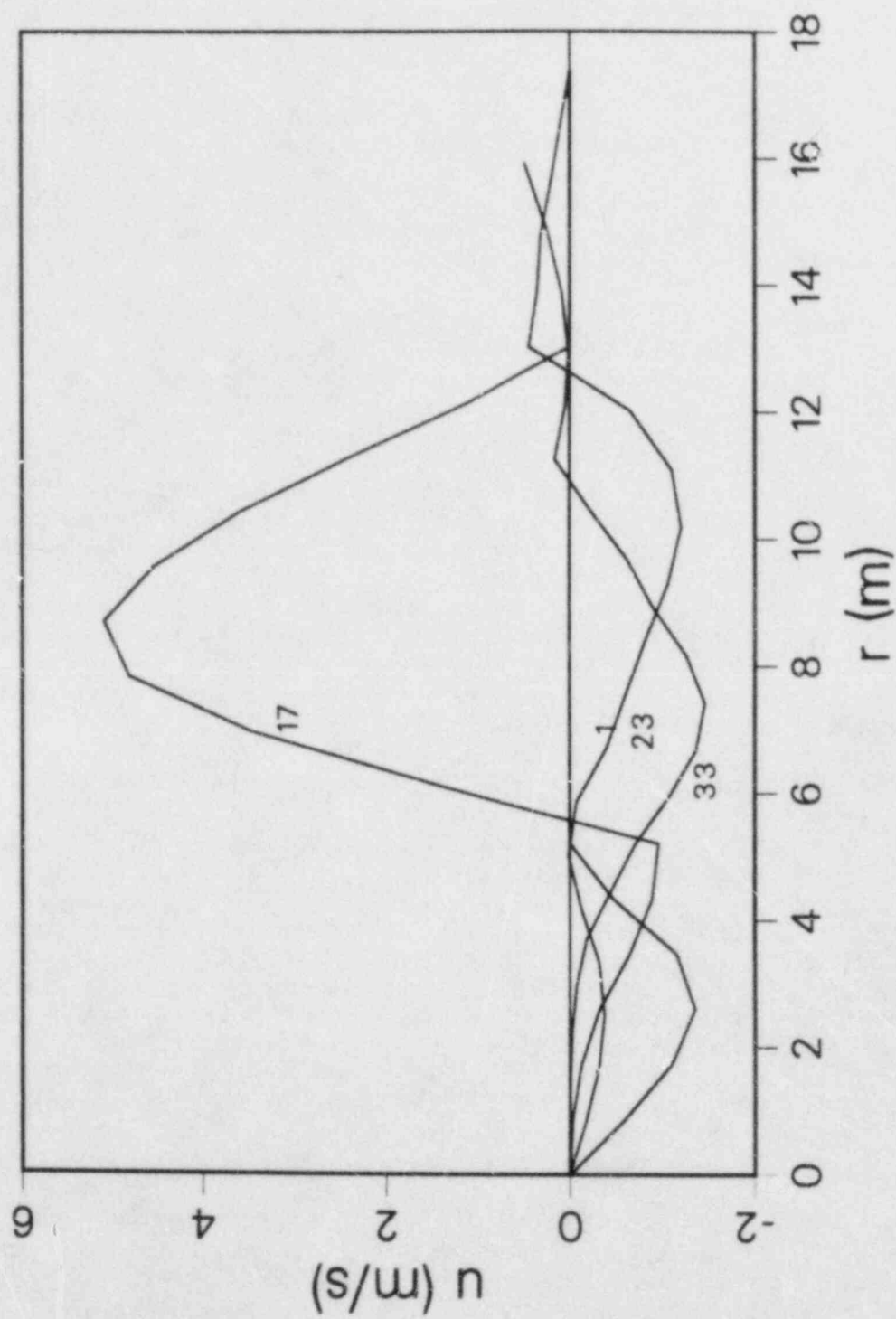


Figure 1.35. Radial Velocity for the Calculation With Ice Condensers, Steam Generator Doghouses, and Concentrated Spray Rings

flux could be undertaken, the number of droplet parcels would have to be increased, and it would be necessary to thoroughly assess the accuracy of the coalescence model.

1.5.2 Hydrogen Combustion in Water Sprays (L. S. Nelson; K. P. Guay, 6427)

It has been predicted theoretically¹⁻²⁷ that during hydrogen combustion, the presence of dispersed water drops in the form of fogs or mist will reduce both the peak pressure and peak temperatures produced during the burn. Instantaneous suspended water densities on the order of 100 g/m^3 are required according to this analysis.

The most common way to produce dispersed water drops, by the use of nozzles, generates turbulence and gas motion in the hydrogen-air mixtures and totally masks the effects of water drops on the burns.¹⁻²⁸ We have been investigating a different method of dispersing the water in a premixed hydrogen-air mixture--spinning disk generators.¹⁻²⁹ These generators produce large quantities of drops of a single diameter and are expected to produce suspended water densities in the usable range as predicted by theory. Moreover, these generators inject the water into the combustion chamber in a gentle sideways motion compared to the violent downward entry of sprays used in the large chamber experiments.¹⁻²⁷ By using the monodispersed drops, we intend to compare experimental values with codes that treat hydrogen burns on reactor scale, in particular HECTR. It should be emphasized that these experiments are not intended to test spray systems used in containments, but rather to examine, diameter by diameter, the effects of water drops and their concentrations on hydrogen burns independent of the effects of gas motion normally produced by sprays.

As described in the previous quarterly report,¹⁻³⁰ a pair of spinning disk drop generators was received from Atmospheric Physics, Inc. These units have 12 cupped disks each and spin with vertical axis up to 7000 rpm. A photograph of one of the generators was shown in the previous quarterly report. Our calculations indicate that these units will produce monodisperse drops as small as $100 \mu\text{m}$ in diameter and will achieve water densities on the order of 100 g/m^3 in the FITS hydrogen combustion chamber.

The generators have been installed in the transparent plastic bag mockup of the FITS combustion chamber, as shown in Figure 1.36. During this quarter we expended most of our effort on debugging the mechanical, electrical, and hydraulic portions of the system. In addition, we installed tachometers with remote readouts and flowmeters on each of the units.

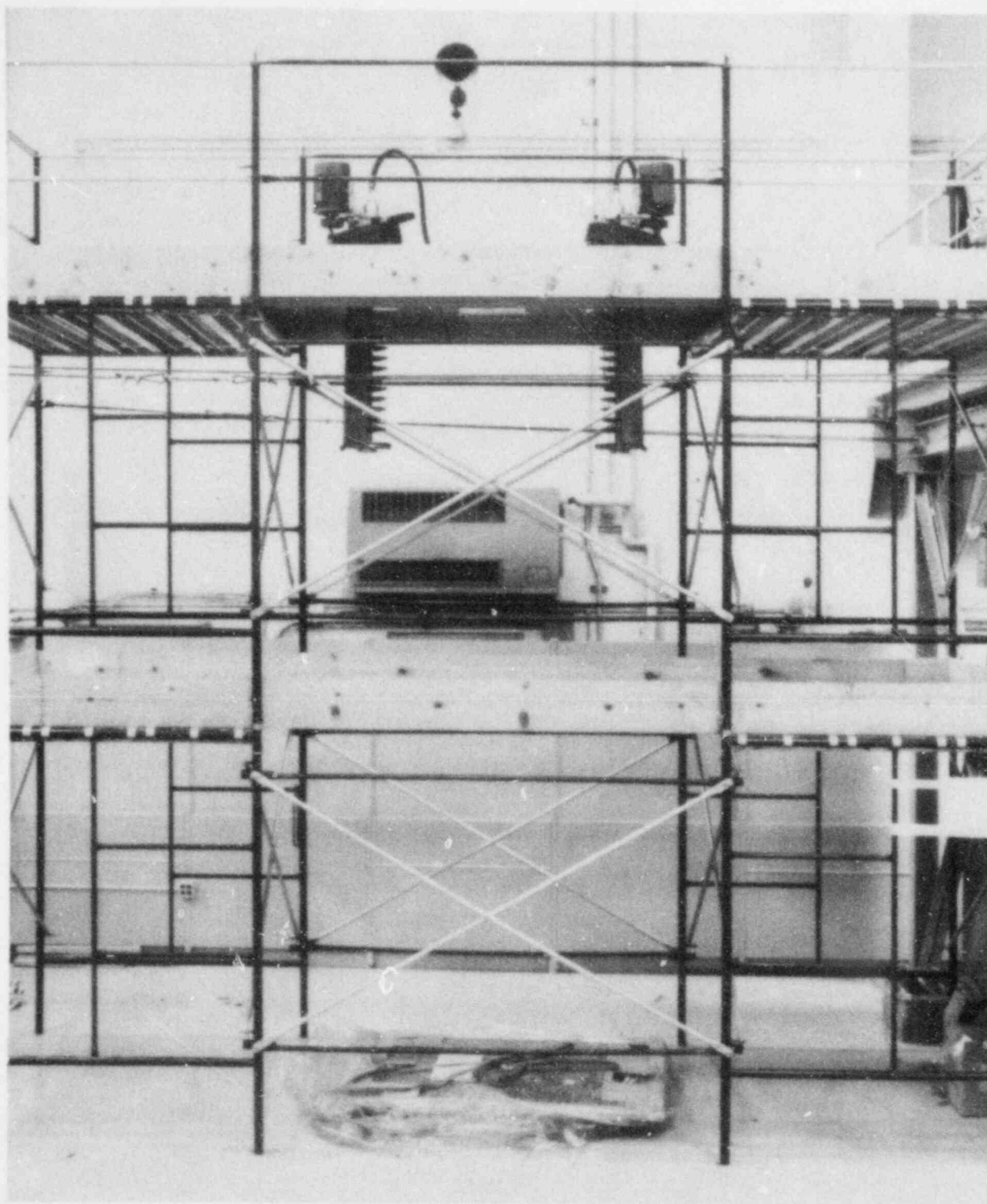


Figure 1.36. View of Spinning Disc Water Drop Generators Installed in Mockup of FITS Combustion Chamber. During operation, the units are enclosed in the 1.7 m-square by 4 m-high transparent plastic bag, shown collapsed on the floor beneath the pair of generators.

Our initial examination of the spray pattern indicated that there was an unusually heavy throw of water to the sidewalls of the mockup adjacent to one edge of the semicircular back support of each generator structure, shown in Figure 1.37. To eliminate this, we added a vertical sheetmetal shield D to each unit to enclose the spinning disks 3/4 of the way around their periphery. Thus, 1/4 of the drops produced by each generator actually enters the chamber, while the remainder is discharged against the back support and from the units in a solid steam.

The water drops injected into the chamber from the spinning disk generators produce a slow vortex-like motion of the entire mass of suspended drops that precesses around the vertical axis of the mockup curved arrows F in Figure 1.37. At this time, we are not prepared to predict what effect this slow motion will have on the hydrogen combustion.

Extensive diagnostics were started at the end of the quarter to measure downward water fluxes and drop diameters as a function of operating parameters of the generators. Results are expected during the next quarter.

1.5.3 Hydrogen Combustion and Aerosols (L. S. Nelson, G. D. Valdez, 6427)

During core degradation or core-melt accidents, large quantities of both nonradioactive and fission product-containing aerosols are hypothesized to be produced in containment along with hydrogen-air mixtures. Many questions arise about the combustion of hydrogen in this situation that involve the effects of the combustion on aerosols, the effects of the aerosols on the combustion, and the overall effects on the deliberate ignition system should it be used in such a situation. During this quarter we have been preparing the 5 m³ VGES chamber for the combustion of hydrogen in the presence of core-simulant aerosols. This effort has involved considerable experimental effort including debugging and testing of the various systems used to perform the experiment. These systems include:

1. Combustion chamber. The 5 m³ VGES chamber has been equipped with a series of diagnostics for the hydrogen burns which includes three pressure transducers, 18 thermocouples dispersed throughout the chamber in a tree; the DAASY-II data acquisition system will be used to record their outputs. In addition, we have installed two passive calorimeters, one at the top facing downward and one at the midpoint of the sidewall facing inward. We also have provisions for taking gas samples before and after the combustion to examine the completeness of the burn. Also installed in the VGES chamber are four cascade impactors for estimating aerosol

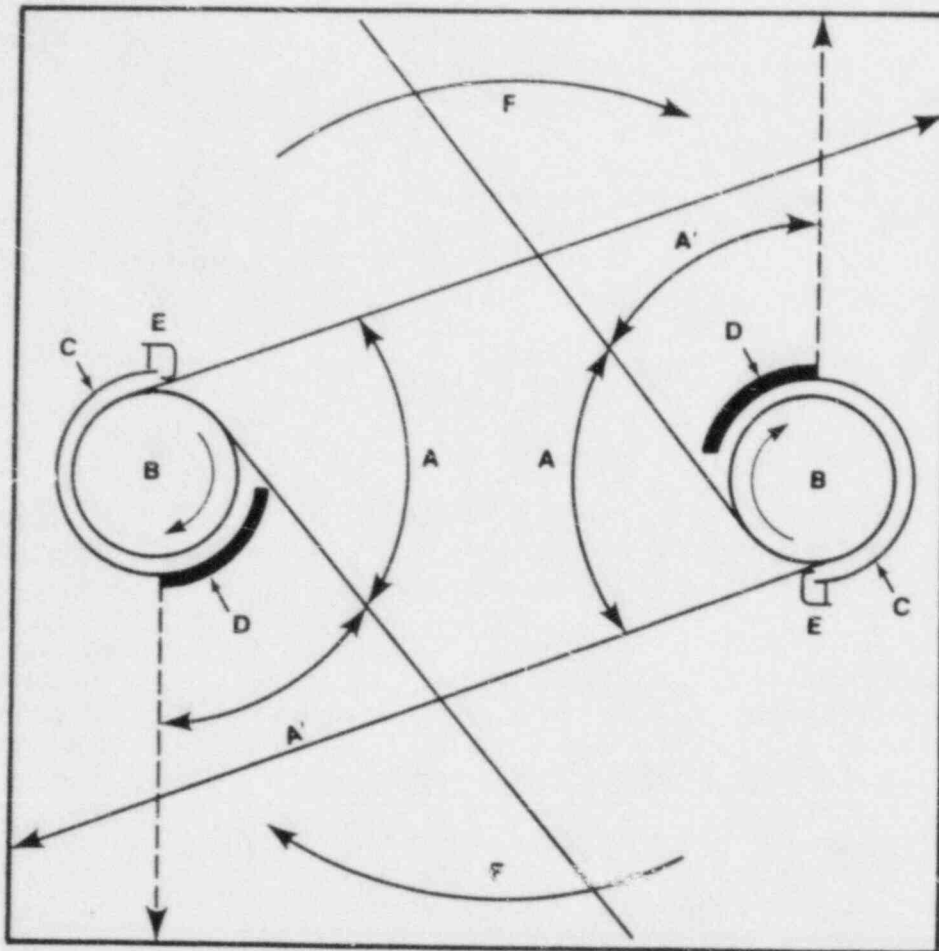


Figure 1.37. Schematic Top View of the Spinning Disc Water Drop Generators Installed in the 1.7 m-square Plastic Bag Mockup of the FITS Combustion Chamber

- A--Angle that contains trajectories of drops admitted to the chamber.
- A'--Angle that contains trajectories of drops which produced very heavy throw of water to chamber wall; these drops were rejected by the addition of the sheet metal shield D to the semicircular rear generator wall C.
- B--Spinning discs.
- E--Scoop to trap water moving along back wall (C+D).
- F--Slow vortex precession induced by drop motion.

particle diameters and concentrations, four total filters for measuring total concentrations of aerosol, and three dish-type fallout samplers. Each experiment is controlled by a Hewlett-Packard 85 computer which sequences the triggering of the experiment and the sampling of the aerosols, both pre and posttest.

2. Powder dispersion apparatus. Aerosols are generated by gas burst dispersal of specially prepared powders. We are using an Ansul dry powder fire extinguisher which contains a burst disk which opens abruptly by gas overpressurization. In order to trigger our experiment properly, a special sensor has been installed and tested both inside and outside the chamber to produce a signal on which to initiate the hydrogen burn.
3. Powder preparation. Techniques have been developed to produce dry, free flowing powders. This involves mainly drying in a vacuum oven.

During this quarter eight experiments were performed with lean hydrogen-air mixtures. Two experiments were attempted in 4.8 v/o hydrogen-air mixtures as shakedown experiments. Ignition was erratic, prompting us to raise the hydrogen concentration of 6.5 v/o for subsequent experiments. Two more shakedown experiments and a control test were performed at this new concentration without aerosols. Then three experiments were performed with gamma-aluminum oxide as the simulant of an insoluble, refractory oxide-type aerosol that might be produced during a reactor core degradation accident. In each experiment, approximately 1 kg of powder was dispersed in approximately 15 s.

The aerosol sampling with the cascade impactors indicated a typical distribution of particle sizes as shown in Figure 1.38, with a peak aerodynamic diameters near 20 μm . Aerosol concentrations, both preburn and postburn, were measured with the impactors and total filters; values ranged between 5 g/m^3 at the top of the chamber and 76 g/m^3 at the bottom.

Pressure-time and temperature-time traces from these experiments are currently being analyzed and will be discussed in the next quarterly report.

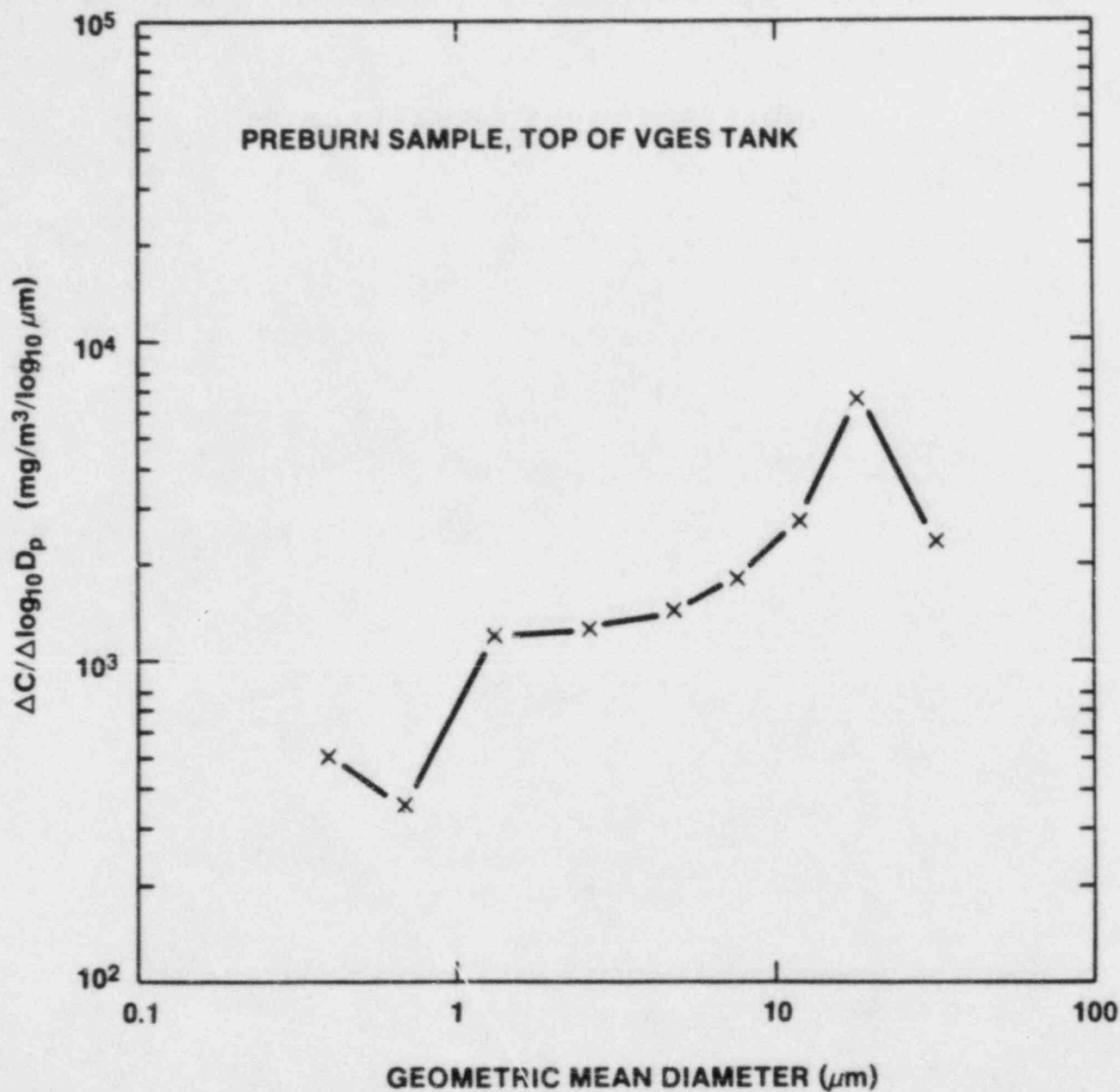


Figure 1.38. Aerosol Diameter Distribution Obtained With a Cascade Impactor Just Prior to a Hydrogen Burn in the 5.1 m^3 VGES Combustion Chamber. The aerosol was generated by discharges $\approx 1 \text{ kg}$ of $\gamma\text{-Al}_2\text{O}_3$ into the chamber.

1.6 References

- 1-1. R. K. Cole, Jr. et al., CORCON-MOD2: A Computer Program for Analyses of Molten Core-Concrete Interactions, NUREG/CR-3920, SAND84-1246, Sandia National Laboratories, Albuquerque, NM, October 1984.
- 1-2. D. A. Powers, VANESA: A Model of Aerosol Generation and Radionuclide Release During Core Debris Interactions with Concrete, Sandia National Laboratories, Albuquerque, NM (to be published).
- 1-3. E. R. Copus, Development of the Inductive Ring Susceptor Technique for Sustaining Oxide Melts, NUREG/CR-3043, SAND82-2546, Sandia National Laboratories, Albuquerque, NM, September 1983.
- 1-4. D. A. Powers and F. E. Arellano, Large-Scale Transient Tests of the Interaction of Molten Steel with Concrete, NUREG/CR-2282, SAND81-1753, Sandia National Laboratories, Albuquerque, NM, January 1982.
- 1-5. A. Suo-Anttila, SLAM - A Sodium Concrete Limestone Concrete Ablation Model, NUREG/CR-3379, SAND83-7114, Sandia National Laboratories, Albuquerque, NM, December 1983.
- 1-6. M. Berman, Light Water Reactor Safety Research Program Semi-Annual Report, October 1983-March 1984, Sandia National Laboratories, Albuquerque, NM (to be published).
- 1-7. D. A. Powers and F. E. Arellano, Direct Observation of Melt Behavior During High-Temperature Melt/Concrete Interactions, NUREG/CR-2283, SAND81-1754, Sandia National Laboratories, Albuquerque, NM, January 1983.
- 1-8. M. Berman, Light Water Reactor Safety Research Program Semiannual Report, October 1983-March 1984, Sandia National Laboratories, Albuquerque, NM (to be published).
- 1-9. A. L. Camp, M. J. Wester, and S. E. Dingman, HECTR: A Computer Program for Modelling the Response to Hydrogen Burns in Containments, NUREG/CR-0038, EPRI RP1932-35, SAND82-2456, Proceedings of the Second International Conference on the Impact of Hydrogen on Water Reactor Safety, Albuquerque, NM, October 1982.
- 1-10. R. D. Cess and M. S. Lian, "A Simple Parameterization for Water Vapor Emissivity," Trans. ASME Journal of Heat Transfer, Vol. 98, No. 4, pp. 676-678, (1976).

- 1-11. H. C. Hottel, Heat Transmission W. H. McAdams, ed.), (New York: McGraw-Hill 1953), p. 83.
- 1-12. D. K. Edwards, "Molecular Gas Band Radiation," Advances in Heat Transfer. T. F. Irvine and J. P. Hartnett, ed., Volume 12, 1976.
- 1-13. P. Thibault, Y. K. Liu, C. Chan, J. H. Lee, R. Knystautas, C. Guirao, B. Hjertager, and K. Fuhre, 19th Symposium (International) on Combustion, The Combustion Institute, Pittsburgh, 599-606 1982.
- 1-14. B. H. Hjertager, "Computer Predictions of Flame Acceleration Characteristics in Some Turbulent Gaseous Fuel-Air Explosions," Chr. Michelsen Report 833403-1, Bergen 1983.
- 1-15. J. H. Lee, R. Knystautas, and A. Freiman, Combustion and Flame, 56, 227-239 1984.
- 1-16. Y. K. Liu, J. H. Lee, and R. Knystautas, Combustion and Flame, 56, 215-225 1984.
- 1-17. N. Manson, C. Brochet, J. Brossard, and T. Pujol, Ninth Symposium (International) on Combustion, 1963, p. 461.
- 1-18. C. M. Tarver, "Chemical Energy Release in One-Dimensional Detonation Waves in Gaseous Explosives," Combustion and Flame, 46, 1982, pp. 111-133.
- 1-19. K. D. Marx, "Air Currents Driven by Sprays in Reactor Containment Buildings," NUREG/CR-4102, SAND84-8258 Sandia National Laboratories, Albuquerque, NM (to be published).
- 1-20. L. D. Cloutman, J. K. Dukowicz, J. D. Ramshaw, and A. A. Amsden, CONCHAS-SPRAY: A Computer Code for Reactive Flows with Fuel Sprays, LA-9294-MS, Los Alamos National Laboratory, May 1982.
- 1-21. J. K. Dukowicz, "A Particle-Fluid Numerical Model for Liquid Sprays," J. Comp. Phys., 35, 229, 1980.
- 1-22. "Sandia Hydrogen Program Bimonthly Report - October-November 1983," January 1984.
- 1-23. "Sandia Hydrogen Program Bimonthly Report - August-September 1983," January 1984.
- 1-24. J. W. Deardorff, "On the Magnitude of the Subgrid Scale Eddy Coefficient," J. Comp. Phys., 17, 120, 1971.

- 1-25. L. S. Nelson, presentation at the Midyear Review of the Sandia National Laboratories NRC Hydrogen Behavior Program, Las Vegas, Nevada, April 4-5, 1984.
- 1-26. R. Palla, U.S. Nuclear Regulatory Commission, Washington, DC, private communication.
- 1-27. M. Berman, M. P. Sherman, J. C. Cummings, M. R. Baer, and S. K. Griffiths, Analysis of Hydrogen Mitigation of Degraded Core Accidents in the Sequoyah Nuclear Power Plant, NUREG/CR-1762, SAND80-2714, Sandia National Laboratories, Albuquerque, NM, March 1981.
- 1-28. L. Thompson, "EPRI Large-Scale Hydrogen Combustion Experiments," in Designing for Hydrogen in Nuclear Power Plants, collection of reports presented at the Joint ASME/ANS Nuclear Engineering Conference, Portland, OR, August 5-8, 1984, The American Society of Mechanical Engineers, New York, NY, pp. 9-14.
- 1-29. W. H. Walton and W. C. Prewett, "The Production of Sprays and Mists of Uniform Drop Size by Means of Spinning Disc Type Sprayers," Proc. Phys. Soc., 62, 341-350. (1944).
- 1-30. Reactor Safety Research Quarterly Reports, April-June 1984, Vol. 31, NUREG/CR-3816 (2 of 4), SAND84-1072 (2 of 4), Sandia National Laboratories, Albuquerque, NM, December (1984).

2. FISSION-PRODUCT SOURCE TERM

2.1 High-Temperature Fission-Product Chemistry and Transport (D. A. Powers, 6422; R. M. Elrick, 6422; R. A. Sallach, 1846)

The purpose of the High-Temperature Fission-Product Chemistry and Transport Program is to obtain data on the chemistry and processes that affect the transport of fission-products under accident conditions. The program now consists of three tasks related to one another. Baseline thermodynamic and reactivity data are being collected for compounds of fission product elements of particular interest. An experiment facility has been built to allow the chemistry of fission products in prototypic steam-hydrogen environments to be studied. The interaction of fission-products with reactor materials such as stainless steel can be examined in this facility. Results of these experimental studies are compared to predictions of thermochemical models to determine if reaction kinetics play an important role in fission-product transport.

Several tellurium experiments were conducted in steam with Inconel 600 and with 304 stainless steel. Tellurium was found by x-ray fluorescence methods on the surface of the Inconel coupons exposed at 800°C. The tellurium x-ray intensity data correlated with the mass gains observed for the coupons, suggesting that the oxidation of the alloy by steam was minor. There was an enhanced (relative to the base metal) nickel x-ray fluorescence signal; the formation of one of the nickel telluride compounds was inferred. This would be consistent with the thermodynamics--nickel not being oxidized in steam-hydrogen mixtures and thus available to the tellurium. This would also be consistent with the previously reported experiments in which lightly preoxidized Inconel coupons were exposed to Te vapor in an argon gas stream and a rapid, complete reaction with Te to form various nickel tellurides was observed.

When stainless steel coupons were exposed to Te vapor at 850°C and above there was significant oxidation and no measurable tellurium x-ray fluorescence signal was obtained from a surface analysis. However, when stainless steel coupons were exposed at 700°C, there was relatively little oxidation and Te was detected on the surface by x-ray fluorescence. When these surfaces were examined with the microprobe the Te was found not to be uniformly distributed, but concentrated in small areas (1-2 μm^2) as shown in Figure 2.1. Only nickel was associated with tellurium.

The composition of local areas encompassing the Te spots were measured by the microprobe. The Te and Ni contents do

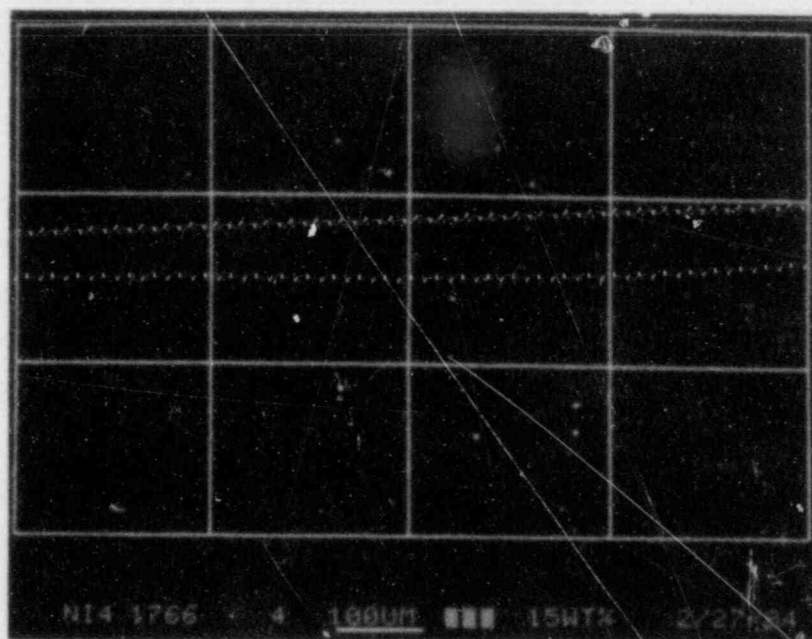
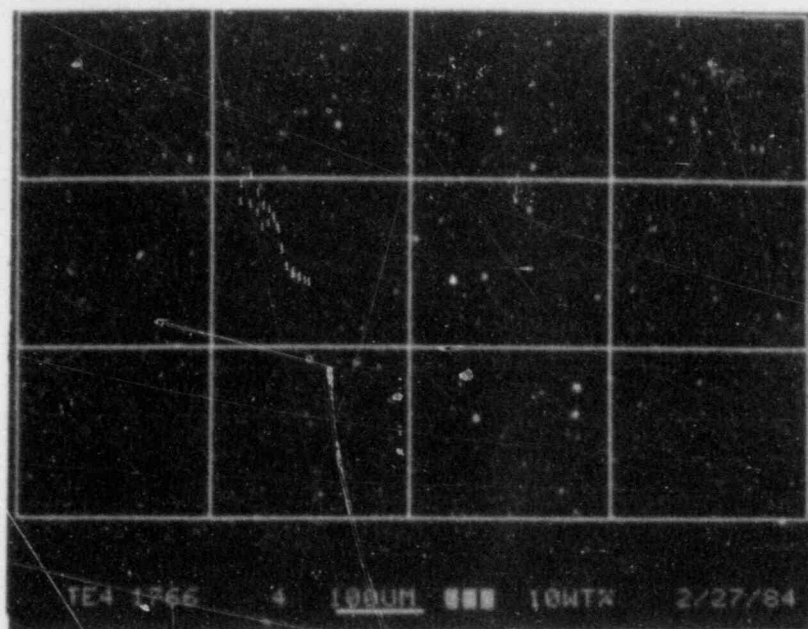


Figure 2.1. Elemental Distributions of Tellurium and Nickel on the Surface of a 304 Stainless Steel Coupon Exposed in Steam at 700°C

correlate, as shown in Figure 2.2. The Te:Ni ratio averages 0.8:0.1. The compound, $\text{Ni}_{2.86}\text{Te}_2$, has a ratio close to this value. Since this is the most nickel-rich telluride and all other nickel tellurides have greater Te:Ni ratios, the measured ratio implies that there has been little incorporation of Fe or other metallic elements into the reaction product. This contrasts with the earlier work with preoxidized stainless steel where the exposure to Te vapor in argon resulted in the rapid reaction of Te to form various iron tellurides on the outer oxide surface. Diffusion of iron through the oxide was necessary for their formation. Such diffusion is apparently blocked by the presence of steam. A counter diffusion of an oxygen species inward from the outer surface would result in the formation of new oxide at some interior location thus negating any uptake of Te unless the latter also were able to diffuse to the interior.

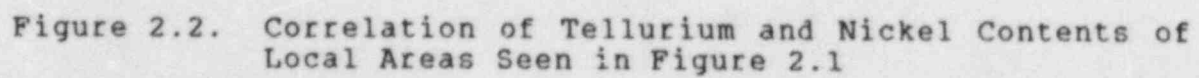
Since oxidation is less of a problem with the Inconel alloy, our tentative conclusion is that this alloy will likely take up tellurium vapor from the steam environment of the reactor system. No conclusion can yet be made for the stainless steel alloy when there is concurrent oxidation by steam. Although no surface content of Te was detected when oxidation was prevalent, the possible retention of Te deeper within the oxide has not yet been disproved. Microprobe analyses of the deeper oxide layers is in progress.

2.2 Quantitative Uncertainty Estimation for the Source Term (P. K. Mast, 6425; D. A. Powers, 6422)

The Quantitative Uncertainty Estimation for the Source Term (QUEST) Program estimates the uncertainty in a few of the calculated radiological source terms reported in the BMI-2401 drafts from Battelle's Columbus Laboratories. In particular, QUEST is considering the TMLB' and S₂D accident sequences in Surry (a PWR with a large, dry containment) and the TC sequence in Grand Gulf (a BWR with a Mark-III containment).

The results for an analysis of the TMLB' and S₂D accident sequences at the Surry plant have already been presented.^{2-1, 2-2} The analysis for the TC sequence at Grand Gulf was completed this quarter and will be reported in detail in a later report.²⁻³ A summary of the results is provided below.

Unlike the Surry TMLB' and S₂D analyses, a detailed assessment of phenomenological uncertainties for the Grand Gulf TC sequence was not performed with the BMI-2104 code suite. Rather, an estimate of the final source term phenomena uncertainty was made by considering only the dominant uncertainties and applying these uncertainties to the base-case results reported in BMI-2104. The dominant uncertainties considered were in-vessel fission-product release and



retention (in RCS) and suppression pool scrubbing effectiveness.

Since containment failure actually precedes vessel failure in this accident sequence, separate early and late source term estimates were not considered. However, there is the possibility that suppression pool disruption might occur at the time of vessel failure due to a high-pressure melt ejection. This case is considered separately and is designated "Early-High."

Table 2.1 gives the general conditions for the various stages of an accident that would be expected to result in the low, high, and early-high source terms. As had been the case in previous analyses, these combinations of uncertainties are not unique in defining high or low source terms. Thus, other combinations of parameter uncertainties could also result in high or low source terms, possibly even outside the ranges we have defined. However, the cases chosen are thought to be representative of the high and low values for the source term uncertainty.

Table 2.1

Conditions Expected to Result in High or Low
Source Terms for Grand Gulf TC Sequence

	<u>Low</u>	<u>High</u>	<u>Early-High</u>
In-vessel production	Hi	Hi	Hi
Net retention in RCS	Hi	Lo	Lo
Drywell production of aerosols by core-concrete interaction	Lo	Hi	Hi
Retention in Drywell	Hi	Lo	Lo
Suppression Pool Retention	Hi	Lo	Lo
Suppression Pool Disruption	No	No	Yes
Retention in Containment	Hi	Lo	Lo

There are several ways a final low release to the environment may occur. The "low" case chosen herein has high in-vessel production coupled with high in-vessel retention so that the bulk of the fission products remain within the RCS. Production of aerosols in the drywell is also assumed to be low with retention in the drywell, suppression pool, and containment all high.

The nominal "high" case defined herein has high production both in-vessel as well as in the drywell. Conditions leading to low retention are assumed in-vessel, in the drywell, in the suppression pool, and in containment.

The case designated "early-high" is identical to the "high" case except that conditions leading to suppression pool disruption due to high-pressure melt ejection are also assumed.

While all of the phenomena uncertainties described above affect the final source term uncertainty, previous sensitivity studies had shown that the in-vessel production and RCS retention and suppression pool behavior dominate.

The assessment of source term uncertainty for the Grand Gulf TC sequence was coupled very closely to the base case that had been reported in BMI-2104. These results are summarized in Table 2.2.

For the purpose of the Grand Gulf TC uncertainty analysis, it was assumed that phenomena uncertainties associated with ex-vessel aerosol production, drywell fission-product retention, and containment building fission-product retention were of secondary importance relative to other uncertainties. Thus, the RCS retention and suppression pool retention uncertainties dominated.

The results of our analyses for the "low" case are summarized in Table 2.3 and the results of the analyses for the "high" case are summarized in Table 2.4. The range in release fractions is seen to be almost a factor of 1000, with the base case falling near the middle of this range. Because of the nature of the analyses, these results for the "high" case were somewhat more "conservative" than the Surry TMLB' and S₂D analyses. However, even this conservative "high" case shows considerable mitigation of release to the environment, with peak values lower than for the Surry cases considered.

The three dominant uncertainties in the determination of the source term for the Grand Gulf TC sequence are:

1. Retention of fission products within the RCS (including the effects of revaporization and resuspension);
2. The effectiveness (decontamination factor) of the suppression pool in removing fission-product gases and aerosols from the gases passing through it (including the effects of pool bypass); and

Table 2.2

Final Distribution of Fission Products in
Grand Gulf TC Base Case (BMI-2104)

Species	Fraction of Core Inventory				
	RCS	Drywell	Pool	Containment	Environment
CsI	0.19	3.6×10^{-2}	0.77	1.4×10^{-4}	6.8×10^{-3}
CsOH	0.51	1.4×10^{-3}	0.49	9.2×10^{-6}	3.5×10^{-4}
Te	0.22	0.32	0.45	4.3×10^{-4}	8.8×10^{-3}

Table 2.3

Final Distribution of Fission Products in
Grand Gulf TC Sequence--"Low" Case

Species	Fraction of Case Inventory				
	RCS	Drywell	Pool	Containment	Environment
CsI	0.90	0.004	0.096	3×10^{-6}	9.7×10^{-5}
CsOH	0.90	0.0003	0.099	2×10^{-7}	7.1×10^{-6}
Te	0.90	0.008	0.92	1×10^{-5}	1.9×10^{-4}

Table 2.4

Final Distribution of Fission Products in
Grand Gulf TC Sequence--"High" Case

Species	Fraction of Case Inventory				
	RCS	Drywell	Pool	Containment	Environment
CsI	0.1	0.04	0.78	2×10^{-3}	7.6×10^{-2}
CsOH	0.1	0.0025	0.89	2×10^{-4}	6.4×10^{-3}
Te	0.1	0.069	0.65	1×10^{-2}	1.7×10^{-1}

3. The likelihood and potential consequences of a high-pressure melt ejection causing severe disruption of the suppression pool such that most of the fission products released in-vessel and during the high-pressure melt ejection would enter the containment building atmosphere.

The phenomenological uncertainties associated with in-vessel fission-product release and retention within the RCS are essentially the same as for the Surry accident sequences and will not be discussed again.

The suppression pool in the Grand Gulf BWR design is an extremely important means of reducing radioactivity release to the environment. Uncertainties associated with the modeling of aerosol removal mechanisms during suppression pool scrubbing lead to a plus or minus factor of 10 uncertainty in the decontamination factor. This has a significant impact on the radioactivity release to the containment building since most of the fission products released from the reactor vessel are trapped in the suppression pool. Even for the most pessimistic assumptions on suppression pool effectiveness, however, suppression pool scrubbing is very effective so that total release fractions are much lower than the "high" estimates for the Surry TMLB' and S₂D sequences.

The largest single uncertainty associated with the Grand Gulf TC sequence concerns suppression pool disruption. It has been predicted that high-pressure melt ejection and the subsequent vessel blowdown could overpressurize the drywell to such an extent that gas flow rates through the suppression pool exceed the fluidization velocity. The suppression pool would then be dispersed into a droplet flow regime. It is likely that if this were to occur, most of the fission products released in-vessel and during the high-pressure melt ejection would enter the containment building atmosphere. A much more detailed analysis of this phenomenon than was done for QUEST, including accounting for the tortuous flow path for ejected core melt from vessel to drywell, would be required to eliminate this concern.

2.3 ACRR Source Term Experiments

(P. S. Pickard, 6423; J. B. Rivard, 6420A; W. J. Camp, 6425; D.A. Powers, 6422)

Release of radionuclides during fuel degradation in a core uncover accident is the first stage in the determination of the amount and nature of the radioactive release from the damaged nuclear plant. Current estimates of the release of the principal fission products over the range of relevant accident conditions are subject to significant uncertainty (e.g., QUEST). A key element in reducing the uncertainty in predicted releases is an improved understanding of fission

products from the fuel under severe fuel damage conditions. The ACRR Source Term program is being developed to provide a data base for fission-product release over a range of fuel temperatures, system pressures, and fuel damage states, where little or no data currently exists, to allow the development of improved fission-product release models for use in consequence evaluation. This program is related to out-of-pile programs at ORNL and BCL.

During this quarter work concentrated on (1) test matrix definition, (2) preliminary test design, and (3) preparing the draft report, "Radionuclide Release from Severely Damaged Light Water Reactor Fuel," SAND84-1582. This document describes a series of in-pile tests of radionuclide release from irradiated reactor fuel rods under conditions to be expected during severe reactor accidents. These tests are to be conducted in Sandia National Laboratories' Annular Core Research Reactor (ACRR) as part of the USNRC's Severe Fuel Damage Program.

The data obtained from the in-pile ST program and the related laboratory experiments at BCL and ORNL will provide the improved data base for the fission-product release models in the mechanistic accident analysis codes being developed by the NRC.

Two models for radionuclide release and transport within the vessel and RCS are currently being developed: the stand-alone, detailed FAST-GRASS release model which is combined with the TRAP-MELT transport model in the SCDAP core degradation model, and the VICTORIA model to be utilized for both release and transport of radionuclides in the MELPROG melt-down model.2-4,2-5

FAST-GRASS and PARA-GRASS provide a highly detailed treatment of the release of radionuclides from intact or nearly intact rods into the fuel/clad gap at low and moderate temperatures. These models attempt to include the full complexity of the irradiated fuel matrix--including the release pathways known to be important for noble gas release and presumed in these models to dominate release of vaporizable species as well. By contrast, VICTORIA treats release from reactor materials under all in-vessel conditions ranging from intact rods (at a less detailed level than FAST-GRASS), to liquefying fuel and cladding, to solid rubble beds, to fully molten pools, and to rapidly fragmenting fuel under melt/water interaction conditions.

From the modeling standpoint, experimental data needs are found in several areas. The variables important to these areas include temperature, steam and hydrogen pressures, clad state, and damage states. Temperature of the fuel is

the most important factor since it affects all characteristics of vaporization and diffusion. Liquefaction and fuel/clad interactions will affect vaporization but the effects are difficult to ascertain from the available data. System pressure and gas composition will affect the driving force for release of the volatile species--notably Ba, Sr, La, and Ce. The range of possible variations is not extensive enough to affect Ru release. Gas phase mass transport is the dominant rate-limiting process when (1) temperatures are high, (2) pressures are high, and (3) gas flow velocities are low. Any "source term" test matrix that is to contribute directly to model development and verification must thus cover the relevant ranges of these variables.

Thermophysical data is also needed throughout this variable space, yet must be considered secondary to obtaining key release measurements covering the important ranges of the variables mentioned above. These variables interact strongly with one another in the actual course of an accident. Similarly during integral experiments, it can be very difficult to sort out the contributions of various effects to the final release results. For this reason, primary emphasis in this program must be devoted to separate-effects experiments in which we can identify major effects on release and separate their contributions. The progression of damage and the integral interplay of these effects provides a major area of uncertainty for in-vessel release during accidents. Much is being learned about damage progression from existing programs such as the ACRR Damaged Fuel Relocation experiments and the PBF Severe Fuel Damage tests, which are leading to improved damage progression models. In addition to separate effects experiments to address release concerns noted above, there is a need for phenomenological accident progression experiments with irradiated fuels. Release data from such experiments may be directly correlated to damage progression during the experiment as a test of the ability of the model to treat combined interactions of the important phenomena. This will also provide a detailed basis for evaluating VICTORIA within the integral context of the MELPROG code, which may be used to model directly such experiments.

In evaluating the available data for release from the fuel under accident conditions, the QUEST study found significant uncertainty in these data. The available data for release of the volatile species showed considerable scatter (Figure 2.3). Uncertainties of factors of 10 on either side of a mean regression line through the data were defined in QUEST. These uncertainty bounds do not span the entire uncertainty range since the data were found to lie outside this range in some cases. Analyses indicated the possibility that gas phase mass transport in pressurized accident sequences could further limit release.

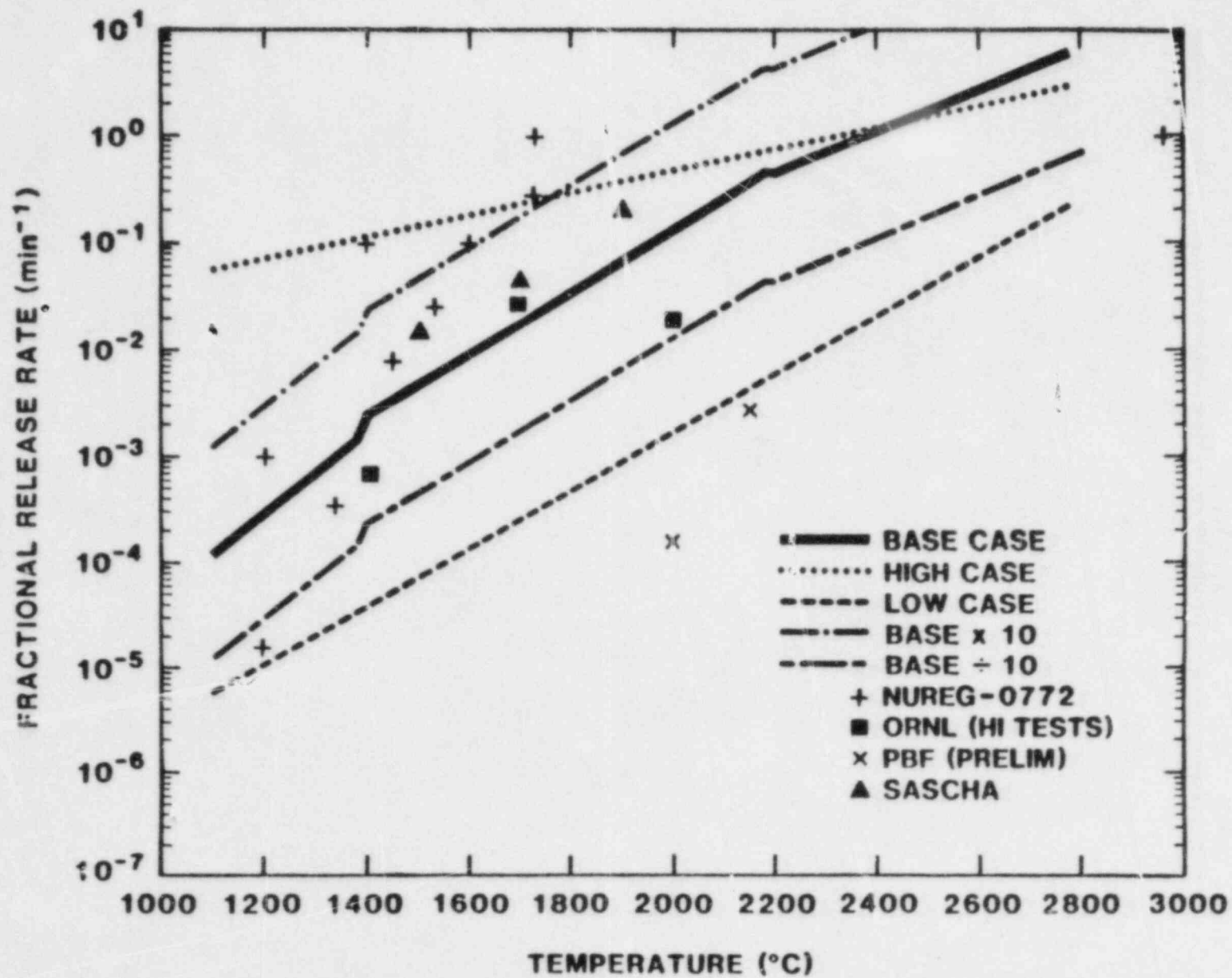


Figure 2.3. Scatter in Available Data for the Release of Iodine From Fuel

Order-of-magnitude uncertainties exist in the release of the volatile fission products such as Cs, I, Br, and perhaps Te, as is demonstrated by comparisons of laboratory and recent PBF tests. An important observation made in QUEST concerning these uncertainties is that the uncertainty is not uniform across the entire temperature spectrum. Once the release rate for a radionuclide is sufficiently high, this radionuclide is quickly released from the fuel. Bases found for further increases in the release rate do not alter this conclusion. Thus, the primary interest in the release of volatile radionuclides is associated with phenomena that would keep the release rates low in the uncertainty range.

The QUEST investigators also assigned order of magnitude uncertainty bounds on the releases of refractory species. They found that the uncertainty in refractory species release could be attributed in nearly equal proportion to uncertainties in release rates and uncertainties in fuel temperatures achieved in the core degradation process. Similar conclusions were reached by investigators involved in BMI-2104.

The interesting portion of the uncertainty range found for the release of the refractory species is the upper portion. Phenomena that would make order-of-magnitude increases in the best-estimates of refractory species release would have ramifications on the analysis of stages of a severe accident that follow core degradation. The amount of radioactive material trapped in the reactor system and available for mechanical resuspension would increase. The amount of refractory radionuclides available for release ex-vessel would drop significantly. Phenomena that would depress releases of refractory species would alter conclusions derived in current best estimate analyses slightly.

The ST experimental program is focused on the release of radionuclides from degrading reactor fuel. The degradation process itself and the behavior of the radionuclides after release from the fuel are being studied in companion programs. These aspects of severe accidents have an enormous bearing on what release experiments should be done in an integrated effort to reduce uncertainties.

In order to cover the range of relevant accident conditions, and to evaluate the effects of interactive fuel damage and fission-product release phenomena, a combination of both integral and separate-effects experiments is being considered:

1. ST Experiments--In-pile separate-effects tests to obtain release data as a function of specific parameters and conditions.

2. DFI Experiments--Integral fuel damage tests to obtain release data during combined-phenomena conditions simulating a continuum of accident states.

2.3.1 Separate-Effects Experiments

The ST experiments are relatively low cost, small-scale separate-effects tests designed to provide data for the development and quantification of fission-product release models, such as FASTGRASS and VICTORIA. The objective of the ST tests is to obtain release-rate data for a range of controlled and characterized conditions including fuel temperature, pressure, gas constituents and flow rates, and fuel damage state.

The ST tests simulate a small section of a reactor core rather than a scaled-down reactor core. By providing a number of tests over a range of test conditions, it is possible to limit the number of rate-limiting processes that occur in a particular test and thus facilitate the interpretation of test results. This approach requires that a relatively low-cost experiment design be developed for the ST test so that the relevant parameter space can be covered within current budget limitations.

The key features of the ST separate-effects experiments are summarized below:

1. Fuel--PWR fuel rod sections of approximately 15 cm length
--300 g/test
--Fuel burnup ~40,000 MWD/T
2. Decay Heat--Neutronic heating in ACRR of up to 5 W/g in ER-3 fuel
--Temperatures to 3100 K at 0.1 g/s per rod steam flow rates
3. Environment--Flowing steam and hydrogen environments will be provided by a closed-cycle recirculation system. Where desired, a copper-oxide hydrogen recombiner section will be included to permit continuous clad oxidation.
4. Fission-Product Collection--Fission products released from the fuel will be collected in a cooled filter system for posttest analysis. Up to six filters will be used sequentially during each experiment to provide time resolution. Each filter will consist of several sections to enhance the quality of the data derived from the sample.

5. Visual Diagnostics--End-on visual observation of the fuel damage state will be provided by cinematography and videotape, taken through windows in the containment vessels.
6. Temperature Measurement--Radiometric measurements of fuel temperatures will be made using the above visual signal path. This is an essential method for obtaining real-time data at high fuel temperatures.

The types of fission-product release experiments required to cover the desired conditions are indicated below:

1. Low Temperature Tests (~1900 K)
--detailed data on volatile fission-product release
--comparison with out-of-pile tests.
2. Molten Zr-fuel Liquefaction Tests
--effect of Zr- UO_2 liquefaction on release.
3. Preoxidized Clad Tests (clad melt temperatures)
--distinguish temperature from liquefaction effects on release.
4. Gas Composition Tests
--effect of oxidizing/reducing environments on release.
5. Elevated Pressure Tests
--effect of system pressure on radionuclide volatility as a function of temperature, damage state, and gas composition.
6. Elevated Temperature Tests (2700-3100 K)
--data base for refractory radionuclide release.
7. Debris Tests (at high temperatures)
--effects of configuration (debris size, surface area, clad) on release at elevated temperatures.

The matrix of experiments for the ST test has been formulated to provide these test conditions. Hardware design and demonstration are proceeding on schedule for the first test to be conducted in CY 1985.

2.3.2 DFI Experiment Description

The integral irradiated Fuel Damage Tests (DFI) are small-bundle irradiated fuel tests to study the combined effects of the above parameters on the rate of fission-product release from fuel. The DFI tests will simulate the progression of fuel damage in a representative accident sequence and allow correlation of the visually observed damage state with fission-product release. It is currently proposed that

two DFI tests be performed. The primary fission-product diagnostics for these tests will be a sequential sampling system that will provide sequential monitoring of fission-product release as a function of damage state. These samplers will be located as close as possible to the bundle exit region to prevent fission-product deposition on test section surfaces before the samplers. The DFI tests are designed to provide fission-product release in an environment which represents a combination of the parameters affecting release to insure that important effects or synergisms from combined processes have not been overlooked.

The key features of the in-pile DFI experiments are summarized below:

1. Fuel--4 to 9 rod bundles, or four irradiated rods with unirradiated guard rods
--Burnup rod sections of 30 to 50 cm in length
--Burnup 10-30,000 MWD/t.
2. Decay Heat--~3 w/g with 10 percent enriched fuel
--Oxidation and fission heated temperatures of approximately 3100 K (4 rods) for 0.03 g/s rod steam flow.
3. Steam System--Flowing steam provided by external boiler-superheater system. CuO recombination sections remove H₂ from effluent downstream from the fission-product samplers. The effluent will be condensed and sequentially collected in the experiment package.
4. Fission-Product Collection System--The primary fission-product diagnostic will be an array of cooled filter/aerosol deposition samplers. These samplers will be similar in design to those used for the ST test described above. These samplers will be used sequentially throughout the test to provide a time record of fission-product release. Up to 10 sequential samplers are planned. In addition to the cooled filter/aerosol deposition samplers, the condensate resulting from the condensation of the sampler effluent will be sequentially stored for subsequent analysis.
5. Visual Observation--Visual end-on observation of the time-dependent damage state will be used. Optical attenuation and absorption spectroscopy techniques are being examined for on-line measurements.
6. Temperature Measurements--Conventional and ZrO₂ sheathed thermocouples near fuel rods to monitor temperatures up to 2500 K. Radiometric temperature

measurements using multiband pyrometry will be made through the end-on window.

7. Hydrogen Measurements--Hydrogen will be monitored using CuO temperature rise techniques and/or Raman Spectroscopy.

As in the separate-effects ST approach, the primary fission-product release diagnostics will be posttest analyses of the sequential passive/reactive filter samplers. These samplers include reactive sections to segregate important volatile elements (Cs, I, Te) and passive sections to retain particulates. Both gamma spectroscopy and chemical techniques (Ion Chromatography, Ion Selective Electrodes (I), and Voltametry (Te)) are being evaluated for use in posttest analyses.

2.4 References

- 2-1. R. Lipinski et al., Uncertainty in Radionuclide Release Under Specific LWR Accident Conditions, SAND84-0410, Volume II, Sandia National Laboratories, Albuquerque, NM, February 1985.
- 2-2. R. Lipinski et al., Uncertainty in Radionuclide Release Under Specific LWR Accident Conditions, SAND84-0410, Volume III, Sandia National Laboratories, Albuquerque, NM (to be published).
- 2-3. P. K. Mast et al., Uncertainty in Radionuclide Release Under Specific LWR Accident Conditions, SAND84-0410, Volume IV, Sandia National Laboratories, Albuquerque, NM (to be published).
- 2-4. J. Rest, in the Proceedings of the International Specialists Meeting on Fission Product Behavior in Reactor Safety Experiments, Cadarache, France, 1984.
- 2-5. W. J. Camp, "Release of Fission Products from Fuel During the In-Vessel Phases of Severe Nuclear Reactor Accidents," SAND84-0519C, Proceedings of the International Behavior in Reactor Safety Experiments, Cadarache, France, 1983.

3. LWR DAMAGED FUEL PHENOMENOLOGY

Sandia's LWR Damaged Fuel Phenomenology Program includes analyses and experiments that are part of the integrated NRC Severe Fuel Damage (SFD) Research Program. Sandia is investigating, both analytically and in separate-effects experiments, the important "in-vessel" phenomenology associated with severe LWR accidents. This investigative effort provides for two related research programs: the Damaged Fuel Relocation (DFR) Program and the Damaged Core Coolability (DCC) Program. The focus of these activities is to provide a data base and improved phenomenological models that can be used to predict the progression and consequences of LWR severe core damage accidents. The DFR experiment program provides unique data on in-vessel fuel damage processes that are of central importance in determining the release and transport of fission products in the primary system. The DCC experiment program provides data on the ultimate coolability of damaged fuel configurations.

3.1 ACRR Damaged Fuel Relocation and Quench

(A. C. Marshall, 6423; P. S. Pickard, 6423; J. B. Rivard, 6420A)

The focus of the LWR DFR experiment program is directed toward providing separate-effects phenomenological data on important severe in-vessel fuel-damage processes to aid in the development of second generation severe accident analysis codes. A better understanding of the phenomena that determine that progression and consequences of the severe core-damage sequence is required for improved source term estimates, assessment of accident mitigation features, and as a basis for adequate emergency response to core uncovering accidents involving fuel damage. The core damage configuration, hydrogen generation, and fission-product release are the primary areas of interest. The DF test series uses photography to record the damaged fuel configuration during an in-pile experiment in which accident conditions are simulated in a small LWR rod bundle. The decay heating in these experiments is simulated by fission heating of the fuel in the ACRR. Steam conditions, similar to expected accident conditions are provided.

3.1.1 In-Pile Experiments

The major effort for this period focused on the assembly of the DF-2 experiment capsule and modifications to the steam skid, optical system, shield plug, and the software for the Data Acquisition and Control System (DACS). The assembly of the DF-2 capsule has been completed. This work included the installation of the condenser, jacket heaters, manifolds,

bulkhead, insulation, the access tube plumbing, and associated hardware. All capsule instrumentation and power electrical connections were also completed. The DF-2 capsule required ≈ 125 thermocouples, seven pressure transducers, and 64 power leads (this count does not include the instrumentation and power requirements for the skid, shield plug, and other systems). The plumbing modifications and installation of the electrical connectors for the shield plug assembly has been completed. Modifications to the steam skid are nearly completed. One of the skid modifications includes the installation AP type flow meters, which have been designed and fabricated by project personnel to permit very low steam velocity measurements. Calibration of these flow meters is underway. Modifications to the DACS software and optical system is near completion. One of the optical system modifications includes the installation of an Optical Multichannel Analyzer (OMA). The OMA should provide additional temperature data and may provide some information on aerosol species.

3.1.2 Posttest Examination for DF-1

Figure 3.1 displays a number of photographs illustrating the posttest configuration of the DF-1 experiment package. Included is a posttest X-radiograph of DF-1. Visible in this photonegative are (1) general retention of pellet and rod geometry, but substantial lateral deformation (bowing) of the fuel rods in the upper half of the bundle, with evident erosion of some fuel pellets, and (2) a 12 cm-long by 7 cm-diameter globular volume of high-density material enclosing a low-density zone that approximates a 5-cm sphere. The globular volume forms a partial blockage near the bottom of the fuel bundle, and its dense portion is positioned at the axial location originally occupied by a PWR-type grid spacer made from Inconel 718.

Perhaps the most unusual feature of the X-radiograph is the evident retention, especially in the upper part of the bundle, of the stacked-pellet geometry into the posttest period despite the loss of most of the cladding structure. This feature is best explained by reference to Figure 3.2, which shows two optical micrographs of an interface between two pellets near the upper end of the fueled section of the bundle. The dark zone in the center of the photographs is a voided zone, to the right of this void is a cross section of the material (light-colored zone) forming the bond between the two pellets above and below it. The bonding material is a zirconium-rich oxide that evidently flowed into the pellet-pellet interface in the liquid state. Because it wet the UO_2 interfaces well, it must have had an oxygen content in excess of 1 w/o. Subsequently, it solidified, forming a strong bond between pellets. The material contains both zirconium and uranium, with the concentration of the

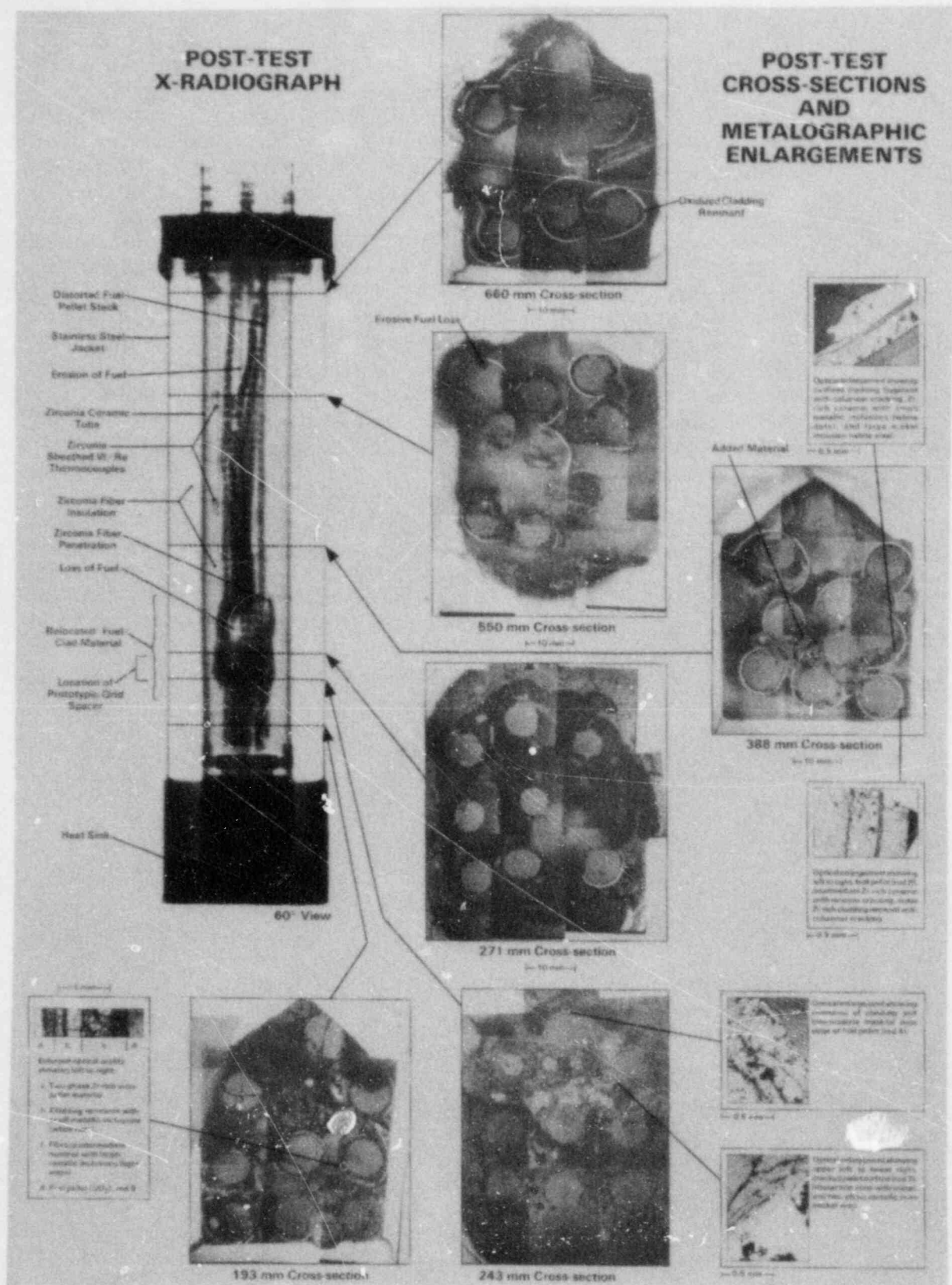


Figure 3.1. DF-1 Posttest Analysis

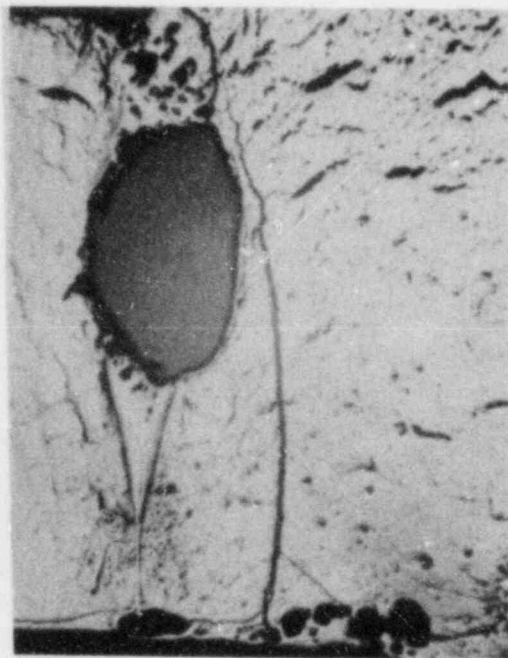


Figure 3.2. View of a Vertical Cut Through Rod 6 Near the 660 mm Cross Section Showing Pellet Bonding

uranium increasing towards each interface. To the left of the void is a two-phase bonding material that is much more porous. The two-phase material consists of a primary phase plus a eutectic constituent. The primary phase and the light eutectic phase are U-Zr oxides, the dark eutectic is aluminum oxide. In both cases, strong interaction and interpenetration of the fuel and interpellet materials is evident at the interfaces, providing excellent bonding.

Figure 3.1 also shows cross sections of the experiment taken at six different axial locations, together with selected enlargements at points of interest. These are described briefly below. Diagrams of each of these cross sections, with rod numbers, are shown in Figure 3.3. The location of the origin of the axial locations shown in Figure 3.1 is 167 mm below the bottom of the 500 mm-long fissile zone of the fuel.

The uppermost cross section, designated "660 mm" is located very near the upper end of the fueled section of the bundle. Only eight of the original nine fuel rods are present. The fuel pellets in the cross section are laterally displaced by significant distances from their original locations. Significant reduction of the diameters of the pellets has occurred, as well as local erosive losses. Some of the pellets show regions with obvious increases in porosity representing significant changes from the original UO_2 density.

The cladding shells present, show complete oxidation, thinning, local erosive losses, and reduced curvature. Pieces of oxidized cladding not easily associated with particular pellets are also present. Only about three-quarters of the peripheral lengths of cladding originally present remain in this cross section. Material near the center of the cross section which is neither cladding nor pellet material appears to fuse two cladding remnants together. The remainder of the cross section is void and there is no evidence of the ninth fuel rod. Some darkening and erosion of the low density zirconia shroud is present, together with small deposits of other material from the bundle.

The nine pellets in the 550 mm cross section (located 110 mm below the 660 mm cross section) also are significantly displaced from their original locations, have reduced diameters, and show local erosive losses. However, there is no evidence of regions of large porosity increase within pellets. Even less of the original cladding is evident in this cross section, and what remains shows complete oxidation, thinning, local erosive loss, and reduced curvature. Some added material is present on the exterior surfaces of the oxidized cladding, as well as between pellets and cladding. The zirconia shroud has picked up some foreign material and is slightly eroded.

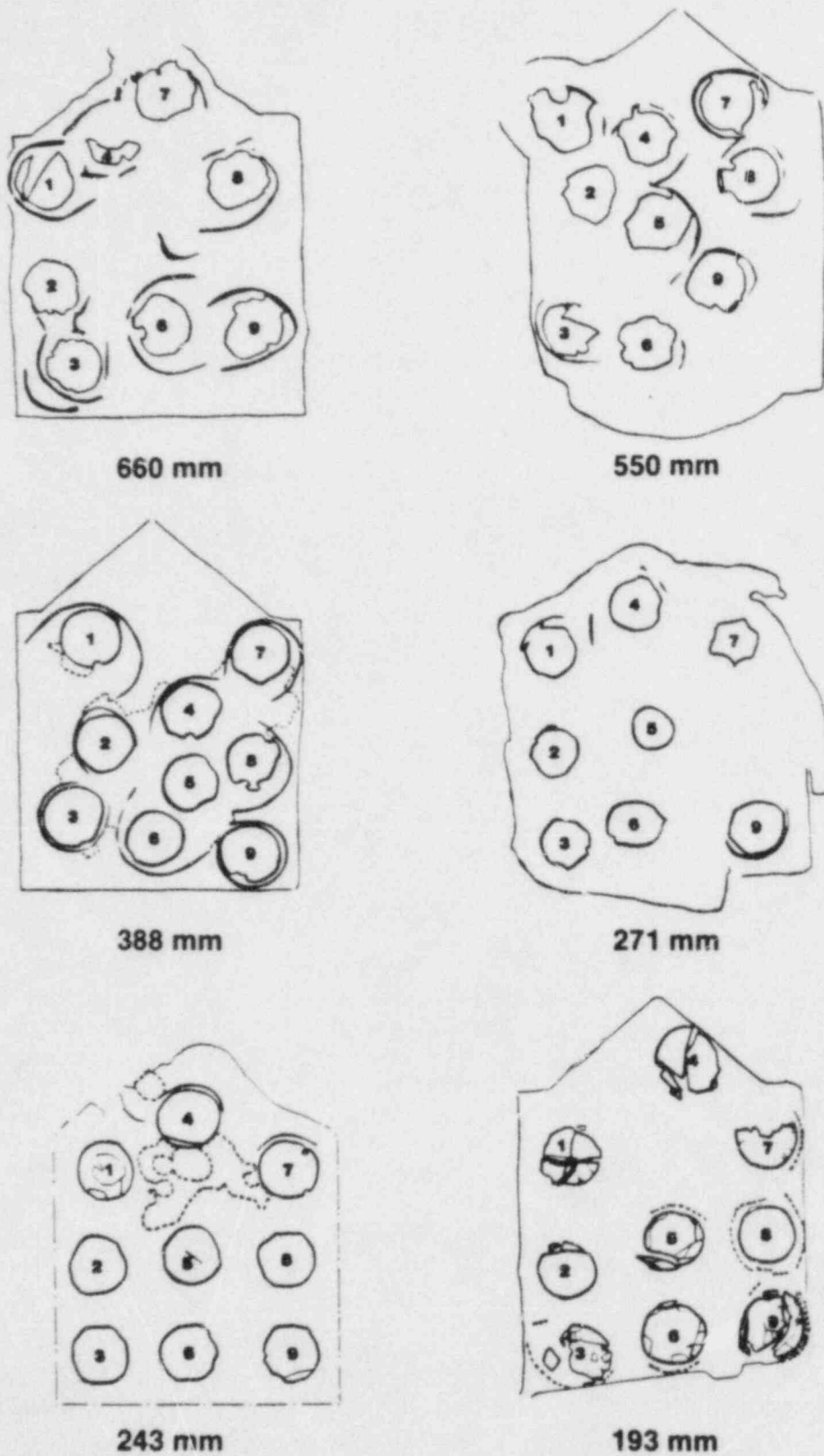


Figure 3.3. Cross Section Diagrams of the Experiment, Taken at Six Different Axial Locations

The cross section at 388 mm, about 200 mm above the bottom of the fissile zone, shows seven of the nine rods fused into a "foamy" mass of an oxidized uranium-zirconium-bearing mixture that has flowed into this zone and solidified. The fuel pellets, which are easily distinguished from the other materials, show reduced diameters and local erosive losses, but contain no regions of increased porosity. Only about 70 percent of the peripheral lengths of cladding originally present remain. All the materials here are fully oxidized, except for some small metallic inclusions visible at higher magnifications. The cladding remnants show general thinning, local erosive loss, and reduced curvature. The zirconia shroud is essentially undisturbed.

The 271-mm cross section is cut through the low-density zone of the large blockage in the lower part of the bundle. It is void except for fuel pellets representing eight of the nine original fuel rods, and a few cladding shells and shards.

Erosion from the surfaces of the fuel pellets in this cross section is greater than for any other posttest cross section, averaging slightly more than 30 percent for the eight rods present. Two rods have lost nearly 50 percent of their original volume. Very little of the original cladding is present; all is oxidized. Damage to the zirconia shroud is extensive; bundle materials have eroded and penetrated the shroud.

The cross section at 243 mm characterizes the dense portion of the globular blockage formed in the lower quarter of the rod bundle. The Inconel-718 grid spacer (Figure 3.2) that originally was present in this cross section has melted and resolidified as large globules among the rods. One of the optical micrographs shows that the interaction between the rod 1 fuel pellet and the molten grid spacer has resulted in interpenetration of the materials. In addition to the metallic material, the interpellet regions contain large quantities of oxidized U + Zr material. The cladding remnants are completely oxidized, their microscopic appearance is shown in Figure 3.1. There has been very little erosion of pellets or shroud. The latter has, however, been damaged by penetration of foreign materials.

The 193-mm cross section represents the lowest cut through the bundle. A large amount of liquid material has flowed into this region. Upon cooling, differential compression caused by the materials added at high temperature has resulted in extensive cracking of pellets. The added materials are all rich in zirconium. The materials between rods 5, 6, 8, and 9 contain oxidized phases with metallic inclusions. The optical micrograph illustrates the complexity of the phases present. Figure 3.4 shows a detail of the partially oxidized cladding between rod 9 and the shroud.

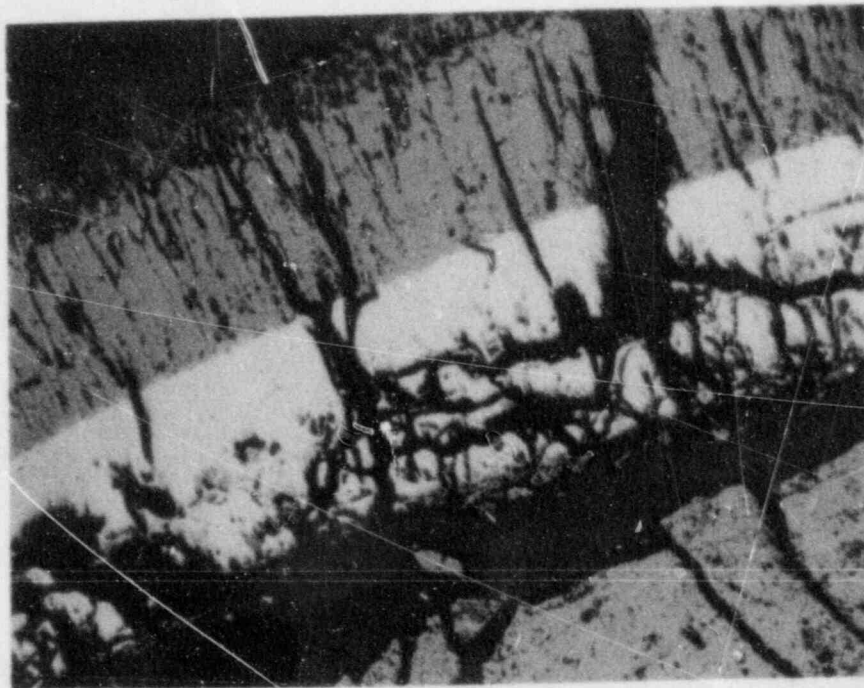


Figure 3.4. Detail of Cladding to the Right of Rod 9 in the 193 mm Cross Section. The outer (darker) zone is oxidized to ZrO_2 while the inner (lighter) zone is oxygen stabilized alpha-phase. The volumetric expansion seen is consistent with the inner zone having an oxygen content close to 30%. The cracked material in the lower right is the pellet of Rod 9.

3.2 ACRR LWR Degraded Core Coolability

(A. W. Reed, 6425; K. R. Boldt, 6421; T. R. Schmidt, 6421)

The LWR Degraded Core Coolability (DCC) Program investigated the coolability of damaged core debris in water. The debris is fission heated in the ACRR to simulate the decay heat expected in an LWR severe core damage accident. The governing phenomenological uncertainties being investigated are pressure effects, deep bed behavior, particle size distributions, stratified beds, bottom coolant feed, and material effects. Each DCC experiment will determine the coolability in three thermal regimes: (1) convection/boiling, (2) dryout, and (3) extended dryout. The staff is using experimental results to confirm and/or modify the present analytical models used to predict degraded core coolability.

The purpose of the DCC-3 experiment is to determine the effects of particle stratification and liquid injection on the dryout heat flux of an internally heated particulate bed. In order that these effects be clearly evident, the following considerations have been followed in the design:

1. The effect of channeling should be minimal on the dryout heat flux.
2. The stratification interface should remain unchanged during the experiment.
3. The difference between the dryout flux of the chosen stratified bed and a bed of equal height but composed of the smaller particle diameter must be at least an order of magnitude.
4. The dryout flux for the chosen bed must increase at least an order of magnitude over the range of water injection rates.

3.2.1 Design

In order to demonstrate the effect of particle stratification upon dryout, the DCC-3 particle bed will have a thick layer of large particles covered by a thin layer of smaller particles. The greater the ratio between the thicknesses, the more pronounced the effect of stratification. A practical limit is reached when channels penetrate a significant portion of the top layer. The channels moderate the effect of the small particles, and, should they penetrate the top layer completely, will virtually eliminate the influence of the top layer. A balance of the tradeoffs indicates that the ratio of the top and bottom thicknesses should be about one to four, and that the channels should be less than or equal to 0.1 of the top layer thickness. Since the total bed height will be 0.5 m, the top layer will be 0.1 m. If

the channels are to be less than 10 mm, the particle diameter of the top layer must be no less than about 1 mm. For DCC-3, the particle diameter of the top layer will be 1.25 mm.

The sizing of the particle diameter in the lower layer is based on similar reasoning. The greater the ratio between the lower and upper particle diameters, the more pronounced the effect of stratification. Physical constraints limit the magnitude of this ratio. In order to guarantee that the lower bed can be considered a continuum, the particle diameter should be no more than one-twentieth of the bed diameter. For the DCC-3 experiment, this places an upper bound of 5 mm for the lower particle diameter.

Another consideration in the particle sizing is the stability of the stratification interface. If the particle diameter ratio is too large, the smaller particles may slip into the interstices between the larger particles creating a bed whose properties are unknown. Furthermore, this process could be a dynamic one in which the configuration of the bed evolves during the experiments. Such a process would make the results of the experiment difficult to interpret. It is therefore imperative that the stratification interface be stable in DCC-3.

The only information that exists about interface stability comes from the experiments at Winfrith.³⁻¹ In these experiments, a layer of 4.0-mm spheres was covered by a layer of 1.2-mm spheres to form an electrically heated particulate bed. The thickness of the top layer was varied to determine the corresponding variation in dryout heat flux. The authors reported that the interface between the two layers was stable for top layer thicknesses greater than 20 mm. For thicknesses less than this mixing of the particles at the interface took place, causing some of the larger particles to migrate to the top of the bed.

The particle circulation was caused by the channels coming close to the layer interface. In the region of the channels, the solid matrix is in a spherical state of stress. The upward migration of the large particles is consistent with this stress state. Regardless of the validity of this speculation, the Winfrith experiments indicate that if the particle diameters are kept in the range of 1.2 mm and 4.0 mm, and the upper layer depth greater than 20 mm, the interface can be expected to remain unchanged throughout the experiment. Therefore, we have chosen the lower particle diameter to be 5.0 mm. This choice has the additional advantage of making the Winfrith data and the DCC-3 data roughly comparable.

To see if this bed configuration will yield adequate evidence of bed stratification and liquid injection, Ron

Lipinski's one-dimensional code, DEBRIS, was used to predict dryout fluxes. A porosity of 0.4 was assumed along with a shape factor of 0.78 for the particle diameter. The results of these calculations are shown in Figures 3.5 through 3.9 for saturation temperatures of 100°C, 150°C, 200°C, 250°C, and 285°C respectively. Plots for dryout heat flux as a function of water injection flux are plotted for two bed configurations. (A dryout flux of 10^6 W/m² is equivalent to 3.14 W/g for this bed depth.) The bottom curve is the predicted dryout flux for the proposed DCC-3 stratified bed. The upper curve is the predicted dryout for a bed of the same height composed only of 1.25-mm particles (shape factor = 0.78). At 1 atm without water injection, the ratio of the dryout fluxes is about 20. This ratio increases to about 26 at a saturation temperature of 285°C. The proposed design is predicted to yield ample evidence of stratification.

Figures 3.5 through 3.9 also contain some interesting information about the nature of bed dryouts with liquid injection. As the injection rate increases, the ratio between the two dryout fluxes decreases. At a sufficiently high injection rate, the two dryout fluxes become the same. To understand this, one must understand the implications of the saturation profile of a volumetrically heated boiling bed (Figure 3.10). Starting from the base of the channels and going downward, the saturation decreases, comes to a minimum, and then recovers. The point where the saturation reaches a minimum is the "pinch point" of the flow. This is the location where, at incipient dryout, the liquid body forces cannot overcome the adverse pressure gradient of the vapor. Upon dryout, all parts of the bed below this point dry out.

In a homogeneous bed, liquid injection serves to raise the location of the pinch point. That is to say, as the liquid injection is increased, the pinch point is raised closer to the surface of the bed (Figure 3.10). The same holds true in a stratified bed, except that the pinch point is strongly controlled by the interface (Figure 3.11). Requiring continuity of pressure across the stratification interface for both the liquid and vapor phases causes a discontinuity in the saturation.³⁻² This dramatic decrease in saturation is the direct cause of the dramatic drop in dryout heat flux. The saturation at the pinch point, and the corresponding critical vapor flux at this point, are much lower than they would be in the absence of the stratification. The effect of liquid injection upon the location of the pinch point is nevertheless the same as that for the homogeneous bed. As the injection rate is increased, the pinch point is raised closer to, and is eventually located at the interface. If the injection rate is increased further, the pinch point is moved above the interface, and become insensitive to the jump conditions imposed at the interface. At

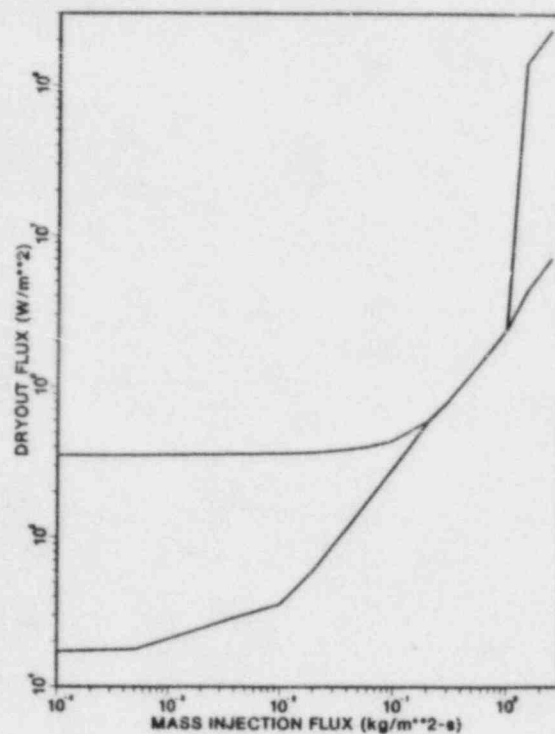


Figure 3.5. Predicted DCC-3 Fluxes (100°C)

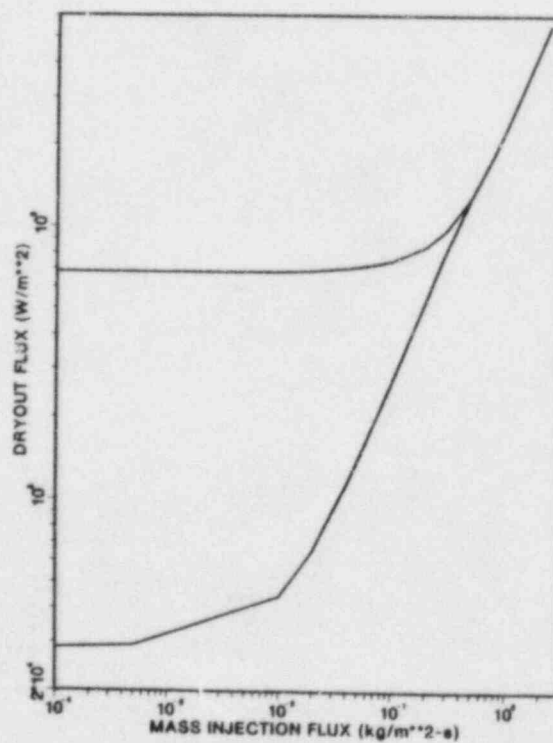


Figure 3.6. Predicted DCC-3 Fluxes (150°C)

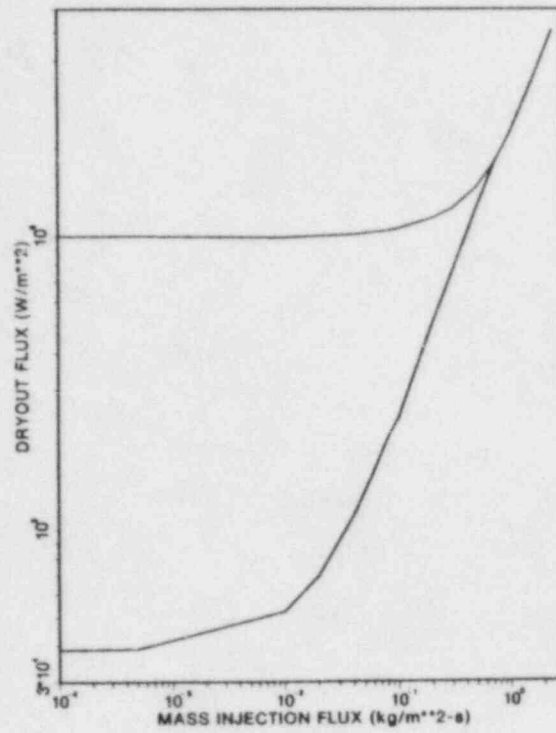


Figure 3.7. Predicted DCC-3 Fluxes (200°C)

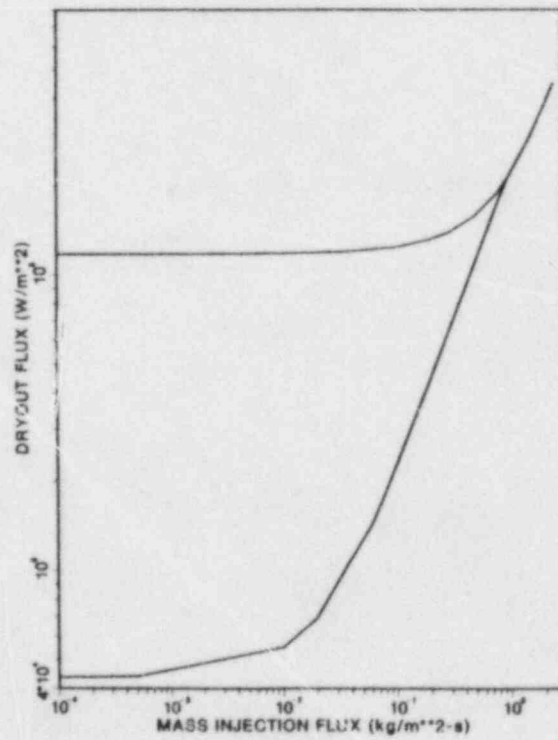


Figure 3.8. Predicted DCC-3 Fluxes (250°C)

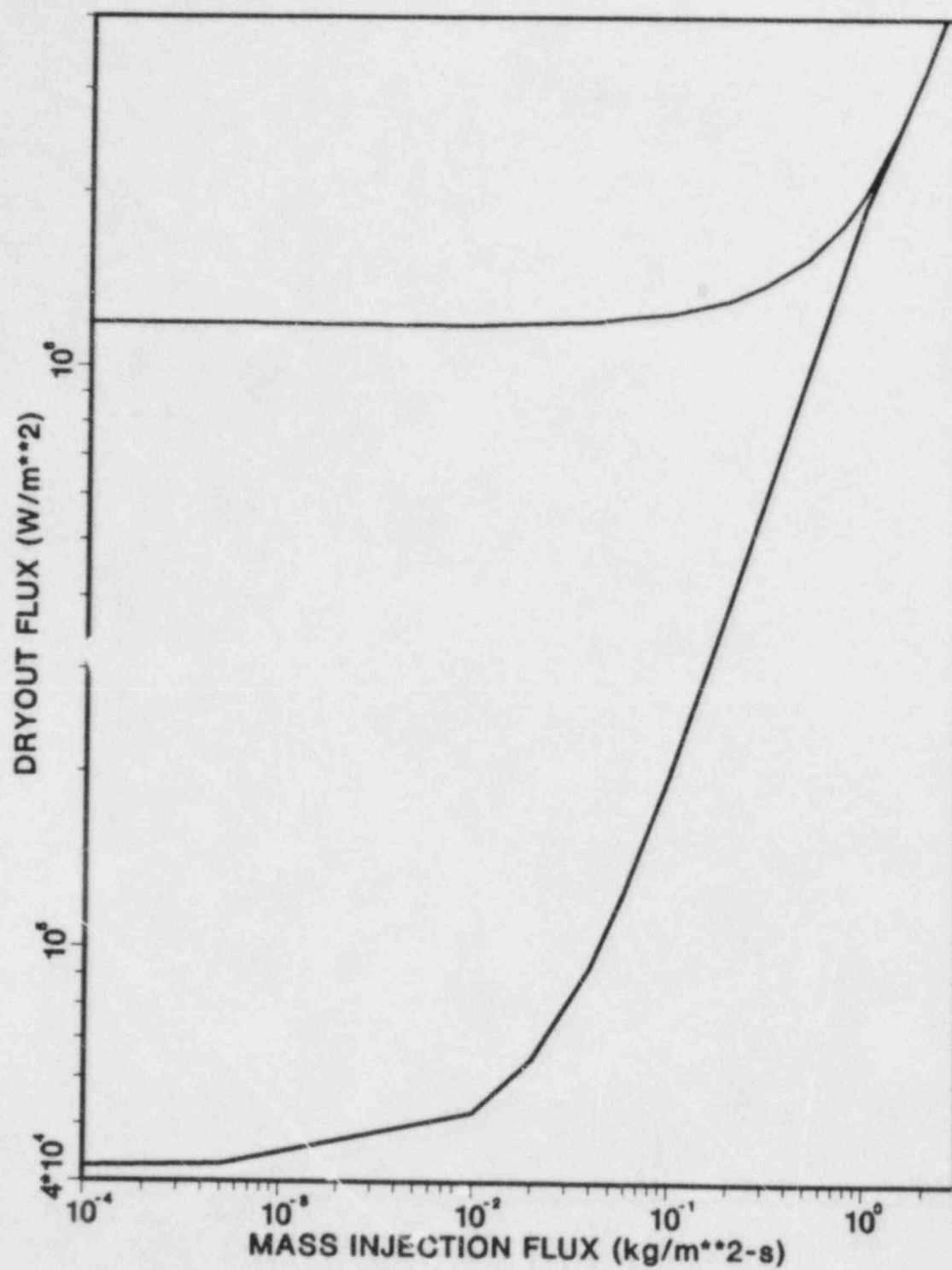


Figure 3.9. Predicted DCC-3 Fluxes (285°C)

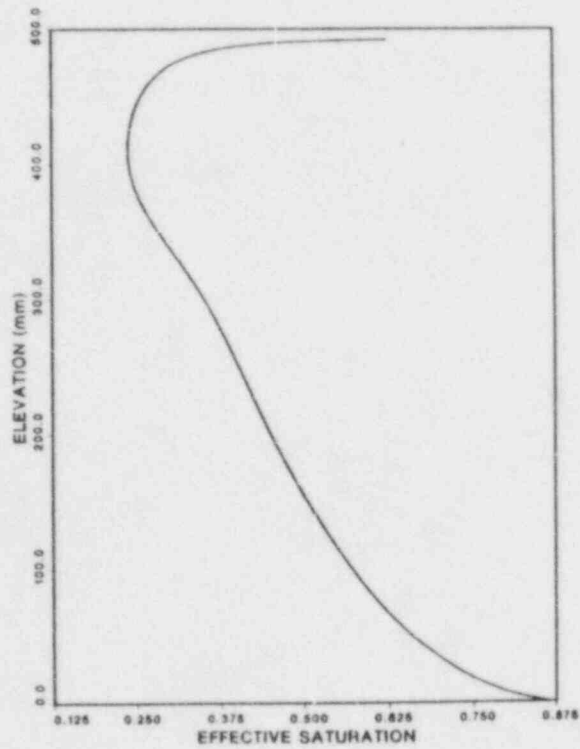


Figure 3.10. Saturation Profile for a Homogeneous Bed

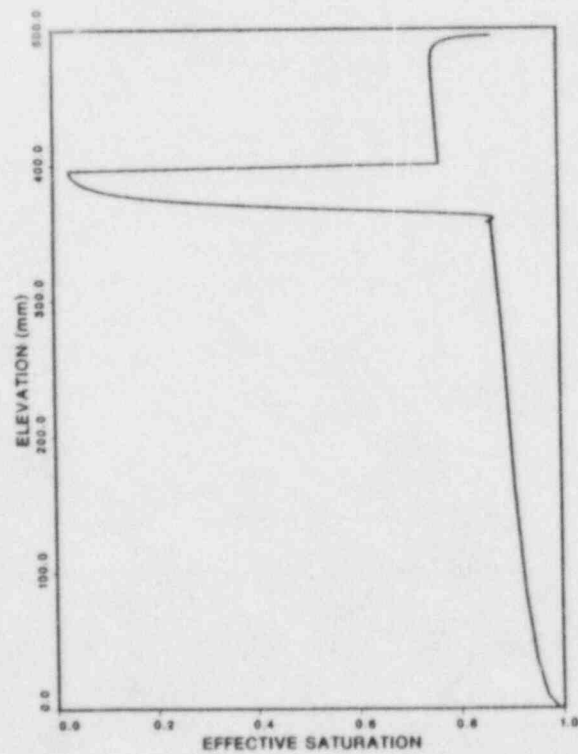


Figure 3.11. Saturation Profile for a Stratified Bed

this point, the dryout fluxes for the homogeneous bed and the stratified bed becomes equal. Figures 3.5 through 3.9 show that the injection rate at which this occurs increases with saturation temperature between 100°C and 285°C.

Figure 3.5 displays a characteristic not observed in the dryout curves at higher temperatures. At a water injection rate of about 1 kg/m²s, the predicted dryout flux for the homogeneous bed increases suddenly. This is directly attributable to the channeling model in the code, which allows the channels to lengthen with increasing vapor flux. In the region of the sudden increase, the model predicts very small saturations at the base of the channel, and correspondingly long channels. The dryout is predicted to occur at the base of the channels. The channel growth model, carried to this extreme is physically unreal, for the purposes of this experiment.

A similar, but far less spectacular jump in dryout flux is predicted to occur in the stratified bed at the same water injection rate. The reason that the predicted increase in dryout flux is less than that for the homogeneous bed is that the channels are limited by the interface. For the injection rates examined, the channels stop at the interface. Again, the dryout location is predicted to occur at the base of the channels. The veracity of the model for this case is not academic. If the channels do indeed extend to the interface, then the interface might become disrupted with the same sort of particle motions observed in the Winfrith experiments.³⁻¹ For this reason, it is important that high injection rates, which might cause significant channel growth, be deferred until the end of the experiment.

In order to keep the operation time of the experiment within reasonable bounds, a finite number of water injection rates must be chosen. These rates are proposed to be 0.03, 0.1, and 2.0 kg/m²s. These correspond (at 20°C) to flow rates of 0.00386, 0.0129, and 0.257 gpm and flow velocities of 0.03, 0.1, and 2.0 mm/s respectively. The first two flow rates are predicted to provide significant increases in dryout flux while keeping the pinch point below the interface. The third injection rate is predicted to cause dryout above the interface at the base of the channels. This is a very interesting regime to investigate, but the current modeling of this case may be inadequate. Additionally, channels may penetrate to the interface at this rate near 100°C causing particle mixing. For these reasons, the first two injection rates should be completely mapped over the desired pressure ranges before the third injection rate is attempted. The third injection rate should be mapped from the highest pressure to the lowest pressure, since the channel lengths increase with decreasing saturation temperature.

An analysis of dryout location indicates that care must be taken in the location of thermocouples to detect injected dryouts. Figures 3.12 through 3.15 are plots of the bottom location of the dry region (lower curve), top location of the dry region (middle curve), and channel extent (upper curve). At 100°C without water injection, the dry region extends from about the 375 mm level to the bottom. With injection (Figure 3.12), the dry region quickly collapses to a line with increasing injection rate. At a power level of 110 percent of dryout power, the dry region appears to be at least 40 mm wide and is generally close to the interface. If thermocouples are not located in this region, the dryout fluxes that we measure may be unacceptably large. It will be necessary to have several thermocouples distributed radially at this level to guarantee the global nature of the dryout. Implantation of the thermocouples may require some practice, since the zone of interest is only 10-particle-diameters thick. Care should be taken that the thermocouples do not affect the local porosity. It may be necessary to manually locate individual particles around each thermocouple.

3.2.2 Safety

Safety considerations require that temperature constraints be placed on the extended dryout experiments. During an extended dryout, a portion of the bed is depleted of water, and the urania particles increase to some temperature in excess of the saturation temperature of the water. When the power is reduced and the dry zone rewets, the urania and water come into thermal equilibrium, causing the urania to decrease in temperature, and the water to increase in temperature. This results in an increase in the vessel pressure. The experiment must be designed such that the maximum pressure during the rewet is within the design limitation. It is also desirable that a reasonable vapor volume remain at the end of such a rewet, since this provides for a margin of error in the analysis.

The design pressure of the canister is 9.65 MPa (1400 psi). The highest operating pressure will be 6.89 MPa (1000 psi). The canister will contain 25 kg of urania and will have 29.1 liters of nonsolid volume. The following analysis predicts the permissible maximum average solid temperature during the extended dryout, and the remaining vapor volume after rewet:

Let state 1 refer to the extended dryout condition, in which the water temperature $1T_{\text{sat}} = 285^\circ\text{C}$, and the solid urania is at some average temperature $1\bar{T}_s$. For the purposes of this analysis, it is assumed that the entire bed has dried out. State 2 is the quenched configuration, in which the urania and the water coexist at temperature $2T_{\text{sat}}$.

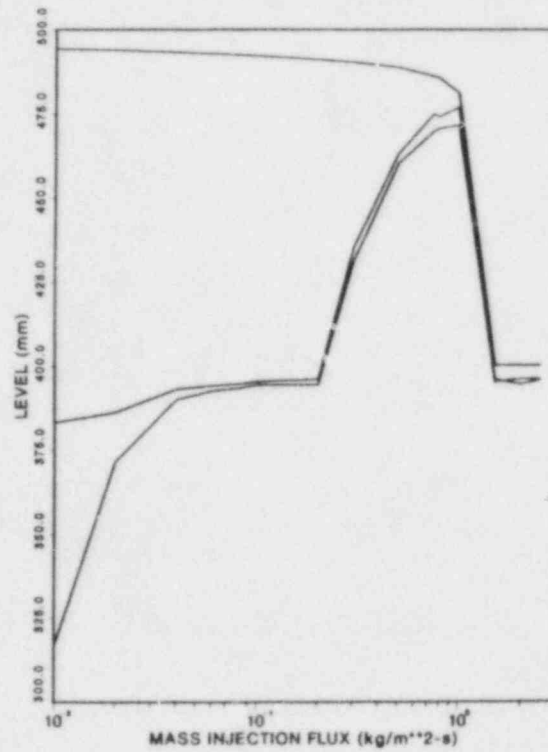


Figure 3.12. Dry Zones and Channel Lengths (1.0 DO Flux, 100°C)

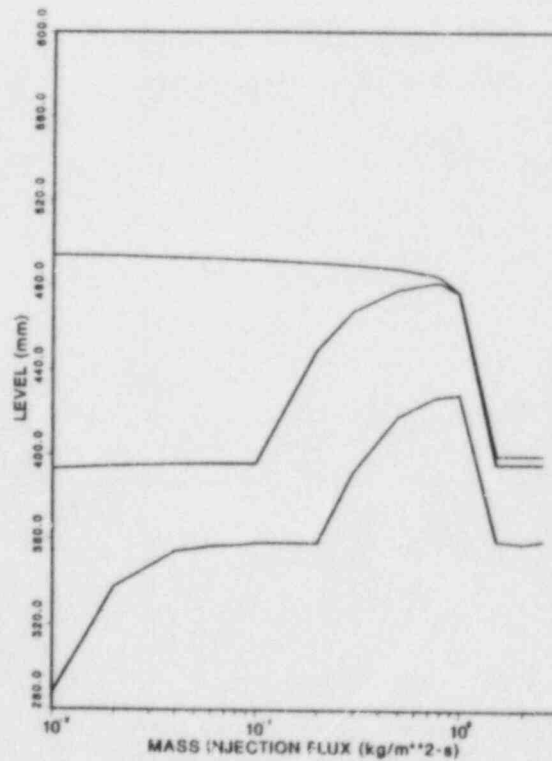


Figure 3.13. Dry Zones and Channel Lengths (1.1 DO Flux 100°C)

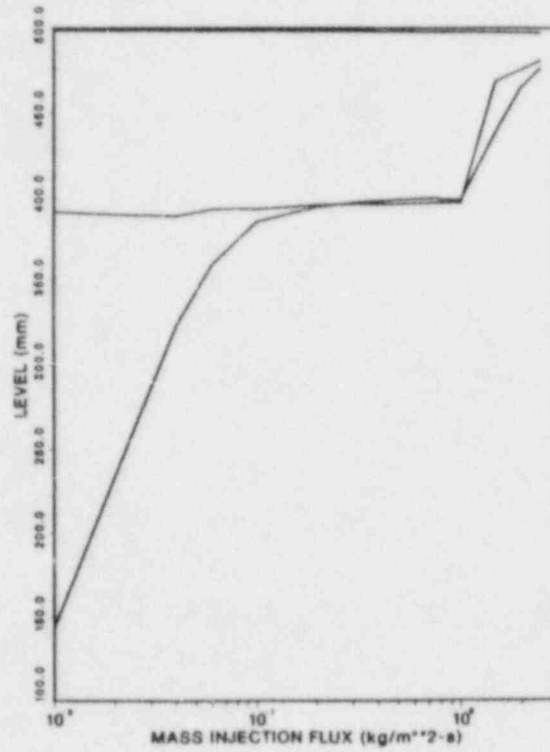


Figure 3.14. Dry Zones and Channel Lengths (1.0 DO Flux, 285°C)

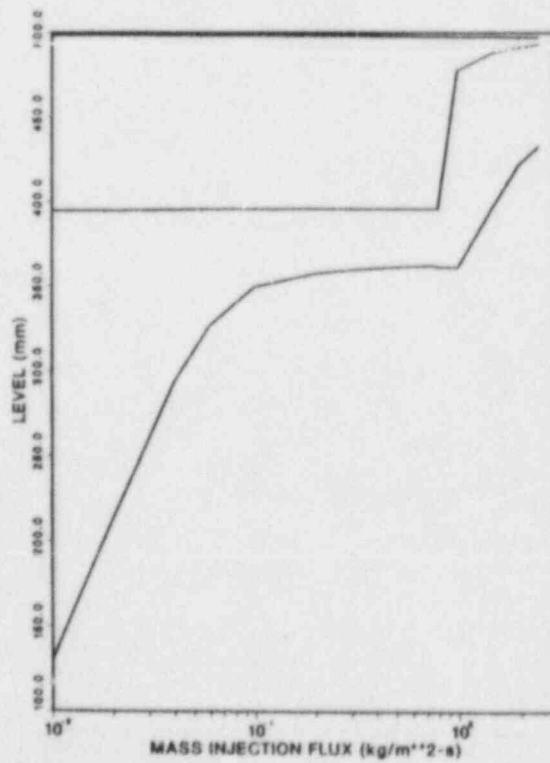


Figure 3.15. Dry Zones and Channel Lengths (1.1 DO Flux, 285°C)

By conservation of energy, and assuming a constant specific heat for the urania, the maximum allowable average temperature of the urania is

$$1\bar{T}_s = (2\bar{e}_{H_2O} - 1\bar{e}_{H_2O}) \left(\frac{M_{H_2O}}{M_s C_{p_s}} \right) + 2T_{sat} \quad (3.1)$$

The specific energies of the water can be written in terms of the qualities of the two states.

$$2\bar{e}_{H_2O} = 2e_{1,H_2O} + 2^X 2e_{1g,H_2O} \quad (3.2)$$

$$1\bar{e}_{H_2O} = 1e_{1,H_2O} + 1^X 1e_{1g,H_2O} \quad (3.3)$$

The qualities are determined by the volume constraint.

$$1^X = \frac{\frac{Vol_{free}}{M_{H_2O}} - 1^v 1_{,H_2O}}{1^v 1g_{,H_2O}} \quad (3.4)$$

$$2^X = \frac{\frac{Vol_{free}}{M_{H_2O}} - 2^v 1_{,H_2O}}{2^v 1g_{,H_2O}} \quad (3.5)$$

The vapor volume in state 2 is:

$$2^{Vol}_{vapor} = Vol_{free} - (1 - 2^X) M_{H_2O} 2^v 1_{,H_2O} \quad (3.6)$$

Results of this analysis are shown in Figures 3.16 and 3.17. The maximum allowable average urania temperature is seen to increase approximately linearly with increasing liquid inventory (Figure 3.16). The effect of changing the allowable system pressure is also displayed. The remaining vapor volume at the end of the rewet decreases linearly with increasing liquid inventory and is reasonably insensitive to

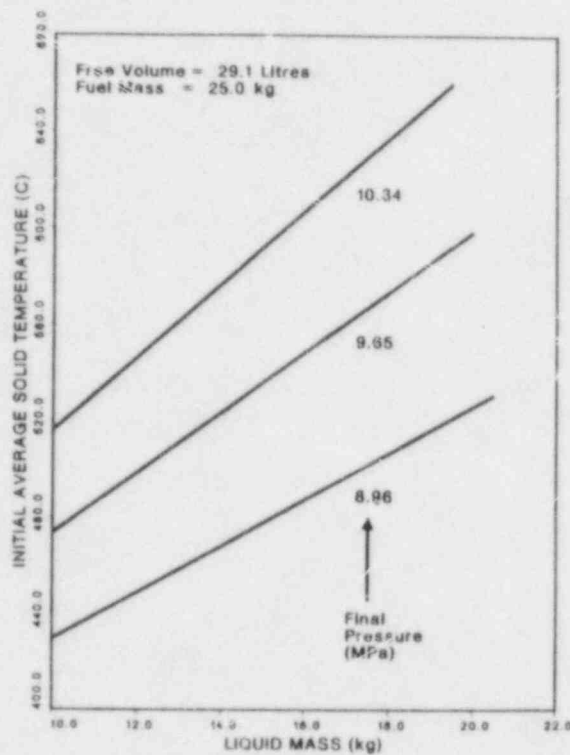


Figure 3.16. Initial Average Fuel Temperature vs. Liquid Inventory

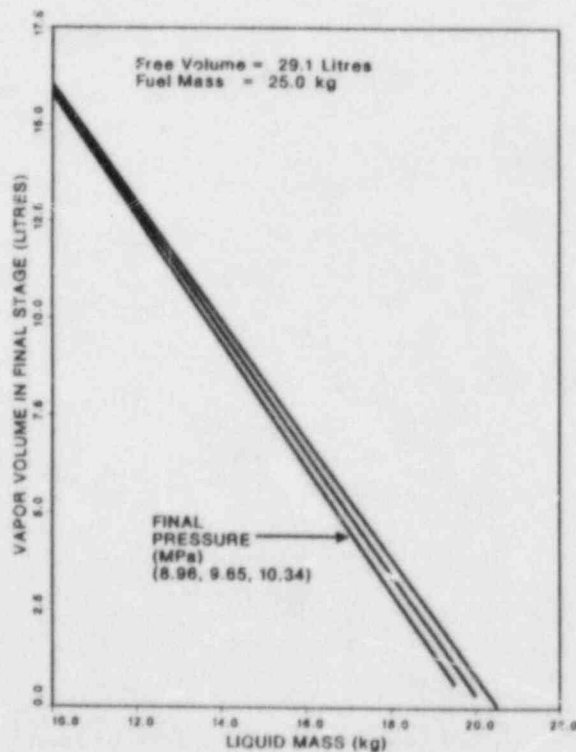


Figure 3.17. Vapor Volume After Quench

the final system pressure (Figure 3.17). If we specify that the minimum vapor volume should be 5 liters, then the maximum liquid inventory is about 17 kg. Referring back to Figure 12, this means that the allowable average urania temperature is about 560°C.

The allowable average urania temperature can be converted to a maximum fuel temperature for dryouts without water injection. Using a one-dimensional conduction analysis with temperature-dependent thermal conductivities generated by R. Lipinski's program, COND, it was found that:

$$\frac{l^{\bar{T}_s} - l^{T_{sat}}}{l^{T_{max,s}} - l^{T_{sat}}} = 0.73 \quad (3.7)$$

For $l^{T_{sat}} = 285^\circ\text{C}$, and $\bar{T}_s = 560^\circ\text{C}$, the maximum allowable fuel temperature is 662°C .

This is a lower maximum fuel temperature than used in the past, and in part reflects the lower design pressure used for DCC-3. No credit is allowed for heat transfer to the wall. This means that the analysis should be valid for the case when the injection pump is accidentally switched on during an extended dryout. A more complete safety analysis will be made at a later date to see if this maximum temperature can be extended or if the controls can be established on the pump actuation.

The maximum temperature of 662°C does not apply for injected dryouts. As observed earlier, the dry zone with injection is much smaller than without injection, and the total internal energy of the solid is correspondingly smaller. The maximum fuel temperature for injected dryouts can therefore be much larger. Predictions of this limit will be made at a later time.

3.2.3 Helium Generation

During DCC-1 and DCC-2, the fill pressure of the canister increased during the course of the experiment. This caused an increase in the lowest obtainable saturation pressure, making it impossible to obtain data below three bars. An analysis of the pressure history of DCC-2 shows that somewhere between $4.E-6$ and $1.8E-5$ kmoles of noncondensable gas per kilogram of fuel were generated during the experiment. We currently believe that this gas is helium which had diffused into the grain boundaries of the fuel during the experiment preparations. Using the measured grain diameter of $20 \mu\text{m}$, and assuming that a monolayer of helium adsorbed

on each grain surface, the estimated adsorption is about $1.E-6$ kmoles of helium per kilogram of fuel. According to Dan Sasmor (Division 6453), this should be a lower bound on the adsorption, since condensation can occur within the grain boundaries.

Dan Sasmor is currently planning to perform BET measurements of helium adsorption in urania fuel. If these tests confirm the amounts of adsorption observed in DCC-2, then the suspected source of the noncondensables will be deemed probable. The remedy involves pulling a vacuum on the canister while it is hot, and holding the vacuum until the fuel has out-gassed completely.

3.3 References

- 3-1. G. F. Stevens and R. Trenberth, "Experimental Studies of Boiling Heat Transfer and Dryout in Heat Generating Particulate Beds in Water at 1 Bar," Atomic Energy Authority, Winfrith. AEEW-R 1545, 1982.
- 3-2. J. Bear, Dynamics of Fluids in Porous Media, American Elsevier Publishing Company, Inc., New York, 1972.

4. MELT PROGRESSION PHENOMENOLOGY

(J. E. Kelly, 6425; P. J. Maudlin, 6425;
J. L. Tomkins, 6425; M. F. Young, 6425;
W. J. Camp, 6425)

The objective of this program is the development of a mechanistic computer model for the in-vessel phases of severe accidents in LWRs. This model, MELPROG, is implicitly linked with the TRAC-PF1 RCS thermal hydraulics models to provide a complete, integrated treatment of the reactor primary system from accident inception up to and through release of core materials and fission products from the reactor vessel. The model also provides materials and thermohydrodynamic input to the CONTAIN reactor containment analysis model.

MELPROG has a modular code structure consisting of a DRIVER routine and eight explicitly coupled modules. The heart of the model is a multiphase, multimaterial implicit hydrodynamics model. The original FLUIDS module (that in MELPROG/MODO) provides a one-dimensional treatment of three momentum fields: a corium field consisting of solid and/or liquid materials, a coolant field consisting of liquid water, and a vapor field consisting of steam, hydrogen, and various fission-product vapors as well as aerosols. Each momentum field has a separate velocity. Continuity equations are solved for mass and energy in each field as well. There can be as many mass continuity equations as desired.

The new FLUIDS module replaces the one-dimensional treatment in MODO with a full two-dimensional (R-Z) capability. In addition, four momentum fields are treated instead of three (the corium field is split into solid and liquid fields). This version (developed at Los Alamos National Laboratory as part of the MELPROG effort) exists currently in stand-alone form and is being incorporated into the developmental version of MELPROG. The major advantage gained through the new FLUIDS module is the ability to treat the important effects of natural circulation in the core and vessel.

The current versions of MELPROG contain a rod heatup and failure model, PINS, developed at Los Alamos National Laboratory. This module allows a detailed treatment of rod behavior up to the point of significant degradation and/or clad and fuel motion. It is anticipated that PINS will be replaced or upgraded to reflect the modeling detail being provided by the SCDAP rod behavior module currently under development at Idaho National Engineering Laboratory (INEL/EG&G). Meanwhile, PINS affords a capability to model accidents from inception.

Radiation heat transfer within the core and from the core to coolant and ex-core structures is of crucial importance to high-temperature accidents. In MELPROG, a two-dimensional radiation model is used. This model--originally developed at Los Alamos National Laboratory--treats three-dimensional structures (through 3-D view factors) within cells as diffuse, grey-body emitters and absorbers. Cell boundaries are treated as diffuse, black-body emitters and absorbers. The model has been greatly enhanced within the MELPROG project at Sandia. In particular, the radiation module now has dynamic view factors that reflect changing geometries of degrading fuel rod structures and debris/rubble beds.

Thermal and mechanical response of vessel and core structures (including the vessel wall itself) are treated by a STRUCTURES module within MELPROG. The STRUCTURES module builds up vessel components from a series of generic structural types (e.g., plates, columns, cylinders). In addition, special structure types are incorporated as needed for the various LWR designs, i.e., Westinghouse, Babcock and Wilcox (B&W), and Combustion Engineering (CE) for PWRs and General Electric (GE) for BWRs. The current (MOD0) version of MELPROG incorporates a Westinghouse PWR structure package.

The STRUCTURES module uses one- and two-dimensional heat transfer analyses for structural heatup. In addition to conduction within the structural member, radiation, convection, and conduction boundary conditions are provided by the code. Structural melting is allowed, as are plateout and refreezing of molten core materials on structural surfaces. Mechanical response is treated by analytical models for both ductile and brittle structure failure--although the latter is probably only important for steam explosion loading of the vessel and cold components.

The DEBRIS module is a finely meshed model for rubble bed formation, heatup, relocation of core materials within the bed, and attack on adjacent structures. It also treats quench of the bed by a rewet front. DEBRIS takes over control of FLUIDS variables within a FLUIDS cell after the cell has completely dried out. Materials that exit the bed are passed back to the FLUIDS module. Similarly, bed growth is controlled by a model that interfaces DEBRIS with the FLUIDS and PINS modules. Since the major core-melt processes occur in the rubblized core state, this module is of key significance in MELPROG.

The melt/water interaction model, TEXAS-II, in MELPROG is essentially a flow regime controller for situations in which corium is brought into rapid contact with liquid coolant. Coarse mixing of the corium/water mixture is controlled by the respective volume fractions of the two materials, the

respective temperatures (which in turn control film boiling dynamics), and their relative velocity. Similarly, fine melt fragmentation is controlled by hydrodynamic mechanisms based on film collapse and hydrodynamic instabilities among other candidate mechanisms. Finally, vapor generation is calculated subject to flow regime and (for explosive interactions) inertial constraints. The module provides the flow regime and heat transfer information in an interactive mode with the FLUIDS module. Both explosive interactions and rapid boiling are treated by the module. Initial development of this module is currently scheduled for FY85.

The melt ejection module consists of models for the flow regime of existing core and coolant materials as well as models for ablation of the initial failure during blowdown. The model treats low-pressure, gravity-driven slumping through the lower vessel head, high-pressure blowdown, and (eventually) ejection through steam-explosion-induced failures. This module is currently under development in a stand-alone version and is scheduled for initial incorporation into MELPROG during FY85.

The VICTORIA module in MELPROG treats release and transport of fission products in the core and vessel. It uses a detailed treatment of thermochemical equilibrium to establish equilibrium partial vapor pressures for the various fission-product molecular species in a high-pressure steam/hydrogen environment. The excess of the equilibrium vapor pressures over the existing partial pressures in the bulk overlying gas determines the local driving force for release. However, three rate limitations to release are explicitly calculated: (1) transport in the bulk fuel/clad phase, (2) Langmuir vaporization kinetics, and (3) boundary layer mass transport to the bulk gas. Chemical reactions in the gas phase are treated, as are condensation to form aerosols onto existing aerosols and onto cold structures. Aerosol transport, deposition and reentrainment are modeled, as is revaporization (due to decay heating) of condensed fission products. Finally, the partitioning of decay heat among corium, vapor, liquid, and structural fields is performed using the release and transport models.

Finally, MELPROG contains a module that provides an implicit numerical coupling between MELPROG's FLUIDS module and the RCS thermal hydraulics models. The current version, i.e., that in MOD0, couples MELPROG to the TRAC-PF1 code.

4.1 MELPROG Code Development

Work has begun on modifying each module to allow the incorporation of the 2-D FLUIDS module. In most cases, this work only involves changing the data transfer section of each module. These changes are necessary to maintain the proper

coupling with the FLUIDS module and do not affect the internal workings of the individual modules. The strategy used in making these modifications has been to write separate 1D and 2D data transfer routines for each module. The appropriate routine is then automatically invoked for each problem. This procedure allows for models to be updated in both the 1D and 2D versions simultaneously.

Documentation of the models in MELPROG has been initiated. The first version of MELPROG (MELPROG-PWR/MOD0) will be described in detail in this report. This report will form the basis of a user's manual for the code.

The VICTORIA fission-product behavior module now contains the chemistry and aerosol behavior submodules. The stand-alone version of this module is undergoing testing. The checkout of the aerosol behavior model (CONTAIN version of MAEROS) by comparisons with several sample problems has been completed.

4.2 Code Testing

In order to test the first version of MELPROG, an S₁D sequence in a Westinghouse PWR was chosen as a calculational exercise. The intent of this effort was two-fold. First, while the various modules had been tested separately, the combined code and the coupling between modules had not been fully tested. Hence, this problem served to identify and resolve inconsistencies between modules. Second, the actual reactor vessel modeling process and running of the problem required certain simplifications which have identified specific areas which require improvement. It is important to note that the current calculation, while complex in itself, contains numerous modeling simplifications and, hence, the calculational results must be viewed as a demonstration exercise and not a quantitative assessment of this accident sequence.

In performing this simulation, the link to TRAC-PF1 was not utilized in order to avoid unnecessary complications. Instead, the RCS was represented by a set of upper plenum pressure, liquid fraction, and temperature boundary conditions obtained from a RELAP5 calculation of this accident.⁴⁻¹ A simulated flow coastdown was used for the lower boundary condition. These simplifications have repercussions on the details of the calculated sequence, since no active feedback to the RCS hydraulics from in-vessel processes is included. However, the use of these boundary conditions presents no limitations on the exercise of individual modules, nor on the overall code itself. Since the exercise was in the nature of a code demonstration and evaluation, these simple boundary conditions were felt to be sufficient.

The S₁D sequence involves a high pressure blowdown through a 66-102 mm diameter break with scram and pump trip. The upper plenum pressure behavior can be characterized as a sharp drop to saturation pressure over about a 50 s time span followed by continuous steam generation and slow pressure drop as water flashes out of the reactor. It was necessary to simulate voiding of the upper plenum by linearly decreasing the liquid fraction at the upper plenum boundary to zero in about 80 s. This rate of voiding will have some influence on the timing of events during the accident sequence.

With these boundary and initial conditions, the calculation was run from initiation through vessel failure. MELPROG was able to calculate, among other things, the core heatup, cladding oxidation, core slumping, debris formation and meltdown, grid plate heatup and failure, debris-coolant interactions, and finally vessel heatup and failure.

Overall, the performance of the modules in MELPROG for this S₁D test problem calculation demonstrated that the current code contains most of the features necessary to calculate a meltdown progression. The code is able to analyze, in an integrated manner, the important in-vessel phenomena anticipated for this accident sequence with the exception of fission-product release and transport, which is currently being added. The code performed largely as designed for this test problem. The timing of events as well as the interaction of the various modules seemed to be consistent. While the simplifications in the modeling of the reactor core and vessel mean that this particular calculation is not a best estimate, it should be clear, that the major components for a best-estimate calculation currently exist in the code.

4.3 Code Applications

Work has continued on the Surry TMLB' calculational sequence. In this problem, the stand-alone mode of MELPROG is being used for the initial calculation. The problem uses simplified boundary conditions, similar to the approach taken in the S₁D Zion calculation. However, the noding is much more extensive; in particular, the problem mesh includes the upper plenum region. Also, several features of the TMLB' sequence related to the water level in down comer being simulated via boundary conditions.

The steady-state calculation has been completed and the transient calculation was initiated. The problem was run to the point of fuel rod failure. At this point, the calculation was stopped, because the code needed to be reoverlaid to accommodate the new 2-D FLUIDS module. Once this reoverlaid work is complete, the calculation will be continued.

4.4 Reference

- 4-1. S. M. Modro et al., Proceedings of the International Meeting on Thermal Reactor Safety, Chicago, Il., NUREG/CR-0027, Vol. 2, p. 839, 1982.

5. ADVANCED REACTOR ACCIDENT ENERGETICS

The Advanced Reactor Accident Energetics Program addresses the key issues in an LMFBR core-disruptive event that determine the progression and severity of the accident. This program involves a series of in-pile experiments and analyses that focus on key phenomena in two general areas:

- a. Initiation Phase--Fuel/Clad Dispersal Experiments
- b. Transition Phase--Fuel Freezing and Streaming Experiments.

5.1 Initiation Phase

S. A. Wright, 6423; P. S. Pickard, 6423; P. Henkel, 6423; G. Schumaker, 6423)

The Sandia Fuel Dynamics Program provides needed experimental data and analysis for the initiation phase of an LMFBR core-disruptive accident. The motion of clad and fuel in the initiation phase of an LOF accident is an important consideration in the subsequent progression of the accident. Early fuel dispersal can lead to neutronic termination while limited dispersal and blockage formation continues the accident into the transition phase and the possibility of further neutronic activity.

To obtain data on the important phenomena involved in this phase of an LMFBR accident, the USNRC is sponsoring the Sandia Transient Axial Relocation (STAR) experiments in the ACRR test facility. Kernforschungszentrum Karlsruhe (KfK), FRG is cosponsor of this program.

5.1.1 Cladding Entrainment Criterion for the SANDPIN/CMOT Code

The clad motion model in SANDPIN/CMOT includes both an annular film flow model and a dispersed drop flow model. The film flow model was described in detail in an earlier quarterly report.⁵⁻¹ This report describes the entrainment criterion that is used in the dispersed drop flow model. It also presents the results of this model when applied to the STAR-1 experiment.

Significant amounts of drop entrainment were seen in the two fresh fuel experiments STAR-1 and 2. In both experiments it is estimated that 60 to 75 percent of the cladding was entrained at some time. The majority of the entrained cladding (50 to 75 percent) had radial velocities large enough to cause the entrained drop to hit the quartz tube. The remainder of the entrained cladding moved axially up the channel at relatively high velocities (4 to 6 m/s).

In the STAR-1 experiment more entrainment occurred near the top of the fissile fuel length than at the bottom. This was probably due to the higher gas velocities at this location. Typical inlet gas velocities and densities were 40 m/s and 1.0 g/m³, while the exit properties were 80 m/s and 0.5 g/m³. These observations led up to believe that entrainment is caused by radial pressure gradients applying a suction force on the drop, which is countered by adhesion forces. If the suction is greater than the adhesion forces, then the whole drop is entrained. This situation is illustrated in Figure 5.1 for a drop on fuel.

The gas flow around a drop reduced the pressure, P_g , in the flow channel. This underpressure causes a force which acts against the surface tension adhesion force. Entrainment of the drop occurs if

$$A_g(P_{\text{drop}} - P_g) > F_{\text{adhesion}} \quad (5.1)$$

where A_g is the contact area between the drop and the gas phase, and $\Delta P = P_{\text{drop}} - P_g$ is the suction. This formalism results in the following entrainment criterion for a liquid cladding drop on a flat surface of UO_2 .

$$\rho(v_g - c)^2 h f_{\text{corr}} > 8 \sin^2(\alpha) \sigma_{l,g} \quad : \quad \text{drop on fuel} \quad (5.2)$$

In these equations h represents the drop height, α is the contact angle, $\sigma_{l,g}$ is the liquid gas surface tension, and f_{corr} is a correction factor given below.

$$f_{\text{corr}} = 0.4 \left(\frac{d_h}{2l_w} \right)^{-0.627} \times \text{Re}_g^{0.229} \quad (5.3)$$

In this equation d_h is the hydraulic diameter of the flow channel, Re is the Reynolds number $(\rho v_g d_h / \mu)$, and l_w is taken as twice the drop diameter. This formalism results in the entrainment criterion presented in Figure 5.2 (see Henkel⁵⁻² for details). For comparison purposes, Ishii's⁵⁻³ film entrainment criterion is also plotted in the same figure. The curves in this figure assume a sodium vapor pressure of 2.5 bar, a liquid film thickness of 0.38 mm, and a drop height and contact angle of 1.4 mm and 106°, respectively.

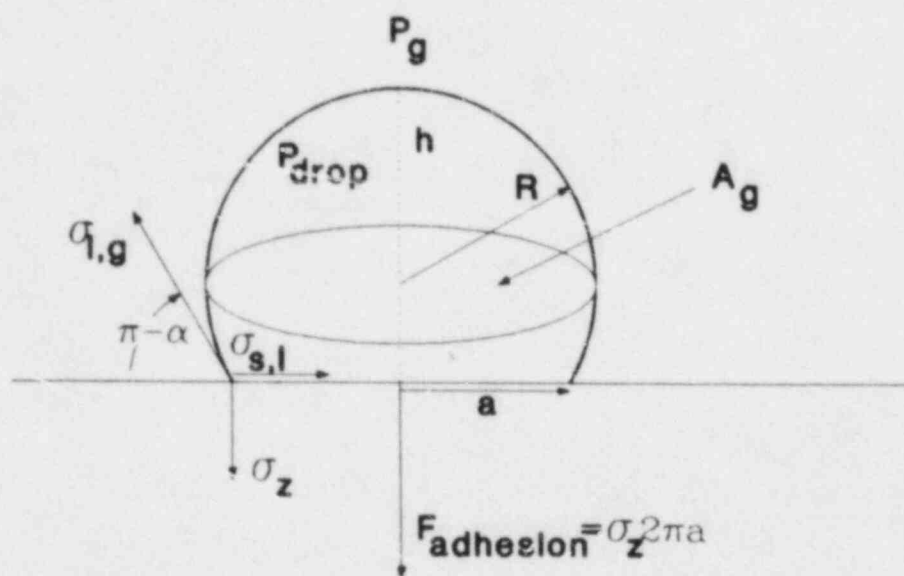


Figure S.1. Entrainment Forces for a Liquid Cladding Drop on a Flat Surface of UO_2

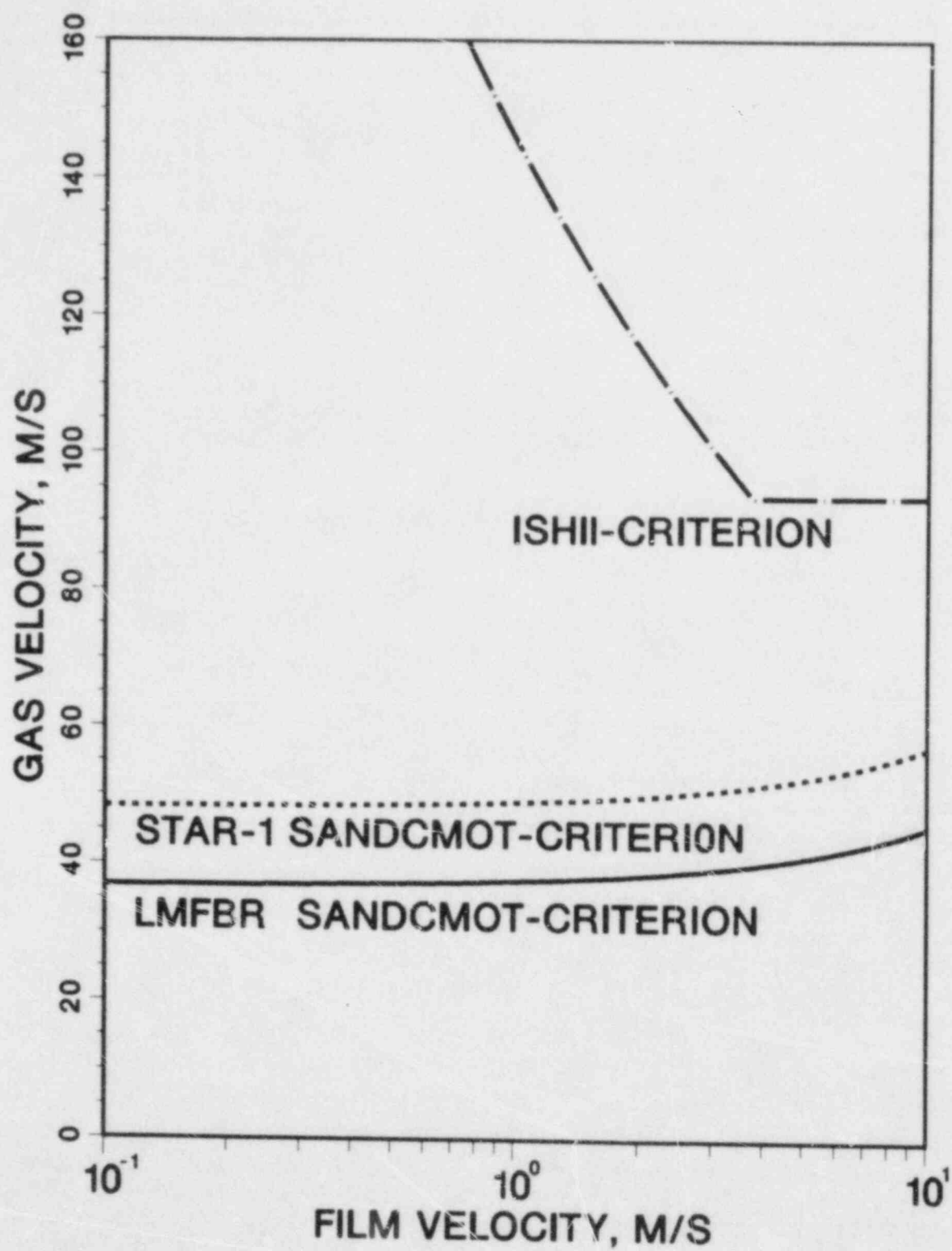


Figure 5.2. Liquid Cladding Entrainment Criterion Used in SANDCMOT Compared to Ishii's Criterion

The Henkel entrainment criterion is more easily satisfied than Ishii's model. It is also more closely related to the observed type of clad motion than is the film flow model of Ishii's, since it is based on entraining a drop of molten cladding which is flowing on either solid UO_2 or cladding. This situation naturally occurs because of the nonwetting behavior of molten cladding on UO_2 . Typical gas velocities required to produce entrainment are low, (approximately 50 m/s), compared to expected sodium vapor velocities (80 m/s). Since sodium vapor velocities may easily reach 80 to 100 m/s during the clad motion phase of an accident scenario, entrainment must be considered the rule rather than the exception. These results suggest that clad motion models should include a dispersed droplet flow regime (with mm-sized drops) as well as a film flow model. For these reasons the clad motion model used in the SANDPIN/CMOT code are both a film-like model and a dispersed drop model.

5.1.2 STAR-1 Clad Motion Results with Entrainment

The modeling of clad motion relies heavily on the modified SANDPIN code.⁵⁻⁴ The SANDPIN code was originally developed for the Fuel Disruption program to model transient thermodynamics and fission gas behavior. The code was developed by Peter K. Mast as an outgrowth of the LAFM code and includes the fission gas phenomenology that was previously developed by Worledge, Briscoe, Ostensen, and Fischer to include fission gas behavior.⁵⁻⁵ through 5-8 The most recent extension includes the coupling of the clad motion model CMOT to SANDPIN.⁵⁻⁹ CMOT was developed at KfK and extended by Henkel to treat the clad behavior seen in the STAR experiments. The code contains a film model and a dispersed droplet model. It is also capable of treating multipin bundles with several coolant and cladding flow regions. The gas flow and clad motion are tightly coupled through the nonstationary continuity, momentum, and energy equations. The overall characteristics of the calculated clad motion, such as the start and end times of motion, the general direction and velocity of motion, and the extent of blockage formation generally agree quite well with the observations.

The calculated clad motion results for the STAR-1 experiment are presented in Figure 5.3 at 0.1 s intervals. The diagonally shaded lines indicate fuel, the cross-hatched shading represents cladding that is solid (either never molten or resolidified), and the black sections are cladding that is molten and moveable (temperatures above $T_{\text{liquidus}} + T_{\text{super}}$). The black cladding rectangles in the coolant channel were entrained drops. In this figure the clad distribution is azimuthally symmetric.

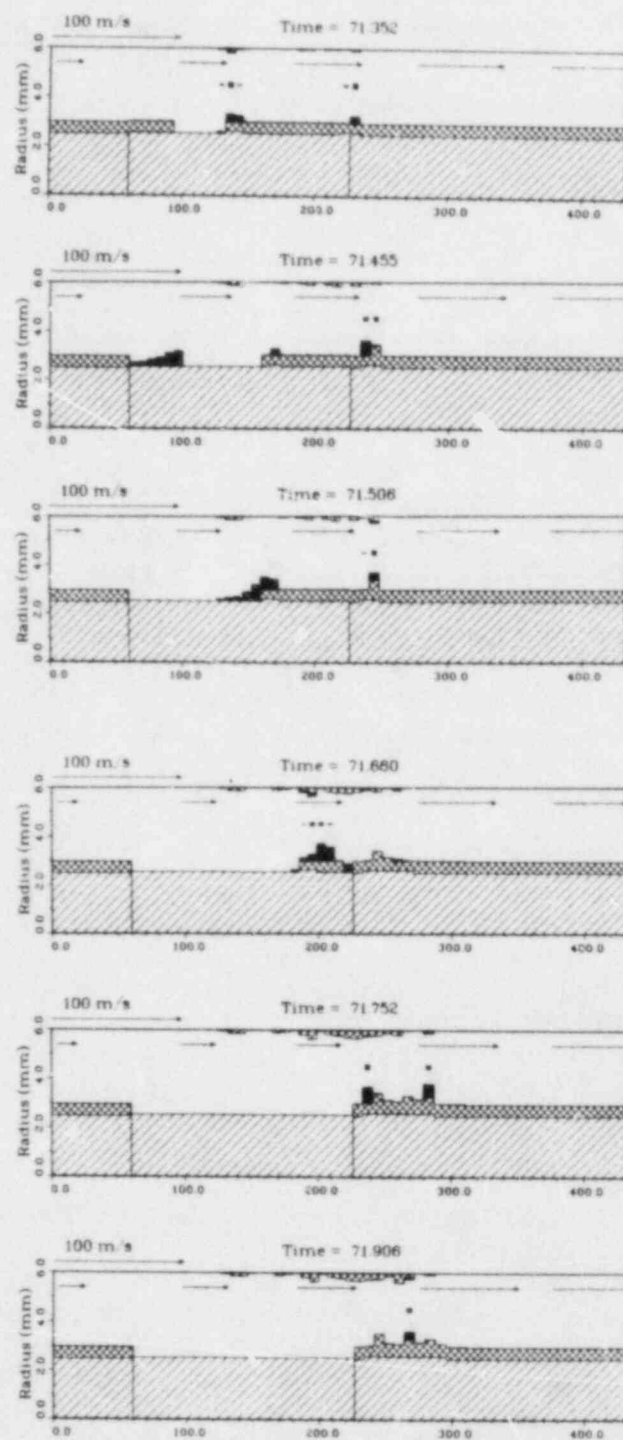


Figure 5.3. SANDPIN/CMOT Calculated Clad Motion With Entrainment for STAR-1. The diagonal shading is fuel, either fissile or fertile, the cross-hatched shading is solid cladding, and the solid shading is liquid cladding.

The calculated time of significant clad motion begins at 71.3 s compared with the observed time of 71.28 s. The motion begins as the film (shown on the figure as a film, but modeled as drops on either fuel or still intact cladding) moves upwards at 0.5 to 1.0 m/s while the entrained drops move at higher velocities (3 to 4 m/s) film. Significant entrainment is predicted, and most of the entrained drops freeze quickly on the quartz tubing. This is seen in the figures by the build-up of solid cladding on the outer boundary. As the cladding moves upwards, it freezes when it reaches the blanket region. A partial blockage with length 4 to 6 cm is predicted to form at 71.85 s, which is within 100 ms of the actual blockage formation time. All of the clad has relocated by this time and no further clad motion is then predicted.

The overall clad motion predicted by SANDPIN/CMOT is in good agreement with the observed motion. In fact, a movie of the predicted clad motion was made, and the agreement is striking. Naturally, the calculated motion does not describe the specific details, but the important trends such as the onset of motion, the mass flux, the direction of motion, and the duration of the motion are accurately predicted.

5.2 Transition Phase

(R. O. Gauntt, 6423; P. S. Pickard, 6423; A. Furutani, 6423)

Many current heterogeneous core designs are characterized by relatively low-sodium void coefficient and incoherent behavior in the initiation phase. These features generally increase the likelihood of a "transition" or "meltout" phase during a core-disruptive accident. The key questions in the transition phase, highlighted in the CRBR safety review, are whether fuel or clad blockages form, leading to a confined or "bottled" core configuration, and the behavior and reactivity implication of this pool of fuel-steel in the core region of the fuel blockages do lead to this state.

The TRAN program addresses the question of fuel-inventory reduction by penetration into the upper core structure and through subassembly (S/A) gaps to the lower core structure. If deep penetrations occur, nonenergetic shutdown is probable while shallow penetration will lead to a transition phase and the possibility of further energetics. First-of-a-kind in-pile experiments, sponsored jointly by the USNRC and the Japanese Power Reactor and Nuclear Fuel Development Corporation (PNC), are being conducted to provide data to evaluate the various models describing fuel penetration.

Current B-Series efforts are focused upon preparing the multipin flow channel experiments, B-4 and B-5. Precalculations for these experiments are being performed with assembly to take place in November 1984. Redesign of the

GAP series fuel melting section is underway with the goal of substantially decreasing the size of the ACRS double pulse, which is necessary to generate a fuel melt with sufficient superheat above the liquidus point. This appears possible through decreasing parasitic neutron absorption and increasing neutron thermalization, at the expense of decreasing somewhat the mass of fuel to be melted. Other GAP package design changes have been implemented that render the GAP geometry more amenable to analytical characterization. Consideration is being given to the possible ways in which the SIMMER-II code may be exercised in the evaluation of the remaining TRAN experiments, in particular, B-4 and B-5.

5.2.1 TRAN B-Series

TRAN B-Series experiments B-1 and B-3 (annular channel experiments), and B-2 (fuel/steel mixture with cylindrical channel) were completed and reported previously. Current B-Series activities have been focused on experiments B-4 and B-5, both of which employ prototypical pin bundle freezing channel geometries. The freezing channel consists of three LMFBF flow subchannels formed by five simulated fuel pins captured in an alumina form (Figure 5.4). Inside the stainless steel clad is a zirconia (ZrO_2) insert that approximates the presence of UO_2 with respect to heat sink and thermal conductivity. Original designs called for either UO_2 or thoria inserts; however, these materials have not been generally available. Zirconia was selected over alumina because of the strong tendency of alumina to form a eutectic with high-temperature UO_2 . The entire length of the flow channel (1.3 m) is to be instrumented with a 20-mm chromel-alumel thermocouples that will provide a time record of the bulk melt flow up the channel.

The initial bulk melt for experiment B-4 will consist of nearly 300 g of pure UO_2 heated in the double-pulse mode to around 3600 K. The double-pulse heating is necessary in order to generate a sufficiently uniform melt temperature with all fuel above the solidus. Experiment B-4 will investigate the upward injection of this melt into the bare clad five-pin bundle which has been preheated to 1173 K such that the interface temperature between the steel clad and the molten UO_2 is above the steel melting point. These conditions then are analogous to those employed in the annular experiment, B-3. Experiment B-5 is scheduled to follow sometime after B-4. The difference in B-5 will be that the freezing channel will consist of five pins with a stainless steel wire wrap. The wire wrap is expected to greatly enhance the potential for steel entrainment through the vigorous convective action of the flowing melt and thereby possibly alter the freezing process.

SIMMER-II has been used to analyze fuel melting in the B-4 geometry with respect to the potential for early fuel move-

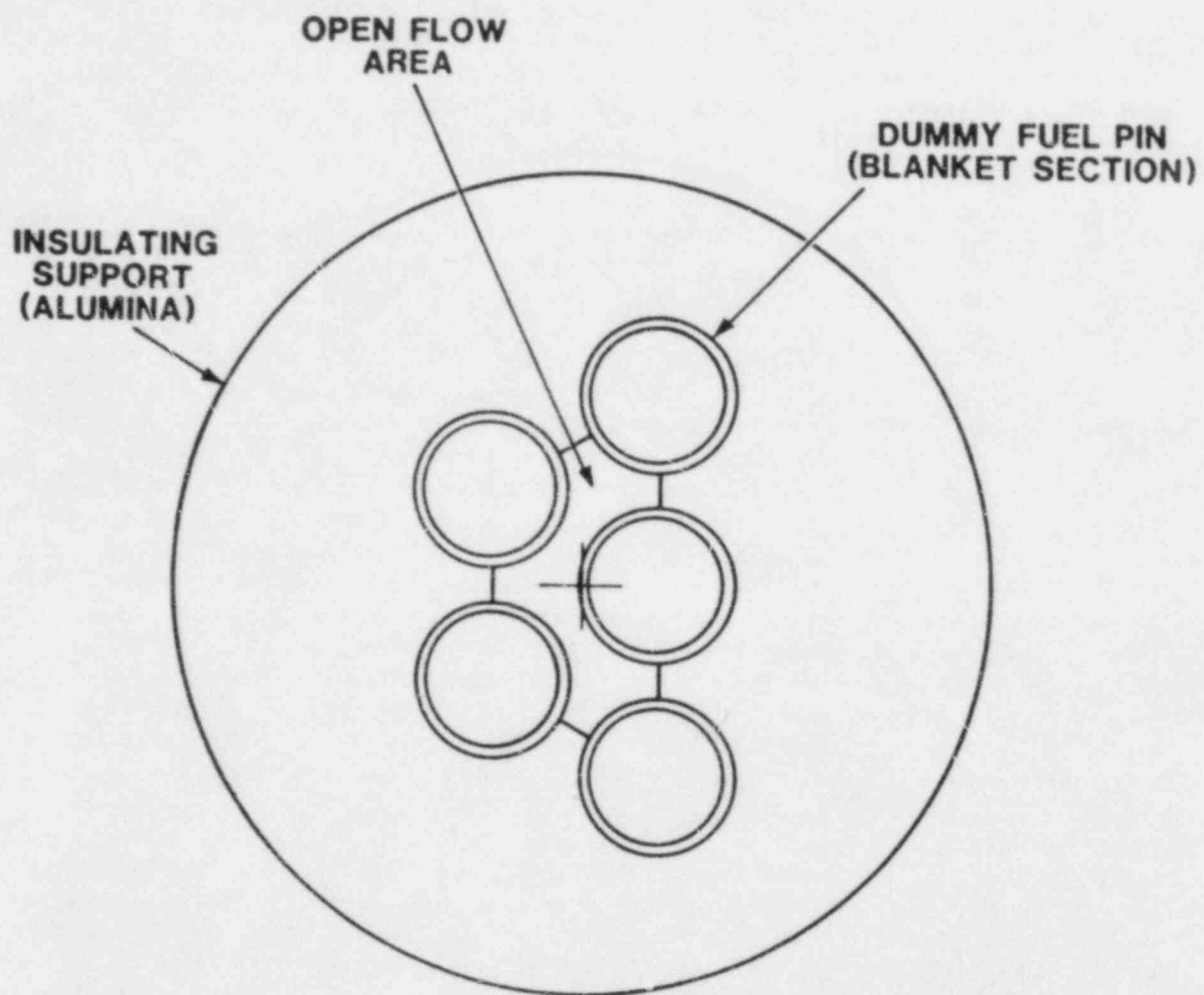


Figure 5.4. Cross Section of the Freezing Channel

ment from pore gas pressurization.⁵⁻¹⁰ A bounding study was performed using the assumptions of either "fully open" or "fully closed" fuel porosity to determine the range of possible effects from the rapid heating of the internal pore gas during the second fuel heating pulse. The results suggest that fuel with tightly trapped porosity gas may experience some early relocation shortly after melting because of a rapid expansion of the gas. A tight gas-liquid momentum coupling aggravates this effect. It was recommended that excessive back pressure in the experiment should be avoided to minimize this effect, because early fuel movement, especially downward movement, is undesirable. The possible use of a melt-away base that might prevent early downward fuel relocation was also examined.

5.2.2 GAP-Series

The GAP series of experiments is directed toward providing data on the potential for penetration and freezing of large amounts of molten core material into the subassembly intercan wall gaps. The fuel melting section of the experiment package has been redesigned to give a substantially higher ACRR coupling factor in order to offset the degradation in reactor yield, which was observed in the G-1 experiment. This has been accomplished by increasing as much as possible the central cavity neutron thermalization and increasing the fuel enrichment, at the expense of some reduction in the melt volume. The new design will involve about 1.5 kg rather than the original 2 kg mass attempted in G-1.

Other changes in the GAP package design will allow for a smoother melt flow transition in the channel entrance region and a more evenly controlled axial preheating of the freezing channel. The majority of the components for the G-2 package have been fabricated and only minor machining tasks remain to be completed. A notable exception to this, however, is the fuel load. Material control regulations imposed upon the fuel fabrication facility at Los Alamos have greatly complicated the filling of multikilogram fuel orders, and delays with cost overruns are likely. The second GAP experiment is planned for sometime early in the second calendar quarter of 1985.

5.2.3 Analytical Efforts

The upcoming B-series experiments will provide more useful experimental information for the evaluation of the SIMMER-II core disruption code in that a substantially more realistic freezing channel structure is being examined. The design of the remaining B-series tests will enhance the possibility of generating molten fuel flow with uptake of steel and/or fuel crust from the melting clad thereby invoking more of the SIMMER-II modeling provisions for melt/structure inter-

action. The increased fuel mass will also discourage the fuel slug blow-through observed in earlier TRAN studies, an occurrence that prevents any observation of plug formation that might occur if the flow regime were not mass limited.

It is anticipated that these experiments may allow for a more thorough examination of the SIMMER-II input options as they affect the predicted experiment outcome, namely, the characteristic size of entrained steel and/or fuel crust "particles" and the effect this has on the bulk melt cooldown and plugging tendency. Following evaluation of simple parameter variations with SIMMER, consideration will be given to using the parameterized code-input control versus control dictated by physical models that predict behaviors in a more complex and realistic manner, such as slurry flow viscosity.

5.3 References

- 5-1. Reactor Safety Research Quarterly Report, January-March 1984. Vol 29, NUREG/CR-3816 (1 of 4), SAND84-1072 (1 of 4), Sandia National Laboratories, Albuquerque, NM, October 1984.
- 5-2. P. R. Henkel, "SANDCMOT Clad Motion Model for LMFBRs," Doctoral Thesis, INR KfK, (to be published 1985).
- 5-3. M. Ishii and M. A. Grolmes, "Prediction of Onset of Entrainment for Liquid Metals," ANS Trans., 21, New Orleans, LA, p. 325, 1975.
- 5-4. S. A. Wright, and E. A. Fischer et al., "In-Pile Fuel Disruption Experiments under Conditions of an Unprotected Loss of Flow Accident in an LMFBR," Journal of Nuclear Technology, (to be published).
- 5-5. P. K. Mast, The Los Alamos Failure Mode (LAFM): A Code for the Prediction of LMFBR Fuel Pin Failure, LA-7161-MS, Los Alamos Scientific Laboratory, Los Alamos, NM, March 1978.
- 5-6. D. H. Worledge, Fuel Fragmentation by Fission Gases During Rapid Heating, SAND80-0328, Sandia National Laboratories, Albuquerque, NM, June 1980.
- 5-7. R. W. Ostensen, FISGAS--A Code for Fission-Gas Migration and Fuel Swelling in an LMFBR Accident, SAND78-1790, Sandia National Laboratories Report, Albuquerque, NM, November 1979.
- 5-8. E. A. Fischer, Comments on the Release of Fission Gas in Molten Fuel in LMFBR Hypothetical Accidents, KfK Report INR 1293, September 1983.
- 5-9. P. R. Henkel, "Numerical Simulation of Model Experiments with the CMOT Code," Proceedings of the LMFBR Safety Topical Meeting, Lyon, France, July 19-23, 1982.
- 5-10. A. Furutani, Internal Memorandum on Preliminary B-4 Calculations, Sandia National Laboratories, Albuquerque, NM, October 26, 1984.

6. POSTACCIDENT HEAT REMOVAL

6.1 Debris Bed Coolability

G. W. Mitchell, 6421; C. A. Ottinger, 6421; T. R. Schmidt, 6421; H. Meister, 6421)

The objective of the Debris Bed Coolability program is to develop experimentally validated models for the behavior of LMFBR core debris after a severe accident. The primary tools in pursuing this objective are coolability experiments using conditions as prototypic as possible so as to determine all the important phenomena needed to develop models to predict coolability limits. Fission heating of UO_2 is the only heating method currently available that can provide an adequate simulation of decay heat for many of the expected debris and coolant configurations. Fission-heated coolability experiments provide the foundation of the debris bed coolability research at Sandia. The program is funded jointly by the USNRC, EURATOM (JRC, Ispra), and the PNC (Japan).

During this quarter, work focused on analysis of the D-10 experiment, and preparations for the D-13 experiment.

6.1.1 D-10 Analysis

The D-10 experiment has provided a large amount of unique data in the field of debris coolability. The limited evaluations performed to date provide some insight as to bed behavior with bottom cooling at high temperatures; however, a more thorough understanding of heat transfer in the D-10 bed will only be gained by additional more complete analyses. The specific areas that appear to be most valuable for continued analyses are data interpretation with respect to current models, bed configuration and cohesion, and dry bed thermal conductivity.

The configuration of the bed during the experiment, especially after the disruption event, is critical to more detailed analyses. This is important to establish the boundary conditions that are the basis for such analyses. The evaluation of the data so far suggests that the disruption event increased the porosity only slightly. The x-ray of the bed taken after the experiment was completed indicating that the bed height varies rather uniformly from 164 to 170 mm, with an average height of 167 mm. This indicates that the average porosity in the bed is about 0.40. A region in the bed extending from 20 to 60 mm, corresponding to the region of maximum temperatures, was evident in the x-ray with density variations that appeared slightly different from the remainder of the bed. Additional data on local porosity, would only be gained by disassembly of the experiment, with detailed PIE, which is not planned.

Although current models are reasonably consistent with the data from D-10 with the bed in a packed state, the data after the disruption event are not consistent with that predicted from a channeled model. Whether or not this is due to uncertainty in the bed configuration could be investigated parametrically with the models. However, a fundamental discrepancy appears in the power that is calculated to be removed by channeling prior to dryout. The depth of channel penetration and the size and number of channels that are assumed in the model should be reevaluated in light of the D-10 data.

The "sticking factor," which appeared to suppress channeling until a substantial overpressure was built up in the bed, has a potentially large influence on the coolability of debris in accident scenarios. An increase in coolability by a factor of 2.5 was observed in D-10. The cause of this cohesion should be found in order to determine the relevant mechanisms that influence the phenomenon. These mechanisms may include particle shape, bed porosity, subcooling, bed chemistry, and bed power. Time-dependent aspects of these parameters should also be studied.

The conductivity of UO_2 debris with sodium vapor present is among the most significant data that will be obtained from the D-10 experiment. Two-dimensional analysis conducted to date indicates that the conductivity is significantly higher than models would predict. The mechanisms that may be responsible for the increase in conductivity are not clear at this time.

An important step in the continuation of this analysis is the ability to properly interpret the experimental data. This interpretation is dependent on the geometry of the dry zone, which affects heat transfer along the instrumentation. The determination of bed configuration will aid in this area. Furnace testing of instrumentation in environments that simulate the conditions existing during the experiment may be helpful in assessing the data. Additional information may be gained by a study of the processes that account for the observed increase in conductivity. These investigations should concentrate on those effects related to the presence of sodium, as the models are consistent with the data for dry debris in argon, investigated in the SNL DC experiments. Based on a more detailed interpretation of the data, two- and three-dimensional thermal analyses should provide an important evaluation of the data in terms of mechanisms that could be responsible for enhanced conductivity. For example, radiation heat transfer should increase as the fourth power of temperature, conduction should be linear with temperature, and mass transport effect may be discernable.

6.1.2 D-13 Preparations

Debris Bed Experiment D-13 is the first experiment designed to study the coolability of stratified particle beds that are cooled both by overlying sodium and from below by structures that support the bed. Maximum debris temperatures in excess of 2500°C are planned to be achieved during the experiment in order to investigate phenomena that might occur at high temperature or with relatively large, dry zones.

A review of plans for the D-13 experiment was presented at the Joint Review Meeting of the LMFBR Coolability Program at Sandia. Representatives of the sponsoring organizations (USNRC, JRC Ispra, and PNC) were present.

The D-13 experiment is identical in design to the previous D-10 experiment. The only differences are in instrumentation and that the bed will be stratified. One of the major changes from D-10 is the elimination of the ultrasonic thermometers from the experiment. The number of C-type thermocouples in the experiment will be increased from 12 to 16 to make up for the elimination of the UTs. Several improvements in the C-type thermocouples are planned including tighter inspection of the rhenium sheaths to avoid flaws, more care in the assembly of the transition from the rhenium sheath to the stainless steel cable, better brazing of the sheaths into the containment feedthroughs, and the addition of potting for the lead wires to avoid breaking during assembly. Additionally, HEDL will perform a performance test to characterize the response of the thermocouple to an environment where the maximum temperature is on the sheath above the junction location.

During the review meeting, it was proposed to form the stratified D-13 bed with 24 layers instead of the 14 layers used in the D-9 experiment. The additional layers will be formed by making a mixture of two adjacent size ranges. This proposal was later accepted by the PNC and the JRC after discussion with European PAHR experts. The UO_2 for each layer in D-13 has been weighed out and mixed where necessary (Table 6.1).

Fabrication of the C-type thermocouples by HEDL is continuing. Four assemblies and one spare are being fabricated, and are expected to be completed in early October.

All of the D-13 components have been fabricated. Modifications to some components, design and machining of fixtures to accommodate the additional thermocouples, and final machining of the crucible basket were accomplished.

Table 6.1

UO₂ Particulate for D-13 Bed

Layer	Layer Wt (g)	2000- 4000 µm	2000- 2800 µm	1400- 2000 µm	1000- 1400 µm	710- 1000 µm	500- 710 µm	355- 500 µm	250- 355 µm	180- 250 µm	125- 180 µm	90- 125 µm	63- 90 µm	45- 63 µm	38- 45 µm
1	263.5	211.7	51.8												
2	260.2	52.9	207.3												
3	205.8		86.4	119.4											
4	238.9			238.9											
5	262.8			119.5	143.3										
6	286.7				286.7										
7	312.4				143.3	169.1									
8	338.1					338.1									
9	360.1					169.0	191.1								
10	382.2						382.2								
11	387.7						191.1	196.6							
12	393.3							393.3							
13	395.0							196.6	198.4						
14	396.9								396.9						
15	369.4								198.5	170.9					
16	341.8									341.8					
17	338.1									170.9	167.2				
18	334.5										334.5				
19	292.2										167.2	125.0			
20	249.9											249.9			
21	229.6											124.9	104.7		
22	209.5												209.5		
23	244.4												104.8	139.6	
24	257.3													139.7	117.6
Total															
Wt (g)	7350.3	264.6	345.5	477.8	573.3	676.2	764.4	786.5	793.8	683.6	668.9	499.8	419.0	279.3	117.6

6.2 Dry Debris Melt Progression

(T. R. Schmidt, 6421; J. E. Kelly, 6425; J. T. Hitchcock, 6421)

In order to establish the release time frame and quantity of radioactive materials following a severe accident, it is necessary to determine the fuel melt dynamics and the characteristics of melting attack by molten fuel on reactor structure and containment barriers should postaccident debris heat removal not be adequate. Simulation of those portions of debris beds undergoing extended dryout and melting is necessary to support modeling activities. This study is aimed at providing such data through in-core experimentation with typical reactor material undergoing sustained, intrinsic heating at temperatures of interest. Models developed are provided to the LWR severe accident code MELPROG as well as to direct analyses of LMFBR debris coolability. This work is cosponsored by the NRC, the Japanese PNC, and EURATOM (JRC, Ispra).

6.2.1 Experimentation

The two experiments in the series have been completed. DC-1 examined the heat transfer of dry, solid urania particulate as a function of temperature up to melt. The urania debris was then heated until half (~1 kg) of the bed formed a molten pool with an overlying void. This experiment was designed to determine the effective thermal conductivity of dry debris at three temperatures on the approach to melt and then to examine the melt progression, pool formation, and heat transfer during the molten phase of the experiment. This is the first experiment to produce a sizeable molten pool of urania with intrinsic heating and full instrumentation.

The DC-2 experiment investigated a dry debris bed composed of UO_2 and stainless steel. It was top and bottom cooled and side insulated to reduce radial heat losses. The experiment was performed in-pile in the ACRR to obtain prototypic internal heating. The debris was contained in two sealed, stainless steel containment vessels and cooled by a closed loop He system, which allowed steady-state operation.

The experiment was carried out in two parts. The heat transfer characteristics of a dry porous particulate bed were studied first. Several steady-state conditions were established spanning the temperature range below melt to obtain data on the bed thermal conductivity. Low-temperature data were obtained for comparison with out-of-pile measurements. High-temperature data provided unique information on the total effective conductivity in the range where radiative heat transfer dominates. In the second phase of the experiment, the bed was taken into steel melt

to observe the agglomeration and migration of steel in a composite bed.

The debris bed in DC-2 was composed of a homogeneous mixture of 1535 g of fully enriched UO_2 and 511 g of stainless steel particulate. Stainless steel fragmented by inert gas was used to minimize the amount of dissolved oxygen. The bed was 70 mm high and 80 mm in diameter with an open porosity of 39.0 percent. The effective particle diameter, calculated by the Fair-Hatch formula, was 270 μm .

Key to this experiment was the bed instrumentation. It consisted of four ultrasonic thermometers and five W/Re thermocouples. Other instrumentation was used throughout the capsule to measure the heat partition and for operational monitoring. The temperature traces from the TCs and UTs are shown in Figures 6.1 and 6.2. The bed power trace is also shown in the TC graph.

The experiment plan involved first attaining three steady-state conditions at different temperatures before any melting occurred. The helium flow rate was held constant and reactor power was adjusted until the desired maximum temperature was attained. The entire package was allowed to equilibrate for at least 1 hr in order to attain a true steady-state condition. Steady-state temperature distributions were measured throughout the bed and capsule with peak bed temperatures at 1173, 1423, and 1673 K (900°, 1150°, and 1400°C). These data will be used to study the thermal conductivity of composite debris.

Following the three steady-state conditions, the reactor power was increased to a high level in order to obtain melting of the steel in the bed. During this step, a peak bed temperature >2773 K (2500°C) was measured. With this high temperature, it was estimated that 90 percent of the steel was molten. Once again, the entire package was allowed to equilibrate to attain a steady-state temperature distribution.

While the main diagnostic for the phenomenological behavior of molten steel is PIE, the thermal data is still useful in obtaining preliminary information. The reactor power required to reach the desired bed temperature was 40 percent above the predicted level, indicating that the steel may have migrated and formed a more coolable configuration. Peak bed temperatures were measured at a radius of 20 mm rather than at the center, indicating that the steel possibly migrated toward the center of the bed.

This is consistent with the results from the SNLA MP-5 experiment involving molten steel in a urania bed heated in the ACRR where the steel tended to agglomerate towards the center of the bed. The migration of the steel is thought to

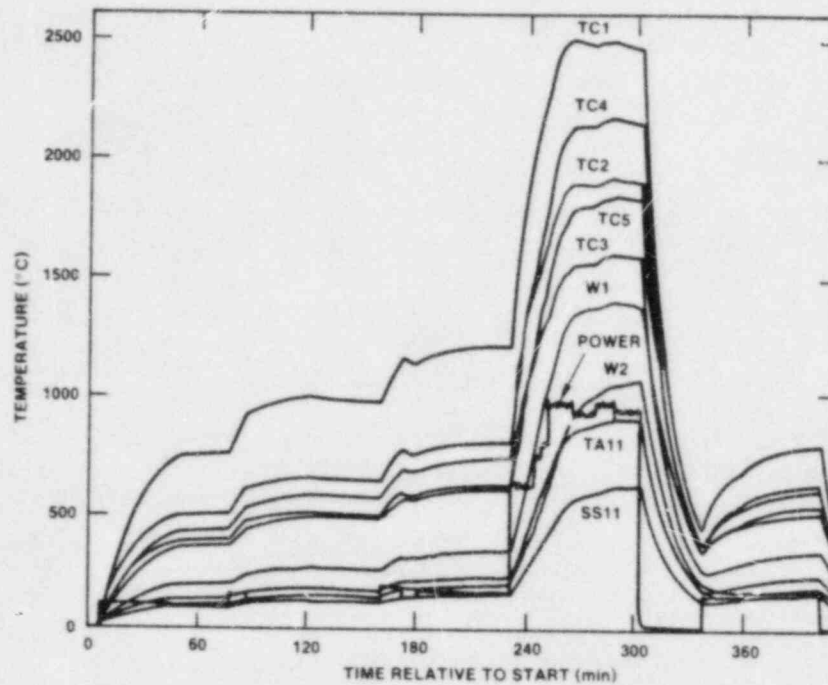


Figure 6.1 DC-2 Thermocouple Data

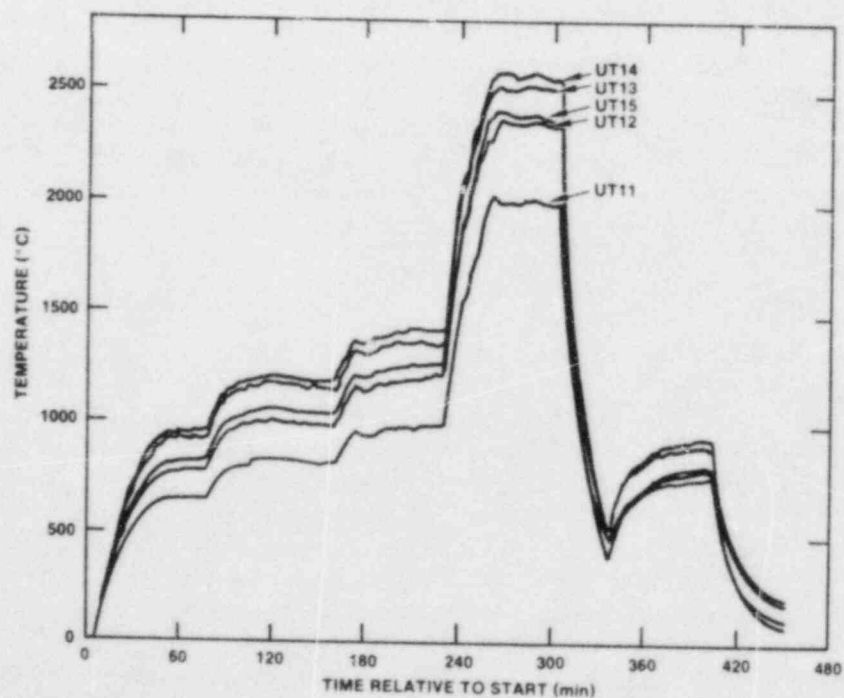


Figure 6.2. DC-2 Ultrasonic Thermometer Data

be strongly affected by the wettability of the urania by the molten steel. With melting of the urania the steel may tend to remain dispersed as small globules.

After the molten debris configuration equilibrated in DC-2, the reactor power was rapidly reduced to a low value. The temperatures in the debris decreased rapidly, and the molten material solidified. After the temperatures were well below the freezing temperature, the reactor power was increased to the same level as used for the third premelt steady-state condition (peak bed temperature (1673 K, 1400°C). The package was then allowed to equilibrate. However, during this step, the peak bed temperature measured 1133 K (860°C), indicating the increase in the gross conductivity of the bed. Following equilibration, the experiment was terminated.

6.2.2 Analysis

Analysis of the thermal data obtained in the DC-1 test has been performed. This data consists of temperature measurements at the various steady-state conditions attained during the test throughout the experimental package. Emphasis has been placed on developing an accurate computer model of the experimental package in order to predict the data. One reason for this effort was that the boundary conditions for the bed were not measured. These are important for determining the temperature distribution within the bed and hence, the bed conductivity. By predicting the temperatures throughout the package, the boundary conditions can be accurately determined by interpolation. The second reason was that the heat flow balance and distribution can only be determined by calibrating a computer model with the measurements. The heat flow balance is important for determining the actual bed power level; the distribution of the heat flow is important for determining the partitioning of the heat within the bed. This is especially important after the molten pool is formed. The heat flow distribution can be obtained from the computer model if the model accurately predicts the temperature distribution.

The two-dimensional heat transfer computer code, TAC2D, has been used in this analysis. This code has excellent flexibility in both the geometrical modeling and in material property modeling. Standard properties were taken for all materials, and the dimensions were based on "as-built" measurements. The key areas of uncertainty were in the sizes of the gaps and the conductivity of the bed.

The conductivity of the bed was calculated using the Willhite/Luikov model, which combined conduction and radiation in the bed. This model had been identified as representing a lower bound to the conductivity. In the preliminary analysis, this model was believed to have overpredicted the conductivity. However, subsequent

analysis revealed that the effective diameter used in the radiation term was too large. By using an effective diameter based on the Fair-Hatch formula, much better agreement is obtained in the measured versus predicted conductivities.

Currently, the model can accurately predict the temperatures measured for the third steady-state condition, but needs to be modified for the other steady-state conditions. Based on these current results, this will not be a major problem. Once the models are established, more detailed analysis of bed conductivity and heat partitioning can be made.

The DC-1 experiment has been x-rayed and indicates that a molten pool containing about 50 percent of the debris (1 kg) was formed in the lower part of the crucible, leaving a sizeable void above the pool and bounded by a fairly uniform dense crust approximately 5 mm in thickness. The overlying crust is intact and may be partially supported by the instrumentation penetrating the experiment.

A two-dimensional meltdown model has been developed at Sandia to calculate such melt phenomena. This model calculates the debris heatup, melting, relocation, crust and void formation, as well as crust remelt, within a debris bed. There are two stages of the postdryout behavior of the debris that the model is designed to calculate. First, the model calculates the transient heatup of the dry debris by solving a mixture energy equation for the debris. This equation includes heat sources in the debris due to decay heat and heat transfer due to conduction, convection, and radiation. From this analysis the temperature distribution, as a function of time, can be calculated for the debris. Second, the model calculates the melting of the debris and relocation of the molten debris within the debris bed. The relocation step involves using simplified laws for porous flow to predict the behavior of the molten material. From this analysis, the porosity distribution of the debris is calculated as a function of time. The model uses two-dimensional geometry (cylindrical) since radial heat flows are important in the experiments. The model accurately predicted the final configuration of the DC-1 experiment to include such details as uranium freezing on instrumentation penetrations in the crust area because of increased heat transfer up the instrumentation sheaths. The model has been incorporated into the LWR melt-progression code MELPROG.

In summary, these experiments are providing valuable data for model development and validation for use in accident analyses involving debris coolability, heat transfer, melt progression, and molten pool formation and behavior. The analysis is continuing and plans are being formulated for the postirradiation examination of the two experiments.

DISTRIBUTION:

U.S. Government Printing Office
Receiving Branch
(Attn: NRC Stock)
8610 Cherry Lane
Laurel, MD 20707
(370 copies for R3 and R7)

U.S. Nuclear Regulatory
Commission (10)
Division of Accident Evaluation
Office of Nuclear Regulatory
Research
Washington, DC 20555
Attn: C. N. Kelber
G. Marino
K. G. Steyer
P. Worthington
R. T. Curtis, Chief,
Containment Systems
Research Branch
B. Burson, Containment
Systems
Research Branch
M. Silberberg, Chief, Fuel
Systems
Research Branch
L. Chan, Fuel Systems
Research Branch
J. Telford, Fuel Systems
Research Branch
R. W. Wright, Fuel Systems
Research Branch

U.S. Nuclear Regulatory
Commission (12)
Office of Nuclear Reactor
Regulation
Washington, DC 20555
Attn: V. Benaroya
W. R. Butler
G. W. Knighton
J. K. Long
J. F. Meyer
R. Palla
K. I. Parczewski
G. Quittschreiber
Z. Rosztoczy
T. M. Su
C. G. Tinkler
D. D. Yue

R. W. Barber
U.S. Department of Energy
Office of Nuclear Safety
Coordination
Washington, DC 20545

U.S. Department of Energy (2)
Albuquerque Operations Office
PO Box 5400
Albuquerque, NM 87185
Attn: J. P. Roeder, Director,
Transportation Safeguards
Division
J. A. Morely, Director
Energy Research
Technology Division
For: C. B. Quinn
R. N. Holton

Argonne National Laboratory
9700 South Cass Avenue
Argonne, IL 60439
Attn: H. M. Chung

Battelle Columbus Laboratory
505 King Avenue
Columbus, OH 43201
Attn: R. Denning

Brookhaven National Laboratory (2)
Upton, NY 11973
Attn: R. A. Vari
T. Pratt

Los Alamos National Laboratory
PO Box 1663
Los Alamos, NM 87545
Attn: M. Stevenson

Los Alamos National Laboratory
TD-7 M/s-231
Los Alamos, NM 87545
Attn: Dr. W. Stratton

University of Michigan
Nuclear Engineering Department
Ann Arbor, MI 48104

University of Michigan
Department of Aerospace
Engineering
Ann Arbor, MI 47109

DISTRIBUTION: (Continued)

Purdue University
School of Nuclear Engineering
West Lafayette, IN 47907
Attn: T. G. Theofanous

McGill University
315 Querbes
Outremont, Quebec
Canada, H2V 3W1
Attn: J. H. S. Lee

Northwestern University
Chemical Engineering Department
Evanston, IL 60201
Attn: S. G. Bankoff

UCLA
Nuclear Energy Laboratory
405 Hilgard Avenue
Los Angeles, CA 90024
Attn: I. Catton

University of Wisconsin
Nuclear Engineering Department
1500 Johnson Drive
Madison, WI 53706
Attn: M. L. Corradini

AEC Ltd. (2)
Whiteshell Nuclear Research
Establishment
Pinawa, Manitoba, Canada
Attn: D. Liu
H. Tamm

Projekt Schneller Brueter (4)
Kernforschungszentrum Karlsruhe
GMBH
Postfach 3640
D75 Karlsruhe
Federal Republic of Germany
Attn: Dr. Kessler
Dr. Heusener
Dr. S. Hagen
Dr. J. P. Hosemann

Gesellschaft fur
Reaktorsicherheit (GRS)
Postfach 101650
Glockengasse 2
5000 Koeln 1
Federal Republic of Germany

Institute fur Kernenergetik
und Energiesysteme (2)
University of Stuttgart
Stuttgart
Federal Republic of Germany
Attn: G. Froehlich
M. Buerger

Battelle Institut E. V.
Am Roemrhof 35
6000 Frankfurt am Main 90
Federal Republic of Germany
Attn: Dr. Werner Baukal

Kraftwerk Union (2)
Hammerbacher strasse 12 14
Postfach 3220
D-8520 Erlangen 2
Federal Republic of Germany
Attn: Dr. K. Hassman
Dr. M. Peehs

UKEA Safety and Reliability
Directorate (4)
Wigshaw Lane
Culcheth
Warrington WA3 4NE
Cheshire
England
Attn: Mr. J. H. Gittus (2)
J. J. Hayn (2)

AERE Harwell
Didcot
Oxfordshire OX11 0RA
England
Attn: J. R. Matthews,
Theoretical Physics
Division

UKEA (2)
Risley
Warrington WA3 6AT
Cheshire
England
Attn: B. Cowking, FRDD
D. Hicks, TRDD

DISTRIBUTION: (Continued)

Dr. F. Briscoe
Culham Laboratory
Culham
Abingdon
Oxfordshire OX14 3DB
UK

UKEA AEA Winfrith (4)
Dorset DT2 8DH
UK

Attn: R. Potter
A. J. Briggs
M. Bird
T. Wickett

Simon Engineering Laboratory
University of Manchester
M139PL,
United Kingdom
Attn: Prof. W. B. Hall

National Nuclear Corp. Ltd.
Cambridge Road
Whetstone, Leicester, LE83LH
United Kingdom
Attn: R. May

CNEN NUCLIT
Rome, Italy
Attn: A. Morici

Dipartimento Di Costruzioni
Meccaniche E Nucleari
Facolta Di Ingegneria
Via Diotisalvi 2
56100 - Italy
Attn: M. Carcassi

Director of Research, Science
Education
CEC
Rue De La Loi 200
1049 Brussels
Belgium
Attn: B. Tolley

Power Reactor Nuclear Fuel
Development Corporation (PNC)
Fast Breeder Reactor
Development Project (FBR)
9-13, 1-Chome, Akasaka
Minato-Ku, Tokyo
Japan
Attn: Dr. Watanabe

Japan Atomic Energy Research
Institute
Tokai-mura, Naka-gun, Ibaraki-ken,
319-11
Japan
Attn: Dr. M. Hirata
Director of Nuclear Safety
Research Center

General Electric Corporation
Advanced Reactor Systems
Department
P. O. Box 3508
Sunnyvale, CA 94088
Attn: M.I. Temme, Mgr.,
Probabilistic Risk Assessment

General Electric Corporation
175 Curtner Avenue
Mail Code N 1C157
San Jose, CA 95125
Attn: K. W. Holtzclaw

Power Authority State of NY
10 Columbus Circle
New York, NY 10019

Offshore Power System
8000 Arlington Expressway
Box 8000
Jacksonville, FL 32211

Electric Power Research Institute
(3)
3412 Hillview Avenue
Palo Alto, CA 94303
Attn: J. J. Haugh
K. A. Nilsson
G. Thomas

DISTRIBUTION: (Continued)

Fauske Associates
627 Executive Drive
Willow Brook, IL 60521
Attn: R. Henry

Mississippi Power & Light
PO Box 1640
Jackson, MS 39205
Attn: S. H. Hobbs

Duke Power Co. (2)
PO Box 33189
Charlotte, NC 28242
Attn: F. G. Hudson
A. L. Sudduth

Westinghouse Corporation (3)
PO Box 355
Pittsburgh, PA 15230
Attn: N. Liparulo
J. Olhoeft
V. Srinivas

General Physics Corporation
1000 Century Plaza
Columbia, MD 21044
Attn: Chester Kupiec

TVA
400 Commerce W9C157-CD
Knoxville, TN 37902
Attn: Wang Lau

EG&G Idaho
Willow Creek Building, W-3
PO Box 1625
Idaho Falls, ID 83415
Attn: Server Sadik

Dr. Roger Strehlow
505 South Pine Street
Champaign, IL 61820

Applied Sciences Association, Inc.
PO Box 2687
Palos Verdes Pen., CA 90274
Attn: D. Swanson

Acurex Corporation
485 Clyde Avenue
Mountain View, CA 94042

Astron
2028 Old Middlefield Way
Mountain View, CA 94043

Bechtel Power Corporation
PO Box 3965
San Francisco, CA 94119
Attn: R. Tosetti

Thompson Associates
639 Massachusetts Avenue
Third Floor
Cambridge, MA 02139
Attn: Timothy Woolf

Factory Mutual Research
Corporation
PO Box 688
Norwood, MA 02062
Attn: R. Zalosh

Institute of Nuclear Power
Operation
Suite 1500
1100 Circle 75 Parkway
Atlanta, GA 30339
Attn: Henry Piper

Sandia Distribution:

1131 W. B. Benedick
1510 J. W. Nunziato (1)
Attn: 1512 J. C. Cummings
1512 J. E. Shepherd
1513 S. N. Kempka
1513 A. C. Ratzel
1530 L. W. Davison (1)
Attn: 1534 J. R. Asay
1541 H. C. Hardee
1830 M. J. Davis
1840 R. J. Eagan (1)
Attn: 1846 R. A. Sallach
1846 R. K. Quinn
3141 C. M. Ostrander (5)
3151 W. L. Garner
6400 A. W. Snyder
6410 J. W. Hickman
6411 A. Benjamin
6412 A. L. Camp
6420 J. V. Walker (2)
6420 M. M. Watkins

DISTRIBUTION: (Continued)

Sandia Distribution: (Continued)

6421 T. R. Schmidt	6427 J. T. Hitchcock
6422 D. A. Powers	6427 M. S. Krein
6422 J. E. Brockmann	6427 B. W. Marshall, Jr.
6422 R. M. Elrick	6427 L. S. Nelson
6422 J. E. Gronager	6427 M. P. Sherman
6422 W. W. Tarbell	6427 S. R. Tieszen
6423 P. S. Pickard	6427 C. C. Wong
6423 A. Furutani	6440 D. A. Dahlgren
6423 R. O. Gauntt	6449 K. D. Bergeron
6423 A. C. Marshall	6450 J. A. Reuscher (1)
6423 K. Muramatsu	Attn: 6451 T. F. Luera
6423 S. A. Wright	6452 M. Aker
6425 W. J. Camp	6454 G. L. Cano
6425 D. R. Bradley	7530 T. B. Lane (1)
6425 W. Frid	Attn: 7537 N. R. Keltner
6425 J. E. Kelly	7537 R. U. Acton
6425 A. W. Reed	7537 T. Y. Chu
6425 M. F. Young	7550 T. S. Edrington (1)
6427 M. Berman	Attn: 7551 O. J. Burchett
	7552 J. H. Gieske
	8024 M. A. Pound

NRC FORM 335 (2-84) NRCM 1102 3201, 3202 SEE INSTRUCTIONS ON THE REVERSE		U.S. NUCLEAR REGULATORY COMMISSION		1. REPORT NUMBER (Assigned by TIDC add Vol. No., if any) NUREG/CR-3816 (3 of 4) SAND84-1072 (3 of 4)	
2. TITLE AND SUBTITLE REACTOR SAFETY RESEARCH QUARTERLY REPORT July-September 1984				3. LEAVE BLANK	
5. AUTHOR(S) Reactor Safety Research Department				4. DATE REPORT COMPLETED MONTH: March YEAR: 1985	
7. PERFORMING ORGANIZATION NAME AND MAILING ADDRESS (Include Zip Code) Sandia National Laboratories Albuquerque, NM 87185				6. DATE REPORT ISSUED MONTH: May YEAR: 1985	
10. SPONSORING ORGANIZATION NAME AND MAILING ADDRESS (Include Zip Code) Division of Accident Evaluation Office of Nuclear Regulatory Research USNRC Washington, DC 20555				8. PROJECT/TASK/WORK UNIT NUMBER 9. FIN OR GRANT NUMBER A-1016, etc.	
12. SUPPLEMENTARY NOTES				11a. TYPE OF REPORT quarterly - technical b. PERIOD COVERED (Inclusive dates) July-September 1984	
13. ABSTRACT (200 words or less) <p>Sandia National Laboratories is conducting, under USNRC's sponsorship, phenomenological research related to the safety of commercial nuclear power reactors.</p> <p>The overall objective of this work is to provide NRC a comprehensive data base essential to (1) defining key safety issues, (2) understanding risk-significant accident sequences, (3) developing and verifying models used in safety assessments, and (4) assuring the public that power reactor systems will not be licensed and placed in commercial service in the United States without appropriate consideration being given to their effects on health and safety.</p> <p>Together with other programs, the Sandia effort is directed at assuring the soundness of the technology base upon which licensing decisions are made.</p> <p>This report describes progress in a number of activities dealing with current safety issues relevant to both light water and breeder reactors. The work includes a broad range of experiments to simulate accidental conditions to provide the required data base to understand important accident sequences and to serve as a basis for development and verification of the complex computer simulation models and codes used in accident analysis and licensing reviews. Such a program must include the development of analytical models, verified by experiment, which can be used to predict reactor and safety system performance under a broad variety of abnormal conditions.</p>					
14. DOCUMENT ANALYSIS - a. KEYWORDS/DESCRIPTORS b. IDENTIFIERS/OPEN ENDED TERMS				15. AVAILABILITY STATEMENT u 16. SECURITY CLASSIFICATION (This page) u (This report) u 17. NUMBER OF PAGES 187 18. PRICE	

120555078677 1 13N1R31R7
US NRC
ADM-DIV OF TIDC
POLICY & PUB MGT BR-PDR NUREG
W-501
WASHINGTON
DC 20555